MICROSTRUCTURE AND PROPERTIES OF REFRACTORY HIGH ENTROPY ALLOYS FABRICATED BY LASER ADDITIVE MANUFACTURING

YONGYUN ZHANG

PhD

The Hong Kong Polytechnic University

2025

The Hong Kong Polytechnic University

Department of Industrial and Systems Engineering

Microstructure and Properties of Refractory High Entropy Alloys Fabricated by Laser Additive Manufacturing

Yongyun ZHANG

A thesis submitted in partial fulfillment of the
requirements for the degree of Doctor of Philosophy

August 2024

CERTIFICATE OF ORIGINALITY

I hereby declare that this thesis is my own work and that, to the best of my knowledge and belief, it reproduces no material previously published or written, nor material that has been accepted for the award of any other degree or diploma, except where due acknowledgement has been made in the text.

______________________(Signed)

____Yongyun ZHANG___(Name of student)

Abstract

Refractory high-entropy alloys (RHEAs), made with refractory elements, offer excellent strength, ductility, wear resistance, and high-temperature stability, making them potential for industrial applications. However, traditional fabrication methods, however, struggle with the direct fabrication of RHEAs for industrial applications. Laser additive manufacturing (LAM) offers a modern solution that efficiently melts refractory metals, refines grains, and adjusts compositions. Despite this, LAM-fabricated RHEAs often have defects, resulting in poor mechanical properties across temperature ranges. Therefore, improving the properties of RHEAs across a large-temperature range via LAM remains a critical challenge.

Understanding the mechanical properties, especially tensile properties, of LAM-fabricated RHEAs is crucial for their potential engineering applications. In our work, we fabricated a $Ti_{42}Hf_{21}Nb_{21}V_{16}$ (T42) RHEA through the Laser Engineered Net Shaping (LENS) method, which exhibits a high yield strength (over one gigapascal) and a significant high tensile strain (around 22.5%), outperforming the as-cast counterpart. The unique nanostructure and doped interstitial atoms produced after the LENS procedure provide an alternative solution to the long-standing issue of the strength-ductility trade-off in RHEAs.

The tensile properties of the LENS-fabricated T42 alloys under elevated temperatures were further investigated, showing good tensile strength stability over a broad temperature spectrum. The T42 alloy has large local lattice strain, and elastic

moduli stability across different temperatures, demonstrating good tensile strength across a broad temperature range. This approach of inducing lattice distortions and maintaining stable elastic constants offers a new way to produce RHEAs capable of high-temperature performance.

The LENS-fabricated T42 RHEA has also demonstrated superior wear resistance at elevated temperatures. The oxidation process of the alloy was examined. It was found that protective oxide nanolayers were formed in the early stage, which then developed into a polycrystalline oxide coating under stress. This significantly reduced wear rates from 2.69×10^{-4} $mm^3/(N \cdot m)$ at room temperature to just 6.90×10^{-7} $mm^3/(N \cdot m)$ at 600°C. These findings show that using LAM to fabricate RHEAs with enhanced high-temperature wear resistance is promising for creating durable coatings at elevated temperatures.

However, the T42 alloy experiences significant oxide formation when the temperature is increased to 800 °C, reducing its mechanical strength and wear resistance. To address this, an in-situ alloying technique with Al was applied to the T42 alloy through LENS, resulting in an Al-doped RHEA with enhanced strength and ductility at high temperatures compared to the T42 counterpart. Al induces even larger lattice distortion, and bolsters strength, but above 600 °C, the yield strength decreases due to a softening effect from a reduced elastic modulus. The addition of Al improves the plasticity of the alloy by forming a dense oxide layer that blocks oxygen diffusion. This approach of in-situ alloying via LENS offers a solution for developing RHEAs with

superior high-temperature capabilities, whilst maintaining robust mechanical properties under elevated temperatures.

This research presents significant advancements in the study of RHEAs fabricated through the LENS approach. Our work successfully fabricates RHEAs with superior performance across a range of temperatures. We have overcome the tensile strength-ductility trade-off in our T42 alloy at room temperature. Furthermore, we provided insights into its high-temperature behaviors relating to the lattice distortions or the oxidation sequence. By employing in-situ alloying, we have further improved the mechanical properties of the fabricated alloy. These findings not only deepen our understanding of RHEAs under diverse conditions but also pave the way for the development of advanced materials, unlocking new possibilities for their industrial applications.

Publications during the PhD period

1. **Zhang, Y.**, Ye, S., Ke, H.*, Chan, K.C.*, Wang, W., 2023. In situ synthesis of N-containing CoCrFeNi high entropy alloys with enhanced properties fabricated by selective laser melting. Mater. Des. 229, 111891.
2. **Zhang, Y.**, Qin, B., Chan, K.C*., Lupoi, R., Yin, S*., Xie, Y., Ye, S., Yu, P., Ke, H., Wang, W., 2023. Enhancement on mechanical properties of CoCrNi medium entropy alloy via cold spray additive manufacturing associated with sintering. J. Manuf. Process. 94, 413–423.
3. **Zhang, Y.**, Yang, C., Ke, H.*, Chan, K.C.*, Wang, W., 2024. A study on the microstructure and mechanical behavior of CoCrFeNi high entropy alloy fabricated via laser powder bed fusion: Experiment and crystal plasticity finite element modelling. Mater. Sci. Eng. A. 893, 14611.
4. **Zhang, Y.**, Qin, B., Ouyang, D., Liu, L., Feng, C., Yan, Y., Ye, S., Ke, H.*, Chan, K.C.*, Wang, W., 2024. Strong yet ductile refractory high entropy alloy fabricated via additive manufacturing. Addit. Manuf. 81, 104009.
5. **Zhang, Y.**, Yu, K., Qin, B., Yang, C., Ye, S., Feng, C., Zhang, F., Ouyang, D., Liu, L., Ke, H.*, Chan, K.C.*, Wang, W., 2024. Origins of strength stabilities at elevated temperatures in additively manufactured refractory high entropy alloy. Mater. Sci. Eng. A. 915, 147225.
6. **Zhang, Y.**, Yang, C., Tong, X., Zhou, J., Liu, L., Xiao, M., Ke, H.*, Chan, K.C.*, Wang, W.*, 2024. Oxidation sequence modulation induced superior high-

temperature tribological performance of the Ti-Hf-Nb-V refractory high entropy alloy fabricated through directed energy deposition. Rare Met. (Accepted)

7. **Zhang, Y.**, et al., Ke, H.*, Chan, K.C.*, Wang, W., Order modulation strategy of strong and ductile body-centered-cubic multi-principal elemental alloys by additive manufacturing. To be submitted.

Acknowledgements

I extend my deepest appreciation to my supervisors, Prof. Chan K.C. and Prof. Wang Weihua, for their exceptional guidance, steadfast support, and mentorship throughout my academic journey. Their profound knowledge, consistent encouragement, and unwavering dedication have been pivotal in my academic and professional growth. I am immensely thankful for their sagacity, patience, and commitment, which have played a crucial role in the fruition of this project.

My heartfelt thanks go to Prof. Ke Haibo of the Amorphous Materials Group at SLAB for his invaluable support during this research. The resources provided by SLAB have been fundamental to the project's success. I am also grateful for the financial support and access to essential research facilities and equipment that have facilitated the progress of my work. Additionally, I acknowledge PolyU for granting access to its cutting-edge equipment, facilities, and resources, which have been vital to my research achievements.

I am deeply thankful to Dr. Ye Shulong from MSU-BIT for engaging in enriching discussions. My thanks also go to Prof. Zhang Fuxiang from SLAB for his specialized knowledge in synchrotron radiation, and to Mr. Feng Shihui from SU for his assistance with TEM. Furthermore, I would like to thank Dr. Yu Kaiping from HKU and Dr. Ren Chuanxi for their insightful input and support. I would also like to convey my sincere thanks to Dr. Ouyang Di, Dr. Li Jiaqiang, Dr. Chen changyong, Dr. Wang Yilin, Mr.

Qin Bailiang, Miss Yang Congrui, Mr. Wang Pengbo, and all the members of the Amorphous Materials group at SLAB. Thank you all.

Table of contents

List of figures and tables

Chapter 1 Introduction

1.1 Research background

The traditional approach to alloy design involves selecting a primary alloying element as the matrix and enhancing its structure and properties by incorporating secondary elements [1]. However, this conventional methodology falls short of meeting the increasing demand for advanced alloys with unique properties. The innovative concept of high-entropy alloys (HEAs) [2,3], also known as multi-principal element alloys, challenges the traditional design paradigm, and positions them at the forefront of metallic materials research [4]. HEAs can be broadly categorized by their crystal structures into face-centered cubic (fcc) and body-centered cubic (bcc) types [5], with the latter often comprising refractory elements and thus termed refractory high-entropy alloys (RHEAs) [6]. The high entropy effect [2] in these multi-component systems favors the formation of a single-phase solid solution, endowing them with exceptional properties such as superior strength and ductility [7], outstanding wear resistance [8], high-temperature oxidation resistance [9], and thermal stability [10]. These attributes extend their range of potential applications from the automotive to the aerospace industries [11].

Currently, HEAs are primarily fabricated through methods such as vacuum arc melting [2], powder metallurgy [12,13], etc. However, the high melting points and significant melting point disparities among RHEA components lead to challenges such as macro-segregation, coarse microstructures [14,15], and severe matrix decomposition

[16] during traditional manufacturing processes. These issues are particularly pronounced for larger alloy components, posing a significant hurdle for the industrialization of RHEAs [17]. Laser additive manufacturing technology, an advanced rapid prototyping technique, offers a solution for designing and producing complex parts [18,19]. This process typically utilizes powder as the raw material and employs computer software to slice digital model data into scanning paths, which are then used to melt and accumulate the powder layer by layer from the bottom up [20]. The flexibility and advantages of laser additive manufacturing for RHEAs include, but are not limited to, high energy density for melting refractory metal powders [21], rapid solidification for the formation of fine grains [14,15], and design freedom for cost reduction [18,19]. Moreover, the composition can be adjusted as required to achieve direct near-net shaping of alloy components, such as high-throughput fabrication of gradient materials [22–24], laying the groundwork for the preparation of RHEAs.

It has been just over a decade since the concept of RHEAs was first introduced [6], and research into their fabrication through laser additive manufacturing has only begun in recent years [14,21–29]. Given the generally poor room-temperature plasticity of most RHEAs, there are limited studies using laser additive manufacturing, with no clear and systematic classification introduced. The mechanical properties of most laser additively manufactured RHEAs are inadequate [25], particularly in terms of tensile ductility—a key indicator of industrial potential [25], not to mention their performance at high temperatures. To address the enduring challenge of balancing strength and ductility in engineering materials, we have now produced RHEAs with an improved synergy of tensile strength and ductility using a laser-engineered net shaping (LENS) process, and we also investigated the high-temperature performance of these RHEAs. An in-situ alloying fabrication process has been proposed to enhance the high-temperature capabilities of RHEAs, providing valuable insights for further research and large-scale production of RHEAs using laser additive manufacturing.

1.2 Research Objectives

The primary goal of this research study is to fabricate RHEA samples that exhibit an excellent balance between strength and ductility, as well as robust performance across a wide temperature range. The aim is to develop novel RHEA materials with enhanced mechanical and tribological properties both at room and at elevated temperatures. The project is structured into the following four key areas:

(1) To overcome the long-standing tensile strength-ductility trade-off in $Ti_{42}Hf_{21}Nb_{21}V_{16}$ (referred to as T42) RHEA fabricated via the LENS process.

(2) To elucidate the mechanical behavior and the role of large lattice distortion in additively manufactured T42 RHEA at elevated temperatures using a combination of experimental and simulation methods.

(3) To investigate the origins of oxidation in the fabricated T42 RHEA, and apply an oxidation sequencing strategy to achieve excellent wear resistance at elevated temperatures.

(4) To employ in-situ alloying in RHEA systems via LENS to further enhance the mechanical properties at room and elevated temperatures and to explore the underlying mechanisms.

1.3 Outline of the thesis

This thesis is organized into nine chapters. The current chapter provides an introduction to RHEAs and additive manufacturing techniques, as well as the primary research gaps and objectives.

Chapter 2 offers a comprehensive literature review, highlighting various aspects of this project and identifying key research gaps that can be addressed through additive manufacturing and the unique properties of RHEAs.

Chapter 3 describes the research methodology, including the materials and methods used for fabrication, property measurement, and microstructure characterization. Theoretical computational approaches such as first principles, phase diagram calculations, and crystal plasticity finite element modeling are also covered.

Chapters 4, 5, 6 and 7 demonstrate the main research results and discussion of fabricating RHEAs with improved performance in terms of mechanical properties, tribological performance, at room as well as elevated temperatures.

Chapter 8 provides a summary and conclusions drawn from the thesis.

Chapter 9 outlines future research directions for investigating RHEAs fabricated using laser additive manufacturing methods.

Chapter 2 Literature Review

2.1 Overview

This chapter provides a comprehensive overview of the scholarly research on the topic of this doctoral project. It begins with an introductory overview in Section 2.1, setting the stage for the detailed discussions that follow. Section 2.2 delves into the concept of HEAs, covering their definition, composition design, development, and distinctive characteristics. Following this, Section 2.3 explores the multifaceted aspects of RHEAs, such as compositional design, microstructure and phase composition, mechanical properties, and the mechanisms behind their strengthening and toughening. The focus then shifts to AM-fabricated RHEAs in Section 2.4, providing an in-depth look at their specific features. Section 2.5 presents the properties of RHEAs fabricated through laser additive manufacturing, offering a detailed examination of this particular method. The chapter concludes with Section 2.6, which summarizes the key findings and insights gleaned from this systematic review.

2.2 High entropy alloy concept

2.2.1 Definition of HEAs

Traditional alloy design typically involves using one or two main elements and adding a few other elements to modify the properties of the alloy. However, this approach is becoming less effective in meeting the growing demand for better properties, leading to a bottleneck in alloy design. There is a common misconception that adding many alloying elements leads to the formation of brittle compounds, making it difficult to develop new materials. In contrast, using multiple main components in an alloy system can create a high entropy effect and promote the formation of a signle solid solution material with a simple lattice structure, rather than a brittle precipitate. The HEA was introduced in 2004 by Yeh et al. [2], involving the mixing of five or more alloying elements in equimolar or near-equimolar ratios. This concept has expanded the range of possible HEA designs, with alloys containing more than four multi-components also considered HEAs [30]. Compared to traditional alloys, HEAs offer excellent mechanical properties [7], corrosion resistance [31], and other unique characteristics, expanding their potential industrial applications and making them cutting-edge materials with high academic value.

HEAs can be categorized into three types: fcc [2], bcc [32], and hexagonal close-packed (hcp) [33] structural HEAs. The high mixing entropy in HEAs typically leads to the formation of a simple solid solution structure, which counteracts the enthalpy contribution to form intermetallic compounds [3]. The entropy, reflecting the degree of chaos in a system, can be calculated using Boltzmann theory [30]:

$$\Delta S_{conf} = k \cdot ln\, w \tag{2. 1}$$

where k = 1.38×10^{-13}J/K is the Boltzmann constant, w represents the number of microstates in a system. Hence, a higher number of microstates in a system results in increased entropy. In solid solution alloys, the configuration entropy induced by the atomic mixing arrangement dominates the overall entropy. Therefore, the mixing entropy in a system can be counted as the configuration entropy and is expressed as follows:

$$\Delta S_{mix} = -R[c_1 lnc_1 + \cdots + c_n lnc_n] = -R\sum_{i=1}^{n} c_i ln\, c_i \tag{2. 2}$$

where R=8.314 J/(K • mol) is the ideal gas constant, c_i is the atomic fraction of the i^{th} element. When $c_1 = c_2 = \cdots = c_n$, the mixing entropy can reach a maximum and is presented as follows:

$$\Delta S_{mix} = R\left[\frac{1}{n} ln\, n + \frac{1}{n} ln\, n \ldots + \frac{1}{n} ln\, n\right] = Rln\, n \tag{2. 3}$$

when the ΔS_{mix}=1.5R was considered as the threshold to differentiate the high entropy alloy and medium entropy alloy [2].

2.2.2 Composition design of HEAs

The formation of solid solution phases in HEAs depends on several factors, including mixing enthalpy (ΔH_{mix}), atomic size difference (δr), and the relative contribution of the mixing enthalpy and mixing entropy (Ω). Yeh et al. [2] discovered that in most alloy systems, the high mixing entropy of five elements with the same atomic ratio balances the mixing enthalpy and favors the formation of a solid solution phase. However, the maximum mixing entropy alone is not always sufficient to form a solid solution phase in some RHEAs [34]. The formation of solid solutions in HEAs results from a decrease in the mixing enthalpy and an increase in the mixing entropy, which reduces the Gibbs free energy. The mixing enthalpy (ΔH_{mix}) is mainly determined by the interaction between different elements shown in Eq. 2.4 [35],

$$\Delta H_{mix} = \sum_{j\neq i}^{n} \sum_{i=1}^{n} 4\Delta H_{ij}^{m} x_i x_j \tag{2. 4}$$

where ΔH_{ij}^{m} denotes the mixing enthalpy of the atomic pair *i-j,*and x_i and x_j are the atomic fractions of ith and jth constituents respectively. The atomic size mismatch rule (*δ)* is used to predict the formation of solid solution phases in HEAs, [36,37], given as follows:

$$\delta = \sqrt{\sum_{i=1}^{n} C_i(1 - r_i/\bar{r})^2)} \tag{2. 5}$$

where $\bar{r} = \sum_{i=1}^{N} x_i r_i$ is the atomic radius r_i of the *i-th* element. It requires Ω>1.1 and δ<6.6% [37]. To predict the formation of a solid solution phase, the effects of both ΔH_{mix} and ΔS_{mix} must be considered. Yang et al. [59] proposed the entropy-enthalpy ratio Ω to describe the balance between ΔH_{mix} and ΔS_{mix}, which illustrates the comprehensive effect of the Ω value on the formation of a solid solution, as shown in the following equation,

$$\Omega = T_m \Delta S_{mix}/|\Delta H_{mix}| \tag{2. 6}$$

where: $T_m = \sum_{i=1}^{N} x_i T_m^i$ is the melting point of the HEA.

2.2.3 Development of HEAs

Since the inception of HEAs, these materials have been extensively researched. The equimolar CoCrFeNiMn HEA, with a fcc single crystal structure, is one of the best-known HEAs and is considered a milestone in their development [38]. Initially, studies focused on creating HEAs with a simple single-crystal structure composed of equimolar or near-equimolar compositions, which limited the development of new HEAs. As a result, non-equimolar HEAs were developed to form structures with multiple phases [39]. **Fig. 2. 1** illustrates the development of HEAs and suggests that the definition of

HEAs can be expanded to include four multi-component HEAs [39]. Additionally, novel alloys based on the concept of HEAs can be used to design new alloys, such as medium entropy alloys.

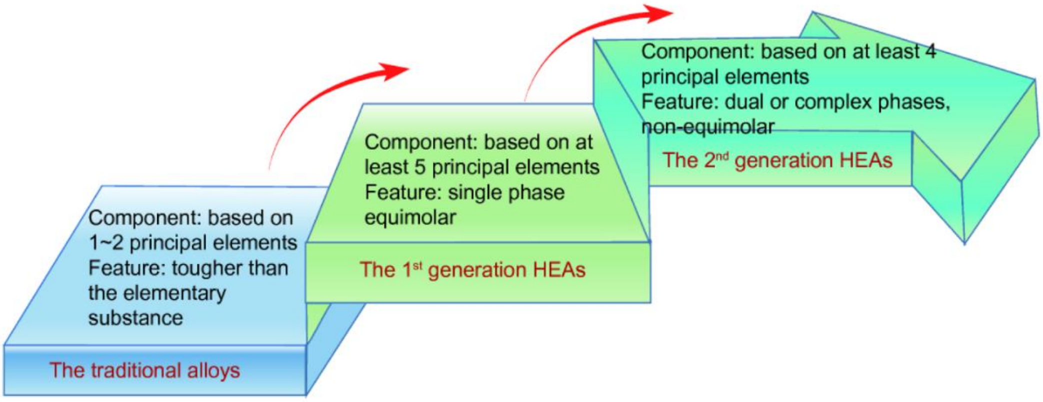

Fig. 2. 1 The evolution of HEAs [39].

2.2.4 Characteristics of HEAs

HEAs exhibit four main characteristics due to their complex chemical composition [40]:

High entropy effect

HEAs typically contain four or more principal elements, leading to complex reactions between the different elements. The increased mixing entropy hinders the formation of brittle intermetallic compounds [41] and improves the stability of the alloy system, especially at high temperatures [42]. However, the strong cohesive force between the components can lead to the separation of precipitation from other compositional elements in a HEA system.

Sluggish diffusion effect

Phase transformation in HEAs is controlled by diffusion, which requires synergistic diffusion between different types of atoms. The atoms in HEAs diffuse through the vacancy mechanism, but with different diffusion abilities [30]. Sluggish diffusion can hinder the nucleation and growth of precipitations but is beneficial for the formation of nano-sized crystals.

Lattice distortion effect

HEAs exhibit random atom occupation on lattice positions, resulting in lattice distortion due to differences in atomic radii [43]. This severe lattice distortion affects the mechanical, electrical, optical, and chemical properties of the material, increasing resistance to dislocation motion and impeding deformation [44].

Cocktail effect

The cocktail effect in HEAs emphasizes the influence of a typical alloying element with specific properties on the overall HEA system [45]. Due to the multi-components in HEAs, a complex cocktail effect on the properties can arise. HEAs with specific atom fractions generally exhibit excellent properties, such as thermal stability, high strength and hardness, and superior oxidation resistance, broadening their application potentials as heat-resistant materials.

2.3 Refractory high entropy alloys

2.3.1 Composition design

RHEAs have attracted attention for their potential industrial applications, particularly at high temperatures [46,47]. RHEAs composed of refractory elements (such as V, Nb, Ta, Mo, W, Ti, Zr and Hf), sometimes combined with elements with lower melting points, as shown in **Fig. 2. 2**, have shown promise as potential superalloys [48,49]. For example, NbMoTaW and VNbMoTaW RHEAs demonstrated good work hardening ability at room temperature and high yield strength, of 405 and 477 MPa, respectively, at 1600 °C, surpassing traditional Ni-based superalloys [49]. However, these RHEAs exhibit brittleness at room temperature [50], limiting their industrial applications. By substituting Hf, Zr, and Ti for W and Mo, the TaNbHfTiZr RHEA has shown balanced room-temperature strength and superior ductility [51], making it a promising high-temperature alloy. To further develop RHEAs, phase diagram calculations [52] or machine learning [53] can be used to predict phase stability. For example, Hamed et al. used Matlab software to identify the optimal alloy compositions based on specific conditions and validated them experimentally.

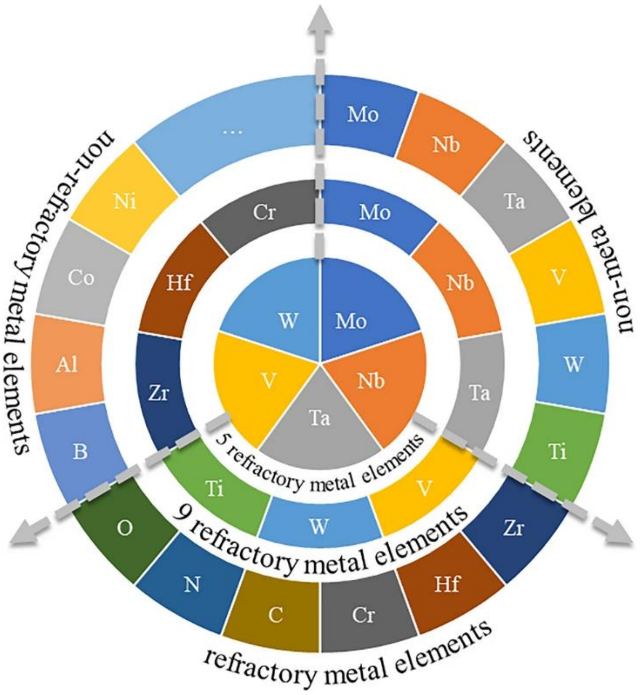

Fig. 2. 2 The composition of RHEAs [47].

Most reported RHEAs form only one bcc phase, with solid solution strengthening as the main mechanism for strengthening [54]. The selection and content of the elements can significantly affect the mechanical properties of RHEAs, including high-temperature strength, creep resistance, high-temperature oxidation resistance, and density [55]. However, in the composition design of RHEAs, metal elements with higher melting points are initially selected as the principal elements [56]. Early RHEA development focused on experimental composition design, particularly with metallic elements having higher melting points [48,49]. The choice of the mixing enthalpy is crucial for selecting the components of RHEAs, with a preference for atom pair mixing enthalpies of zero or small positive or negative values [57]. Based on mixing enthalpy criteria [35], the phase structure of the alloy is mainly a single solid-solution structure, such as in WMoVCrTa [56], TaNbHfZrTi [51], MoNbTaTiV [58], $Nb_{42}Mo_{20}Ti_{13}Cr_{12}V_{12}Ta_1$ [59], HfNbTaTiZr [60] alloy, NbMoTaW [49], WMoVCrTa [56], CrNbVMo [61], VNbMoTaW [62] and HfMoTaTiZr [63] alloys. These constituents play an important role in modifying the properties of RHEAs. For example, the addition of Cr to the CrHfMoNbTiZr RHEA can improve its high-temperature performance [64], while the presence of Ti and Zr in the CrNbTiZrAl RHEA [65] can effectively reduce its density and increase the specific strength. Nb is the most frequently used element in the selection of RHEA elements, contributing to improved ductility [55]. Ta, with superior high-temperature softening resistance and stability, enhances the high-temperature properties of RHEAs [66]. However, Mo and W are considered inherently brittle metals in TiMoNbTaV RHEA [55], and reducing their content can improve the ductility of RHEAs.

Reducing the average valence electron concentration (*VEC*) is another method of creating more ductile refractory alloys [35]. A large *VEC* (≥ 8) favors the formation of an fcc solid solution, whereas a smaller *VEC* (<6.87) favors the formation of a bcc solid solution [67], as seen in the example of the WMoVCrTa alloy with a *VEC* value of 5.6 [56]. Ti is frequently used in RHEAs due to its low *VEC* and performance at medium and high temperatures. The addition of Ti to the NbMoTaTiNi alloy improves its overall plasticity and resistance to thermal stress [68]. The addition of non-refractory elements such as Al [67,69], O [32,70–73], N [71,73,74], C [50,73], B [50,75,76], and Si [77,78] into the RHEA matrix can modify their properties and decrease the density of the target RHEA. Adding Al can reduce the *VEC* effect of the system by forming a strong directional *p-d* polar bond, promoting the formation of order in the system and reducing bond length [67]. In the TiAlVNbMo [68] alloy, Al and Ti are added to reduce the alloy density and increase the alloy strength, and Ti, V, Nb and Mo are used to ensure the high-temperature properties of the alloy. The addition of interstitial atoms has been proven to be an effective approach for improving the performance of RHEAs [32,50,70–76]. For example, the addition of B to the NbMoTaW RHEA (within a reasonable range) can solve oxygen embrittlement in this type of RHEA by purifying the grain boundaries to improve their strength and ductility simultaneously [50], while the introduction of N can significantly improve the strength of fabricated RHEAs

[32,74]. The addition of interstitial atoms, such as B and C, has been proven to improve the strength and ductility of RHEAs [50].

2.3.2 Microstructures and phase composition

Microstructure plays an important role in the mechanical properties of alloys [55]. Casting is one of the most commonly used fabrication methods for the preparation of RHEAs. The microstructure of as-cast RHEAs is usually dendritic or coarse grains [14,15], as shown in **Fig. 2. 3 a** and **b**, which harm the mechanical properties of the alloy. In contrast, alloys with ultra-fine grains and uniform microstructures usually exhibit excellent mechanical properties. To solve the problem of brittleness at room temperature, Juan et al. [63] obtained a grain-refined TaNbHfZrTi RHEA by controlling the annealing temperature and time to realize simultaneous improvement of strength and plasticity under room temperature compression conditions. Zhu et al. [66] prepared nano-sized TiZrNbMoTa alloy powders by the mechanical alloying (MA) process, as illustrated in **Fig. 2. 3 a** and **b**. Among the reported RHEAs, the phase composition of most alloys is single-phase BCC solid solution, and some of them have dual-phase (bcc +hcp/Laves, etc.) microstructures [79]. In addition, alloys composed of bcc structures have high strength and hardness, but low ductility [80], which hinders their application as structural materials. The NbMoTaW RHEA with bcc structure is composed of several highest-melting point elements in the periodic table with a high melting point and excellent high-temperature stability but poor room-temperature ductility [66]. Wang et al. [81] found that the V_xNbMoTa alloy with single-phase bcc structure has unprecedented phase stability over a wide temperature range. As the concentration of

V continued to increase, the grains of the alloy became significantly refined, as shown in **Fig. 2. 3 d**.

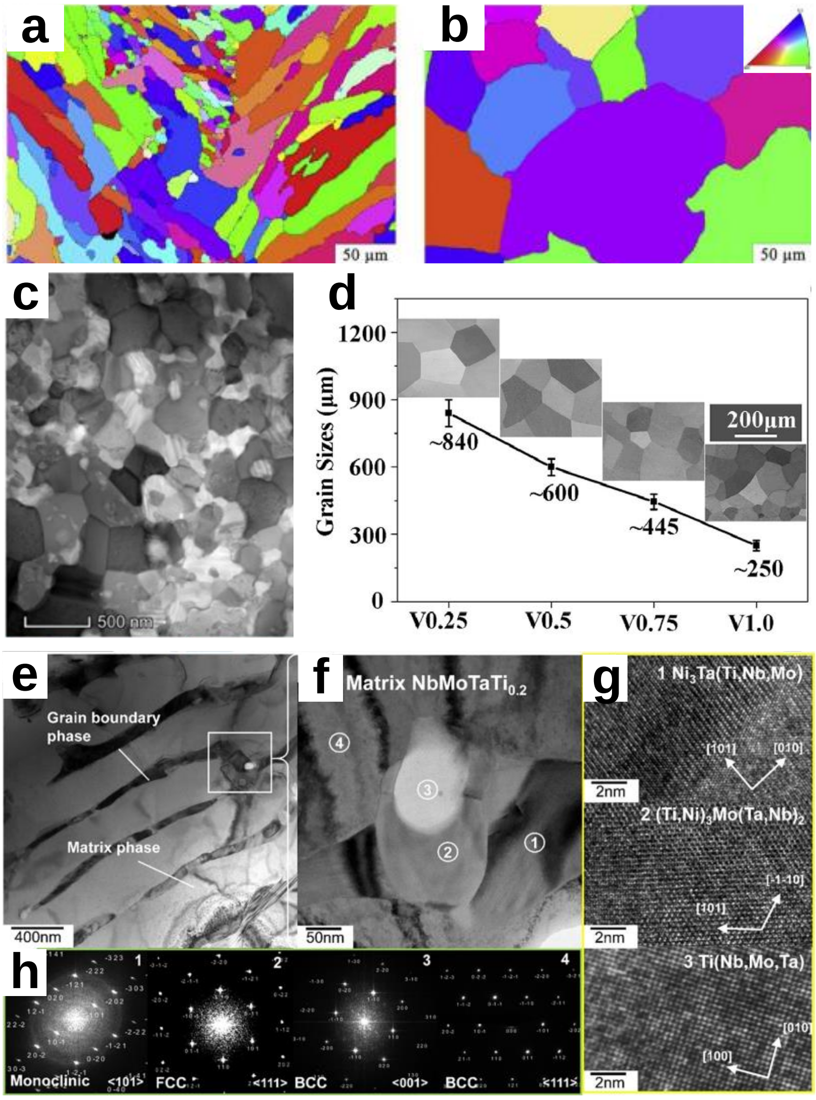

Fig. 2. 3 Microstructural analysis of RHEAs fabricated through various techniques[14,66,68,81]**.** The NbMoTa MEA fabricated through **a**, laser metal deposition and **b**, arc melting [14]. **c,** TiZrNbMoTa RHEA fabricated through MA and spark plasma sintering with nano-crystals [66]. **d**, Increasing the content of V in $V_xNbMoTa$ RHEA achieves grain refinement [81]. **e-h**, TEM results indicate the formation of fcc structure in NbMoTaX RHEA [68].

When the room-temperature brittleness of RHEAs is difficult to eliminate, researchers began to study fcc-based RHEAs. At present, according to the literature, RHEAs with a single fcc structure are rarely reported. High-strength alloys composed of fcc and bcc structures not only have high strength and hardness but also good ductility. For example, the fcc+bcc structure NbMoTaTiNi alloy (as shown in **Fig. 2. 3 e-h**) [68] and the dual-phase fcc and bcc $Ti_{1.5}VNbMoTa$ alloy [55] exhibit excellent room-temperature strength and high-temperature mechanical performance. Similarly, the TiZrNbMoTa alloy with a bcc+fcc structure [66] and the (NbTaTiV)/Ti-C-O composite with dual fcc+bcc structures show competitive mechanical properties [82]. RHEAs with dual-phase structures are expected to have significantly better mechanical properties than single-phase alloys, particularly with higher strength under high-temperature conditions, making them a promising new type of superalloy with practical engineering value [60,66].

Similar to eutectic high-entropy alloys [83], some RHEAs can have a solid solution phase (mainly bcc phase) matrix and an intermetallic compound (IM) phase [75,77,79,84]. The solid solution phase ensures good plasticity and toughness. Adding trace elements to the bcc matrix can form a dual phase of the bcc + IM phase, with the intermetallic phase (mostly the Laves phase [79,84]) providing high hardness and strength, strengthening the alloy during deformation. For example, Long et al. [84] prepared NbMoTaWVCr RHEA with bcc+Laves phases to ensure higher strength and better plasticity. Additionally, Zhu et al. [79] added trace Al elements to the bcc structure CrNbTiZr alloy to obtain the bcc + Laves phase $CrNbTiZrAl_{0.25}$ alloy, which exhibited higher tensile strength and better plasticity. Gao et al. [75] improved the comprehensive mechanical properties of the $Hf_{0.5}Mo_{0.5}NbTiZr$ RHEA at room temperature by adding B elements to form the boride of the MB_2 phase as a strengthening phase. The $Hf_{0.5}Mo_{0.5}NbTiZrB_{0.3}$ alloy showed larger elongation (27%) and higher strength, while the $Hf_{0.5}Mo_{0.5}NbTiZrB_{0.9}$ alloy had higher strength but decreased plastic deformation of 12%.

Nano-scale structures, including local chemical fluctuations (LCF) [25,57], local chemical order (LCO) [69], nano-scale secondary phase [85], B2 phase [86–88] etc., has been shown to enhance the mechanical performance of HEAs. These structures typically have a greater impact on ductility through their interaction with dislocations. Interestingly, by adding Al into the RHEA matrix, the goal of designing B2, LCO, or chemical fluctuations can be achieved [25,57,69,86–89]. For example, by increasing the Al content in the NbTiZr matrix, a B2 phase was gradually produced, as shown in **Fig. 2. 4 a**, which significantly improved the mechanical performance of the base metal [87]. Wang et al. [69] introduced Al, with a smaller atomic radius, into the bcc-matrix to design a high content of LCO in the matrix, shown in **Fig. 2. 4 b**, which can tailor the secondary planar slip to achieve large uniform elongation in the aged sample with a high content of LCO. As Al has a large negative mixing enthalpy with the commonly used constituents in RHEAs [57], the addition of Al to a Hf-Nb-Ti-V RHEA system can successfully promote the formation of LCFs, as illustrated in **Fig. 2. 4 c**, delivering high strength and ductility in the designed alloy. Moreover, the presence of LCF is nearly an intrinsic feature in HEAs, the presence of LCF in RHEA can modify the local stacking fault energy (SFE) to modify the motion path of dislocation [90], resulting in improved ductility in RHEA.

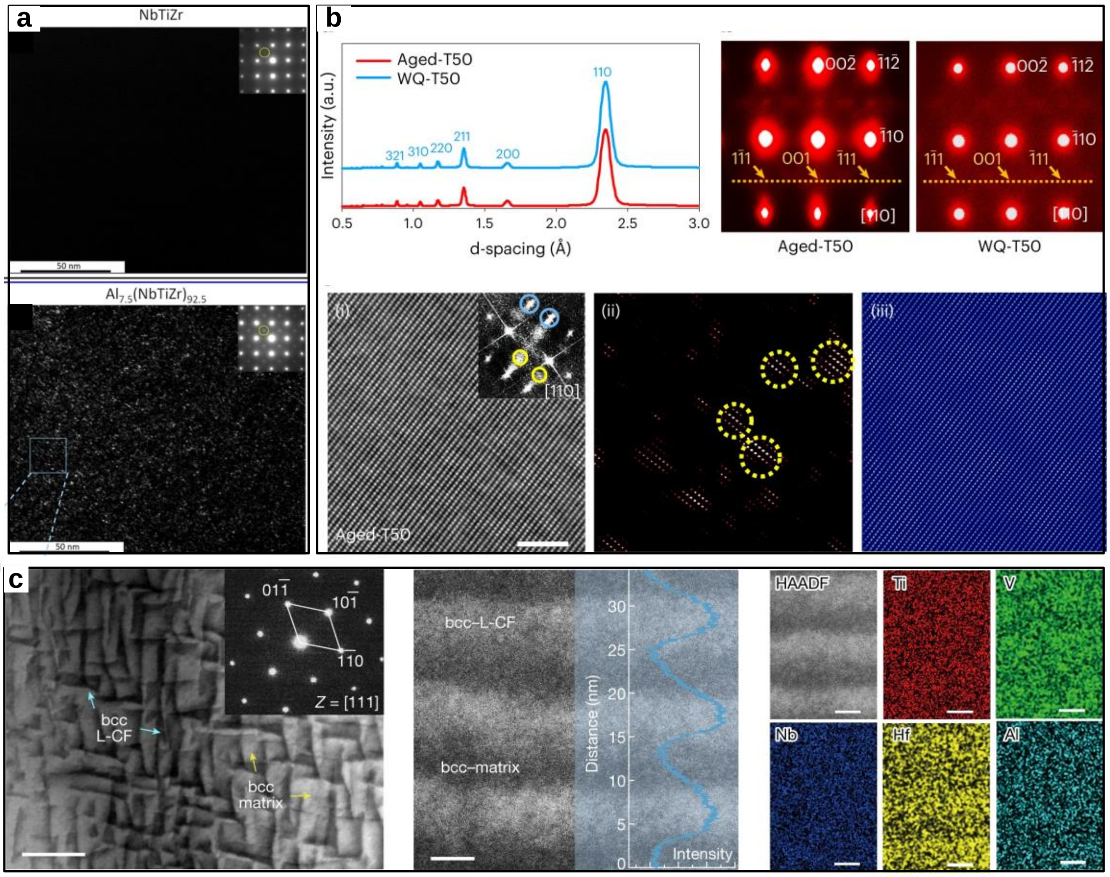

Fig. 2. 4 Formation and design of phases in Al-containing RHEA [57,69,87]**. a,** B2 phase forms in $Al_{7.5}(NbTiZr)_{72.5}$ alloy [87]. **b,** Applying the ageing approach to form LCO in an Al-containing HEA [69]. **c,** Using negative mixing enthalpy strategy to design L-CF in Al-containing RHEA [57].

2.3.3 Mechanical properties

RHEAs exhibit outstanding mechanical properties, including high yield strength [7], high-temperature softening resistance [10], superior wear resistance [8], etc. For example, a quaternary equiatomic NbMoTaW RHEA reported by Senkov et al. [49] demonstrated a high yield strength of 405 MPa at 1600 °C, while a quinary NbMoTaWV alloy showed a yield strength of 477 MPa under the same conditions, surpassing Ni-based superalloys, as shown in **Fig. 2. 5 a**. Additionally, the quinary NbMoTaTiNi alloy designed by Zhang et al. [68] displayed large high-temperature yield strength and ductility, with values of 555 MPa and 11%, respectively. Juan et al.

[63] reported on two RHEAs, with the five-element HfMoTaTiZr alloy exhibiting a yield strength of 1600 MPa and 404 MPa under quasi-static compression conditions at room temperature and 1200 °C, respectively, and high-temperature plastic deformation exceeding 30%. However, it's important to note that blindly pursuing high entropy may not always optimize material performance, as it can lead to increased costs and complexity. To enhance the high-temperature mechanical properties of RHEAs, trace elements such as Al and O can be added to the base alloy to modify the microstructure[61,91]. Kang et al. [61] utilized powder metallurgy to create lightweight Al-Cr Nb-V-Mo alloys, resulting in improved yield strength and elongation at high temperatures. The addition of trace Al elements reduced the density of the CrNbVMo alloy while maintaining high strength and plasticity at high temperatures [91]. Similarly, the addition of trace O elements improved the high-temperature mechanical properties of the $ZrTiHfNb_{0.5}Ta_{0.5}$ alloy, leading to increased yield strength at elevated temperatures [92]. Additionally, Fu et al. [82] developed Ti-C-O particle-reinforced NbTaTiV-based composites with enhanced yield strength under quasi-static compression at 1000 °C.

The high strength of RHEAs at high temperatures is mainly not attributed to their multi-phase structure, which differs from the high-temperature strength of nickel-based superalloys controlled by precipitated phases [93]. RHEAs offer significant advantages and simplify alloy design by adding elements with high melting points to enhance their high-temperature performance [94]. Many RHEAs transition from brittle to ductile fractures at high temperatures, exhibiting better plasticity above 600 °C. For instance, the single-phase BCC MoNbTaW and MoNbTaVW alloys maintain a high yield strength of over 400 MPa at 1600 °C but exhibit brittle fracture at room temperature [95]. Introducing Ti into MoNbTaW increases ductility at room temperature to 11.5% and raises the yield strength to 1455 MPa, while maintaining a stable phase structure at high temperatures [96]. Similarly, adding W and Mo to the HfNbTaTiZr alloy enhances its high-temperature performance, resulting in higher yield strength without new phase formation at 1200 °C. Adjusting the content of Mo, Zr, and Ti in the HfMoNbTiVZr alloy affects its strength [97]. The addition of Al to the NbMoTaW alloy increases the strength but is not suitable for Hf-contained RHEAs [98]. By replacing Hf or Cr and V with Al, the $AlMo_{0.5}NbTa_{0.5}TiZr$ RHEA [89] exhibits a dual-phase structure with improved mechanical properties and reduced density, enhancing the high-temperature ductility through the formation of a disordered BCC matrix phase and a discontinuous B2 precipitate phase during high-temperature deformation, as shown in **Fig. 2. 5 b**. Moreover, a metastable engineering strategy was applied to improve the strength and ductility synchronously, like twinning-induced plasticity (TWIP) in deformed TaNbHfTiZr RHEA under an ultralow temperature [99] and transformation-induced plasticity (TRIP) in TaxHfZrTi RHEA [100].

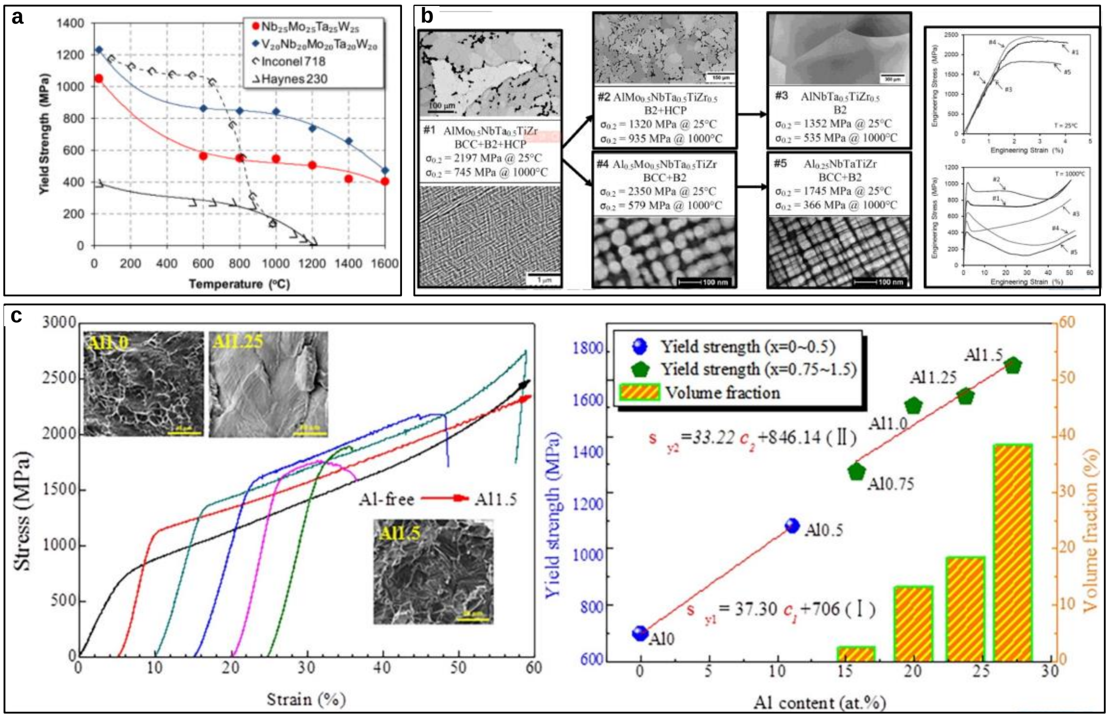

Fig. 2. 5 Enhanced high-temperature mechanical properties and structural design in RHEAs compared to traditional superalloys [49,89,101]. a, The high-temperature mechanical properties of RHEA surpass the traditional superalloy [49]. **b,** Designing B2 structure in $AlMo_{0.5}NbTa_{0.5}TiZr$ RHEA to improve the mechanical performance under elevated temperatures [89]. **c,** The addition of Al into HfNbTiZr RHEA but stuck in the strength-ductility trade-off dilemma [101].

RHEAs not only have excellent high-temperature mechanical properties, but also have superior mechanical properties at room temperature. The single-phase bcc structure TiVNbMoTa alloy reported by Liu et al. [55] had a high compressive yield strength of 2208 MPa and a large elongation of 24.9%. In $Nb_{42}Mo_{20}Ti_{13}Cr_{12}V_{12}Ta_1$ RHEA, the RT compressive strength reached 3892 MPa, but with an elongation of 5.2 % [59], trapped in the well-known strength-ductility trade-off dilemma [7]. The addition of Al reduces the density of RHEAs and increase their yield strength, but sacrifices the plasticity in HfNbTiZr RHEAs [101], as depicted in **Fig. 2. 5 c**. Therefore, it is necessary to add an appropriate amount of the Al element, so that the density can be reduced and the strength can be improved. The plasticity of RHEAs can be improved by adding Ti, Zr, Hf, and other group IV subgroup elements in the hcp structure. Therefore, the combination of these elements can be considered in the composition design of RHEAs, and the plasticity can be enhanced while improving the strength of RHEAs.

The dual-phase RHEAs are also considered potential candidate alloys for structural materials. The dual-phase RHEAs fabricated via metallurgy powder methods, such as $Ti_2MoNbTaV$ [55], $NbMoTaTi_{0.5}Ni_{0.5}$ [68], and TiZrNbMoTa [66], have high strength and acceptable ductility. The (NbTaTiV)/Ti-CO composite with a two-phase structure has a large room temperature yield strength of 1760 MPa and an elongation of 11% [82]. The $Cr_{0.3}Hf_{0.5}Mo_{0.5}NbTiZr$ alloy with bcc and Laves phases has a room temperature yield strength of 1176 MPa and an elongation of 14.61% [68], while the 1600 °C sintered NbMoTaWVCr alloy has a high room-temperature yield strength of 3658 MPa and a small elongation (2%) [84]. The $Ti_{30}Cu_{15}Ni_{33}Nb_{22}$ alloy, which also has a multi-phase structure, has a yield strength of 2427 MPa, but the room temperature compression elongation is only 0.88%, while the $Ti_{32}Cu_{16}Ni_{31.2}Nb_{20.8}$ alloy with a lower yield strength of 1338 MPa can have a higher elongation (7.9%) [75]. In addition, the multiphase $Hf_{0.5}Mo_{0.5}NbTiZrB_{0.3}$ alloy has a higher elongation of 27%, and its yield strength is lower (1464 MPa) [75]. Therefore, improving the strength and plastic deformation of multiphase RHEAs is still the goal pursued by material researchers.

2.3.4 Strengthening-toughening mechanism in RHEAs

High-performance metal materials are essential in various fields, such as transportation, national defense equipment, and aerospace [39]. Developing metallic materials with high strength and plasticity is crucial to meeting increasingly demanding service conditions. The bcc-structured high-entropy alloys, typically composed of RHEAs, exhibit excellent yield strength over a wide temperature range but have poor tensile plasticity at room temperature [95,100], limiting their manufacturing ability and applications. To overcome the strength-ductility trade-off in HEAs and achieve high-strength and tough materials, the heterogeneous structure [102] of high-entropy alloys has been proven effective. The unique interface structure in heterogeneous HEAs leads to a heterogeneous deformation-induced strengthening and hardening mechanism [102], enabling the synchronous improvement of material strength and ductility. Therefore, in addition to the excellent solid solution strengthening of HEAs, the construction and development of new heterostructures through microstructure design are crucial for obtaining excellent mechanical properties.

The distribution of elements in HEAs is highly chaotic, resulting in a typical atomic-scale heterogeneity material [103]. This solid solution strengthening effect is particularly evident in bcc-structured HEAs due to the greater atomic radius difference of the constituent elements [48,104,105]. For example, the $(HfNbTiV)_{90}Al_{10}$ RHEA exhibits long-range chemical fluctuations, resulting in a yield strength of 1390 MPa and a high fracture plasticity of ~ 30% (see **Fig. 2. 6 a**), surpassing other high-entropy alloy materials [57]. Adjusting the atomic radius difference, electronegativity difference, and mixing enthalpy of high-entropy alloys can improve the compositional inhomogeneity[57,106], forming LCFs in the size range of 1–3 nm [107]. The existence of LCF enhances the hindrance to dislocation movement, improving the work hardening ability of materials and effectively enhancing their strength and plasticity [107]. Further, the addition of O atoms (2 at.%) to HfNbTiZr RHEAs forms ordered oxygen complexes (OOCs), modifying the dislocation slip mode and achieving a perfect combination of high yield strength (1100 MPa) and high tensile plasticity (27.7%) [32], as shown in **Fig. 2. 6 b**. Short-range order (SRO) structures [108–111], smaller-scale heterogeneous structures, also exist in HEAs and affect their mechanical properties. SRO is an ordered arrangement of chemical elements due to the difference in binding enthalpy between the alloying elements, increasing local lattice distortion and dislocation movement resistance. However, the limited effect of SRO on dislocation hindrance means that this type of heterogeneous strengthening mechanism often does not act alone in improving the mechanical properties of alloys, especially in fcc-based HEAs, but is still debated regarding their impact on the mechanical properties, especially the strength, of CoCrNi MEA [112,113]. However, the presence of LCO in $Ti_{50}Zr_{18}Nb_{15}V_{12}Al_5$ was proven to be effective in modifying the second planar slip to maintain a large uniform elongation (~ 25 %) and nearly 50% elongation-to-failure, as shown in **Fig. 2. 6 c**. After the interaction with dislocations, these LCOs were crushed to form large local lattice distortions which can contribute to strain hardening. As a result, the necking would be postponed, and a large uniform elongation was formed.

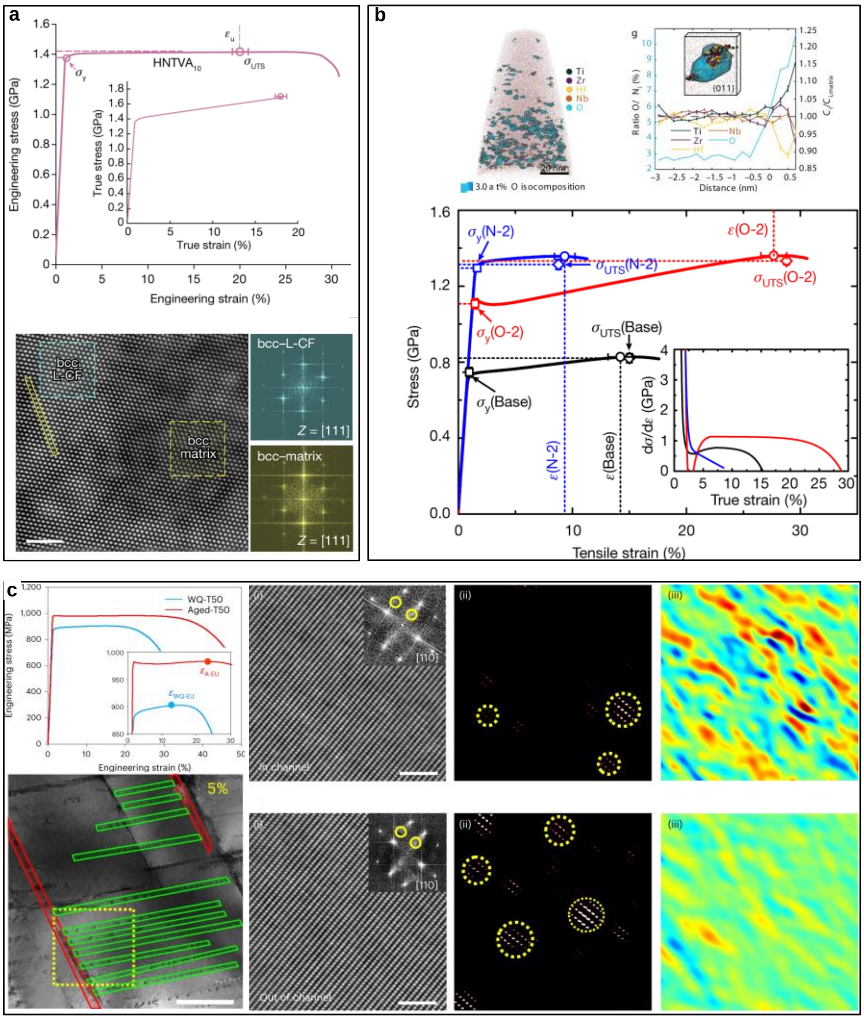

Fig. 2. 6 Tensile properties and nano-structural enhancements in RHEAs [32,57,69]**. a,** Tensile properties of $(HfNbTiV)_{90}Al_{10}$ RHEA showing evidence of LCF [57]. **b**, Formation of OOCs in oxygen-doped HfNbTiZr RHEA, enhancing both strength and ductility [32]. **c**, LCO presence in $Ti_{50}Zr_{18}Nb_{15}V_{12}Al_5$ alloy induces second planar slip and significant lattice distortion, contributing to strain hardening [69].

Heterogeneous HEAs with nano-scale precipitates demonstrate excellent mechanical properties, achieving a synergistic improvement in alloy strength and plasticity [114]. An et al. [115] utilized the phase decomposition design concept to prepare HfNbTiV RHEAs with nanoscale heterogeneous structure, resulting in a yield strength of 1100 MPa and an elongation of approximately 28%, given in **Fig. 2. 7 a**. The continuous heterogeneous interface hinders the movement of dislocations during the deformation process, leading to a strengthening effect. Materials with uneven grain size and distribution, such as bimodal, layered, and gradient structures, have been used in traditional metallic materials to simultaneously improve strength and plasticity [116], providing a reference model for the development of high-strength and tough heterogeneous HEAs [117–119]. Zhang et al. [120] achieved a yield strength of about 620 MPa and a uniform elongation of approximately 6% by creating a layered heterogeneous grain structure composed of fine and coarse grains in the $Nb_{55}Ta_{25}Ti_{15}Hf_5$ refractory alloy through cold rolling and low-temperature heat treatment, as given in **Fig. 2. 7 b**. This structure exhibited a heterogeneous deformation-induced strengthening and hardening effect, maintaining a high work-hardening effect within a certain strain range.

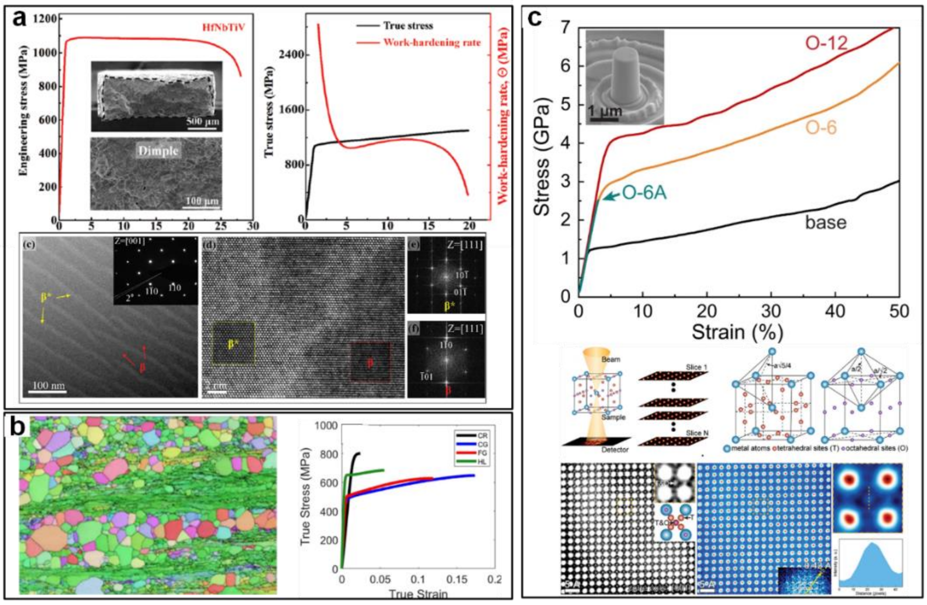

Fig. 2. 7 Superior mechanical properties and structural improvements in RHEAs [72,73,115,120]**.** **a,** Spinodal structure in HfNbTiV RHEA induces superior tensile strength and ductility synergy [115]. **b,** Layered heterogeneous grain structure strengthens $Nb_{55}Ta_{25}Ti_{15}Hf_5$ alloy [120]. **c,** High oxygen content in TiNbZr alloy achieves near theoretical strength with the direct observation of oxygen atoms [72,73].

The introduction of interstitial atoms is one solution to address the strength-ductility trade-off dilemma. For example, the addition of Si in the $Mo_{0.5}NbHfV_{0.5}TiSi_x$ system and $Ta_{0.5}Nb_{0.5}HfZrTiO_x$ RHEA has been shown to increase room- and high-temperature strength without significantly decreasing ductility [92,121]. Additionally, the alloying method, particularly the addition of boron in the NbMoTaW refractory high entropy alloy, can overcome oxygen embrittlement by replacing segregated oxygen on the grain boundaries [50]. Oxygen has been proven to be an effective interstitial atom for optimizing mechanical properties in the equimolar HfNbTiZr refractory HEA [32]. In a recent study, the massive interstitial solid solution (MISS) TiNbZr alloy exhibited a near theoretical yield strength of 4.2 GPa with a large strain of 65%, representing a new strategy for designing metallic materials with superior mechanical properties [72,73]. The addition of Al to the refractory elements matrix not only decreases the density but also improves ductility at room temperature [89,122–124]. However, the inherent brittleness between the ordered B2 and matrix can limit the compressive ductility at room temperature in RHEAs [123,125]. Complex heat treatment strategies [94,126,127] have been used to address these challenges, resulting in enhanced room temperature ductility and maintained strength at elevated temperatures. These studies demonstrate that the mechanical properties of RHEAs can be improved by modifying the processing strategy or changing the compositions, further enhancing the relationship between the structure and properties in RHEAs in future studies.

2.4 RHEAs fabricated via laser additive manufacturing

RHEAs have garnered attention for their exceptional high-temperature structural stability and mechanical properties, positioning them as a promising alternative to nickel-based superalloys in industries such as the aerospace, nuclear reactor, and petrochemical fields [128]. Currently, RHEAs are primarily produced using methods like vacuum arc melting (VAM) [14] and powder metallurgy (PM) [16]. While VAM is commonly used, it can result in coarse structures and composition segregation due to its low cooling rate [14]. On the other hand, PM technology, while capable of producing alloys with uniform elements and fine structures, may introduce porosity and impurities due to high-temperature sintering and mechanical alloying processes [16]. These traditional methods present challenges such as complex manufacturing processes, low material utilization rates, and high costs, significantly limiting the practical application of RHEAs. Therefore, there is an urgent need to explore more advanced manufacturing techniques in preparing RHEAs.

2.4.1 Additive manufacturing approaches

Laser additive manufacturing (LAM) is a cutting-edge technology that digitally controls the layer-by-layer deposition of materials, allowing for the direct formation of three-dimensional parts with a high degree of freedom [129]. This method is particularly well-suited for addressing the brittleness and processing challenges of RHEAs at room temperature. The non-equilibrium rapid solidification characteristics of the additive manufacturing process result in fine and dense alloy structures with minimal macro-segregation [15], although porosity and oxidation issues may arise

[130]. Despite these challenges, the rapid and direct forming capabilities of LAM offer advantages that traditional preparation methods cannot match, making it an attractive option for the production of RHEAs. As a result, the use of LAM technology for forming RHEAs has garnered significant attention from researchers and has successfully provided a technical foundation for the rapid development and engineering applications of RHEAs.

Laser melting deposition (LMD), also known as laser direct energy deposition (LDED) or laser-engineered net shaping (LENS), is a metal additive manufacturing technology that utilizes coaxial powder feeding [131]. In the LENS process, metal powder is fed into the laser melting pool through inert gas, and multiple powder buckets can be used to supply powder simultaneously [132]. This approach offers significant advantages in the preparation of multi-component HEAs, allowing for high-throughput in-situ preparation and the formation of larger size and composition gradient parts [23]. As a result, LENS has become the most mainstream additive manufacturing technology for RHEAs. On the other hand, selective laser melting (SLM), also known as laser powder bed fusion (LPBF) technology, is a widely used metal additive manufacturing technology that involves selectively melting a layer of powder on the substrate using a high-energy laser beam [133]. This method offers higher-quality processing of metal parts and is particularly advantageous for the preparation of high-precision and complex parts. However, due to the requirement for pre-alloyed powder, there are limitations in the development of new materials, resulting in relatively fewer studies on RHEAs formed by selective laser melting [134].

2.4.2 Formability of RHEAs prepared through LAM

RHEAs are primarily composed of refractory elements, initially W, Ta, Mo, Nb, and V, which have been expanded to include other metallic or non-metallic elements [46,47]. The melting points of the refractory elements in RHEAs are generally above 1600 °C, with W having the highest melting point of 3410 °C. This necessitates a higher energy input for sufficient melting of the powder during the LAM of RHEAs. Generally, to customize the composition of designed RHEA systems, pure elemental powder mixture is used for LAM of RHEAs by mechanical mixing [21,25,28,29] or high-throughput in-situ powder mixing [22–24]. The large difference in the melting points of the constituent elements poses challenges in achieving complete melting of all the element powders, leading to deviations between the actual alloy composition and the theoretical design composition due to the evaporation of some low melting point elements, as well as the generation of pore defects [135].

The additive manufacturing of RHEAs faces challenges due to the large difference in the melting points of the constituent elements, resulting in un-melted particles in the additively manufactured RHEAs. To address this issue, Dobbelsteina et al. [21] adopted a remelting strategy to obtain laser-deposited ZrNbTiTaMo RHEAs samples with a smooth surface and uniform composition. This strategy significantly improved the surface quality and composition uniformity of the samples, particularly as the deposition height increased, as described in **Fig. 2. 8 a**. Since LAM is a complex thermal-mechanical coupling process, continuous rapid heating and cooling tends to generate large thermal stress in the deposited layer. With the brittle and hard characteristics of RHEAs, it is easy to crack and deform during the forming process. When Melia et al. [22] prepared the MoNbTaW gradient material by LENS, severe cracking occurred in all samples due to improper process control. However, in the $(MoTaW)_x(Nb)_{1-x}$ gradient composition samples, it was observed that the cracks mainly appeared near the substrate with less Nb content, while there were almost no cracks in the upper part of the samples with higher Nb content. This is because an increase in Nb content improves the fracture toughness of the MoNbTaW alloy, thereby suppressing cracking, as shown in **Fig. 2. 8 b**. In addition, Zhang et al. [136] studied the temperature distribution and thermal stress and strain during the SLM process through finite element simulation. Then, according to the simulation results, the process parameters of different printing layers were optimized, which effectively reduced the thermal stress during the printing process, avoided the occurrence of warping (**Fig. 2. 8 c**), and successfully prepared large-height RHEA samples. The results showed that the combination of experiment and numerical simulation is conducive to in-depth research on the effect of process parameters on the forming quality of LAM RHEAs, and finally achieves good forming of parts.

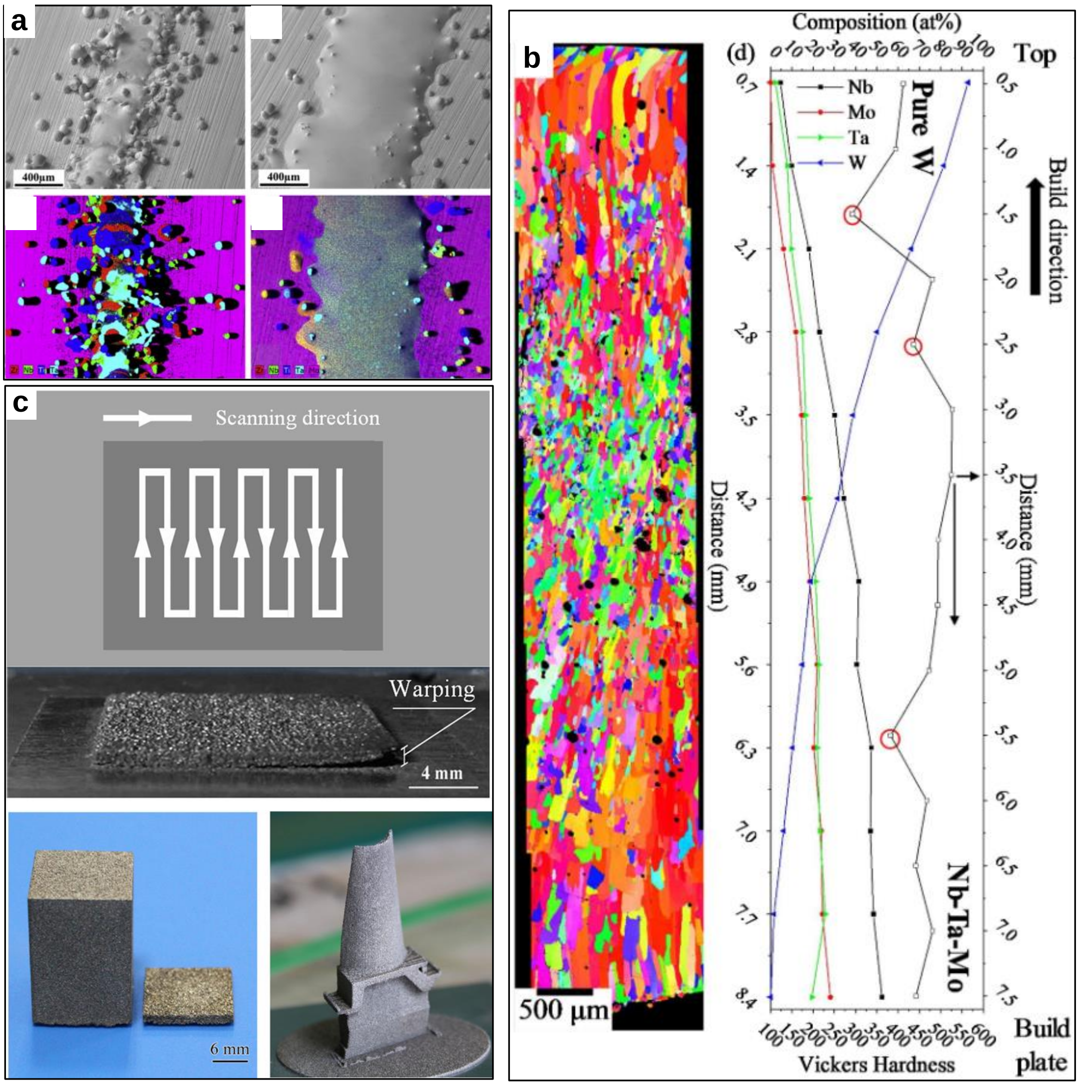

Fig. 2. 8 Improvement on elemental homogeneity and structural integrity in RHEAs [21,22,136]. **a,** Remelting procedure increases elemental homogeneity in ZrNbTiTaMo RHEA [21]. **b,** High-throughput additive manufacturing of MoNbTaW RHEA results in cracks and pores [22]. **c,** SLM-fabricated WTaMoNb RHEA solves the warping problem through parameter optimization [136].

In samples prepared by LAM, pore defects can limit the alloy's fatigue performance. Optimizing the molten pool overlap and selecting the optimal energy density can help partially eliminate pore defects in the $Nb_{30}Mo_{10}Ta_{30}Ti_{20}Ni_{10}$ RHEA [137]. During the LAM procedure, the high-energy laser beams used in the manufacturing process can create a significant temperature gradient, leading to thermal stress greater than the material's fracture strength, and results in crack defects.

Suppressing crack defects, which are detrimental to the mechanical properties of the alloy at both room and high temperatures, is essential for improving the mechanical performance of RHEAs. While optimizing the process window can reduce cracks, it cannot completely eliminate them [68]. Therefore, in the laser additive manufacturing process of RHEAs, the main approach to eliminating cracks is to optimize the composition to enhance the alloy's toughness, such as through phase engineering [25], which improves the alloy's toughness by controlling the content of brittle elements. Controlling the generation of cracks in RHEAs, fabricated through LAM, is a challenging research area and a key focus in the field. Addressing crack defects is crucial for the application of RHEAs prepared by LAM.

2.4.3 Microstructure and Phase Composition of LAM-Fabricated RHEAs

The microstructure of RHEAs produced by laser additive manufacturing is finer compared to traditional arc melting technology due to the high-temperature gradient and rapid solidification [14]. Huber et al. [138] found that the solidification structure of MoNbTaWV RHEAs showed a typical dendrite morphology in a study of selective laser melting. The elemental distribution results showed that the contents of the Mo and Nb elements in the interdendritic and dendritic stems were basically equal. While W and Ta are mainly concentrated in the dendrite stem region, V elements are largely segregated in the interdendritic region, as depicted in **Fig. 2. 9 a**. Zhang et al. [68] showed that in NbMoTaX (X=Ti, Ni) RHEAs, Ti and Ni elements would segregate between the dendrites and grain boundaries, forming precipitates such as α-Ti and Ni3Ta, shown in **Fig. 2. 9 b**. These precipitated phase particles can be used as the base point of nucleation during the solidification process, and play a role in refining the alloy grains. The grain morphology of laser additive manufacturing RHEAs varies with different composition systems. For example, when preparing LAM-fabricated TiZrNbHfTa RHEAs rod samples, Dobbelstein et al. obtained a fully equiaxed crystal structure [139] and the same grain morphology was also observed in LAM-fabricated HfNbTiZr RHEAs [25], as shown in **Fig. 2. 9 c**. They also found that the grain structure was sensitive to the Zr content in the $Ti_{25}Zr_{50}Nb_0Ta_{25}$~$Ti_{25}Zr_0Nb_{50}Ta_{25}$ composition gradient material deposited by LENS [21]. As the Zr content decreased along the deposition direction, the alloy grain size gradually coarsened, and the equiaxed crystal morphology transformed into an elongated morphology (**Fig. 2. 9 d**). The refinement effect of the Zr element was verified, and changes in the composition of different elements significantly affected the microstructure of the alloy, demonstrating the potential of rapid screening of RHEAs for high-throughput design and characterization by additive manufacturing.

The phase structures of RHEAs produced by laser additive manufacturing are primarily bcc single-phase structures, similar to those prepared by other reported processes [140]. This is due to the equimolar or near-molar ratio mixing of the main elements in RHEAs, resulting in high mixing entropy that enhances the solid solution phase stability and hinders the formation of intermetallic compounds. However, when the formation enthalpy of intermetallic compounds in the alloy is sufficiently significant to overcome the influence of the high entropy effect, intermediate or complex phases may form [141]. High-throughput CALPHAD calculations on the Mo-Nb-Ta-W series RHEAs have indicated that the vast majority of alloys will remain thermodynamically stable as a single disordered bcc phase at low temperatures, but in some compositions, a second phase may form [23]. Additionally, the presence of Fe and Nb elements can lead to the formation of a topologically close-packed (TCP) structure Laves phase (Fe_2Nb) during the solidification process, which can significantly improve the high-temperature oxidation resistance, creep resistance, and high-temperature strength of the alloy, despite reducing its toughness at room temperature [142].

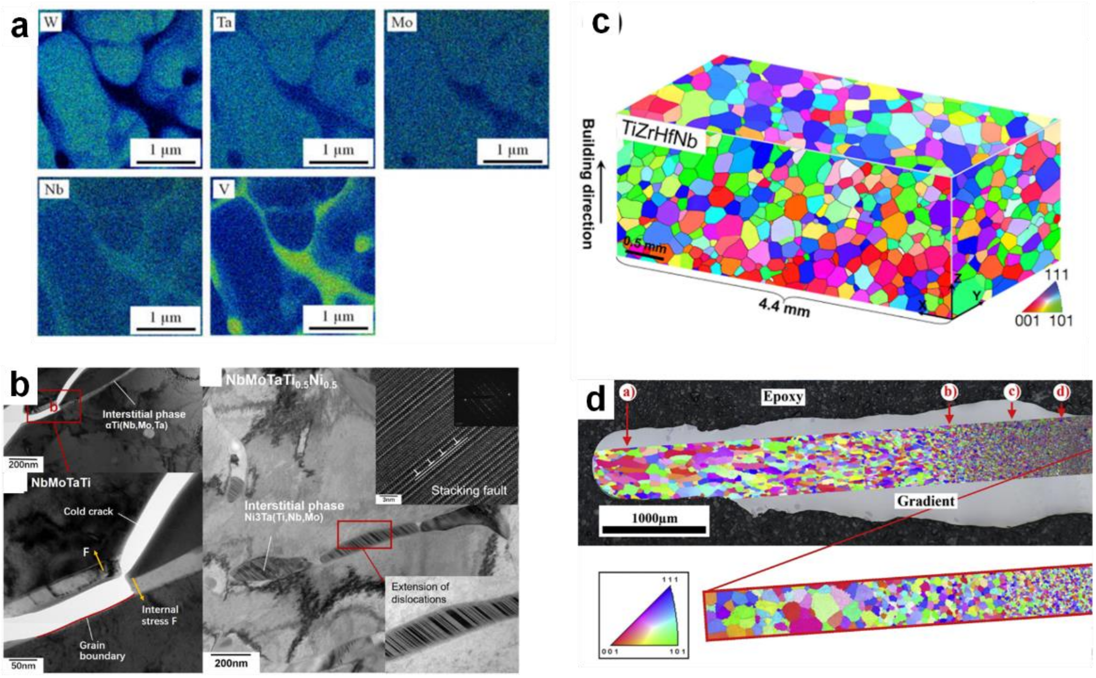

Fig. 2. 9 Microstructures in AM-fabricated RHEAs [21,25,68,138]**. a,** The micro segregation of elements in SLM-fabricated MoNbTaWV RHEA [138]. **b,** The presence of precipitation in LAM-fabricated NbMoTaTiNi-based RHEA [68]. **c,** Equiaxed grains forms in DED-fabricated HfNbTiZr RHEA [25]. **d,** The Zr gradient would modify the grain morphology in TiZrNbTa-based RHEA fabricated via LENS [21].

2.5 Properties of RHEAs fabricated by LAM

2.5.1 Mechanical properties

Hardness

RHEAs manufactured by laser additive technology generally have relatively high hardness, which is mainly due to the relatively fine structure of the coating. Due to the difference in process conditions, even RHEAs with the same composition will have large differences in hardness. The MoNbTaW alloy coating prepared by Zhao et al. [143] was only 753 HV, but after ultrasonic-assisted strengthening, the hardness of the alloy was 980 HV, which is higher than that of MoNbTaW RHEAs (~ 800 HV) prepared in other approaches. In addition to process conditions, the hardness of RHEAs also has a significant relationship with the constituents and proportions of elements contained in them. Wang et al. [142] studied the effect of different Nb content on LAM-fabricated $MoFe_{1.5}CrTiWAlNb_x$ (x=1.5, 2, 2.5, 3) HEAs. The results showed that the microhardness of the alloy increases gradually from HV 810 to 910 HV with the increase of Nb content. The increase of Nb element forms more Laves phase with the Fe element in the alloy, which gradually increases the hardness of the alloy. Li et al. [144] found that an increase in W content would increase the hardness of $W_xNbMoTa$ (x = 0, 0.16, 0.33, 0.53) RHEAs fabricated via LENS. This is mainly because RHEAs have mainly solid-solution strengthening mechanism, and as the W content increases, the enhancement of the solid-solution strengthening effect improves the strength of the alloy bcc matrix.

Compressive properties

Due to limitations in forming size, current strength tests for laser additive manufacturing RHEAs primarily focus on compressive strength. Changes in element composition can modify the phase composition and microstructure of RHEAs, impacting their mechanical properties. Dobbelstein et al. [24] conducted compression tests on 8 variations of HfNbTaTiZr RHEAs, revealing significant changes in yield strength based on alloy composition. The highest yield strength reached 1460±30 MPa, while the lowest was only 795±4 MPa. They also noted that powders with regular shapes and sizes produced alloys with superior properties. Zhang et al. [68] studied the impact of Ti and Ni content on SLM-formed MoNbTa, finding that the addition of Ti and Ni elements significantly refined the alloy's structure and reduced cracks. The dispersion strengthening resulting from the precipitation of certain compounds notably improved the alloy's strength. Even at 1000 °C, the alloy maintained a compressive yield strength of 554.61 MPa, demonstrating the potential of RHEAs as a new generation of superalloys.

Tensile properties

Due to the high brittleness of RHEAs and the significant thermal stress experienced during additive manufacturing, which can lead to defects in the forming process, there have been relatively few studies on their tensile properties (as indicated in **Table 2. 1** [25,28,29,137,145–147]. The assessment of compressive properties is more common for RHEAs fabricated via LENS, but tensile properties are more relevant for evaluating their potential in engineering applications [25]. Zhang et al. [145]

conducted tests on the tensile properties of the LPBF-formed NbMoTaTiNi refractory high entropy alloy, revealing a yield strength of 1205 MPa and an elongation after fracture, of 0.82%. By optimizing the contents of Mo, Ti and Ni elements, $Nb_3Ta_3Mo(Ti2Ni)_3$ with a yield strength of 1184 MPa, an ultimate tensile strength of 1403 MPa, and an elongation after fracture of 4.4 %, was produced [146]. The parameter optimization was also applied to the pores suppression, resulting in a tensile strength of 1.46 GPa and an elongation of 5.5 % in $Nb_{30}Mo_{10}Ta_{30}Ti_{20}Ni_{10}$ RHEA [137]. Jeong et al. [147] utilized LDED to create a refractory TiNbCrVNi alloy with a lower density, resulting in a tensile yield strength of 852 MPa, a compressive strength of 1021 MPa, and a tensile strain of only 2.3%. Previous studies have shown that RHEAs prepared by LAM often contain harmful phases, leading to a decrease in tensile plasticity [25]. Gou et al. [25] were the first to report the LDED method for preparing a tensile ductile alloy, $TiZrHfNb_x$ ($x = 0.6, 0.8, 1.0$). This alloy has an equiaxed crystal structure and does not require special process control or additional treatment. Increasing the Nb content stabilizes the BCC phase and inhibits the formation of the ω phase. When the load is along the horizontal direction, the tensile yield strength of the TiZrHfNb RHEA is 1034 MPa, with an elongation after fracture of 18.5%, demonstrating excellent tensile properties. Heat treatment has also been shown to effectively control harmful precipitation phases. Zhang et al. [28] conducted solid solution treatment on $Al_{0.3}NbTi_3VZr_{1.5}$ prepared by LDED, eliminating the Laves phase in the LDED-fabricated sample and reducing the ω-phase particle size. The tensile plasticity of the sample increased from 1% to 25%, and the yield strength increased to

1032 MPa. Furthermore, the precipitate phase in LAM-prepared RHEAs can be controlled by adjusting the process parameters. For example, Cui et al. [29] used different energy densities to prepare the $Ti_{41}V_{27}Hf_{13}Nb_{13}Mo_6$ RHEA. A RHEA prepared with high energy density can achieve the effect of in-situ aging, effectively suppressing the precipitation of the bcc phase on the grain boundary and resulting in a sample with a yield strength of 1.2 GPa and a fracture elongation of 11.3%.

Table 2. 1 Tensile properties and phase composition of LAM-fabricated RHEAs [25,28,29,137,145–147]. (HT: heat treatment; V:vertical direction; H: Horizontal direction; LE: low energy; HE: high energy; GB: grain boundary; σ_y: yield strength; UTS: ultra tensile strength; ε_f: fracture elongation)

Process	Composition	Phase	σ_y/MPa	UTS/MPa	ε_f/%	Ref
LPBF	$Nb_{30}Mo_{10}Ta_{30}Ti_{20}Ni_{10}$	bcc+TiNi+Ti_2Ni	1460	-	5.5	[137]
LPBF	NbMoTaTiNi	BCC+Trigonal	1205	-	0.82	[145]
	NbMoTaTiNi (HT)		1105		1.1	
LPBF	$Nb_3Ta_3(Ti_2Ni)_4$	bcc1+bcc2+fcc	671	1036	9.2	[146]
	$Nb_3Ta_3Mo(Ti_2Ni)_3$	bcc1+bcc2+fcc	1184	1403	4.4	
	$Nb_3Ta_3Mo_2(Ti_2Ni)_2$	bcc1+bcc2+fcc	1212	-	0.82	
LDED	TiNbCrVNi	bcc1+bcc2+Ti_2Ni	852	1021	2.3	[147]
LDED	$TiZrHfNb_{0.8}$	bcc+ω	782	-	13.1	[25]
	TiZrHfNb $_{(V)}$	bcc	1048		10	
	TiZrHfNb $_{(H)}$	bcc	1034		18.5	
LDED	$Al_{0.3}NbTi_3VZr_{1.5}$	bcc+ω+Laves	902	-	1	[28]
	$Al_{0.3}NbTi_3VZr_{1.5\ (HT)}$	bcc+ω	1032		25	
LDED	$Ti_{41}V_{27}Hf_{13}Nb_{13}Mo_{6\ (LE)}$	bcc1+bcc2 $_{(GB)}$+hcp	1171	-	4.7	[29]
	$Ti_{41}V_{27}Hf_{13}Nb_{13}Mo_{6\ (HE)}$	bcc1+bcc2 $_{(GB)}$↓+hcp	1195		11.3	

2.5.2 Tribological performance

Guo et al. [148] investigated the friction properties of laser-clad $(TiZrNb)_{14}SnMo$ RHEAs coatings and found that the main wear mechanism was adhesive wear, resulting in a higher friction coefficient and wear volume. They attributed the excellent wear resistance of the coating to its increased hardness and reduced intermetallic compounds, which eliminate abrasive wear behavior. Wang et al. [142] studied the effect of Nb content on the mechanical properties of $MoFe_{1.5}CrTiWAlNbx$ alloy coating. They observed that as the Nb content increased, the wear volume loss of the coating gradually decreased (**Fig. 2. 10 a**), with the wear mechanism being mainly abrasive wear. The friction coefficient of the coating was significantly lower than that of the substrate. The increase in Nb content led to an increase in MC and C14-Laves in the coating, hindering the movement of dislocations during the deformation process and improving the wear resistance of the coating. Additionally, they studied the effect of annealing heat treatment on the structure and properties of the $MoFeCrTiWAlNb_3$ alloy coating, observing changes in the phase composition after annealing at different temperatures and durations. Zhao et al. [143] modified the MoNbTaW RHEA coatings using an ultrasonic vibration-assisted method, resulting in enhanced spreadability of the liquid molten pool, a smoother surface, increased molten pool width, and a more uniform structure. Friction testing showed reduced friction coefficients and wear rates under the influence of ultrasonic vibration, with the wear mechanisms being a combination of abrasive wear and adhesive wear. At elevated temperatures, the wear mechanisms shifted to oxidation wear and adhesive wear, with the formation of high-melting point oxides on the worn surface, improving the high-temperature tribological properties.

2.4.3 Corrosion and oxidation resistance

RHEAs are known for their excellent corrosion resistance [31] and high-temperature oxidation resistance [9]. Due to their simple solid solution organization, RHEAs generally exhibit better corrosion resistance compared to 316 L stainless steel, as shown in **Fig. 2. 10 b**. For example, in a comparison with 316L stainless steel, SLM-fabricated MoNbTaW RHEAs showed significantly better corrosion resistance in a 3.5% NaCl solution due to the formation of a passivation film during the corrosion process [149]. Additionally, RHEAs can be effectively improved by combining them with oxidation-resistant elements such as Al, Cr, and Ti [150]. High-temperature oxidation experiments on laser-melted deposited $MoFe_{1.5}CrTiWAlNb$ RHEAs at 800 °C (as illustrated in **Fig. 2. 10 c**) showed that a high content of Cr and small amounts of Al and Ti significantly improved the oxidation resistance by forming a dense and smooth oxide film on the alloy's surface. These findings demonstrate the potential of RHEAs for various high-temperature environments.

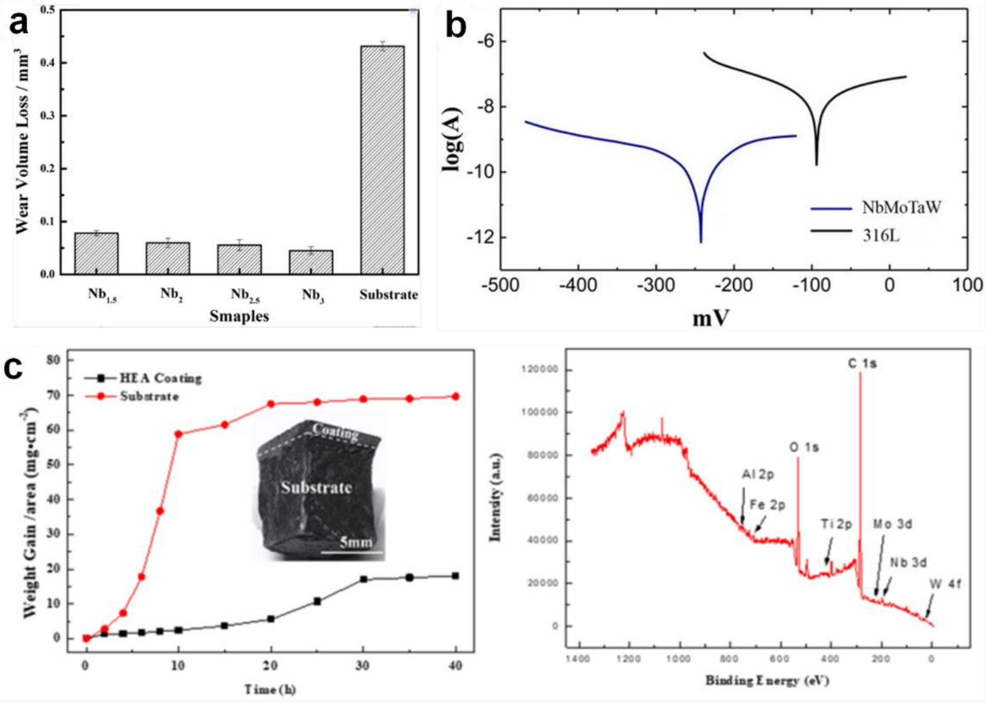

Fig. 2. 10 Other properties of RHEAs [142,149,150]. a, Wear volumes of $MoFe_{1.5}CrTiWAlNbx$ alloy coating [142]. **b,** Polarization curves of LENS-fabricated WMoNbTa RHEA and 316 L [149]. **c,** Mass gain of fabricated $MoFe_{1.5}CrTiWAlNb$ RHEAs at 800 °C for 40 h with corresponding XPS full spectrum [150].

2.6 Summary

The mechanical properties of laser additively manufactured RHEAs are crucial for determining their suitability for engineering applications. The material's ability to withstand short-term acceleration, structural load-bearing, and long-term fatigue depends on whether its room-temperature tensile properties and plasticity meet the necessary criteria. However, there is a lack of reports on the room-temperature tensile properties of RHEAs, which directly hinders their application in the aforementioned scenarios. Therefore, overcoming the room temperature tensile strength and plasticity trade-off of laser additively manufactured RHEAs is an important area of research. Furthermore, in high-temperature application scenarios, such as high-temperature structural load-bearing, thermal protection, and resistance to kinetic energy strikes, the material's tensile strength, friction, and wear properties are of utmost importance. However, there is a performance blank in these aspects for RHEAs prepared by LAM. The unique effects, such as high entropy and lattice distortion, in HEAs require further in-depth research to enhance their high-temperature tensile strength, friction, and wear properties.

Chapter 3 Research Methodology

3.1 Overview

This chapter delineates the research methodologies employed in this study. Section 3.1 provides a thorough overview of the approaches taken. Section 3.2 details the techniques utilized for microstructural characterizations and phase identification. Section 3.3 outlines the methodologies adopted for gathering data on the RHEA properties, ensuring a comprehensive understanding of the material's behavior under various conditions. Finally, Section 3.4 elaborates on the computational modeling techniques used, highlighting the theoretical framework and simulations that support the experimental findings.

3.2 Materials and fabrication methods

Compared with water/gas atomization processes for fcc-based HEA powder, the plasma rotating electrode process (PREP) has a lower cooling rate, which can aid in preparing powders with high sphericity and good fluidity, especially for those powders with melting points higher than 1600 °C. The prepared powder is pure with low oxygen content due to the avoidance of contamination of the crucible. In this project, we used pure elemental powders, like Ti, Hf, Nb, V etc., as shown in **Fig. 3. 1 a**, fabricated through the PREP approach, as the raw materials for fabricating bulk RHEAs via the additive manufacturing approach. Additionally, we selected the $T_{38}V_{15}Nb_{23}Hf_{24}$ alloy, which exhibits excellent tensile strength-ductility synergy [85], as our target RHEA. These powders with a size ranging from 50-100 μm, illustrated by **Fig. 3. 1 a**, indicating good flowability, were blended in a powder mixer (Turbula, T2F) at room temperature for 2 h, with a revolving speed of 200 r/min, within a sealed container, to in-situ synthesize RHEAs with specific compositions. Considering the elemental volatilization during the laser-engineered net shaping (LENS) procedure, the actual compositions of fabricated samples were revealed by energy-dispersive X-ray spectroscopy (EDS). A pure Ti plate with a dimension of 100 × 110 × 6 mm was used as the substrate in this study, which should be cleaned without stains and oxide films before additive manufacturing.

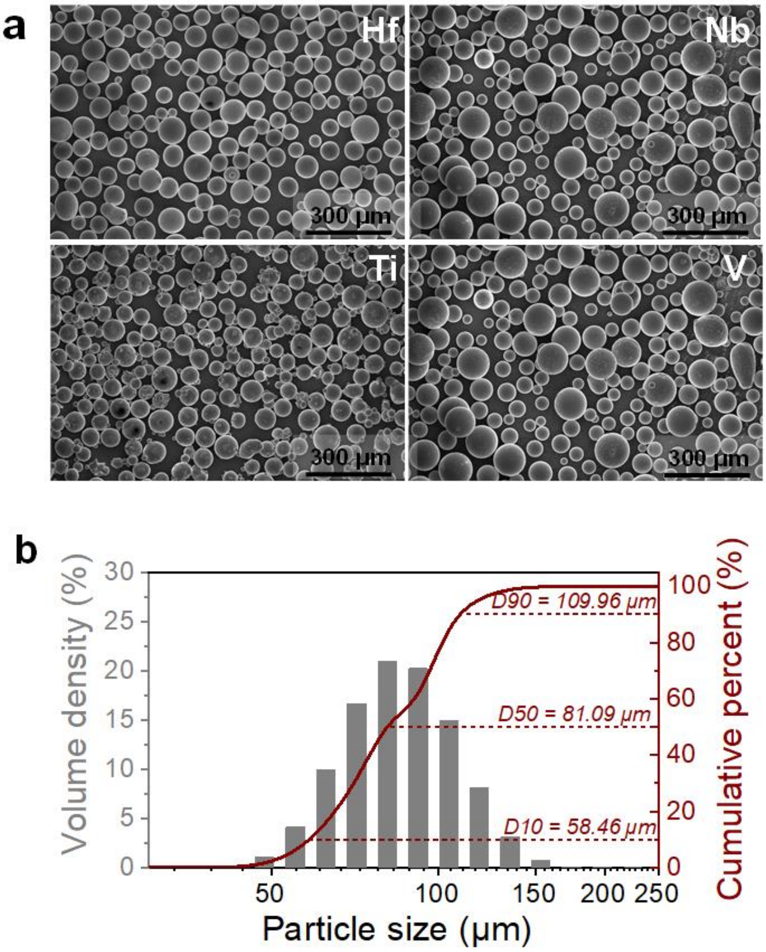

Fig. 3. 1 Characterization of raw elemental powders. a, powder morphologies of raw elemental powders (Hf, Nb, Ti and V). **b**, Powder size distribution map.

Laser additive manufacturing technology diverges from traditional subtractive mechanical processing, significantly enhancing material utilization and forming efficiency [151]. Techniques such as LENS and selective laser melting (SLM) epitomize laser additive manufacturing. LENS, in particular, is adept at producing large, high-performance components and gradient materials with varying compositions and proportions, making it especially suitable for in-situ fabrication of RHEAs using mixed elemental powders. In this project, we used the OPTOMEC LENSTM MR-7 System for the fabrication of RHEAs, which integrates computer numerical control, high-powered lasers, gas control, and powder-feeding systems, as illustrated in **Fig. 3. 2 a**. The computer numerical control system processes digital models, such as CAD models, into sliced models executable by the LENS system. A high-power laser with a wavelength of 1070 nm is generated and transmitted through a fiber to the deposition layer, where it is focused by a lens on the deposition head. The LENS process occurs in an argon-filled chamber equipped for argon circulation and oxygen absorption, maintaining oxygen content below 200 ppm. Argon gas is supplied to the chamber, powder feeder, and nozzle to ensure an inert gas protection environment for the working atmosphere, powder-carrying airflow, and laser coaxial protection gas. The laser, with a spot size of ~ 600 μm, was used to form the melt pool and remelt the previous path. It is common to encounter un-melted powders when fabricating RHEAs via laser deposition of blended elemental powder, due to the difference in melting points [21,23,26]. To ensure a uniform elemental distribution, a remelting procedure was employed in our study, as schematically shown in **Fig. 3. 2 b.**

The scanning strategy for the fabrication process is as follows,

1) First layer building: The first layer was scanned in a zigzag strategy, with a powder feed rate of 4 g/min and a laser power of 550 W;
2) First remelting procedure: After the first layer was finished, the powder delivery nozzle moved upward by 200 μm (offset value) and the remelting process began. The procedure involved a 45 °rotation compared to the previous layer. No powder was delivered to the molten pool during this step, and the laser power was increased to 800 W;
3) Second layer building: Once the remelting process was completed, the powder delivery nozzle was immediately raised by 200 μm, and the powder feed rate was initiated. The working laser power was set to 550 W, and a 45°rotation was applied for layer building;
4) Second layer remelting procedure: A scan rotation of 45°, compared to the previous layer, was applied, and a similar remelting procedure (2) was applied to remelt the previously built layer.

The four steps were repeated periodically until a bulk specimen with a thickness of ~ 4 mm was built. The other parameters used in this study remained constant, including a working distance of 10 mm, a scanning speed of 5 mm/s, and a hatching space of 381 μm. Before the experiment, flowing argon was used to reduce the oxygen level to ~ 200 ppm in the atmospheric chamber which was maintained throughout the entire printing process.

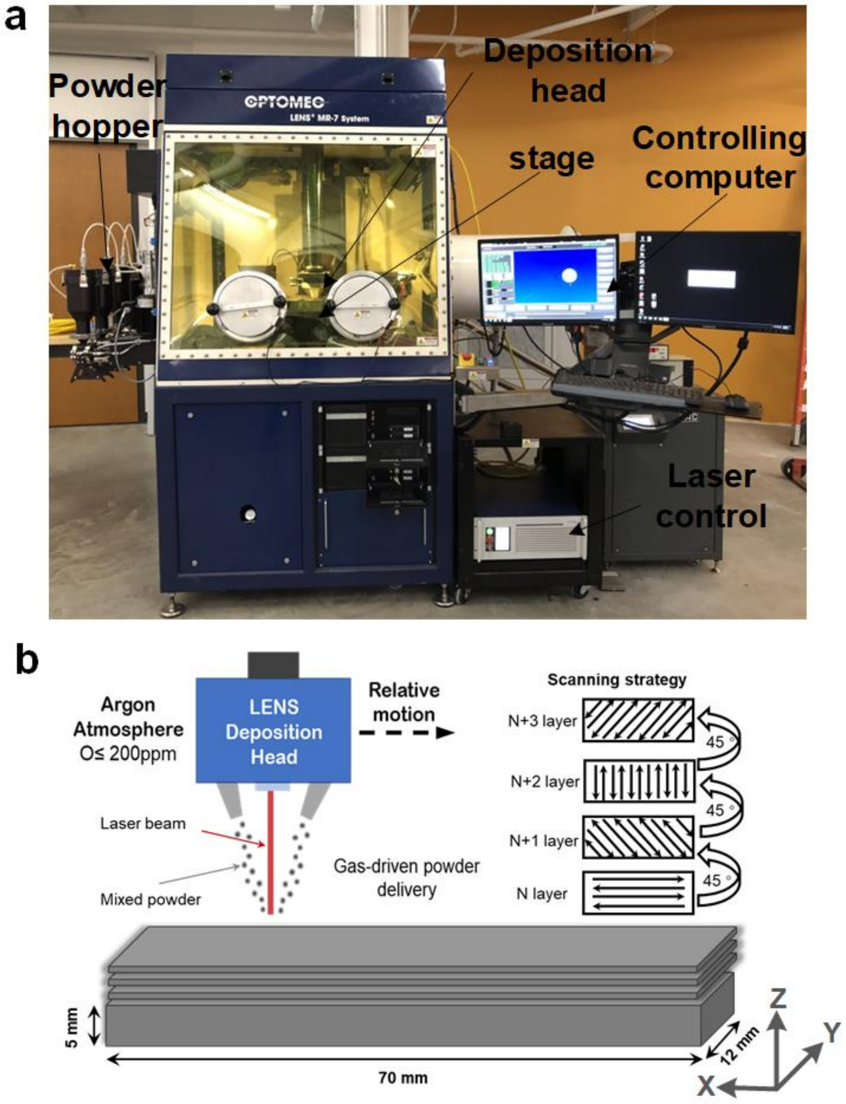

Fig. 3. 2 System overview and fabrication strategy of LENS approach. a, OPTOMEC LENS^{TM} MR-7 System. **b,** Schematic diagram illustrating the fabrication strategy during the LENS procedure.

3.3 Microstructural characterizations and phase identification

3.3.1 Microstructure analysis

Microstructure analysis encompasses high-resolution scanning electron microscopy (SEM), EDS, electron backscatter diffraction (EBSD), and transmission electron microscopy (TEM). SEM samples, including the deformed samples, are prepared by electrical discharge cutting. These samples are ground with 2000-grit SiC paper, polished with 1 μm micro-sized polycrystalline diamond solutions (Struers), and then finished with a finer polishing using a 50 nm sized SiO_2 particle solution (OPS, Struers). To eliminate surface stress which would affect the confidence factor of EBSD results, flat Ar-ion beam milling (Leica, EM TIC 3X) was applied, at a working voltage of 5.5 kV for 40 min. The step size or the magnification during the EBSD experiment varies on the different samples, deformed or undeformed. The working voltage in SEM was maintained at 30 kV during the EBSD procedure. The collected EBSD results were analyzed using Aztec Crystal software (Oxford Inc.). The microstructure of the different samples, either the deformed or the originally stated, was observed in SEM (ThermoFisher, Verios 5UC) in the backscattered electron (BSE) mode, while the fracture morphology analysis was performed in the secondary electron (SE) mode. TEM observations were conducted on samples prepared differently: some RHEAs were prepared by the Ar-ion milling (PIPS II 695c) on a ~30 μm thick disc with a diameter of 3 mm, while the deformed microstructure specimen was prepared via focused ion beam (FIB, ThermoFisher, Helios 5UX). The further microstructures at an atomic level were revealed on TEM (ThermoFisher, Talos F200X) operated at 200 kV as well as an aberration-corrected TEM (ThermoFisher, Spectra 300) equipped with a high-angle annular dark field (HAADF) and EDS (Super-X) detectors. To perform in-situ tensile testing on the LENS-fabricated sample, a dual-tilt straining holder was utilized in the Talos F200X TEM operated at 200 kV. The tensile specimen, in a dog-bone shape, was prepared via Helios 5UX FIB, with a dog-bone shape and loaded to a TEM in-situ force-heat coupling test system (INSTEMS-MT, Bestron, China).

TEM samples are prepared using ion beam milling and focused ion beam (FIB) techniques. Ion beam milled samples are cut from bulk material and ground to 3 mm round discs with a thickness of 30 μm, while FIB samples are lifted out with thicknesses under 100 nm for TEM observation. Various TEM modes are employed for different purposes: bright field mode for microstructure observation, high-angle annular dark field (HAADF) mode for atomic microstructure study, selected area electron diffraction (SAED) for phase identification, and atomic-scale EDS for local chemical fluctuation analysis.

3.3.2 Phase identification

Understanding the phase composition is also crucial to studying the relationship between the microstructure and the properties of RHEAs. In this study, the diffraction methods, including X-ray diffraction (XRD), EBSD, as well as selected area electron diffraction (SAED) approaches, were applied to investigate the phase composition of REHAs. XRD is based on the coherent scattering of X-rays, with the Bragg formula of $2d\sin\theta=n\lambda$, crystal theory, and the Ewald diagram of the reciprocal lattice as the main principles [152]. In this project, XRD experiments (Rigaku, Smartlab) were conducted with copper radiation (λ=1.54 Å) by setting a step size of 1 °/min to perform the phase analysis of fabricated RHEAs after different post-treatments. Additionally, atomic pair distribution function (PDF) analysis was conducted utilizing X-ray total scattering data collected from a laboratory X-ray scattering instrument (SmartLab, Rigaku) equipped with a rotating anode silver target (λ=0.56 Å for Ag Kα), and then extracted from the program of PDFgetX3 [153]. During the data collection procedure, the transmission setup utilized a capillary sealed with the sample and subtracted the data from the empty capillary to obtain the scattering signal of the detected sample. The acquired data were processed using Fourier transform on the normalized X-ray scattering function ($F(Q)$), $Q = 4\pi \cdot sin\theta/\lambda$, to obtain the respective PDF ($G(R)$). After obtaining the required PDF, the PDFgui package [154] was used to fit different structure models of the as-fabricated RHEA.

3.4 Measurement of properties

3.4.1 Room temperature tensile test

We used a universal testing machine (ZwickRoell, Proline), as shown in **Fig. 3. 3**, to obtain the room temperature tensile properties of fabricated RHEAs equipped with a digital image correlation (DIC, ZwickRoell) system under a strain rate of 1×10^{-3}/s. This equipment is composed of three parts: a tensile system, a heating system and a measuring system. During the test, to obtain accurate stress and strain data, the DIC optical measurement equipment was used to measure the deformation data of the material in this test which was processed by the testXpert III software to obtain test curves such as speed, test force, displacement, and time. The DIC measurement is used to calculate the local strain field of the sample by capturing random points in the stretching process. The tensile bars were cut from the built sample with a dog-bone shape via wire-cut electrical discharge machining with gauge dimensions of 6×2×1 mm^3. Those tensile bars were ground through progressively finer sandpaper before carrying out the tensile tests. We can obtain the strain-stress curves during the whole tensile tests to obtain the yield strength, elongation as well as tensile strength. The engineering stress (σ_e) and engineering strain (ε_e) can be directly collected after tensile tests. The true stress (σ_t) and strain (ε_t) can be calculated via the following equations:

$$\sigma_t = \sigma_e \times (\varepsilon_e + 1) \tag{3. 1}$$

$$\varepsilon_t = ln(\varepsilon_e + 1) \tag{3. 2}$$

3.4.2 Hot tensile test

Temperature is also an important influencing condition affecting the mechanical properties of RHEAs. The universal testing machine is also equipped with a high-temperature furnace and an environmental test chamber (ZwickRoell) to ensure a wide working temperature range (-80°C to +2000°C). The temperature control and monitoring system (testControl II, ZwickRoell) can realize the high-temperature stretching of the material by precisely controlling the temperature in the furnace. Before the high-temperature tensile test, the furnace was set to the target temperature and maintained for 5 minutes, with a load force of 50 N applied during heating to prevent thermal expansion effects. The specimen was then stretched to fracture at a tensile strain rate of 1×10^{-3}/s. The test conditions mirrored those of the room temperature tensile test, and the true stress-strain curves were derived from the engineering strain-stress curves.

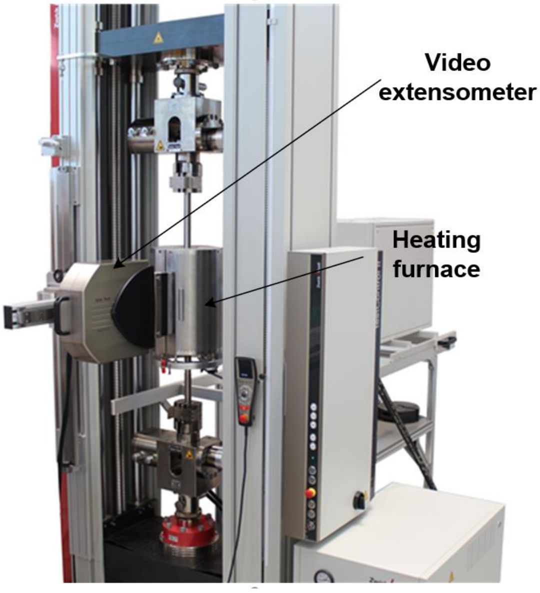

Fig. 3. 3 Tensile testing machine.

3.4.3 Tribological test

The tribological properties at both room and elevated temperatures were evaluated using a ball-on-disk tribometer (MFT-5000, RTEC Instruments) through dry-sliding wear tests. An Al_2O_3 ceramic ball with a 9.53 mm diameter served as the counter material, chosen for its hardness and stability at high temperatures. Wear tests were conducted at room temperature, 400 ℃, 600 ℃, and 800 ℃, with a 10 N normal load, a 2 mm stroke length, a 5 Hz reciprocating frequency, and a 30-minute duration. Samples measuring 20 × 20 × 3 mm were polished and subjected to wear testing at the specified temperatures, with the coefficient of friction (COF) monitored in real-time. Post-wear analysis of the surfaces and volumes of the alloys was performed using a 3D optical profiler (S Neox, Sensofar). The tribological morphology and chemical composition of the worn surfaces, as well as the cross-sectional worn tracks, were investigated using scanning electron microscopy (SEM, Verios 5UC, ThermoFisher) coupled with energy-dispersive spectroscopy (EDS, X-max 80, Oxford). Subsurface morphology was characterized by TEM (Talos F200X) with EDS, with sample preparation facilitated by a focused ion beam (FIB, Helios 5 UX).

3.4.4 High-temperature oxidation resistance test

To investigate the oxidation mechanism of the as-fabricated RHEA, we carried out 873 K and 1073 K oxidation tests. The oxidized samples were cut into dimensions of 10 × 10 × 4 mm via an electrical discharge cutting machine and then underwent grinding as well as polishing procedures. The samples were oxidized in an open-air tube furnace. The weights of the oxidized samples processed at 1h, 3h, 6h, 12h, 24h, 48h, 72h, 96h, and 120h were collected by a precise balance (Sartorius SQP), and the corresponding microstructure and phase composition were achieved via SEM (Verios 5 UC) and XRD (Smartlab, Cu $\lambda = 1.54$ Å) experiments.

3.5 Computational modeling

3.5.1 Thermodynamic calculation

Thermo-Calc software is recognized as the best and most comprehensive multi-system thermodynamics and phase diagram calculation software in the world. It is an important calculation software in the field of material genetic engineering. Thermo-Calc software currently mainly includes three modules [155]: The Thermo-Calc thermodynamic calculation module, the DICTRA diffusion dynamics calculation module and the TC-PRISMA precipitation calculation module. The most commonly used is the thermodynamic calculation module, which contains: (1) Single-point equilibrium: Calculating the fixed composition, the equilibrium phase and phase composition of the material at a fixed temperature and pressure. (2) Uniaxial equilibrium: With the change of a single variable (temperature/composition), the equilibrium phase and phase composition of the material change. (3) Phase Diagram/Binary System Calculation/Ternary System Calculation: Calculating the equilibrium phase and phase composition changes of materials under two variables. (4) Scheil solidification process simulation: Simulation of non-equilibrium solidification and microscopic composition segregation of multi-component alloys. We use the recently established TEHEA database, which consists of 105 binary and 200 ternary systems, and almost all stable phases and intermetallic compounds.

3.5.2 DFT calculations

Density Functional Theory (DFT) is the most popular first-principle calculation method in quantum chemistry and computational chemistry [156]. Because its calculation amount is lower than other quantum chemical methods, it has practical application value in the field of computational simulation and has a wide range of applications and a long history. In this project, the lattice constant, elasticity and other properties of the RHEA were calculated using the virtual crystal approximation (VCA) based on the Cambridge Sequential Total Energy Package (CASTEP) [157]. During the calculation, the OTFG norm serving pseudopotential was selected with a custom cutoff energy of 1200 eV and k-points vary with different calculation tasks. In the MonkhorstPack scheme, the Brillouin zone was sampled with the maximum total energy loss of 1×10^{-5} eV • atom^{-1}. The forces on a single atom converged to less than 0.03 eV • Å^{-1}, while the maximum atom placement was less than 0.001Å and the total stress tensor order was reduced to 0.05 GPa.

3.5.3 Crystal plasticity finite element modeling

Crystal Plasticity Finite Element Modeling (CPFEM) describes the anisotropic plastic deformation of crystals under complex boundary conditions, integrating dislocation theory and continuum mechanics [158–165]. CPFEM is implemented in Düsseldorf Advanced Material Simulation Kit (DAMASK) software [166] in this project, which simulates crystal plasticity within a continuum framework and solves elastic-plastic boundary value problems. This package has the characteristics of high modularity, good flexibility, and clear structure. It is mainly used to simulate crystal plasticity in the continuum framework of finite strain and solve the elastic-plastic boundary value problem in the process of material deformation. In addition, it can also solve damage and thermophysical problems. The solution to the continuum boundary value problem requires constructing the constitutive response of stress and strain at the junction of each material element. Therefore, the overall simulation process can be divided into four basic levels from top to bottom, as shown in **Fig. 3. 4**. To solve the relationship between the total deformation gradient tensor $\bar{\boldsymbol{F}}$ and the first Piola-Kirchhoff stress at each discrete unit under given boundary conditions and finite strain conditions, it is necessary to assign the total deformation velocity gradient tensor to the homogenization division in the material units. The deformation velocity tensor $\boldsymbol{F}$ and the homogenized stress $\boldsymbol{P}$ received by each unit are obtained. The deformation velocity gradient tensor is decomposed into different values of elastic strain and plastic strain, namely $\boldsymbol{F_e}$ and $\boldsymbol{F_p}$. Through the actual elastic and plastic constitutive equations, the elastic deformation velocity gradient $\boldsymbol{F_e}$ and the plastic deformation velocity gradient $\boldsymbol{L_p}$ and the second Piola- Kirchhoff stress ($\boldsymbol{S}$) are linked to complete the elastoplastic deformation throughout the process. DAMASK conducts the entire simulation process in the above-mentioned hierarchical structure. The software is built in a strictly modular fashion. This modular structure makes it easy to add and customize other constitutive models and solve the stiffness matrix using a Fast Fourier Transform (FFT) solver.

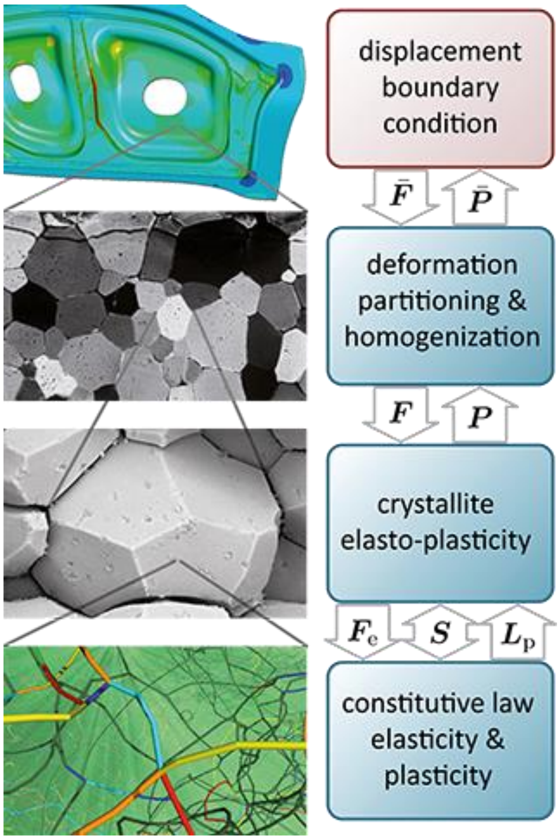

Fig. 3. 4 Overall simulation process in CPFEM.

Chapter 4 Strong yet ductile T42 RHEA fabricated via additive manufacturing

4.1 Introduction

HEAs have the potential to create exceptional alloys based on the periodic table of elements [2,3]. RRHEAs are being considered for high-temperature applications due to their constituents with higher melting points [94,95]. While many RHEAs show ductility in compression tests at room temperature [41], only a few demonstrate acceptable tensile ductility without sacrificing yield strength [115], leading to a strength-ductility trade-off [7]. Various studies have shown promising results in improving strength while preserving ductility in RHEAs, such as introducing local chemical fluctuations [106], forming oxygen complexes [32], creating spinodal modulations [115], or employing metastability engineering [100], etc. LAM technology offers a solution to this challenge by introducing unique structures, like heterogeneous structures [167] or dislocation structures [168], etc. LAM processes, such as laser-engineered net shaping (LENS), have the potential to fabricate RHEAs with improved mechanical properties.

In this study, we focused on the $Ti_{42}Hf_{21}Nb_{21}V_{16}$ (T42) RHEA system, which exhibited excellent ductility and impressive mechanical performance after the LENS procedure. By maintaining a low content of oxygen and nitrogen atmosphere during the LENS procedure, the fabricated RHEA showed improved mechanical properties. Our findings propose a solution to the strength-ductility trade-off in RHEAs, guiding the design of refractory alloys that are both strong and ductile, and opening up the possibility of directly manufacturing RHEA products in the future.

4.2 Results

4.2.1 Composition identification

As the composition offset generally formed in the LENS-fabricated alloys prepared by mixed pure elemental powders with the nominal compositions [135,169,170], we conducted the EDS tests on the LENS-fabricated RHEA as well as its heat-treated one to determine their actual compositions after LENS. Moreover, we dispense the antithetical RHEA through casting by referring to the actual composition in the LENS-fabricated sample, whose results are listed in **Table 4. 1**. Considering the absorption of oxygen and nitrogen in Ti-based alloys under high temperatures [171], we also conducted the precise oxygen and nitrogen determination by the ON836 Oxygen/Nitrogen system (LECO, USA) with the ultra-precision of 0.025 ppm under the Ti-based method. In addition, the addition of oxygen or nitrogen in the RHEA matrix has been shown to effectively enhance its strength [32]. It is necessary to collect the precise measurements of oxygen and nitrogen contents in the RHEA matrix, as these elements can improve yield strength. Details are provided in **Section 4.3.2**. The pre-weighted RHEAs (~ 200 mg) fabricated through different approaches were placed in the graphite crucible and then melted to release analyte gases. The detected oxygen and nitrogen content in those RHEAs is also listed in **Table 4. 1**. Based on the EDS results, the LENS-fabricated RHEA has an atomic ratio of Ti:Hf:Nb:V=42:21:21:16. As a result, the fabricated RHEA is referred to as T42 RHEA, and we also prepared the as-cast counterpart with the same composition for comparison.

Table 4. 1 Nominal and EDS results, along with oxygen and nitrogen contents, of the fabricated RHEAs.

Element	Ti	Hf	Nb	V	O	N
	at.%					
Nominal composition	38	24	23	15	-	-
As-cast	41.89	21.17	21.15	15.79	0.007 (13 ppm)	0.018 (29 ppm)
As-LENS	41.71	21.33	20.90	16.06	0.028 (52 ppm)	0.111 (185 ppm)
As-HT	41.77	21.25	21.23	15.75	0.028 (52 ppm)	0.107 (179 ppm)

4.2.2 Calculation results

The LENS process involves high cooling rates (~10^3 – 10^4 K/s [172]), which deviates the microstructure from the equilibrium calculations. The Scheil solidification process simulations can be performed in ThermoCalc software based on the assumptions of liquid-solid interface equilibrium, infinite diffusion in the liquid and no diffusion in the solid. This allowed us to predict the as-solidified microstructures in RHEAs prepared via the LENS method. The equilibrium and no-equilibrium phase diagrams are given in **Fig. 4. 1 a** and **b**, respectively, indicating that a single bcc-structure phase would be formed after the LENS procedure based on the given compositions.

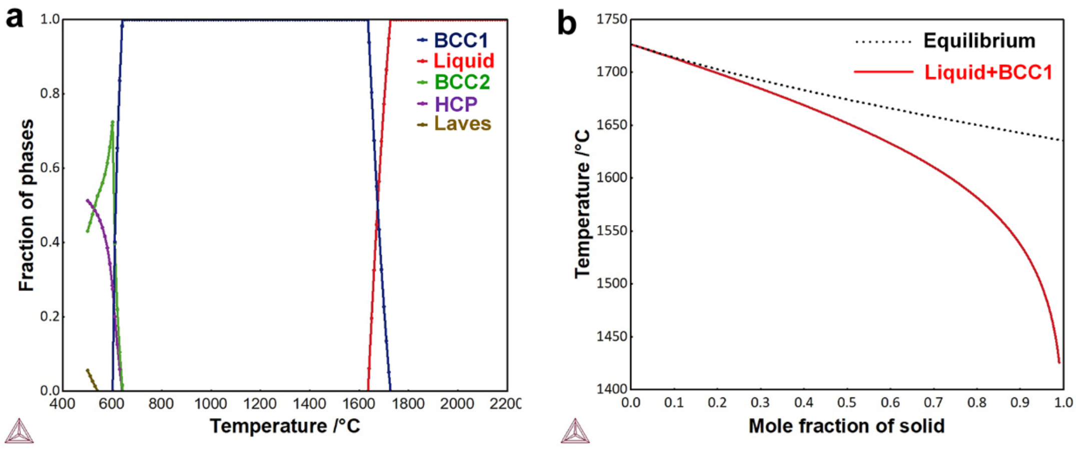

Fig. 4. 1 The CALPHAD calculation results of the fabricated RHEA system. a, Fraction of phases as a function of temperature. **b,** Scheil diagram

Before the calculation of the lattice constant, we ensured the convergence parameters until the error on the calculated total energy reached the criteria of 0.001 eV/atom [173]. We used the VCA method to study the lattice constant of T42 RHEA, which was calculated to be 3.318 Å, with an error of less than 1% compared to the experimental result of the as-cast sample (given in Section 3.2). This indicates that the parameter setting in this calculation procedure was reasonable. By establishing the relationship between the unstable stacking fault energy (USFE) and surface energy (SE), the intrinsic embrittlement or ductility can be reflected through these mentioned parameters (details can be found in Section 4.1). **Fig. 4. 2 a** illustrates a supercell consisting of 13 atomic layers with an ABABABABABABA stacking sequence of the closed-packed (110) plane, with a vacuum layer of 15 Å. The formation of an unstable stacking fault (USF) at the shear direction of the upper part along [111] at the step of 0.1 is also shown. The GSFE can be obtained based on the following equation [174]:

$$\gamma_{SFE} = \frac{1}{A}(E_u - E_0) \tag{4. 1}$$

where A is the stacking fault area, E_u and E_0 denote the total energy of the supercell with and without a shear displacement, respectively. After the calculation, we obtained the GSFE curve (see **Fig. 4. 2 b**), with the USFE of 313.9 mJ/m^2.

For the unrelaxed surface energy calculation, the divided two parts underwent the compressive and tensile calculations (see **Fig. 4. 2 c**) with a step of 0.1 Å to fit the energy *vs.* displacement curve to obtain the free surface energy of the (110) lattice plane using the universal binding-energy relation (UBER) method, describing as follows [175]:

$$E_x = -\gamma_S \left(1 + \frac{x}{l}\right) e^{-\frac{x}{l}} + C \qquad (4.\ 2)$$

where γ is the unrelaxed (110) surface energy, l is a scaling length and C is a constant in this equation. Thus, based on the change in total energy E_x with displacement obtained by calculation results, plotted in **Fig. 4. 2 d**, yielding the surface energy value of 3190 mJ/m^2 in the target RHEA.

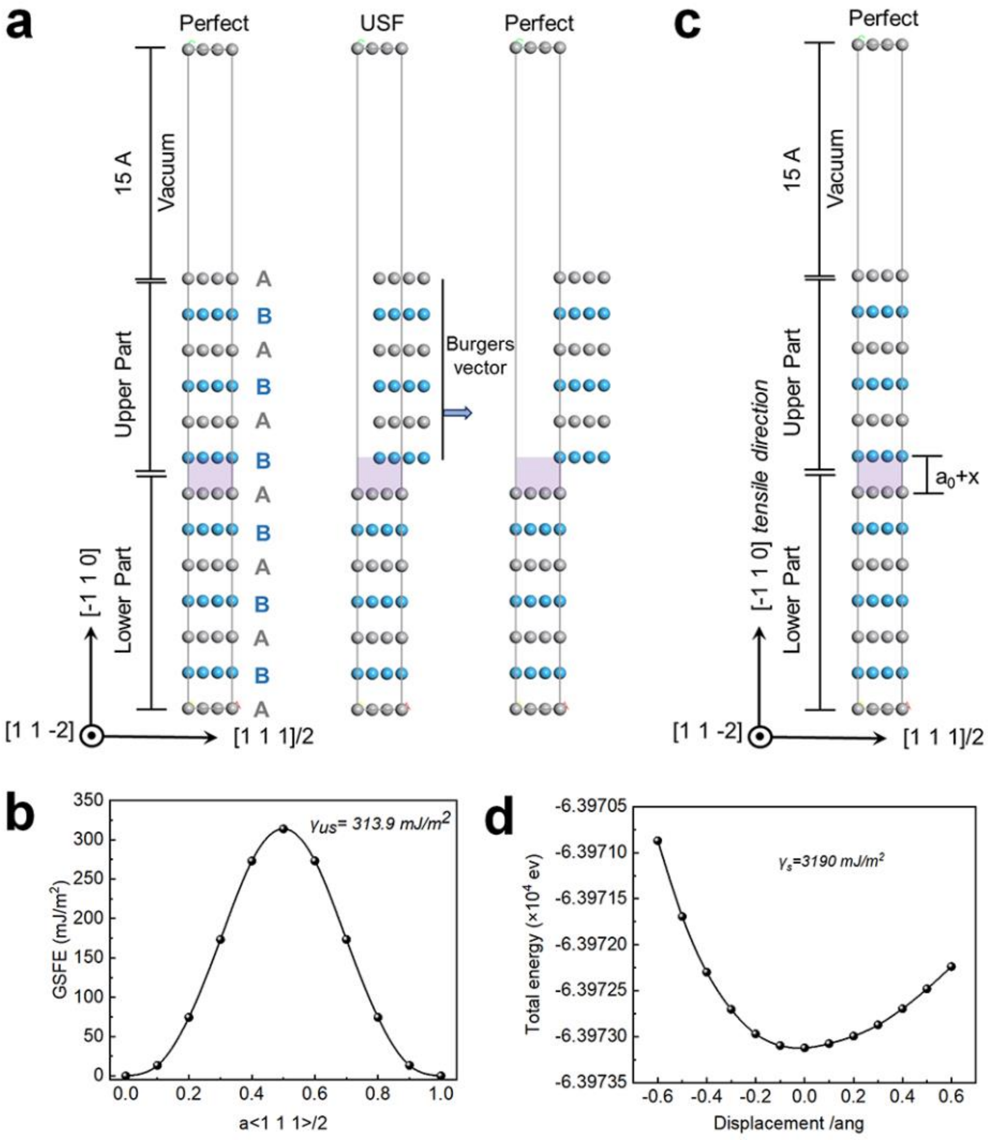

Fig. 4. 2 DFT calculations on T42 RHEA. a, The BCC supercell containing the atomic stacking. **b**, First-principle calculated GSFE curves of targeted RHEA system. **c**, The BCC supercell is used for tensile and compression DFT calculations. **d**, The fitted total energy versus displacement curve via the UBER method.

4.2.3 Microstructure of fabricated RHEAs

In our study, we examined the microstructures of RHEA specimens fabricated using different methods: casting (as-casting), LENS (as-LENS) and LENS-fabricated RHEA followed by heat treatment (as-HT). The microstructure collected from the top surface revealed that the LENS-fabricated RHEA exhibited an equiaxed grain morphology (**Fig. 4. 3 a**), and its corresponding elemental mapping results (**Fig. 4. 3 b**) demonstrated an even distribution of alloying elements, indicating the absence of macro-elemental segregations and un-melted powders when employing a higher laser powder remelting approach. The EBSD IPF figures collected from the XY and XZ planes are given in **Fig. 4. 3 a,** showing that the LENS-fabricated T42 RHEA has a columnar grain morphology along the building direction (BD) and the equiaxed grains on the top surface (**Fig. 4. 3 a**). This difference in grain morphology is attributed to the higher ratio between the temperature gradient in the solid/liquid interface (G), which can increase to 10^3 K/mm in the additive manufacturing process [25], and solidification velocity (R) [176,177], differing from the equiaxed grains formed in LENS-fabricated HfNbTiZr RHEA [25].

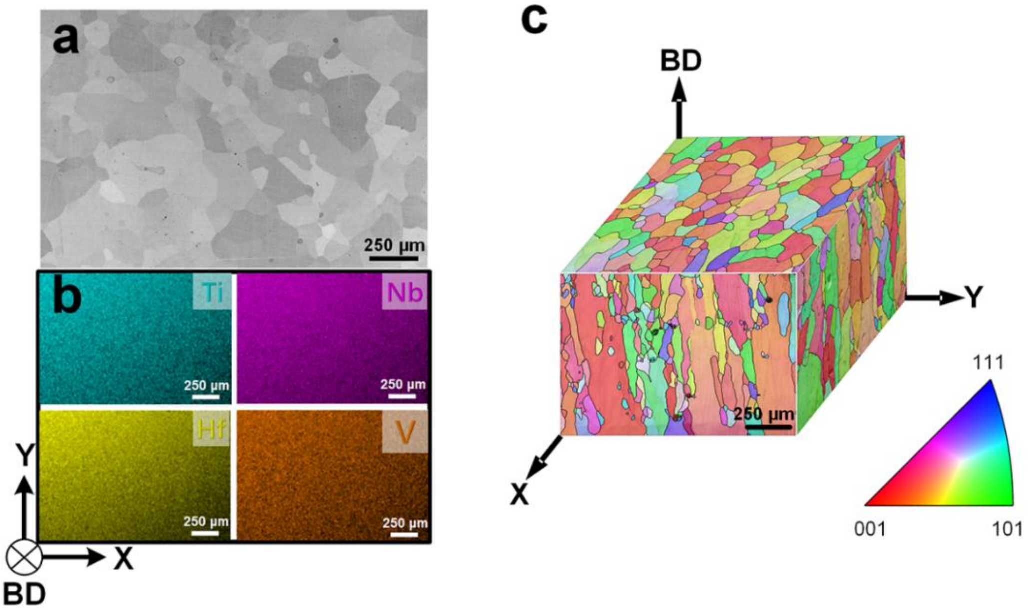

Fig. 4. 3 The microstructure of LENS-fabricated RHEA. a, The BSE image from the as-LENS specimen. **b,** Corresponding EDS mapping. **c,** a 3-dimensional reconstructed EBSD structure showing the presence of columnar grain growth along the BD.

Further analysis of the microstructure of different RHEAs fabricated using several approaches was studied as follows. The EBSD IPF maps (**Fig. 4. 4 a**) collected on the top surfaces of tensile bars from RHEAs reveal the formation of equiaxed grains, whereas the grain size and preferable orientations vary among those samples. The LENS-fabricated sample exhibits the smallest grain size of 196 μm, while the grain sizes of the other samples are at the same level of ~ 240 μm (as shown in the statistical chart in **Fig. 4. 4 b**). The kernel average misorientation (KAM) figures (**Fig. 4. 4 c**), which can be used to assess the geometrically necessary dislocation densities [178] and the dislocation structures [179], revealed no significant difference in their densities among the RHEAs fabricated using different approaches. This is in contrast to the unique dislocation networks typically formed in the FCC alloys [168,180] fabricated via the additive manufacturing method. The pole and inverse pole figures derived from the top surface of LENS-fabricated samples (**Fig. 4. 4 d**) illustrate the presence of <001>/(110) texture in the as-LENS RHEA with a preferable growth orientation of <0 0 1> parallel to the BD. Conversely, the pole figures of the as-cast T42 RHEA (**Fig. 4. 4 e**) indicate the absence of any noticeable obvious texture, while long-time high-temperature annealing primarily promoted grain growth rather than altering its preferable orientation.

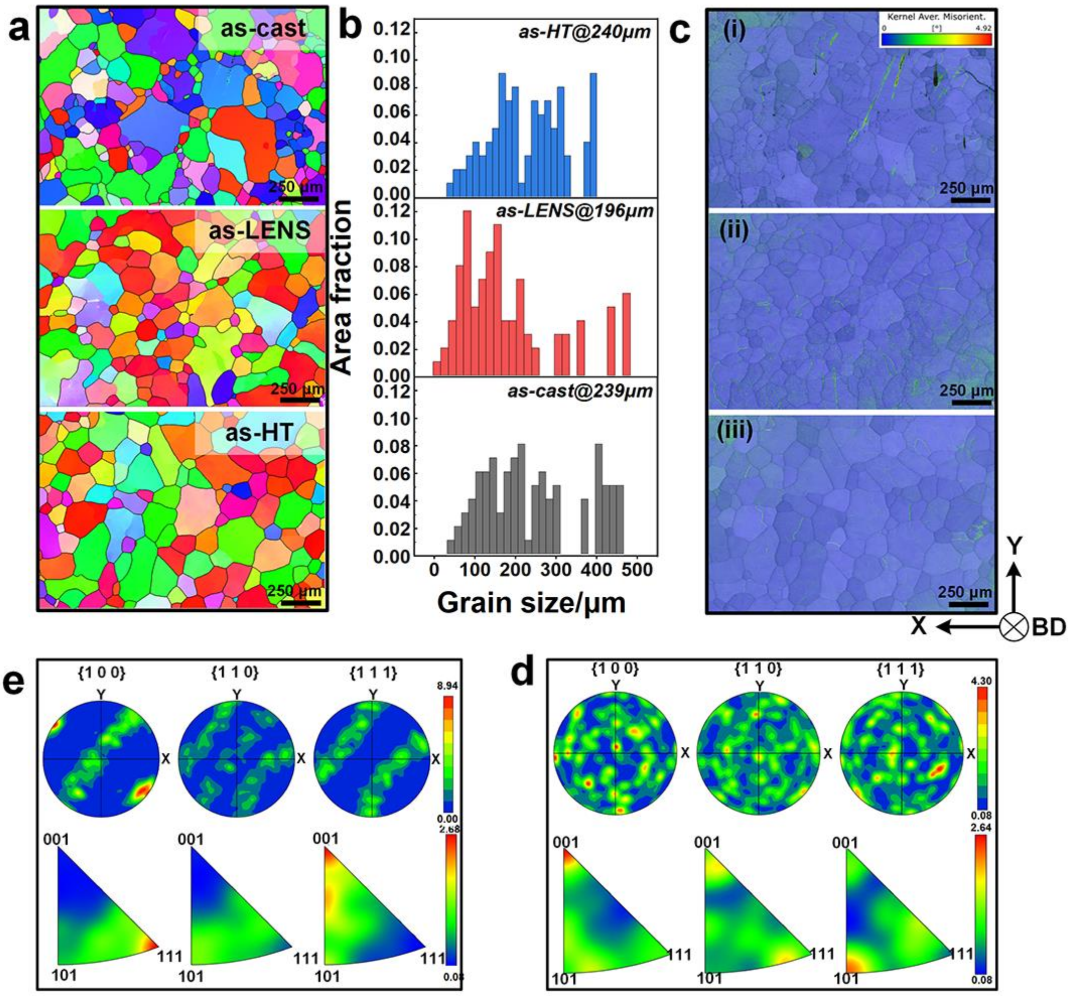

Fig. 4. 4 The microstructural characterization of T42 RHEAs prepared via different approaches. a, The EBSD IPF maps from RHEAs fabricated using different approaches with corresponding statistics of grain size distribution given in **b. c**, KAM maps showing that no dislocation networks formed in RHEAs fabricated after LENS. **d,** The collected pole figures and inverse pole figures from the top surface of as-LENS RHEA. **e**, The pole figures and inverse pole figures of as-cast RHEA.

The CALPHAD method demonstrates that the target system can produce a single BCC structure in the non-equilibrium cooling processes (**Fig. 4. 1 b**). Additionally, EBSD phase maps (**Fig. 4. 5 a (i-iii))** indicate that there seem to be single BCC structures among those RHEAs. However, the XRD profile (**Fig. 4. 5 b**) reveals the formation of a single BCC phase in the as-cast specimen with a lattice constant of ~ 3.325 Å. Conversely, the as-HT RHEA exhibits diffraction peak splitting of the (310) crystal plane, similar to HfNbTiV RHEA [115], suggesting the separation of the BCC matrix into the primary phase of β_1 and the secondary separated phase of β_2. The lattice constant of the BCC matrix in the as-LENS and as-HT RHEAs is larger, approximately 3.330 Å, compared to the as-cast sample, due to the solid soluble interstitial atoms in the RHEA matrix [73].

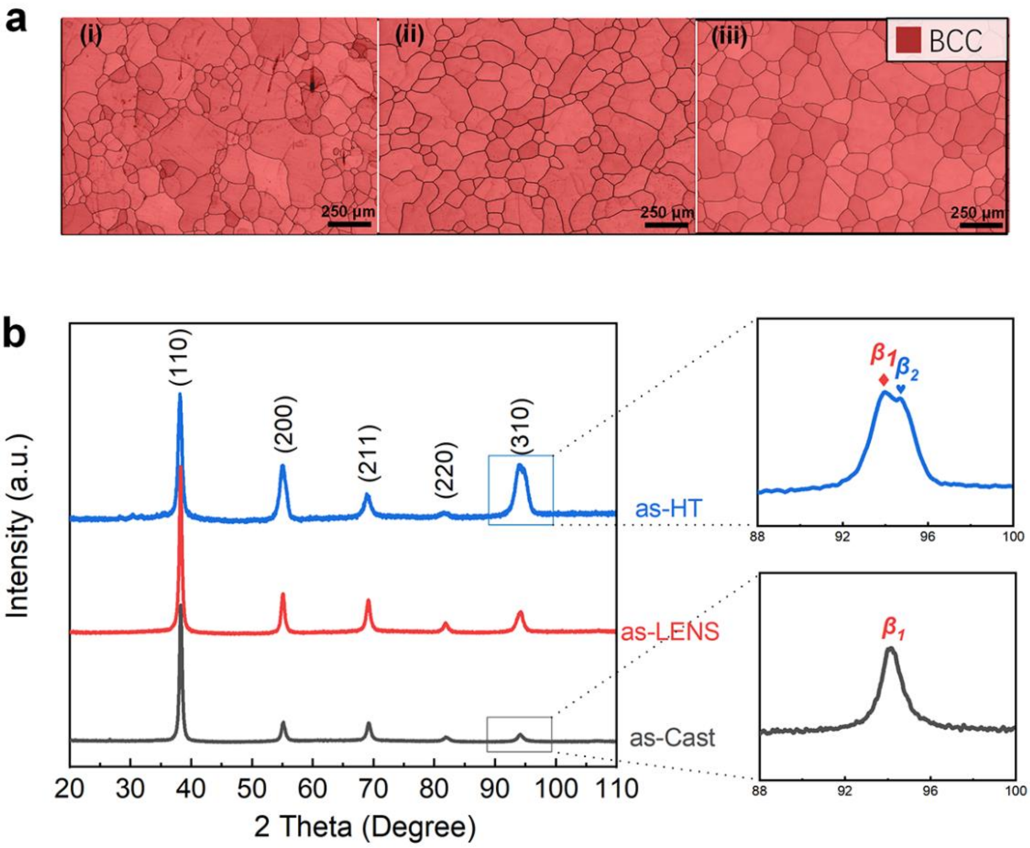

Fig. 4. 5 Phase identification of T42 RHEAs prepared via different approaches. a, The EBSD phase maps. **b**, The XRD profiles of RHEAs fabricated using varied methods.

The TEM observation in **Fig. 4. 6 a** illustrates that the nano-scale phase separation occurs not only in as-HT RHEAs (**Fig. 4. 6 a** (iii)) but also in the as-LENS one, despite the selected area electron diffraction (SAED) patterns showing the characteristic of a single BCC phase in the inserts of **Fig. 4. 6 a**. To confirm the presence of phase separation in the as-LENS RHEA (**Fig. 4. 6 b**), the atomic-scale characterization and the corresponding Fast Fourier Transformation (FFT) images ((ii-iii)) of the marked area are given in **Fig. 4. 6 b** (i), revealing a structure different from the BCC matrix. A distinct interface between the BCC matrix and separated phase was characterized as given in **Fig. 4. 6 c** (i), with the corresponding FFT images showing an even more obvious BCC matrix separation after heat treatment. Although the spinodal modulations were observed in the equimolar HfNbTiV RHEA [115], the separated structure would not be a secondary BCC structure due to the distortion of the SAED patterns between **Fig. 4. 6 b** (ii) and (iii). Based on the FFT patterns compared with simulated ones via the CrysTBox package [181] and XRD profile, a contracted body-centered tetragonal (BCT) structure (similar to the structure in $Ti_{38}V_{15}Nb_{23}Hf_{24}$ RHEA [85]), with the lattice parameters of a=c=3.330 Å and b=3.315 Å, was formed in the as-LENS sample and promoted by high-temperature annealing. Significant atomic distortion (x and y directions) obtained via geometrical phase analysis (GPA) [182] occurs at the interface between the separated phases (**Fig. 4. 6 c** (iii-iv)), consequentially resulting in the complex interaction with dislocation that would modify the deformation process in those RHEAs. The presence of Hf atoms with a relatively larger atomic radius induces a larger lattice distortion [183] leading to the lattice strain and higher strength in the HEAs compared to the conventional alloys [105]. The atomic EDS mapping collected from the as-LENS RHEA shows the nano-scale chemical heterogeneity (see **Fig. 4. 6 d**) and the formation of elemental rich clusters pointing by the green and white arrows, regardless of the manufacturing approaches, which can contribute to the ductility increase instead of strengthening RHEA [25].

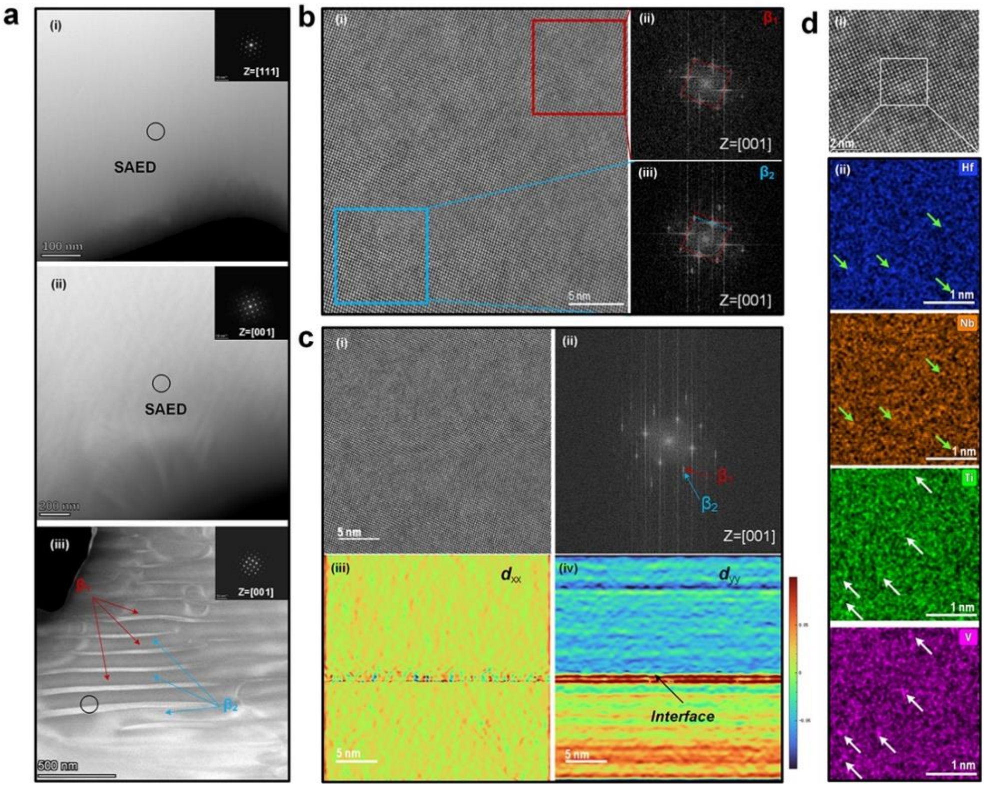

Fig. 4. 6 Nano-scale microstructure of RHEAs fabricated via different approaches. a (i-iii) bright field TEM images collected from RHEAs prepared via casting, LENS as well as-HT with the SEAD patterns insert. **b**, The HRTEM figure with the corresponding FFT figures (**ii** and **iii**) from the as-LENS sample. **c(i)**, The HRTEM figure collected from the as-HT sample shows a clear interface of separated phases illustrated by (**ii**) the corresponding FFT image and (iii-iv) gives atomic distortions near the interface. **d(i)**, The HRTEM image with (**ii**) corresponding atomic scale EDS mapping. TEM figures are collected along the [001] zone axis.

4.2.4 Improved tensile strength-ductility synergy

We performed room temperature tensile tests on the RHEA specimens fabricated using different methods, and the results are presented in **Fig. 4. 7**. Among these samples, the LENS-fabricated sample shows the best strength-ductility combination (see **Fig. 4. 7 a**) with a yield strength of 1034 MPa and fracture strain of 22.5 %. In comparison, the as-cast RHEA has a yield strength of 780 MPa and fracture strain of 20.2 %. The results indicate that LENS fabrication can significantly increase the yield strength (by almost 32%) without compromising ductility, effectively overcoming the strength-ductility trade-off in specific RHEAs. It is worth noting that, after high-temperature annealing of the LENS-fabricated samples, the yield strength and the fracture strain were both slightly decreased to 970 MPa and 21.6 %, respectively. Additionally, we also converted the slope of the true stress-strain curve into the strain-hardening rate (SHR) curves, as shown in **Fig. 4. 7 b**, showing the plummet (Stage I), steady increase (Stage II) and then decreased trends (Stage III) on the plastic flow. During the deformation Stage I, a sharp drop in SHR is formed, while a gradual decrease in SHR also occurs in the deformation stage III. The plastic deformation stage II, characterized by a slight increase in SHR, terminates at different true strains of RHEAs fabricated via different approaches. Insert of **Fig. 4. 7 b** reveals the local strain profiles by DIC at the last frame before fracture collected along lines in **Fig. 4. 9 a** and also displays the necking onsets, giving that the as-cast RHEA has the longest necking length while the as-HT counterpart has the shortest one (details are given as follows). For comparison, we included Ashby plots of Ti-based alloys fabricated using additive manufacturing processes [184], the as-cast RHEAs [94], the previously reported LENS-fabricated HfTiZrNb RHEA [25], and our results (see **Fig. 4. 7 c)**. Our T42 RHEA fabricated using LENS stands out and has a superb strength-ductility synergy as well as specific yield strength-strain matching among the reported well-performed RHEAs (see **Fig. 4. 7 d**) [115]. Only a few others, such as equimolar HfNbTiV [115], and oxygen-doped

HfNbTiZr RHEAs [32], can succeed in this RHEA, attributed to the presence of the spinodal structure as well as the oxygen complex. However, their SHRs plunge to under true stress at the early plastic deformation [115], yet they still exhibit superior strength-ductility synergies in those RHEAs.

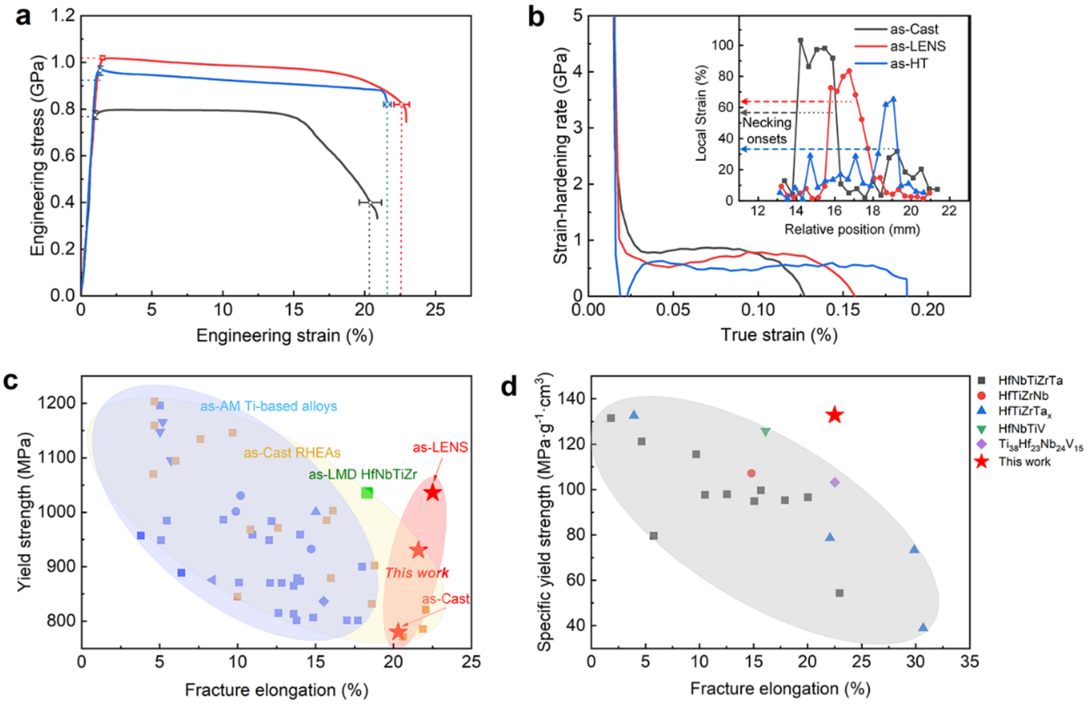

Fig. 4. 7 Enhanced tensile strength-ductility synergy in as-LENS RHEA compared to other fabrication methods. a, The engineering stress-strain curves of RHEAs fabricated different approaches. **b,** The corresponding strain hardening rate curves show different deformation stages. Insert of **b** is the local strain profiles by DIC. **c,** the tensile yield strength versus fracture elongation in comparison with previously reported Ti-based alloys prepared via AM methods [184], the bcc-type RHEAs [94] as well as the as-LENS HfNbTiZr RHEA [25]. **d,** giving the comparison with previously reported RHEAs on the specific yield strength versus the fracture elongation.

The fracture surface morphologies show the presence of complete ductile dimples without forming cleavages or intergranular fracture surfaces (see **Fig. 4. 8 a-c**), indicating the formation of through-sample ductile fractures in those RHEAs. **Fig. 4. 8 d** depicts the splicing BSE images of upper tensile surfaces from RHEAs fabricated using different methods, indicating the less uniform tensile strain in as-cast RHEA and obvious shear bands in the severely deformed zone. Moreover, the macro area of the LENS-fabricated T42 alloy shows no micro-cracks, despite the presence of micro-pores. Previous studies indicate that while micro-pores can lead to stress concentration during deformation [185], micro-cracks are detrimental to the ductility of LAM-fabricated RHEAs [22,25,68,137]. This explains the scarcity of LAM-fabricated RHEAs with superior ductility in earlier research. In our study, the ductile nature of T42 was already confirmed through DFT analysis, as detailed in **Section 4.2.2.** Notably, significant defects such as pores and cracks were absent in the as-cast T42 alloy (**Fig. 4. 8 d**), demonstrating a superior strength-ductility synergy compared to its as-cast counterpart.

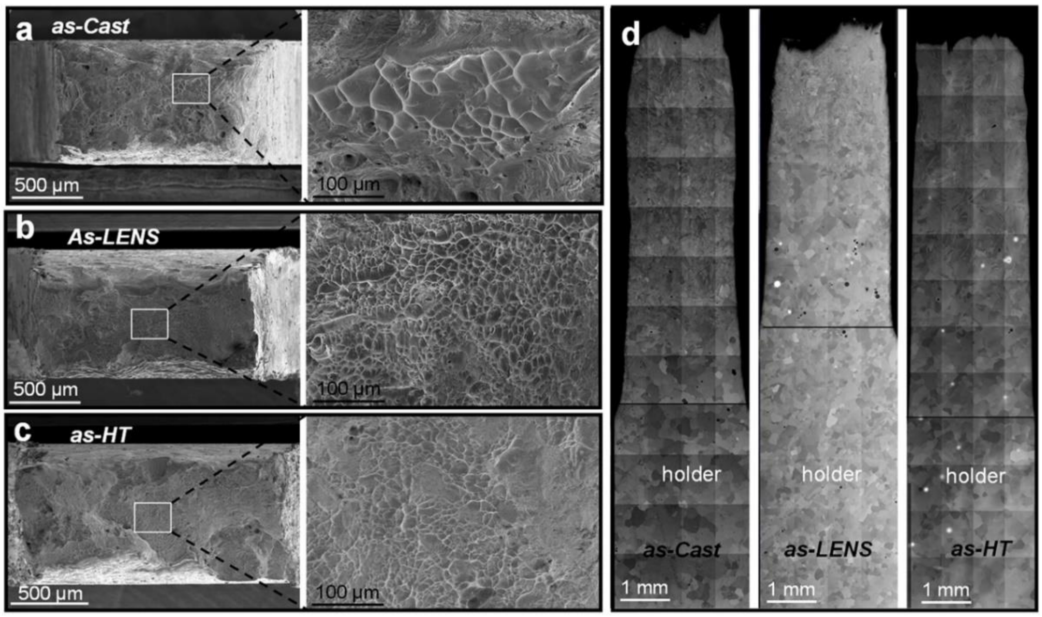

Fig. 4. 8 Fracture morphology of T42 RHEAs. a-c, SEM images of fracture surfaces from as-cast, as-LENS and as-HT RHEAs, respectively, with magnified figures showing the ductile dimples without cleavages. **d,** Splicing BSE images of as-cast RHEA, as-LENS RHEA and as-HT RHEA, respectively.

Due to the presence of the plateau-like plastic response in these alloys [85] (**Fig. 4. 7 b**), the Considère criterion [186] may not be applicable for predicting the onset of necking [85]. Therefore, we employed a digital image correlation measurement by involving the time-dependent methodology [187] to study the onset of necking in those RHEAs (see **Fig. 4. 9**). **Fig. 4. 9 a** illustrates the local strain distributions of the deformed samples at the last frame before fracture, obtained through post-processed DIC results. By analyzing the time-dependence local strain increasing trends at different points (shown in **Fig. 4. 9 a**), an abrupt decrease in the time-dependence local strain curve indicates the initiation of necking [187], as demonstrated in **Fig. 4. 9 b**. Thus, the area of abrupt change (point 3) on the local strain maps (see **Fig. 4. 9 a)** can be considered as the necking boundary. As a result, the as-LENS and as-HT RHEAs exhibit larger uniform tensile strain compared to the as-cast counterpart (see **Fig. 4. 9 b insert**), which is also supported by the splicing BSE images of the tensile bar top surfaces (see **Fig. 4. 8 d**).

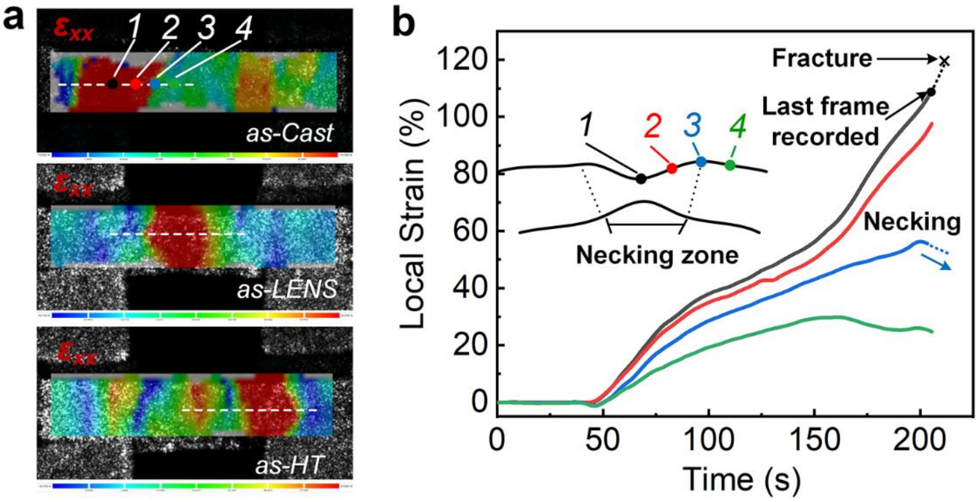

Fig. 4. 9 Digital image correlation measurement results. a, local strain maps display the two-dimensional local strain distribution of RHEAs fabricated via different methods. **b,** The experimental time evolution of the local strain on different points (marked in **a**) shows the various increasing trends.

4.2.5 Deformation behavior

We then conducted the in-situ and ex-situ tensile observation on those REHAs to study their deformation behaviors. Despite having different local strains in the necking area (**Fig. 4. 7 b insert**), the RHEAs fabricated through different approaches exhibit similar deformation characteristics (**Fig. 4. 10 a**). The IPF figure near the fracture area reveals the formation of crushed grains (**Fig. 4. 10 a**). Their corresponding KAM figures in **Fig. 4. 10 b** indicate the formation of slip bands and a high density of dislocations after the plastic deformation due to the higher KAM contrast in the deformed area [188], which is also revealed by the BSE images as illustrated in **Fig. 4. 10 c**. For further studying their formation mechanism, we analyzed the misorientation variations along the marked lines in **Fig. 4. 10 a**. There are slip bands formed during the deformation with the relative lower misorientations of Line 1 generally below 10°, while Line 2 exhibits larger misorientations above 15° (**Fig. 4. 10 d**), eliminating the possibility of forming twin boundaries (generally ~50° for {332}<113> twining [25]). The formation of large-angle grain boundaries (or higher misorientations) is attributed to the presence of shear bands in highly deformed alloys, a common occurrence in highly deformed titanium [189]. At the end of the plastic deformation, the dislocation motion, excluded from the deform-induced phase transformation because of the single BCC formed after deformation demonstrated in **Fig. 4. 10 e**, accompanied by the shear band deformation to induce the local stress concentration and crystal-crushing to form new grains.

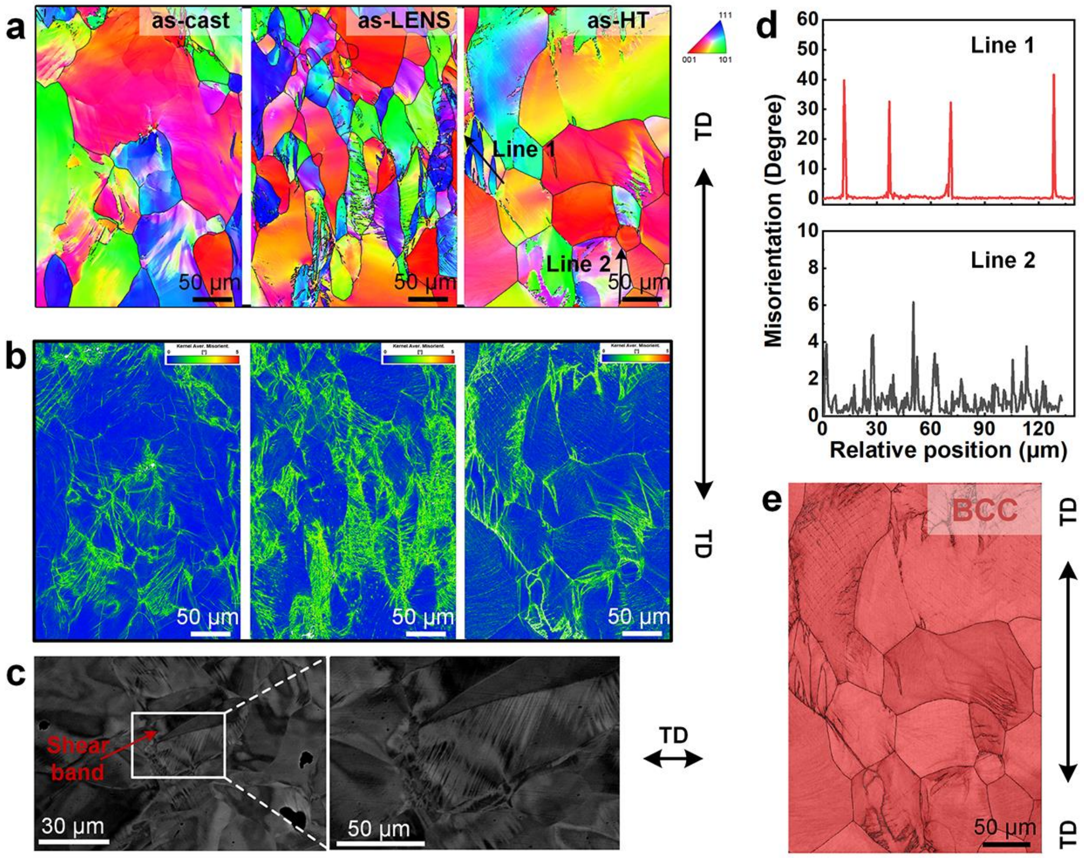

Fig. 4. 10 Microstructure evolution of different approaches fabricated T42 RHEAs after deformation. **a**, The EBSD IPF maps and **b**, KAM figures collected near the fracture areas from the corresponding RHEAs fabricated using different methods. **c**, BSE image of the deformed area. **d**, The corresponding local misorientation variation along the lines marked in **a.** **e**, The EBSD phase image of as-HT RHEA gives that only a single BCC was formed after deformation.

To study the dislocation evolution during the deformation, in-situ tensile testing was conducted in TEM on the LENS-fabricated specimen, which exhibits excellent strength-ductility synergy. During the in-situ tensile test, the deformation was terminated at certain pre-strains. At the early plastic deformation stage (~2%), the formation of dislocation dipoles as well as dislocation loops indicates the role of screw dislocations in the plastic deformation process. A dislocation pinning effect can occur in that deformation stage in **Fig. 4. 11 a (iii)**. As the sample was strained to 5%, continuous planar-slip bands and a high density of dislocations dominated this deformation stage (**Fig. 4. 11 b**). With further straining, the cross-slip is further promoted in this RHEA, and with the characteristics of wavy slip (**Fig. 4. 11 c (i)**) [76], dominating the plastic flow at this deformation stage. Additionally, the formation of dislocation walls is also observed (**Fig. 4. 11 c (ii)**) and the SAED pattern **Fig. 4. 11 d** indicates no phase or twin formation during deformation. The inverse Fourier transformation image from the HRTEM image of the deformed area (**Fig. 4. 11 e (i)**) confirms the presence of mixed dislocations of both the edge and screw characters, as shown in **Fig. 4. 11 e (ii)**.

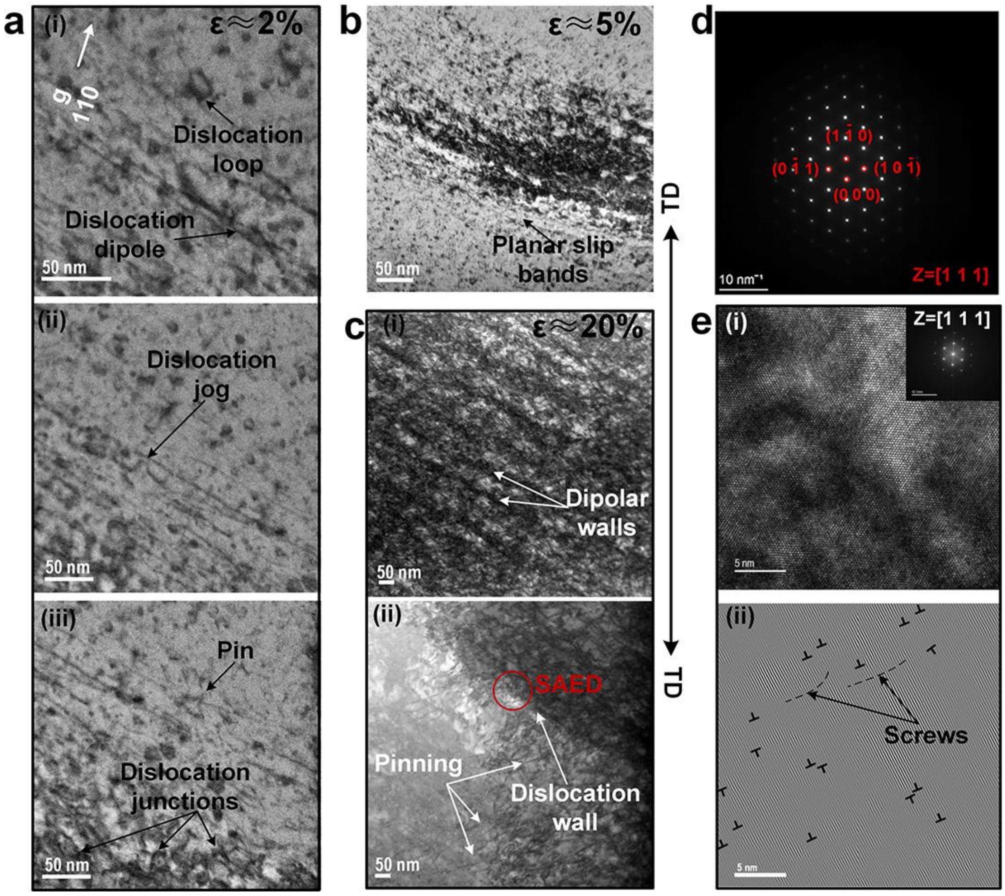

Fig. 4. 11 In situ deformed microstructure observations. a (i-iii), The TEM bright field (BF) image of the as-LENS RHEAs at a terminated strain of 2%. **b,** TEM BF figure of the deformed microstructure at a strain of 5%. **c(i),** Deformed microstructure at a strain of 20% showing the formation of dipolar walls and **c(ii)** formed dislocation wall accompanied with dislocation pinning effects. **d,** SAED pattern

of marked area in **c(i) e(i),** HRTEM image of deformed microstructure collected along [111] zone axis with corresponding FFT image insert and **d(ii),** The corresponding iFFT figure shows the presence of mixed edge and screw dislocations with huge density.

4.3 Discussion

4.3.1 The origins of ductility in fabricated RHEA

The stacking fault energy plays a crucial role in regulating the stacking fault in FCC-based HEAs, which in turn can generate deformed twins [190] to strengthen these HEAs. Although BCC-based materials have equivalent slipping systems as FCC-based alloys, the lower stacking compact on the slipping surfaces in BCC-based materials compared to FCC-based alloys is responsible for the even worsened ductility in BCC-based metals. The stacking fault energy (SFE) is a useful parameter for estimating the ductility levels in BCC-based materials, with higher SFE leading to lower ductility in BCC-based materials [191]. The dislocation movement near the crack tip would affect crack growth and further reflect the fracture characteristics. Rice et al. [192] established a relationship between the critical crack propagation force for I-type crack (G_c) and the unstable stacking fault energy (γ_{us}), as shown in the following function:

$$G_c' = 8\frac{1+(1-v)tan^2\theta}{(1+cos\varphi)sin^2\varphi}\gamma_{us} \tag{4. 3}$$

where v is Poisson's ratio, θ is the angle between the initial cracking and prolonging directions, φ represents the angle between the cracking lattice plane and slip planes.

According to the Griffith fracture theory [193], the cracking expansion force (G_c), known as the brittle cracking critical energy, is determined by surface energy (γ_s), given as follows:

$$G_c = 2\gamma_s \tag{4. 4}$$

As a result, when G_c is higher than G_c', the dislocation nucleation occurs near the crack tips, resulting in ductile fracture; otherwise, cracking expansion would be formed, leading to brittle fracture. When $G_c > G_c'$, the following equation can be derived:

$$\frac{\gamma_s}{\gamma_{us}} = 4\frac{1+(1-v)tan^2\theta}{(1+cos\varphi)sin^2\varphi} \tag{4. 5}$$

Hu et al. [191] used a factor of *D*, the ratio of γ_s and γ_{us}, which can be used for predicting the ductile level in RHEAs. When *D* exceeds 3.5, the fabricated RHEAs generally have a higher compressive fracture strain [191], indicating the occurrence of dislocation nucleation before cracking, resulting in ductile fracture [192]. The ratio between the surface energy (γ_s) and (γ_{us}) greatly exceeds the criteria for ductile or brittle materials, indicating that the dislocation nucleation precedes the crack formation. On the other hand, the stress field near the crack tip can also influence crack propagation. For instance, tensile stress near the crack tip promotes cracks to overcome the energy barrier for crack formation, while shear stress at the crack tip promotes ductility by facilitating dislocation or stacking fault motion to overcome the energy barrier from USFE [194]. Mei et al. [195] introduced a dimensionless factor of ξ to estimate the ductile-brittle properties, demonstrating that:

$$\xi = \frac{\gamma_s}{\gamma_{us}} cot\frac{\theta}{2} \tag{4. 6}$$

We can realize that the ductile-brittle properties of I-type cracks are influenced by the surface energy, the USFE as well as the cracking angle. For materials with the same surface energy and USFE, the angle between the initial cracking direction and prolonging direction determines the brittle-ductile properties. When the initial cracking and prolonging directions have a smaller angle, a brittle fracture characteristic is produced, otherwise, the materials have ductile fracture properties. Hence, the designed RHEA system in this study exhibits the characteristics of ductile materials, making it suitable for the additive manufacturing process.

4.3.2 Intrinsic strength of farbricated RHEA

By utilizing additive manufacturing processes on metallic materials, especially those alloys with FCC phase structure, the effect on the strength-ductility trade-off contributes to the unique heterogeneous structures [167] as well as the dislocation network [168]. While there are other methods such as refinement grain strengthening [196], twining or transformation-induced plasticity [32], and even the local chemical order [69] that can potentially enhance the strength of alloys while maintaining ductility, these approaches are absent in this study. To better understand the effects on yield strength, the contributions to yield strength are typically considered as follows [25]:

$$\sigma_y = (\sigma_{0.2})_{mix} + \sigma_G + \sigma_S + \sigma_D + \sigma_P \tag{4. 7}$$

1. Mixed intrinsic yield strength of pure metals

In **Eq. 4. 7**, $(\sigma_{0.2})_{mix}$ refers to the mixed intrinsic yield strength of pure metals, which can be expressed using the rule of mixtures:

$$(\sigma_{0.2})_{mix} = \sum c_i \, \sigma_{0.2i} \tag{4. 8}$$

where c_i and $\sigma_{0.2i}$ denote the atomic fraction of i_{th} element and its yield strength at the given temperature respectively, as listed in **Table 4. 2**. Consequently, the calculated value of $(\sigma_{0.2})_{mix}$ for T42 RHEA is 203.22 MPa.

Table 4. 2 Basic physical properties of the pure constituents of the fabricated RHEAs [69,197]**.**

Element	Ti	Hf	Nb	V
Melting point (K)	1941	2506	2750	2183
R (pm)	140	155	145	135
G (GPa)	44	30	38	47
Yield strength/ MPa	225	230	114	228
Atomic fraction	0.42	0.21	0.21	0.16

2. Grain boundary strengthening value

In **Eq. 4. 7**, σ_G is the strength attributed to the grain boundary strengthening, is given as follows [198]:

$$\sigma_G = \sigma_f + K_{HP} \cdot d^{-0.5} \tag{4. 9}$$

where K_{HP} and d are the Hall-Petch coefficient and grain diameter respectively, σ_f represents the lattice friction stress, which can be replaced by the Peierls-Nabarro (P-N) stress (σ_{P-N}) [199], given by:

$$\sigma_f = \sigma_{P-N} = G\exp\left(-2\pi d/b\right) \tag{4. 10}$$

where G denotes the shear modulus which can be obtained by the rule of mixtures, b is the Burgers vector and d represents the temperature-dependent dislocation width, demonstrated as follows:

$$d = d_0(1 + \alpha T) \tag{4. 11}$$

in which d_0 denotes the dislocation core at absolute zero and α is a constant, approximately equal to the reciprocal of the melting temperature ($\frac{1}{T_m}$), and T is the test temperature (298 K). Using the rule of mixtures, the melting point (T_m) and shear modulus (G) are calculated to be 2668 K and 40.28 GPa, respectively. When $d_0 = b$, the friction stress (σ_f) is calculated to be 37.29 MPa. For the Hall-Petch coefficient, Sriharitha et al. [200] provided an estimation using the following equation:

$$K_{HP} \approx 0.05G\sqrt{b} \tag{4. 12}$$

where b is the Burgers vector which is used to calculate K_{HP} as 35.59 MPa·μm$^{-1/2}$. Based on the EBSD grain size collection results and **Eq. 4. 9**, the contribution to the yield stress from the grain boundaries is 39.54 MPa in the as-cast RHEA samples.

3. Solid strengthening in RHEA

Unlike conventional metallic materials, HEAs exhibit superior mechanical strength due to lattice distortion, which induces a significant solid solution strengthening effect [51]. The nature of solid solution strengthening arises from the interactions between dislocations and distorted stress fields from the solute [201]. Wang et al. [199] gave an expression that considers the contribution of lattice distortion and modulus mismatch as follows,

$$\sigma_S = \sum_i^n (AGc_i^{\frac{2}{3}}\delta_i^{\frac{4}{3}} + BGc_i\delta_i) \tag{4. 13}$$

where *A* and *B* are dimensionless constants of 0.1 and 0.03, respectively. [51,202]. c_i is the atomic fraction of i_{th} consistent, δ_i is the stress contribution from i_{th} consistent in terms of lattice distortion as well as the modulus mismatch. Based on Labusch's model [202], the modified models express the lattice distortion (δr_i) and the modulus mismatch (δG_i), and the calculated results, given in

Table 4. 3, are expressed as follows [51],

$$\delta r_i = \frac{9}{8} \cdot \sum_{i \neq j} c_j \cdot \delta r_{ij} \tag{4. 14}$$

$$\delta G_i = \frac{9}{8} \cdot \sum_{i \neq j} c_j \cdot \delta G_{ij} \tag{4. 15}$$

where $\delta r_{ij} = 2(r_i - r_j)/(r_i + r_j)$ and $\delta G_{ij} = 2(G_i - G_j)/(G_i + G_j)$ provide details of the atomic radius and shear modulus differences between the i_{th} and j_{th} atoms, respectively, listed in **Table 4. 4**. The properties of the constituents are listed in **Table 4. 2**, by which the calculated solid solution stress is 468.25 MPa.

Table 4. 3 The calculated atomic modulus and atomic size mismatch.

Element	Ti	Hf	Nb	V
δr_i	-0.0258	0.0886	0.0137	-0.0667
δG_i	0.1120	-0.3136	-0.0517	0.1854

Table 4. 4 Calculated values for atomic radius mismatch of δr_{ij} (underlined numbers) and shear modulus difference of δG_{ij} for different atomic pairs.

Element i/j $\underline{\delta r_{ij}}/\delta G_{ij}$	Ti	Hf	Nb	V
Ti	0	0.3780	0.1463	-0.0659
Hf	$\underline{0.1017}$	0	-0.2353	-0.441
Nb	$\underline{0.0351}$	$\underline{-0.0667}$	0	-0.2118
V	$\underline{-0.0364}$	$\underline{-0.1379}$	$\underline{-0.0714}$	0

4. Dislocation strengthening in RHEA

The higher dislocation density has an impact on the yield strength, which can be determined using Taylor's hardening law [158]:

$$\Delta\sigma_D = M\alpha G b \rho^{0.5} \tag{4. 16}$$

in which M and α denote the Taylor factor of 3.06 [203] and correction constant of 0.3 [204], G represents the shear modulus, b is the Burgers vector and ρ gives the dislocation density. The dislocation density can be obtained through X-ray or neutron diffraction methods, expressed in the modified Williamson-Hall plot proposed by Ungar and Borbely [205] as follows:

$$\Delta K \approx \frac{0.9}{d} + \left(\frac{\pi A b^2}{2}\right)^{\frac{1}{2}} \rho^{\frac{1}{2}} \left(K \bar{C}^{\frac{1}{2}}\right) + O(K^2 \bar{C}) \tag{4. 17}$$

where ΔK is the full width at half-maximum (FWHM). The first term in **Eq. 4. 17** shows the grain size contribution to the line broadening and d denotes the average grain/particle size. The second term in **Eq. 4. 17** expresses the strain contribution, mainly from the dislocation density (ρ), to the line broadening. In this term, A is a constant of 10 [206,207] for a wide range of dislocation contributions which depends on the effective outer cutoff radius of dislocations, while b is the Burgers vector. $K = 2sin\theta/\lambda$ and $\bar{C}$ denotes the average contrast factor of dislocations of the *hkl* indices under different reflections [208]:

$$\bar{C} = \bar{C}_{h00}(1 - q\frac{h^2k^2+h^2l^2+k^2l^2}{(h^2+k^2+l^2)^2}) \tag{4. 18}$$

where $\bar{C}_{h00}$ and q are the constants determined by the elastic constants, especially the elastic anisotropy $A_i = 2C_{44}/(c_{11} - c_{12})$ and the ratio of c_{11}/c_{44}. Based on the calculated elastic stiffness constants (C_{11}=161.326 GPa, C_{44}=49.034 GPa) using a VCA model by CASTEP after the convergence test, the $A_i = 2.08$ and $\frac{c_{11}}{c_{44}} = 3.29$. When edge and screw dislocations have an equal proportion, the $\bar{C}_{h00}$ can be obtained according to Ref [209] as 0.25884. The last term in **Eq. 4. 17** refers to the higher order of $K^2\bar{C}$, which can be considered negligible. Hence, **Eq. 4. 17** can also be rewritten as [210]:

$$(\Delta K)^2 \approx \left(\frac{0.9}{d}\right)^2 + \frac{\pi Ab^2}{2}\rho K^2\bar{C} \tag{4. 19}$$

By inserting **Eq. 4. 18** into **Eq. 4. 19** yields:

$$[(\Delta K)^2 - \alpha]/K^2 \approx \beta\bar{C}_{h00}(1 - qH^2) \tag{4. 20}$$

where $\alpha = \left(\frac{0.9}{d}\right)^2$ and $\beta = \frac{\pi Ab^2}{2}\rho$. By plotting $[(\Delta K)^2 - \alpha]/K^2$ versus H^2 [209], we can obtain a q value of 0.9355. Depending on **Eq. 4. 17**, the FWHM of T42 RHEA versus the $K\bar{C}^{\frac{1}{2}}$, gives a slope value of $\left(\frac{\pi Ab^2}{2}\right)^{\frac{1}{2}}\rho^{\frac{1}{2}}$. As a result, the dislocation density in the as-cast T42 RHEA is around 1.16 $\times 10^{13}$ m^{-2}. By **Eq. 4. 16**, we can obtain the dislocation contribution to the yield strength as 37.16 MPa. The dislocation densities of as-LENS as well as the as-HT are 6.15 $\times 10^{13}$ m^{-2} and 1.40$\times 10^{13}$ m^{-2}, respectively. Therefore, the contribution to the yield strengths in the as-LENS as well as the as-HT samples are 85.56 MPa and 40.77 MPa, respectively.

4.3.3 Mechanisms of improved strength-ductility synergy

The as-LENS T42 RHEA exhibits the best strength-ductility synergy among those fabricated via other methods. In general, the mixed yield strength from the pure metals, the intrinsic solid-solution strengthening, the grain boundary strengthening, as well as the dislocation strengthening [25] contribute to the yield strength of the RHEA. Since those RHEAs have the same nominal compositions, the mixed yield strength and the intrinsic solid strength, considering the atomic radius and shear modulus mismatch [51], are expected to be the same. Although there are grain size differences among the fabricated REHAs, the Hall-Petch coefficient shows that the shear modulus sensitivity has a relatively low level, resulting in an insignificant effect of grain size difference on the yield strength. The KAM figures (**Fig. 4. 4 c**) do not show significant dislocation differences, but the modified Williamson-Hall method [205] reveals subtle differences in dislocation densities among the RHEAs fabricated using different approaches.

Specifically, the as-LENS RHEA exhibits the highest dislocation density (~6.5$\times 10^{13}$ m^{2}), which is 2 orders of magnitude lower than that in FCC alloys fabricated via AM methods [211] to form the dislocation networks. Although the contribution of dislocation strengthening to the yield strength in the LENS-fabricated HfNbTiZr RHEA was neglected [25], the dislocation density fluctuations were observed in RHEAs fabricated via different approaches. Comparing the as-cast and annealed samples, the LENS-fabricated RHEAs show an increase of ~ 40 MPa in yield strength compared to the as-HT sample, as calculated using Taylor's hardening law [158], which can account for the decreased value of a yield strength after annealing (**Fig. 4. 7 a**). However, there is still a question regarding the increase in yield strength from the as-cast sample to the as-LENS sample, as the nominal composition, grain size and dislocation densities are similar (as listed in **Table 4. 5**).

Table 4. 5 The calculated and experimental yield strength values of T42 alloy show acceptable error margins.

	$(\sigma_{0.2})_{mix}$	σ_S	σ_G	σ_D	σ_{s-i}	σ_{y-cal}	σ_{y-exp}
As-cast			39.54	37.16	-	748.17	780
As-LENS	203.22	468.25	39.84	85.56	178.36	975.23	1030
As-HT			39.54	40.77	177.46	929.24	970

Although the nano-scale heterogeneity, like the LCFs [25], the LCO [69], even the nano-scale secondary phase (BCT) [85], as well as the nano-ceramic particles [212], etc., has been proven to be effective in improving the mechanical performance of HEAs, these structures generally have a great influence on ductility through their interaction with dislocations than strength. In our study, we conducted nitrogen and oxygen (N&O) tests on the RHEAs fabricated using different approaches, considering that the BCC matrix in the as-LENS RHEA has a higher lattice constant than the as-cast counterpart (**Fig. 4. 5 b**). The results showed an increase in oxygen and nitrogen content in the LENS-fabricated RHEA compared to those in as-cast one, ~0.02 at.% (oxygen) and ~0.10 at.% (nitrogen) (**Table 4. 1**), respectively. Based on the oxygen/nitrogen analysis results, the LENS-fabricated sample has higher O/N contents compared to the as-cast one, while those contents are similar in the as-LENS and as-HT samples. Interstitial atom strengthening, such as oxygen and nitrogen, has been proven to significantly improve the yield strength of the HfNbTiZr RHEA by forming the ordered complexes [32]. In general, square distortion is generally attributed to the solid solution by interstitial atoms, resulting in the appearance of significant shear strain. During the room temperature deformation, the screw dislocations play a crucial role in work hardening [213], interacting with the square distortion center [203]. Fleishcher [214] provided an estimation of the yield strength increase resulting from square distortion in the following equation,

$$\Delta\sigma = \frac{G\Delta\varepsilon c^{1/2}}{3} \tag{4. 21}$$

where $\Delta\varepsilon$ is the difference between the longitudinal and transverse strain in the square distortion. Based on the experimental results of the oxygen-doped $Ti_{41}V_{27}Hf_{15}Nb_{15}$ RHEA [70], the difference between the longitudinal and transverse strains resulting from an oxygen solid solution ($\Delta\varepsilon_O$) is estimated to be 0.338, while $\Delta\varepsilon_N$ is calculated to be 0.275 based on the N-doped HfNbTiZr study [32]. Consequently, the yield strength increase from the interstitial atom strengthening is estimated to be approximately 178 MPa, which accounts for the increase in yield strength in the LENS-fabricated RHEA compared to the as-cast RHEA. In conclusion, the increase of yield strength in the LENS-fabricated RHEA compared to the as-cast sample is mainly attributed to the solid-soluble interstitial atoms in the RHEA matrix, while the slightly decreased dislocation density would account for the yield strength decrease in the as-HT samples compared to the LENS-fabricated RHEA. These results demonstrate that a limited amount of interstitial atoms in RHEAs would not embrittle the fabricated sample but instead increase the yield strength. This can also explain the yield strength increase when comparing the yield strength between the LENS-fabricated HfNbTiZr (1030 MPa) [25] and the as-cast HfNbTiZr alloy (750 MPa) [32].

We then proceeded to discuss the improved ductility observed in LENS-fabricated T42 RHEA. During the early plastic deformation stage (~2%), considerable dislocation loops and dipoles were initially formed (**Fig. 4. 11 a**), indicating the occurrence of multiple dislocation interactions [76]. Under continuous external stress, dislocation junctions and dislocation jogs were formed and induced by triggering multiple slip systems [215], facilitated by the presence of interstitial atoms [213], which can hinder the motion of lateral and cross kinks [213]. As depicted in **Fig. 4. 11 a**, a dislocation pinning effect can be observed during this deformation stage.

By straining the sample to 5%, continuous coplanar-slipped dislocations (**Fig. 4. 11 b**) are mainly triggered by external stress, resulting from the glide plane softening phenomenon and the reduced energy barrier on the same gliding plane for the successive dislocations [216]. The LENS-fabricated sample exhibits phase segregation (**Fig. 4. 6 b (iii)**) due to the complex thermal history during the additive procedure [15]. During the deformation, the phase interfaces would make the dislocation motion sluggish and even retard the movement of dislocations [115]. The large interfacial lattice distortion (**Fig. 4. 6 d (iii)**) acts as an effective barrier for dislocation motion. After loading, the stored dislocations necessitate cross-slip to promote the stuck screw dislocations, which is the key factor in controlling the ductility as well as the strain hardening [213], to move forward to the barrier [115]. The inverse Fourier transformation image confirms the presence of mixed dislocations of both the edge and screw characters, as shown in **Fig. 4. 11 d (ii)**.

With further straining, the cross-slip is further promoted in the LENS-fabricated RHEA, dominating the plastic flow at this deformation stage with wavy slip characteristics [76]. Apart from the cross-slip of the dislocations, similar to other bcc-type RHEAs like the TiZrHfNbTa RHEA, the formation of dislocation loops as well as dipoles is attributed to the work hardening rate [217], and cross-slip of screw dislocations prevails during deformation to form the dipolar walls [32,218]. The high density of the dislocation walls (DWs) is also formed on account of the successive cross-slip, as shown in **Fig. 4. 11 c (ii).** The complex interactions between the cross-slip and DWs promote dislocation reactions, multiplication, and storage [115], resulting in an increasing strain hardening rate during this deformation stage. Additionally, the presence of interfaces would retard the movement of dislocations [115] and generate the reverse interface energy [85], leading to increased dislocation slip resistance to strain hardening and delaying the formation of necking. Furthermore, the local chemical fluctuations (**Fig. 4. 6 d**) can alter the local SFE to modify the motion path of the screw dislocation cores, by increasing the energy barrier for dislocation motion, and thereby improving the intrinsic ductility [90].

4.4 Conclusions

In summary, we propose an AM process involving the remelting and low oxygen & nitrogen environments to fabricate T42 RHEAs with significantly enhanced mechanical properties. The main conclusions of this study are as follows,

1) A T42 RHEA was selected for LENS fabrication due to its ductile nature, which was verified via DFT calculation. The LENS-fabricated T42 RHEA exhibits a giga-pascal yield strength with a fracture strain higher than 22 %, a level that is difficult to achieve through casting.

2) The LENS procedure induces a complex thermal-stress environment and ultra-fast cooling rate, which promotes the decomposition of the BCC matrix and the formation of a coherent interface. These interfaces act as barriers to dislocation motion, thereby enhancing the ductility. By applying heat treatment to the LENS-fabricated sample, the BCC matrix decomposition is further promoted, leading to improved uniform deformation without significantly sacrificing the yield strength.

3) RHEAs with similar nominal compositions, fabricated through different approaches, exhibit approximate intrinsic yield strength. The increase in yield strength from the as-cast one to the as-LENS RHEA is attributed to the interstitial atom strengthening, rather than the formation of commonly found dislocation networks in FCC-based alloys fabricated through the AM process.

4) This study provides novel insights into overcoming the strength-ductility trade-off of RHEA, not only by tailoring the microstructures but also more importantly by regulating the composition during the manufacturing process.

Chapter 5 Origins of strength stabilities at elevated temperatures in additively manufactured T42 RHEA

5.1 Introduction

As described in **Chapter 4**, our LENS-fabricated T42 alloy overcame the long-standing strength-ductility trade-off, enabling its potential application in industry. Generally, RHEAs composed of refractory elements demonstrate exceptional mechanical properties under elevated temperatures, presenting opportunities for advanced high-temperature applications [6,94]. However, successfully fabricating RHEAs via LAM with superior mechanical properties among a large temperature range has been challenging [25,28,29,137,145–147], and there is still a lack of data on the tensile properties of RHEAs across a wide temperature range. Our T42 alloy comprises elements with huge radius differences, enabling its huge lattice distortion in the designed alloy. Customizing lattice distortion in RHEAs is crucial for achieving remarkable properties [44], particularly superior high-temperature strength [48]. Designing lattice distortion in RHEAs to achieve exceptional strength while maintaining ductility [69,104,219] is significant in the additive manufacturing of RHEAs. It is crucial to fully understand the mechanisms behind the superior mechanical properties induced by lattice distortion at elevated temperatures.

In this chapter, we investigated the high-temperature tensile properties of LENS-fabricated T42 alloy. The strength stability under elevated temperature was connected to the large local lattice strain and elastic moduli insensitivity to temperature. Our findings pave the way for the direct manufacturing of RHEAs with superior mechanical properties and provide insights into the mechanical responses of these RHEAs under extreme conditions.

5.2 Experimental and simulation results

5.2.1 Large lattice strain in fabricated RHEA

Although the formation of the bcc phase in our fabricated T42 alloy was fully discussed in **Chapter 4**, we still conducted a precise XRD experiment to investigate its phase structure, as illustrated in **Fig. 5. 1**. As previously mentioned, local lattice strain is produced in the as-fabricated T42 RHEA. To demonstrate the presence of local lattice strain/distortion, the atomic pair distribution function (PDF), acquired via Fourier transformation from the total scattering data, is presented in **Fig. 5. 1 a**, providing inter-atomic distances in real space [220]. Our PDF curve exhibits a similar characteristic to the Hf-contained BCC HEA [183], indicating the accuracy of the total scattering data collected using the Ag target (λ=0.559 Å). By fitting the PDF data, we obtained a fitting curve in **Fig. 5. 1 a** (red line), which yields a lattice constant of 3.32626 Å. However, an overlap of the first and second atomic shells was also observed in our Hf-containing RHEA, as shown in **Fig. 5. 1 a** (i), indicating a strong local lattice distortion (LLD) caused by the severe motion among neighboring atoms [221]. We fitted different r regions separately to reveal the LLD, which are [222]: 1) local range (one unit cell < Å); 2) long-range (3 unit cell), and 3) intermediate range, as shown in **Fig. 5. 1 a** (i-iii).

As the LLD can be reflected as the shift of the PDF peak [183], the local strain can be obtained via [183,222]:

$$\varepsilon = \frac{|a_{fit} - a_{ave}|}{a_{ave}} \tag{5. 1}$$

where a_{fit} is the fitting lattice constant in different r regions while a_{ave} denotes the average lattice constant in the whole r range. Consequently, we obtained the LLD in different regions, as shown in **Fig. 5. 1 b**, indicating a local range lattice strain of 3.68%, much higher than that in the FCC HEAs [223] but also slightly larger than the values in Hf-/Zr-containing RHEA [183].

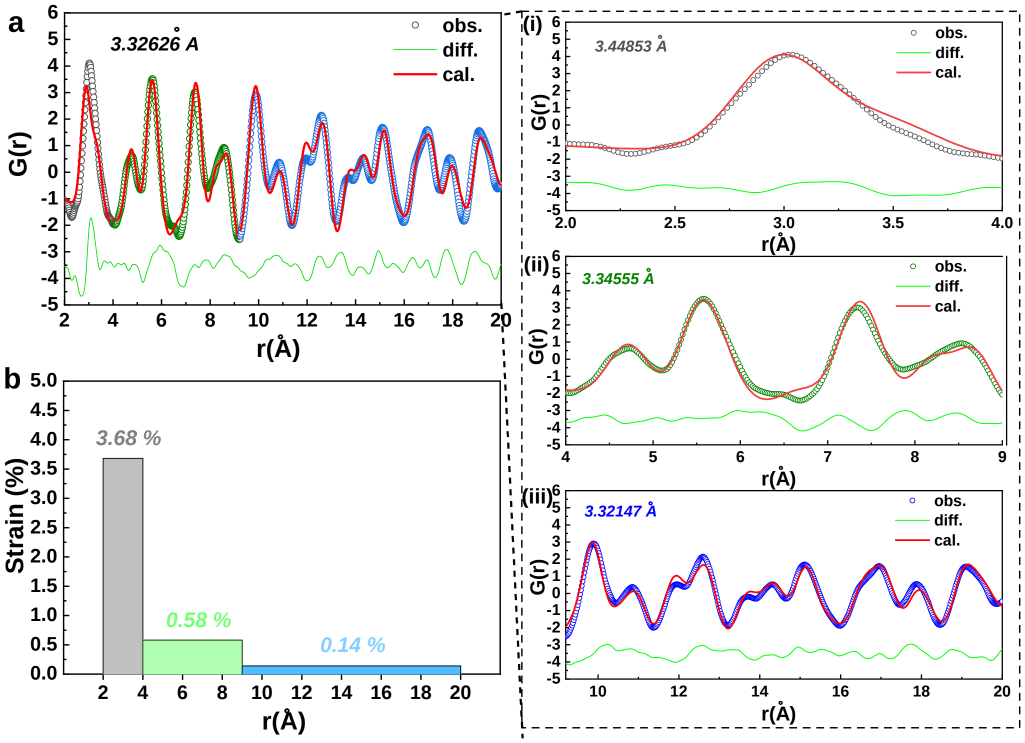

Fig. 5. 1 PDF results. a, The PDF curve of different r regions (i-iii) fitted via the PDFgui package. **b,** Calculated local lattice strain derived from PDF fitting.

5.2.2 Mechanical properties under elevated temperatures

To obtain the mechanical responses of the as-fabricated T42 alloy, we conducted tensile tests at different temperatures, which would be more valuable than compressive tests for evaluating its engineering applicational potential [25], with the results presented in **Fig. 5. 2 a**. When the tensile temperature was kept at 673 K, the yield strength of the as-fabricated T42 alloy decreased to ~ 681 MPa compared to that at RT (**Fig. 4. 7a**), while the fracture strain increased to 27.8% in our study. According to the Considère criteria [186], strain hardening was observed during the high-temperature tensile test. Upon further increasing the temperature to 773 K, a decrease in the yield strength to ~ 661 MPa was observed in the as-fabricated T42 alloy. Additionally, the fracture strain decreased to ~ 16.8% compared to the tensile curve obtained at 673 K. Following the tensile test at 873 K, a slight decrease (approximately 25 MPa) in the yield strength and a significant decrease in the fracture strain (~ 7.5%) were observed compared to the curves obtained at lower temperatures. It should be mentioned that we cannot obtain the valid tensile curve at 1073 K, due to the pulverizing before stretching. Additionally, we compared the yield strength versus temperature of the as-fabricated T42 alloy to the as-cast RHEAs [86,224–227] and the AM-fabricated superalloy [228–230] and other alloys with reported high-temperature tensile properties [231,232], due to the absence of reported data in the AM-fabricated RHEAs, as shown in **Fig. 5. 2 b**. Under elevated temperatures, the tensile yield strength slightly decreased but remained competitive among the AM-fabricated superalloys [228–230], although it was negligibly lower than the as-cast HfNbTiZrTa alloy [226,227]. The latter generally included the high melting point alloying element Ta, enabling a higher melting point [233] compared to our target alloy. However, under a high-temperature tensile test, especially above 823 K, matrix decomposition would occur [234], significantly deteriorating both strength and ductility in the HfNbTiZrTa alloy [226,227,235]. Although there are Ni-based superalloys with even superior mechanical performance at higher temperatures than our alloy fabricated alloy, successful fabrication of superalloys with superior mechanical properties by AM is still a long way to go [228–230]. In conclusion, although our as-fabricated T42 alloy has a relatively lower melting point, it still exhibits superior mechanical properties at elevated temperatures.

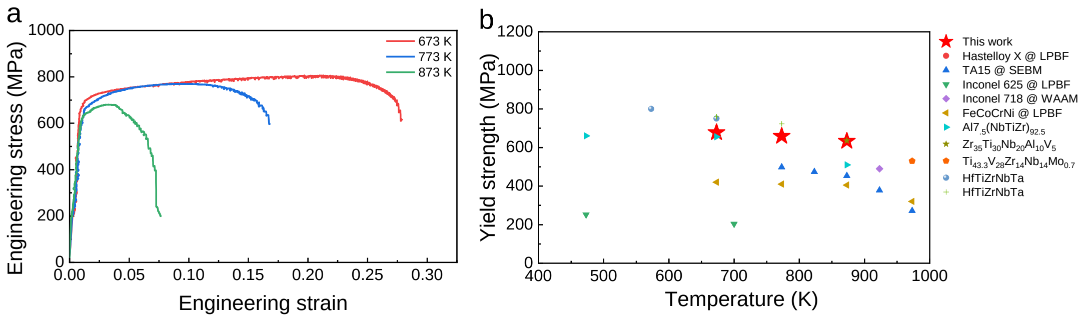

Fig. 5. 2 The tensile properties of as-fabricated T42 alloy. a, typical tensile curves of as-fabricated T42 alloy tensioned at different temperatures. **b**, Yield strength as a function of tested temperatures in comparison to other as-cast RHEAs [86,224–227] and AM-fabricated alloys with reported hot tensile properties [228–232].

Following the tensile tests, we examined the fractured surfaces and the external surfaces parallel to the tensile direction using SEM, as depicted in **Fig. 5. 3**, which illustrates the fracture morphologies under different temperatures. After 673 K tensile tests, complete ductile fracture surfaces were observed, as shown in **Fig. 5. 3 a** (i), characterized by the formation of dimples. When the tensile temperature was increased to 773 K, surface cracks were observed (**Fig. 5. 3 a** (ii)), and most of the fracture surfaces had dimples, with the presence of cleavage fracture characteristics under the surface cracks. Upon further increasing the tensile temperature to 873 K, a few dimples were observed, but most of the fracture surface exhibited river patterns (**Fig. 5. 3 a** (iii)), indicating the formation of quasi-cleavage fracture under that particular temperature and external stress. Regarding the observation of the external surface, as shown in **Fig. 5. 3 b**, the 673 K tension samples exhibited large plastic regions, composed of highly deformed grains with shear bands and a high density of dislocations. In contrast, a small plastic deformed region was observed in the 873 K tension sample, with surface cracks occurring during the tensile test. As the external surfaces were prepared by grinding and polishing, surface cracks were rarely observed in the 773 K tension sample, which can be seen from the front fracture surface in **Fig. 5. 3 a** (ii).

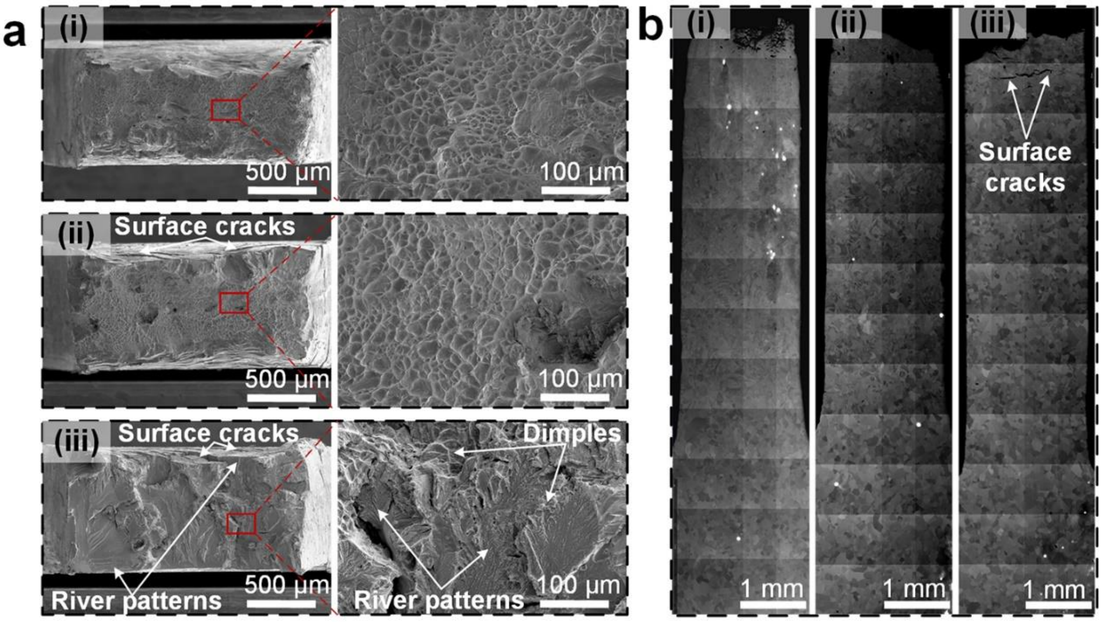

Fig. 5. 3 The fracture morphology observation in SEM. a (i-iii), Front fracture morphologies with corresponding enlarged microstructure of samples tensioned under 673 K, 773 K and 873 K respectively. **b (i-iii),** External deformed microstructure of 673 K, 773 K and 873 K tensioned T42 alloy.

5.2.3 Deformed microstructure under elevated temperature

To further investigate the deformed microstructure of the as-fabricated T42 samples after tension under elevated temperatures, we conducted EBSD experiments, the results of which are presented in **Fig. 5. 4**. In the EBSD IPF figures, we observed extensive shear bands, rather than the formation of deformed twin structures [25], formed under the RT tensile test (as shown in **Fig. 4. 10a**). However, the amount of shear bands was noticeably reduced in samples tensioned under elevated temperatures. Additionally, we utilized KAM maps to study the degree of deformation or the distribution of geometrically necessary dislocations [179]. From the KAM figures, it was evident that highly deformed regions near the grain boundaries or the shear bands exhibited a high density of dislocations. As the twinning-induced plasticity effect [236] was eliminated in our study, we also examined the phase structure of the deformed surfaces, which indicated that no phase transformation occurred under tensile deformation, regardless of the temperatures applied in the study.

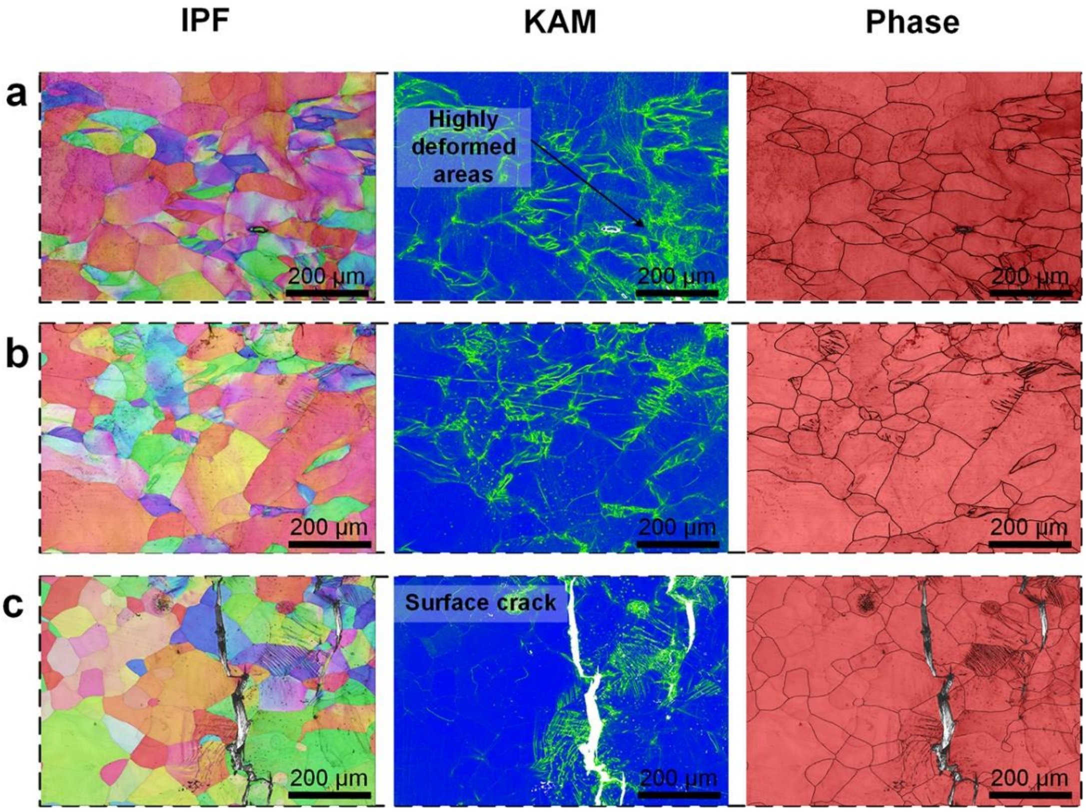

Fig. 5. 4 The EBSD deformed microstructure under elevated temperatures. a-c, 673 K, 773 K, 873 K, respectively.

We then investigated the dislocation evolution during deformation under different temperature tensile tests using TEM. For the 673 K tensioned T42 sample, as shown in **Fig. 5. 5 a**, we also observed bits of slip bands, dislocation walls, and pinning effects in the sample tensioned at that temperature. Additionally, the deformed structure after the 873 K tensile test, as depicted in **Fig. 5. 5 b**, indicates tangled dislocations, dislocation jog, and dislocation loops, with the pinning effect still present in the high-temperature deformed nanostructures. Based on the high-resolution TEM picture (**Fig. 5. 5 b** (iii)) and its corresponding inverse fast Fourier transform (iFFT) (**Fig. 5. 5 b** (iv)), we can assert that the combined effect of edge and screw dislocations was at work during the high-temperature deformation process. To verify the presence of dislocation loops and eliminate the formation of oxides after high-temperature tensile tests, the EDS maps of **Fig. 5. 5 b** (ii) are shown in **Fig. 5. 5 c**, indicating evenly distributed compositions even after high-temperature tensile tests.

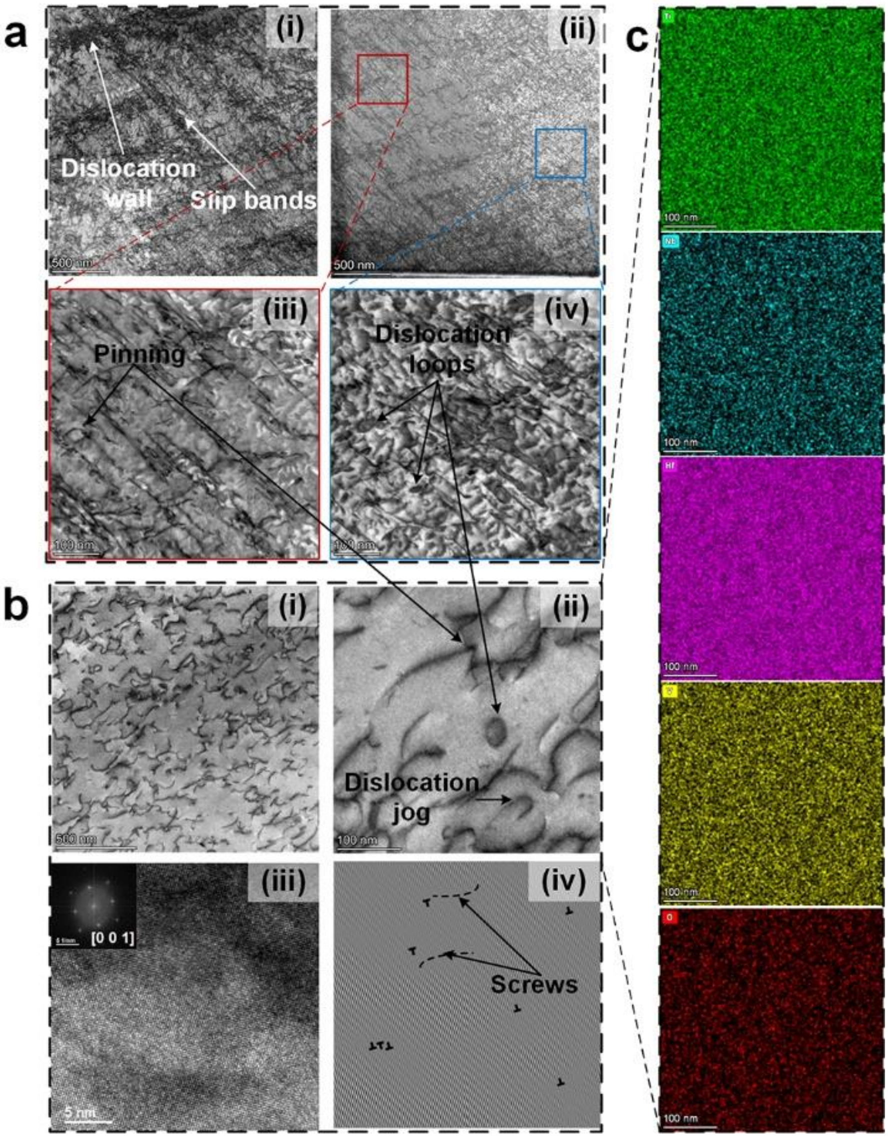

Fig. 5. 5 Nano-scale deformed structure in TEM. a, 673K deformed nano structure showing. **b**, dislocation structure in the deformed T42 alloy under 873 K, with HRTEM given in (iii) and the corresponding iFFT figure indicating the presence of mixed dislocation structure in the deformed sample. **c**, the EDS elemental mappings of 873 K deformed structure.

5.2.4 High-temperature oxidation property

Despite the superior mechanical properties exhibited by the as-fabricated T42 alloy under elevated temperatures, it proved to be not applicable under a tensile test at 1073 K. Consequently, we conducted a long-term (120-hour) oxidation experiment under atmospheric conditions at 1073 K. After a 1-hour oxidation test, we observed the oxidized surfaces of the as-fabricated T42 sample, as shown in **Fig. 5. 6 a**, where surface cracks were present in the oxidation layer. Subsequently, we collected the elemental distributions on the oxidation layer, as depicted in **Fig. 5. 6 b**, indicating the formation of oxides of corresponding constituents in the T42 alloy. The mass gain of oxidized samples under different processing times (1 h, 3 h, 6 h, 12 h, 24 h, 48 h, 72 h, 96 h, as well as 120 h) is shown in **Fig. 5. 6 c**, clearly demonstrating a nearly linear increase in mass gain with an increase in processing time. Additionally, we conducted XRD tests to study the phase evolution of the oxides of the AM-fabricated T42 alloy (see **Fig. 5. 6** d), indicating that prolonging the processing time would not affect the oxide species, only the number of oxides.

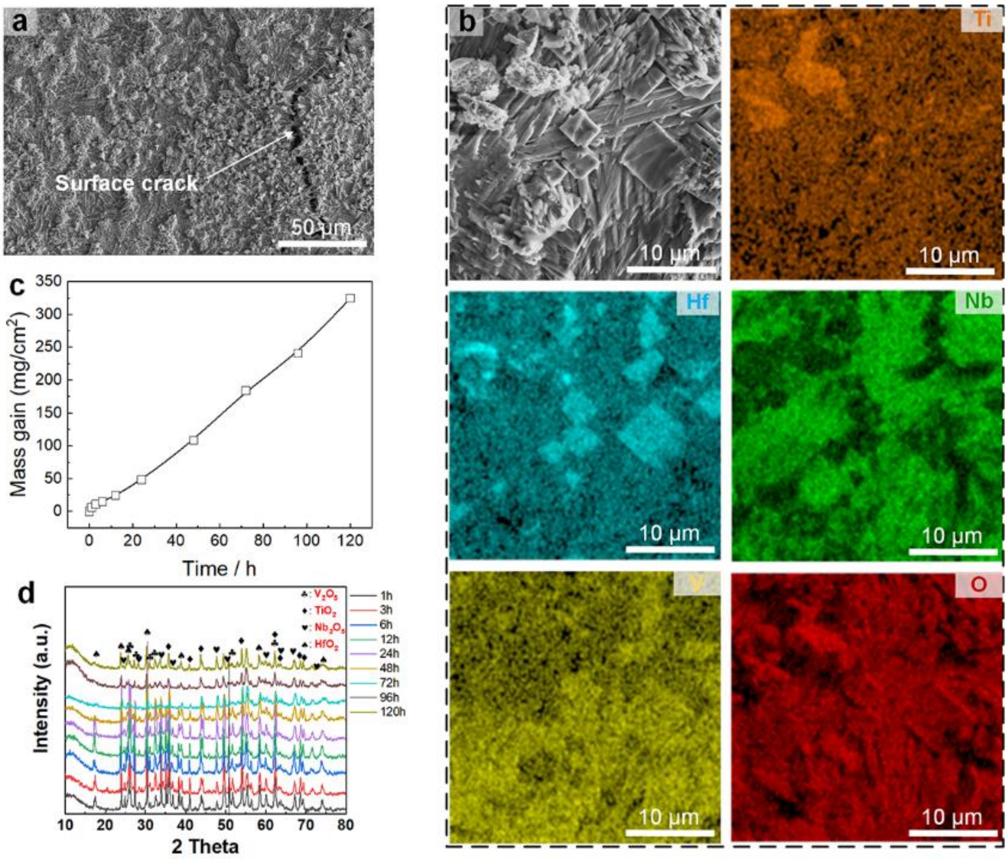

Fig. 5. 6 1073 K oxidation results. a, The oxidation layer morphology after 1h oxidation test. **b**, Amplified microstructure as well as the corresponding elemental distribution maps showing the presence of oxides of corresponding constituents. **c**, the mass gain as a function of processing time. **d**, XRD profiles of oxidized T42 alloy under different processing times.

5.2.5 Basic physical properties of selected RHEA at elevated temperatures

To study the basic physical properties of the selected RHEA at elevated temperatures, we conducted first-principles calculations to obtain the temperature dependence of the elastic constants using the VCA method [237] on the original structure of Nb. In contrast to the study by Feng et al. [48], we utilized the Birch-Murnaghan equation of state (EOS) method to calculate the energy of the RHEA crystals with different volumes. The relationship between the energy and volume of the selected RHEA is depicted in **Fig. 5. 7**, with the minimum energy occurring at the equilibrium volume. The E-V curve was then fitted through the third-order Birch-Murnaghan equation based on the EOS method, as given in [237],

$$E(V) = E_0 + \frac{9V_0B_0}{16}\{\left[(\frac{V_0}{V})^{2/3} - 1\right]^3 B_0' + \left[(\frac{V_0}{V})^{2/3} - 1\right]^2 [6 - 4(\frac{V_0}{V})^{2/3}]\} \quad (5.2)$$

where E_0 and V_0 are the equilibrium energy and the corresponding volume, respectively; V represents the volume change and B_0 is the bulk modulus while B_0' means a constant. Subsequently, the quasi-harmonic Debye model was applied to reveal the thermal response of the selected RHEA using the Gibbs 2.0 program [238] to obtain its thermodynamic properties. In the EOS method, the unbalanced Gibbs function$G^*(V;P,T)$ is described as [237]:

$$G^*(V;P,T) = E(V) + PV + A_{vib}(\Theta/T) \quad (5.3)$$

where $E(V)$ is the total energy of the primitive cell of T42 RHEA at 0 K, calculated by the EOS function; PV is a constant hydrostatic pressure, Θ corresponds to Debye temperature and A_{vib} denotes the vibrating Helmholtz free energy expressed as follows:

$$A_{vib}\left(\frac{\Theta}{T}\right) = nkT\left[\frac{9}{8}\frac{\Theta}{T} + 3\ln\left(1 - e^{-\Theta/T}\right) - D(\Theta/T)\right] \quad (5.4)$$

where $D(\Theta/T)$ represents the Debye integral, defined as below [238]:

$$D(x) = \frac{3}{x^3}\int_0^x \frac{y^3 e^{-y}}{1-e^{-y}} dy \quad (5.5)$$

The Debye temperature Θ is calculated by considering the isotropic solid, given as [237]:

$$\Theta = \frac{1}{k}\left(6\pi^2 V^{\frac{1}{2}} n\right)^{\frac{1}{3}} \{3[2\left(\frac{2}{3}\frac{1+\sigma}{1-2\sigma}\right)^{3/2} + (\frac{1}{3}\frac{1+\sigma}{1-\sigma})^{3/2}]^{-1}\}^{1/3}\sqrt{\frac{B_S}{M}} \quad (5.6)$$

where n denotes the sum of atoms number, σ is the Poisson ratio and B_S corresponds to the adiabatic bulk modulus, and M is the molecular weight of the primitive cell of the target system. Once the Gibbs free energy is obtained, the heat capacity C_v can be obtained, as described in [237]:

$$C_v = 3nk[4D\left(\frac{\Theta}{T}\right) - \frac{3\Theta/T}{e^{\Theta/T-1}}] \tag{5. 7}$$

Then, based on the Debye-Grüneisen model [239], we can obtain thermal expansion (α) given as follows [237]:

$$\alpha = -\frac{dln\Theta(\mathrm{V})}{dlnV} C_v/[V^2(\frac{\partial^2 G(V;P,T)}{\partial V^2})] \tag{5. 8}$$

Thermodynamic properties are essential for understanding the thermal response of materials. In **Fig. 5. 7 b**, the heat capacity (C_v) versus temperature is depicted, demonstrating a strong dependence on temperature at lower temperatures (less than 300 K), attributed to the limitations of the Debye model at low temperatures [237]. The C_v value gradually increases to the Dulong-Petit limit (~ 24.9 J/mol·K) at a higher temperature [240]. Another crucial parameter, the thermal expansion coefficient, is valuable for studying the thermodynamic and thermoelastic deformation behavior of materials, particularly at high temperatures [240]. This value is also essential for obtaining the lattice constants at corresponding temperatures, which can be used in CPFEM to investigate the relationship between the microstructure and mechanical response in LENS-fabricated RHEAs during hot tensile testing. While obtaining this parameter through experimental methods can be time-consuming, first-principles calculations can effectively address this issue. The volume thermal expansion coefficient versus temperature of the selected RHEA is plotted in **Fig. 5. 7 c,** reflecting the thermodynamic and thermoelastic deformation behavior, especially at high temperatures [241]. In **Fig. 5. 7 c**, the predicted volume thermal expansion coefficient increases rapidly at lower temperatures (under 300 K) and gradually becomes flat at elevated temperatures. The temperature dependence was then used to calculate the lattice constants at corresponding temperatures, as listed in **Table 5. 1**, showing good consistency with the experimental results. Subsequently, we utilized first-principles calculations to obtain the independent elastic constants, C_{11}, C_{12}, and C_{44}, based on the calculated lattice parameters. Following the Voigt-Reuss-Hill modulus principle [6], the bulk modulus (B), shear modulus (G), Young's modulus (E), and Zener anisotropic ratio (A) were calculated using the following equations:

$$B_v = B_r = (C_{11} + 2C_{12})/3 \tag{5. 9}$$

$$G_v = (C_{11} - C_{12} + 3C_{44})/5 \tag{5. 10}$$

$$G_v = 5 \cdot (C_{11} - C_{12}) \cdot C_{44}/[3 \cdot (C_{11} - C_{12}) + 4 \cdot C_{44}] \tag{5. 11}$$

$$B = (B_y + B_R)/2 \tag{5. 12}$$

$$G = (G_y + G_R)/2 \tag{5. 13}$$

$$E = 9 \cdot B \cdot G/(3 \cdot B + G) \tag{5. 14}$$

$$A = 2 \cdot C_{44}/(C_{11} - C_{12}) \tag{5. 15}$$

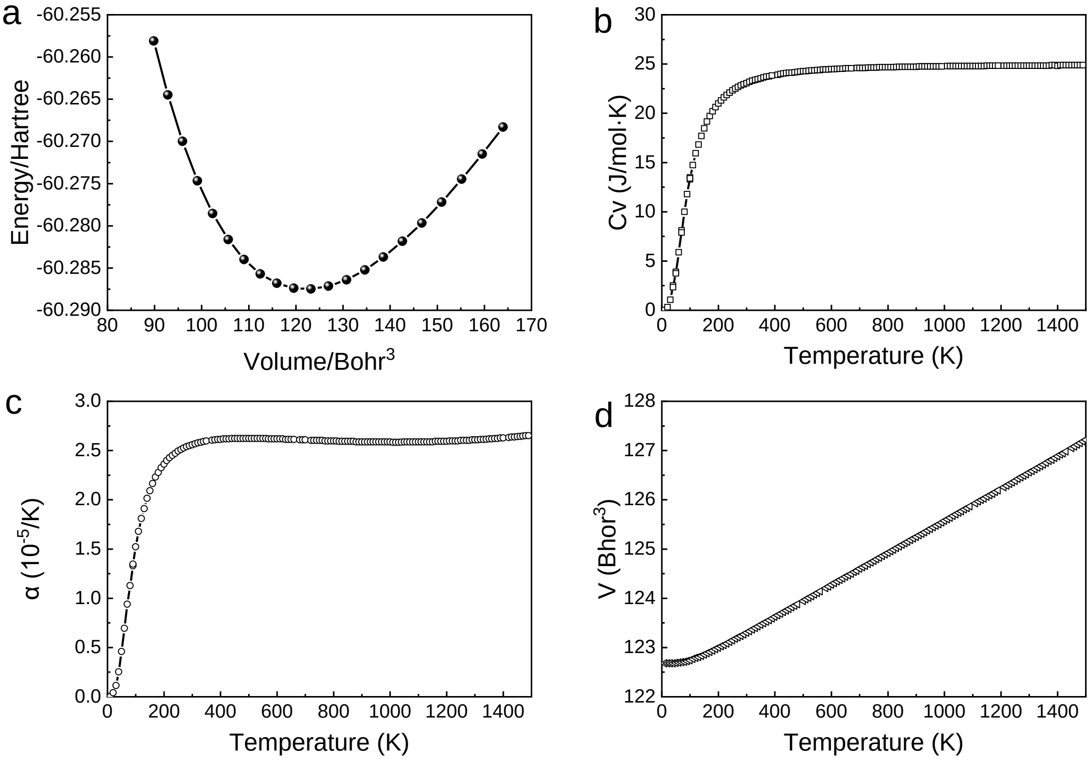

Fig. 5. 7 Thermodynamic properties of T42 RHEA obtained via first-principles calculations. a, Fitted EOS equation between the volume and energy. **b**, The heat capacity as a function of temperature. **c**, The coefficient of thermal expansion with corresponding temperature and **d**, The calculated volume of the primitive cell of RHEA under different temperatures.

In our study, we utilized the EOS approach to obtain the thermal dynamic parameters of the selected RHEA (as shown in **Fig. 5. 7**) and then obtained the temperature dependence of the lattice constant as listed in **Table 5. 1**. After the calculation, the lattice constant of the T42 alloy was determined to be 3.3176 Å, which is very consistent with the fitted PDF result of 3.32626 Å, indicating that an appropriate parameter setting was applied in this calculation procedure. Based on the calculated lattice constants, we applied first-principles calculations to obtain the independent elastic constants, C11, C12, and C44, which also meet the requirements of the Born-Huang mechanical stability criterion [242], as expressed in the following equation:

$$C_{11}-C_{12}>0,\ C_{11}+C_{12}>0,\ C_{44}>0 \tag{5. 16}$$

Fig. 5. 8 shows the basic physical properties of the T42 alloy at corresponding temperatures. The linear increase of the lattice constant was found as a function of temperature, as illustrated in **Fig. 5. 8 a**. The selected RHEA exhibits a degree of anisotropy that is less than 1 (see **Fig. 5. 8 b**) among the test temperatures, indicating the loss of anisotropy at higher temperatures. The independent elastic constants of C_{11} and C_{12} slightly increased with elevated temperatures, while C_{44} slightly decreased, resulting in a slight decrease of Young's moduli and shear moduli (seen **Fig. 5. 8 c** and d) in the selected RHEA and a weak temperature dependence on the basic moduli of the selected RHEA. By applying similar calculations on the pure constituents in Ti-based RHEA, we showed the temperature-dependent Young's and shear moduli in **Fig. 5. 8 c** and **d**, which illustrate a weak temperature-dependence on E and G in those pure metals, similar to the results given in the study by Feng et al. [48].

Table 5. 1 Calculated lattice constants and Young's moduli under different temperature

Temperature/K	RT	673 K	773 K	873 K	1073 K
Lattice constant/Å	3.3176	3.3293	3.3321	3.3350	3.3408
Young's modulus/GPa	105.99	106.26	106.18	106.03	105.55

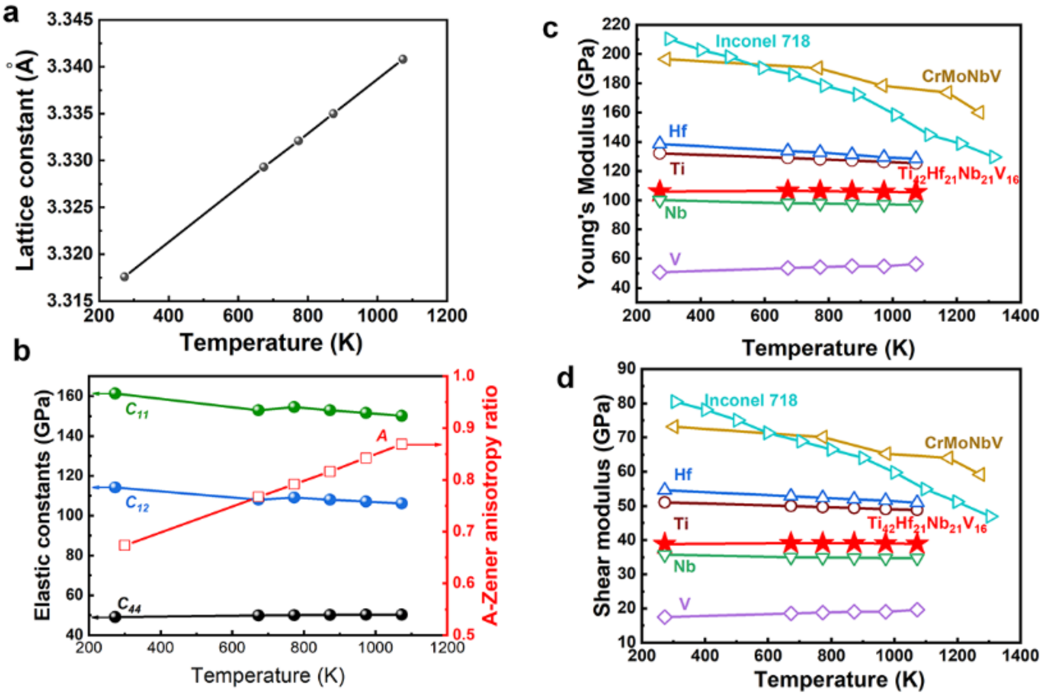

Fig. 5. 8 Temperature dependence on the basic physical properties of T42 alloy. a, Lattice constants as a function of temperature. b, Influence of temperature on elastic constants (C_{11}, C_{12}, C_{44}) and Zener anisotropy ration. c and d, Comparison of Young's and shear moduli between the target RHEA with pure constituents as well as CrMoNbV and Inconel 718 alloy [48].

5.2.6 CPFEM constitutive law and results

1. Constitutive law

The constitutive law of the crystal plasticity model is given in this section, which contains the framework for finite deformation by defining the kinematics for elasto-plastic deformation [243] and implemented in the DAMASK package [166]. The Orowan equation [244] gives the relationship between the shear rate ($\dot{\gamma}^{\alpha}$) and the mobile dislocation density (ρ^{α}) on the slip system α as follows:

$$\dot{\gamma}^{\alpha} = \rho^{\alpha} b v^{\alpha} \tag{5. 17}$$

where b is the length of the Burgers vector, and v^{α} represents the average velocity of mobile dislocations, and is mainly determined by the average distance between short-range barriers (l) and average activation energy to overcome barriers, expressed as follows:

$$v^{\alpha} = \frac{l}{t_w + t_r} \tag{5. 18}$$

where t_w and t_r are the waiting time to overcome a barrier and running time for a dislocation to move between neighbor barriers. In general, the t_r is much smaller than t_w, and can be neglected [245]. Kocks et al. [246] gave an estimation of the waiting time as:

$$t_w = \omega_0^{-1} \exp\left(\frac{\Delta G}{k_B T}\right) \tag{5. 19}$$

in which ω_0 is the attempt frequency, ΔG denotes the average activation energy to overcome the short-range barrier, k_B and T are Boltzmann's constant and the absolute temperature, respectively. From **Eq. 5.18** and **19**, we can obtain the dislocation glide velocity expressed as follows:

$$v^{\alpha} = v_0 \exp\left(\frac{\Delta G}{k_B T}\right) \tag{5. 20}$$

where v_0 is the dislocation glide velocity pre-factor equal to $\omega_0 l$. Simultaneously in **Eq. 5.17** and **20**, the shear rate of slip system α can be estimated as:

$$\dot{\gamma}^{\alpha} = \rho^{\alpha} b v_0 \exp\left(\frac{\Delta G}{k_B T}\right) \tag{5. 21}$$

where ΔG can be expressed as follows:

$$\Delta G = \Delta F\{1 - [\frac{\tau_T^{*\alpha}}{\tau_0^{*}}]^p\}^q \tag{5. 22}$$

where ΔF is the total short-range barrier energy. $0 < p \leq 1$ and $1 \leq q \leq 2$ are the shape factor of the short-range barrier [246]. $\tau_T^{*\alpha}$ represents the thermal component of the stress, which can be formulated as:

$$\tau_T^{*\alpha} = \begin{cases} |\tau^\alpha| - \tau_\mu^\alpha & \text{for } |\tau^\alpha| > \tau_\mu^\alpha \\ 0 & \text{for } |\tau^\alpha| \leq \tau_\mu^\alpha \end{cases} \tag{5. 23}$$

where τ^α denotes the total resolved shear stress (RSS) on the slip system α and τ_μ^α is the athermal component of the RSS, given as follows:

$$\tau_\mu^\alpha = \mu b (\textstyle\sum_{\alpha'=1}^{N_s} \xi_{\alpha\alpha'} (\rho^{\alpha'} + \rho_d^{\alpha'}))^{1/2} \tag{5. 24}$$

where μ is the shear modulus, $\xi_{\alpha\alpha'}$ denotes the interaction coefficient matrix between slip systems of α and α' and ρ_d^α is the dislocation dipole density of the slip system α.

τ_0^* is the barrier strength that can overcome short-range barriers without thermal assistance, given in the following formulation:

$$\tau_0^* = (|\tau^\alpha| - \tau_\mu^\alpha \;\; at\; T = 0\; K \tag{5. 25}$$

By combining **Eqs. 5.24** and **5.25**, the shear rate for the slip system α, is given as:

$$\dot{\gamma}^\alpha = \rho^\alpha b v_0 \exp\,(\tfrac{\Delta F}{k_B T}\left\{1 - \left[\tfrac{\tau_T^{*\alpha}}{\tau_0^*}\right]^p\right\}^q) sign(\tau^\alpha) \tag{5. 26}$$

However, under a high temperature, especially for temperatures higher than the critical temperature, the running time (t_r) in **Eq. 5.18** would not be negligible. Hence, **Eq. 5.18** can be written as follows:

$$v^\alpha = \frac{l}{t_w + t_r} = \frac{1}{\frac{t_w}{l} + \frac{t_r}{l}} = \frac{1}{\frac{1}{v_b^\alpha} + \frac{1}{v_r^\alpha}} \tag{5. 27}$$

where $v_b^\alpha = t_w/l$ when t_r is neglected. In addition, the running velocity is given in the following:

$$v_r^\alpha = \frac{\tau_T^{*\alpha} b}{B} \tag{5. 28}$$

where *B* denotes the drag coefficient. The v_b^α in **Eq. 5.27** can be formulated as:

$$v_b^\alpha = v_0 \exp\left(\frac{\Delta F}{k_B T}\left\{1 - \left[\frac{\tau_T^{*\alpha}}{\tau_0^*}\right]^p\right\}^q\right) sign(\tau^\alpha) \tag{5. 29}$$

During high-temperature deformation, the evolution rate of the mobile dislocation density can be estimated as [166]:

$$\dot{\rho}^\alpha = \frac{|\dot{\gamma}^\alpha|}{b\Lambda^\alpha} - \frac{2d_{dipole}^\alpha}{b}\rho^\alpha|\dot{\gamma}^\alpha| \tag{5. 30}$$

In **Eq. 5.30**, the second term gives the mobile dislocation density decrease by annihilating or forming dipoles, while the dislocation multiplication rate (first term) depends on the dislocation mean free path Λ^α, given as [166]:

$$\frac{1}{\Lambda^\alpha} = \frac{1}{d_g} + \frac{1}{\lambda^\alpha} \tag{5. 31}$$

where d_g means the effective grain size and

$$\lambda^\alpha = \frac{1}{C_\lambda}\left(\sum_{\alpha'=1}^{N_s} g_{\alpha\alpha'}\left(\rho^{\alpha'} + \rho_d^{\alpha'}\right)\right)^{1/2} \tag{5. 32}$$

where C_λ denotes the coefficient determining the number of passed dislocations before trapping by forest dislocations. $g_{\alpha\alpha'}$ are the interaction coefficients between dislocations on different slip systems.

Whereas the evolution rate for dislocation dipole density is expressed as follows [247]:

$$\dot{\rho}_d^\alpha = \frac{2(d_{dipole}^\alpha - d_{anni}^\alpha)}{b}\rho^\alpha|\dot{\gamma}^\alpha| - \frac{2d_{anni}^\alpha}{b}\rho_d^\alpha|\dot{\gamma}^\alpha| - \rho_d^\alpha\frac{4v_{climb}}{d_{dipole}^\alpha - d_{anni}^\alpha} \tag{5. 33}$$

where d_{anni}^{α} is the critical distance for the annihilation of two mobile dislocations with a reverse sign, which has the following relationship between the dislocation annihilation coefficient (C_{anni}):

$$d_{anni}^{\alpha} = C_{anni} b \tag{5. 34}$$

The critical distance for dipole formation is expressed as:

$$d_{dipole}^{\alpha} = \frac{\mu}{16\pi|\tau^{\alpha}|} b \tag{5. 35}$$

When the distance between two mobile dislocations with opposite signs is higher than d_{anni}^{α} but less than d_{dipole}^{α}, a dipole is prone to be formed to reduce the mobile dislocation density, while the reduction of the dislocation dipole density is represented in **Eq.5.33** in the third term. The dislocation climb velocity is defined as:

$$v_{climb} = \frac{3\mu D_0 \Omega}{2\pi k_B T} \left(\frac{1}{d_{dipole}^{\alpha} + d_{anni}^{\alpha}}\right) \exp\left(-\frac{Q_c}{k_B T}\right) \tag{5. 36}$$

where D_0 is the self-diffusion coefficient, Ω and Q_c are the activation volume and activation energy for the dislocation climb, respectively.

2. CPFEM results

To verify the accuracy of the calculated moduli as a function of temperature, we modeled the tensile properties of the as-fabricated T42 alloy using the DAMASK package [166] and a dislocation-based crystal plasticity constitutive model. We utilized the actual 3D EBSD construction (**Fig. 4. 3 b**) to create polycrystalline representative volume elements (RVEs) with near-identical experimental morphologies (**Fig. 5. 9 a**) via the DEREAM3D package [248]. Taking into account the presence of preferable orientations formed in the as-fabricated T42 alloy (**Fig. 4. 4 d**), we assigned near-identical preferable orientations in our RVEs, as shown in **Fig. 5. 9 b**. The RVEs used for CPFEM were meshed into 60 × 60 × 60 elements, containing 27 grains, and a tensile rate of 0.001 s^{-1} was applied in the X-direction during hot-tensile simulations. By fitting the experimental tensile curves and simulations, as illustrated in **Fig. 5. 9 c**, we introduced the average absolute relative error (AARE) and the correlation coefficient (R) to verify the reliability of the CPFE model used in this study, as follows [249]:

$$AARE(\%) = \{\frac{1}{N}\sum_{i=1}^{N} |\frac{E_i - P_i}{E_i}|\} \times 100 \tag{5. 37}$$

$$R = \frac{\sum_{i=1}^{N}(E_i - \bar{E})(P_i - \bar{P})}{\sqrt{\sum_{i=1}^{N}(E_i - \bar{E})^2 \sum_{i=1}^{N}(P_i - \bar{P})^2}} \tag{5. 38}$$

where *N* denotes the data points, E_i and P_i are stress values of experimental and simulation results, respectively, while $\bar{E}$ and $\bar{P}$ refer to the average value obtained from the experiment and simulation methods, respectively. We summarized the AARE and R values in **Table 5. 2**, showing small AAREs but high R values in our simulations, indicating a strong correlation between experimental and simulation results. Additionally, we obtained the temperature dependence on the constitutive parameters, listed in **Table 5. 3**, and the activation energy for glide evolution as a function of temperature [250], which are 3.53 × 10^{-19} J (RT), 2.3 × 10^{-19} (673 K), 2.2 × 10^{-19} (773 K) and 2.1 × 10^{-19} (873 K), respectively. The well-fitted experimental and simulation results indicate the accuracy of the DFT calculations and show the way to directly predict the mechanical response of novel alloys.

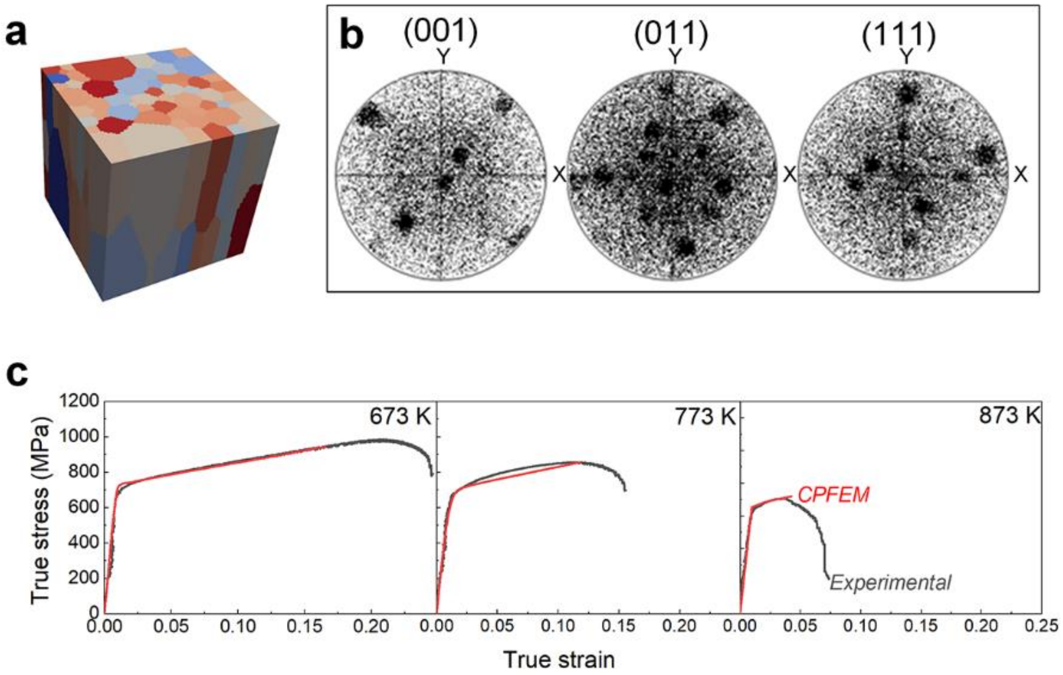

Fig. 5. 9 Experimental and CPFEM analysis. a, RVEs used in CPFEM with a similar crystal structure of experimental results**. b,** Assigned grain orientations in the built RVEs used for CPFEM**. c,** Comparison between the experimental and simulation results**.**

Table 5. 2 Calculated AARE and R values.

	RT	673 K	773 K	873 K
AARE (%)	0.71	0.84	3.20	2.64
R (%)	99.82	99.91	99.18	99.86

Table 5. 3 Constitutive parameters obtained via CPFEM of T42 RHEA.

	Symbol	Description	Value
Elastic parameters	C_{11}, C_{12}, C_{44}	Elastic constants	Via DFT
	b_s	Burgers vector for slipping	2.87 × 10^{-10} m

Dislocation glide parameters	N_{slip}	Total number of slip systems	12
	△F	The activation energy for dislocation glide	Changing response to temperature
	τ_0^*	Short-range barriers strength	850 MPa
	ρ_0^α	Initial dislocation density	6.3×10^{13} m^{-2}
	p/q	Exponents in slip velocity	1.0/1.15
	v_0	Reference velocity for slipping	10^{-4} m/s
	i_s	Parameter controlling the dislocation MFP	85
	$\xi_{\alpha\alpha'}$	Interaction coefficients between slip systems	0.122, 0.122, 0.625, 0.07, 0.137, 0.122

5.3 Discussion

5.3.1 Origins of lattice distortion in RHEAs

We examined the LLD produced in the AM-fabricated T42 alloy. Although the XRD method is effective for investigating lattice distortion by reducing peak intensity [251,252], the peak intensity and width are still influenced by the crystal microstructure, size, and textures [44,253]. Due to the presence of LCFs, commonly reported in Hf-containing RHEAs [106], fractal-like lattice distortion was observed in HRTEM and confirmed by the FFT patterns of their corresponding selected areas (**Fig. 4. 6 b** (ii)) and the atomic strain map obtained via the GPA method (**Fig. 4. 6 c** (ii)), commonly used for studying LLD in other HEAs [107,254]. Conversely, PDF converted from the diffraction total scattering data can provide valuable inter-atomic positions [220]. Tong et al. [183] found that Zr- and Hf-containing RHEAs have an overlap of the 1st and 2nd atomic shells, similarly depicted in **Fig. 5. 1 b** (i), indicating the presence of large LLD in these alloys. Compared to the increase of chemical complexity in RHEAs, inducing atomic size mismatch seems to be more effective in increasing LLD, such as adding Hf or Zr large atomic radius elements [183]. We fitted different regions in our PDF curve (refer to **Fig. 5. 1 b**), as the PDF peak position is a function of the lattice constant [183]. Ultimately, a significantly higher lattice strain/distortion of 3.68% than that in previous Hf- and Zr-containing RHEAs was obtained (see **Fig. 5. 1 c**), resulting from the solution interstitial atoms [236], which indicates the presence of large LLD in the as-fabricated T42 HEA.

5.3.2The mechanical responses at different temperatures

The lattice distortion in traditional alloys is well-established, typically involving solute atoms in the matrix, resulting from the atomic size and elastic modulus mismatch [51,199], which can distort the local elastic field and hinder dislocation movement [44] to ensure a higher yield strength. In RHEAs, the solute and solvent atoms show no significant differences [2], hence the accumulated contribution by lattice distortion and modulus mismatch to the solid strengthening in RHEAs is considered [199]. RHEAs composed of high melting point elements exhibit excellent structural stability and heat softening resistance [49,255], contributing to their superior high-temperature strength. RHEAs, typically characterized by significant lattice distortion and modulus mismatch, demonstrate superior strength [49,255] or super-elasticity [256] under high temperatures. For instance, in the CrMoNbV RHEA, a gigapascal compressive yield strength at 1273 K was formed due to the substantial modulus mismatch and atomic-size mismatch between Cr and other constituents [48]. In our study, we discovered that a large lattice strain was formed in our T42 HEA (refer to **Fig. 5. 1**) due to a significant lattice radius mismatch but less modulus mismatch [236] than the CrMoNbV alloy [48]. This can enable superior yield strength at RT (refer to **Fig. 5. 2** a) in our LENS-fabricated T42 RHEA. Under elevated temperatures, strength softening would occur [48] and deteriorative mechanical properties would result from phase decomposition in the HfNbTiZrTa alloy [234], even though the mentioned RHEA has significant lattice distortion [183]. We conducted EBSD and TEM experiments on deformed structures under different temperature conditions, revealing the presence of a single phase regardless of temperatures rather than the phase decomposition (**Fig. 5. 4** and **Fig. 5. 5**) supported by the calculated phase diagram in **Fig. 4. 1**. Additionally, the value of lattice distortion shows a positive correlation with temperature increase [48], indicating that larger lattice distortion would be produced under elevated temperatures, enabling the stability of high yield strength in our T42 alloy under elevated temperatures.

On the other hand, the high-temperature strength can also be influenced by the temperature dependence of the elastic modulus [48], which determines the zero-temperature yield strength as well as the energy barrier for the thermal-activated flow [257,258]. In other words, the insensitive temperature dependence in the elastic constants can maintain the yield strength at elevated temperatures [48] and postpone the formation of softening. Although we did not include the lattice distortion in our first principles calculation. The calculated moduli were used in the CPFEM, demonstrating significant consistency between the experimental and simulation results (**Fig. 5. 9 c**). This validates the proposed methods for studying the temperature-dependence on the basic physical properties under elevated temperatures. Although a larger temperature-dependence in both E and G was observed in CrMoNbV and Inconel 718 alloys [48], the rule of mixtures on moduli [259] can also be used for calculating the modulus of materials, especially for Nb and V, with a weak temperature dependence [48,260], which were proven to maintain the high-temperature strengths in the reported alloy.

We proceeded to discuss the deformation mechanism in the deformed T42 alloy. The presence of lattice distortion led to the observation of wavy-like and pinned dislocations in the deformed alloy under room temperature (RT), as depicted in **Fig. 5. 5**. This is due to the interstitial solute atoms creating a heterogeneous stress field [261], which pins the gliding dislocations and transforms the straight dislocation line into a wavy configuration [262]. At elevated temperatures, dislocation loops were also observed in samples deformed at 673 K and 873 K (see **Fig. 5. 5 b** and **c**), facilitated by the strong solute pinning effect caused by the even larger distorted lattice [263] under these temperatures. Despite non-screw dislocations being proven effective for improving high-temperature hardening in RHEAs [257,258,264], our study observed mixed characteristics of dislocations in the deformed T42 alloy at 873 K (**Fig. 5. 5 c**), exhibiting a similar dislocation structure to the hot compressed CrMoNbV alloy [48].

5.3.3 The failure mechanism of RHEA under higher temperature

The work-hardening effect present in the 673 K tensioned T42 sample makes it easier to understand that effective work-hardening delays the formation of necking [265] than in the RT-deformed sample. When the tensile temperature was increased to 773 K, oxidation of the base metal occurred [266], inducing surface cracks under external stress [267], and presenting regional transcrystalline fracture characteristics on the fracture surface (**Fig. 5. 3 a** (ii)). Further increasing the tensile temperature resulted in a mixed fracture structure of transcrystalline with regional ductile dimples (**Fig. 5. 3 a** (iii)), due to the transgranular internal oxidation [268]. At a tensile temperature of 1073 K, failure occurred even before the application of external stress. Therefore, we conducted a long-term high-temperature oxidation test, with the oxidation gain summarized in **Fig. 5. 6 c**, showing a linear increase with processing time. This indicates that a stable and thick oxide layer cannot be maintained due to the presence of easily oxidized elements like Hf and V [266]. During the high-temperature oxidation test, surface cracks formed spontaneously (**Fig. 5. 6 a**), indicating the need for a stable and thick oxide layer formation element in the future [48].

5.4 Conclusions

In this chapter, the T42 RHEA was successfully synthesized using the LENS approach, and its microstructure, high-temperature tensile properties, lattice distortion, and high-temperature elastic constants were thoroughly investigated. The main conclusions are as follows:

1) The LENS-fabricated T42 alloy exhibited a large local lattice strain of 3.68%, detected via the PDF approach, attributed to the presence of a large radius

mismatch and local chemical fluctuations. These factors contribute to the excellent yield strength at room temperature.

2) As the temperature increases, the fabricated T42 alloy demonstrates stable yield strengths ranging from 680 to 635 MPa in the elevated temperature range. The modulus of the fabricated T42 alloy shows low sensitivity to temperature, enabling it to overcome heat softening at elevated temperatures. The effect of lattice distortion remains significant, providing considerable yield strength compared to other RHEAs under certain temperature ranges.
3) However, increasing the working temperature to 1073 K results in severe oxidation without the formation of a solid oxidation layer, leading to the complete fracture of the fabricated T42 alloy in our study. This highlights the need to consider the addition of elements that can promote the formation of solid oxidation films in future studies.

Chapter 6 Tribological performance of additive manufactured T42 RHEA

6.1 Introduction

The development of alloys with excellent wear resistance is crucial to prevent mechanical component failures and material losses [269]. In general, the wear resistance of alloys is closely related to the strength/hardness of the material. The improvement in strength and hardness of HEAs mainly comes from solid solution strengthening [236], dislocation strengthening [168,270], and precipitation phase strengthening [270]. However, simply increasing the content of precipitated phases may not significantly improve wear resistance [142,144], and a single-phase structure may be more applicable for enhancing the wear resistance in HEAs. On the other hand, LAM technology can be used to produce HEA coatings with strong metallurgical bonding, enhancing surface wear resistance [271,272]. The preparation of high-quality coatings with excellent strength-ductility synergy, and minimal defects significantly improves their wear resistance [272,273]. As discussed in the previous chapters, LENS can fabricate RHEA bulk with superior strength-ductility synergy and a single bcc phase among large temperature ranges, offering the potential for superior tribological performance at elevated temperatures. Considering the complex application conditions at high temperatures faced by RHEAs [274], the wear resistance of RHEAs is easily affected by ambient temperatures [275–277]. While ensuring the superior strength-ductility synergy of the fabricated T42 alloy at elevated temperatures, controlling the formation order of oxidation products is crucial for improving the tribological properties of RHEA coatings at elevated temperatures.

In this chapter, we investigate the tribological performance of LENS-fabricated T42 alloy, which exhibits well-performed wear resistance at elevated temperatures. By controlling the formation order of oxidation products, we achieved a dramatic improvement in wear performance from room temperature to 600 ℃. Additionally, we systematically explored the wear mechanisms of LENS-fabricated RHEAs under elevated temperatures, providing novel insights into the fabrication of RHEAs with superior properties for high-temperature conditions.

6.2 Results

6.2.1 The hardness of fabricated alloy

The microstructure of the fabricated T42 alloy was fully presented in the above chapters. In this work, we conducted hardness assessments to ascertain the mechanical characteristics of the synthesized alloy. The alloy exhibits an average microhardness of approximately 367 $HV_{0.2}$. To further explore the mechanical behavior of the alloy, nanoindentation tests were performed, with the resulting load versus depth curves presented in **Fig. 6. 1**. These curves are characterized by their smooth and uninterrupted nature, with no evident pop-in phenomena. The nanoindentation hardness of the alloy is measured to be around 4.40 GPa, while its elastic modulus is estimated to be approximately 107 GPa. Additionally, the temperature dependence of the yield strength reveals that the alloy maintains a gigapascal level yield strength at room temperature

(RT), yet exhibits a yield strength ranging between 630 and 680 MPa at elevated temperatures (**Fig. 5. 2 a**).

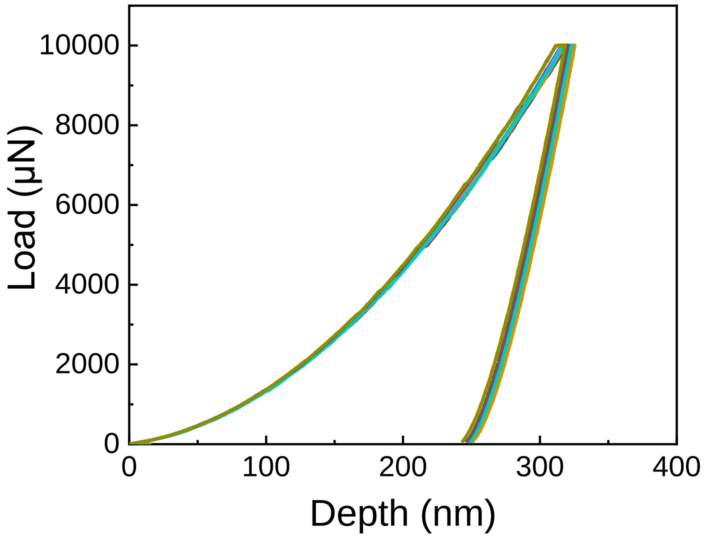

Fig. 6. 1 Load vs depth curves from nano-indentation experiments.

6.2.2 Tribological properties

We conducted a series of reciprocating dry friction tests at variable temperatures on the fabricated alloy. **Fig. 6. 2 a** illustrates the COF curves as a function of sliding duration under different thermal conditions. The average COFs (**Fig. 6. 2 a**) of the alloy exhibit variations, ranging from 0.4 to 0.5 for temperatures below 800°C, while the COF for the 800°C dry friction test decreased to approximately 0.28. Notably, at 800°C, the COF is significantly lower than at other temperatures, yet the temporal stability of the COF during the friction test at this temperature shows marked fluctuations compared to those at lower temperatures.

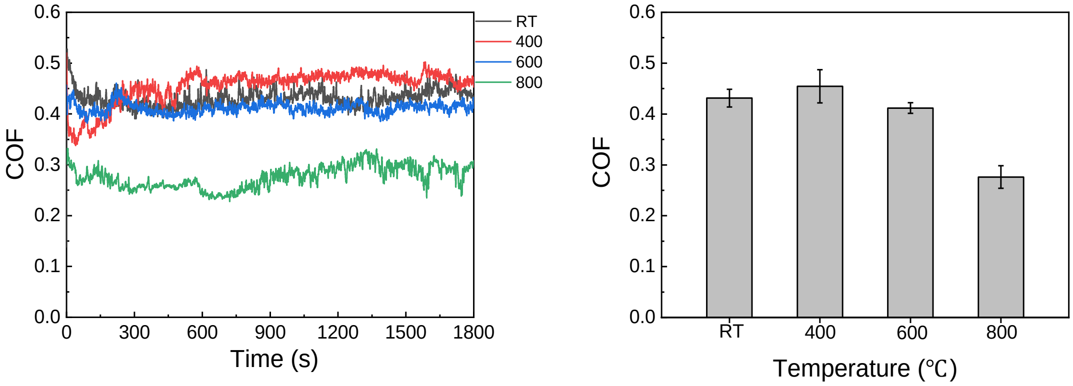

Fig. 6. 2 COFs of fabricated RHEA. a, COF curves as a function of temperature. **b,** Comparison of average COFs at different temperatures

Fig. 6. 3 presents the 3D morphologies of the worn surfaces on the sliding balls and the tested alloy at various temperatures. **Fig. 6. 3 a** captures the 3D morphology of the wear region on the Al_2O_3 ball surface after interaction with the RHEA at different thermal conditions. At RT and 400°C, the wear on the ball surface is characterized by distinct two-dimensional circular planes, whereas at higher temperatures, the wear is less pronounced. **Fig. 6. 3 b** displays the 3D profiles of the wear scars on the RHEAs that were subjected to grinding against Al_2O_3 balls at varying temperatures. The topographic contours reveal that the depth and width of the wear tracks evolve differently with increasing temperature. **Fig. 6. 3 c** provides 2D profiles of the central area of the corresponding wear scars along the cross-section. As the test temperature rises from RT to 400°C, the width of the wear scar decreases by approximately 19%, from 2285 μm at RT to 1860 μm at 400°C, while the maximum depths remain consistent at around 41 μm. Additionally, the formation of accumulation ridges around the wear scars suggests that the RHEA tends to extrude laterally between the grinding pairs during the dry sliding wear tests, indicative of the alloy's commendable plastic

deformation capability. As the temperature increases to 600 °C, a dramatic decrease in the width as well as the depth of the wear scar is formed and the maximum wear depth is lower than 1 μm. Additionally, although the same trend on the wear scar was observed on the 800 °C worn surface compared to the sample worn at a temperature lower than 400 °C, a deeper and wider wear scar was still produced compared to the 600 °C worn surface.

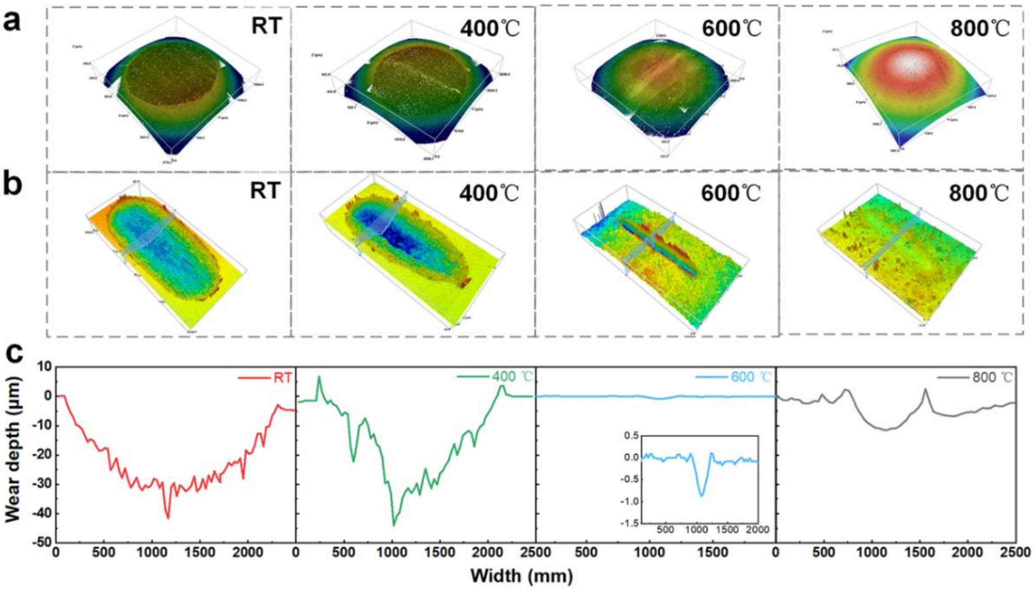

Fig. 6. 3 3D profiles and wear analysis of as-fabricated RHEA at various temperatures. a, 3D profiles of Al_2O_3 sliding counterpart and **b,** worn scars of as-fabricated RHEA at various temperatures. **c,** line profiles of the cross-section from the corresponding worn scars.

The wear volumes for each sample were determined from the 3D profiles of the worn surfaces. The wear rate (ω) was then calculated using the following equation [8]:

$$\omega = \frac{V}{L \times F} \tag{6. 1}$$

where V corresponds to the wear volume (mm^3), L denotes the total sliding distance (m), and F refers to the applied normal load (N). **Fig. 6. 4 a** shows the wear rates as a function of temperature, indicating that the wear rate decreases with increasing temperatures from RT to 600 °C. At RT, the wear rate of the RHEA is approximately 2.69×10^{-4} mm^3/(N·m), while at 600°C, it is nearly three orders of magnitude lower, at about 6.90×10^{-7} mm^3/(N·m). Upon raising the temperature to 800°C, the wear rate increases to 3.10×10^{-5} mm^3/(N·m), suggesting that the RHEA exhibits optimal wear resistance around 600 °C. A comparison of the tribological performance of our fabricated RHEA with other reported RHEAs [275–280] is shown in **Fig. 6. 4 b**. From this analysis, it is evident that our designed RHEA demonstrates exceptional wear resistance at high temperatures, particularly at an applied temperature of around 600 °C.

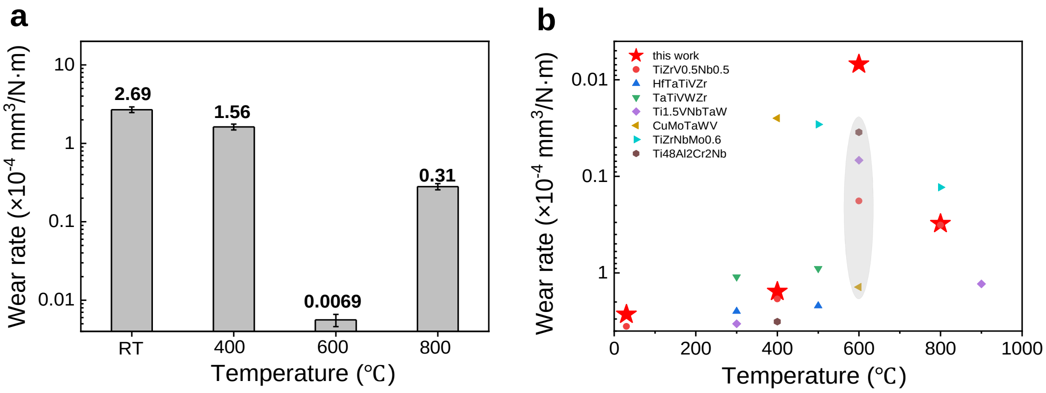

Fig. 6. 4 Wear performances of RHEAs under various conditions. a, Wear rates of fabricated RHEA under different temperatures and **b,** Comparison of wear rates between different HEAs [275–280].

6.2.3 Microstructure of worn surfaces

To gain a deeper understanding of the wear mechanisms at play in the fabricated RHEA after dry friction tests, we examined the worn surfaces of the specimens and the Al_2O_3 sliding ball counterpart. **Fig. 6. 5 a-d** present the SEM images and EDS analyses of the Al_2O_3 ball surface post-friction tests at various temperatures. A comparison of

Fig. 6. 5 a(i)-**d**(i) reveals pronounced wear on the ball surface following the tests at RT and 400°C, characterized by a two-dimensional circular plane, consistent with the morphology depicted in the 3D profiles of **Fig. 6. 5 a**. The images in Fig. xx a(ii) and b(ii) show regular granular Al_2O_3 beneath the adhesive layer, suggesting the detachment of Al_2O_3 grains along their grain boundaries during the friction tests. EDS results (**Fig. 6. 5 a** (iii) and b(iii)) indicate that the adhesive material consists of alloy elements such as Ti, Hf, Nb, V, and O, mixed with the Al_2O_3 from the ball. Adhesive wear is thus identified as the primary wear mechanism for the counter-grinding system at these temperatures.

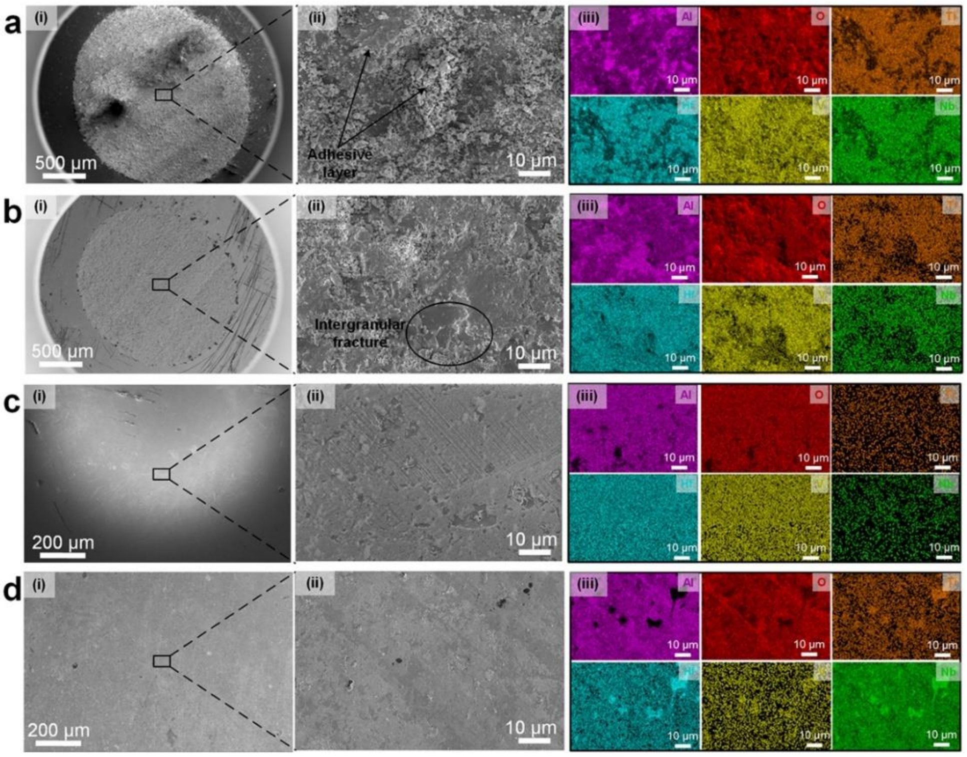

Fig. 6. 5 Morphologies of Al_2O_3 sliding ball counterparts with corresponding elemental maps under different temperatures. a, RT. **b,** 400 ℃. **c,** 600 ℃ and **d,** 800 ℃.

Further analysis of the wear mechanism is provided by the SEM morphologies and EDS mappings of the RHEA's worn surfaces after dry friction tests at different temperatures, as shown in **Fig. 6. 6**. **Fig. 6. 6 a** reveals an abundance of wear debris and deep grooves on the wear tracks at RT, indicative of severe abrasive wear. At 400°C (**Fig. 6. 6 b**), the worn surface resembles that at RT, with copious wear debris and deep grooves, as well as significant plastic deformation leading to delamination, suggesting that abrasive wear and plastic deformation still dominate the wear process at this temperature. The wear surface of the RHEA at 600°C, as shown in **Fig. 6. 6 c**, appears relatively smooth, with a conspicuous oxide layer and minor delamination of this layer. The oxides, which are worn away as debris, suggest a transition to oxidative wear at 600°C. At 800°C (**Fig. 6. 6 d**), the friction surface is relatively smooth, but the formation of various oxides (Hf, Nb, and their oxides) at this temperature adversely affects the wear performance, resulting in an increased wear rate.

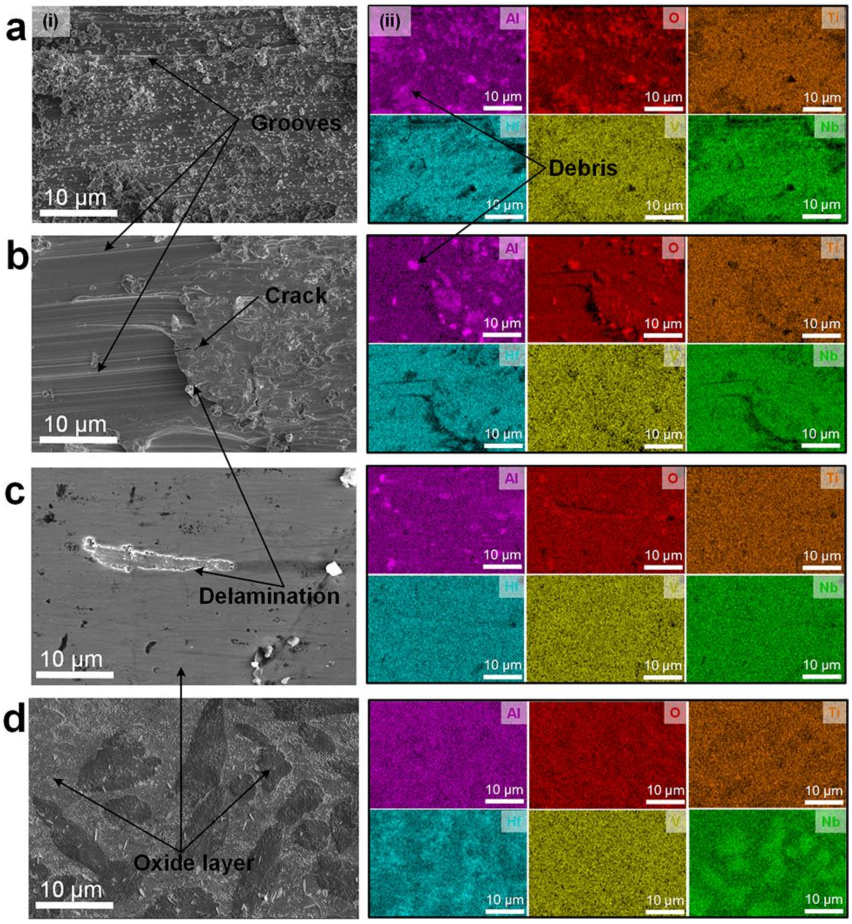

Fig. 6. 6 Wear surface morphologies and corresponding EDS analysis of fabricated RHEAs after dry friction tests under different temperatures. a, RT. **b,** 400 ℃. **c,** 600 ℃ and **d,** 800 ℃.

6.2.4 Cross-sectional subsurface microstructure

We examined the cross-sectional morphologies of the wear tracks on the fabricated RHEA, as depicted in **Fig. 6. 7**. At temperatures ranging from RT to 400 °C (**Fig. 6. 7 a** and **b**), a distinct friction layer is observed, formed by the accumulation and compaction of wear debris generated during the partially oxidative wear process [8,281]. At RT (**Fig. 6. 7 a**), the friction layer exhibits cracks both on its surface and within, which likely contribute to the disintegration and spalling of the layer, thereby accelerating wear. At 400 °C, the cross-sectional morphology is similar to that of the RT-worn sample, but without the formation of cracks, as shown in **Fig. 6. 7 b** suggesting enhanced wear resistance at this temperature. Increasing the temperature to 600 °C results in a smoother cross-sectional worn surface without a thick oxidation layer, as shown in **Fig. 6. 7 c**. At 800 °C, the formation of bulk oxides within the matrix and the occurrence of cracks inside these oxides, which are given in **Fig. 6. 7 d,** can lead to their detachment and exacerbate wear.

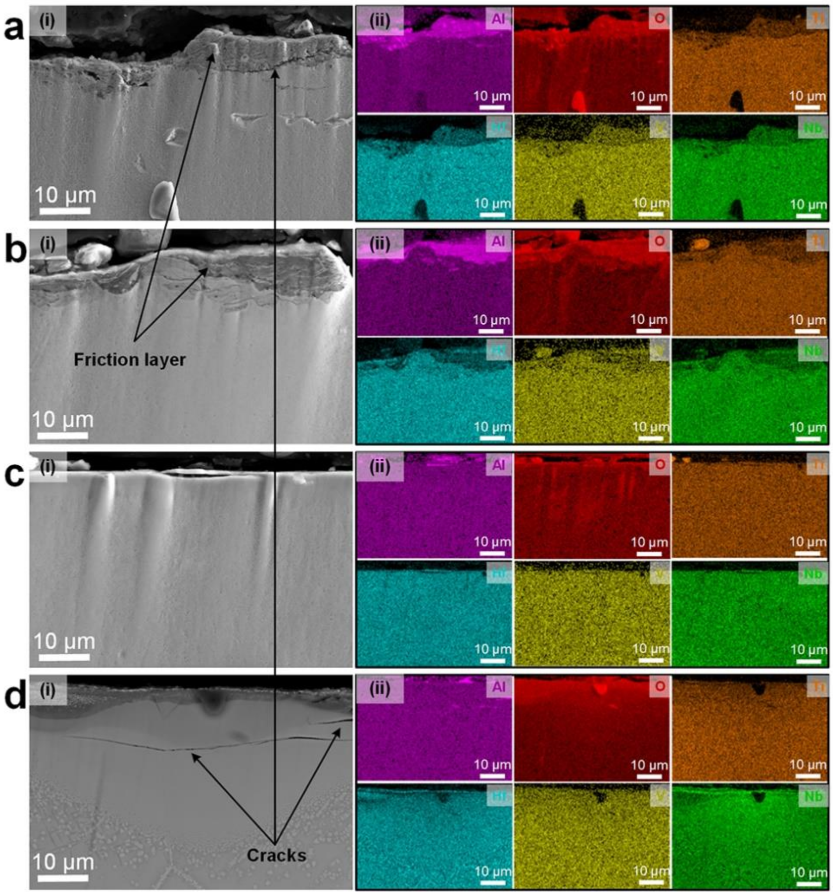

Fig. 6. 7 Cross-sectional morphologies of wear subsurface with their corresponding EDS maps. a, RT. **b,** 400 ℃. **c,** 600 ℃ and **d,** 800 ℃.

To investigate the deformation and oxidation behavior of the fabricated RHEA after dry friction tests at various temperatures, we sampled the worn scars from the RT and 400°C tests using FIB and subsequently characterized them using TEM. **Fig. 6. 8 a** shows the FIB lift-out sampling location along the sliding direction, with visible grooves. The reciprocating sliding at RT induces plastic deformation beneath the wear scar, as illustrated in **Fig. 6. 8 b**. The deformed nano-grains formed after the RT dry friction test increase in size with depth (**Fig. 6. 8 c** (i-ii)). The SAED pattern in **Fig. 6. 8 c** (iii) confirms the presence of nano-sized grains post-RT dry sliding test, identified as the single BCC phase of the RHEA matrix. The high-resolution TEM atomic morphology and corresponding FFT image in **Fig. 6. 8 c** (iv) further support the formation of nano-sized grains after the RT test. To assess oxidation post-RT test, **Fig. 6. 8 d** presents the highly deformed structure and corresponding EDS, revealing an even elemental distribution and the absence of extensive oxide formation after the RT dry friction sliding.

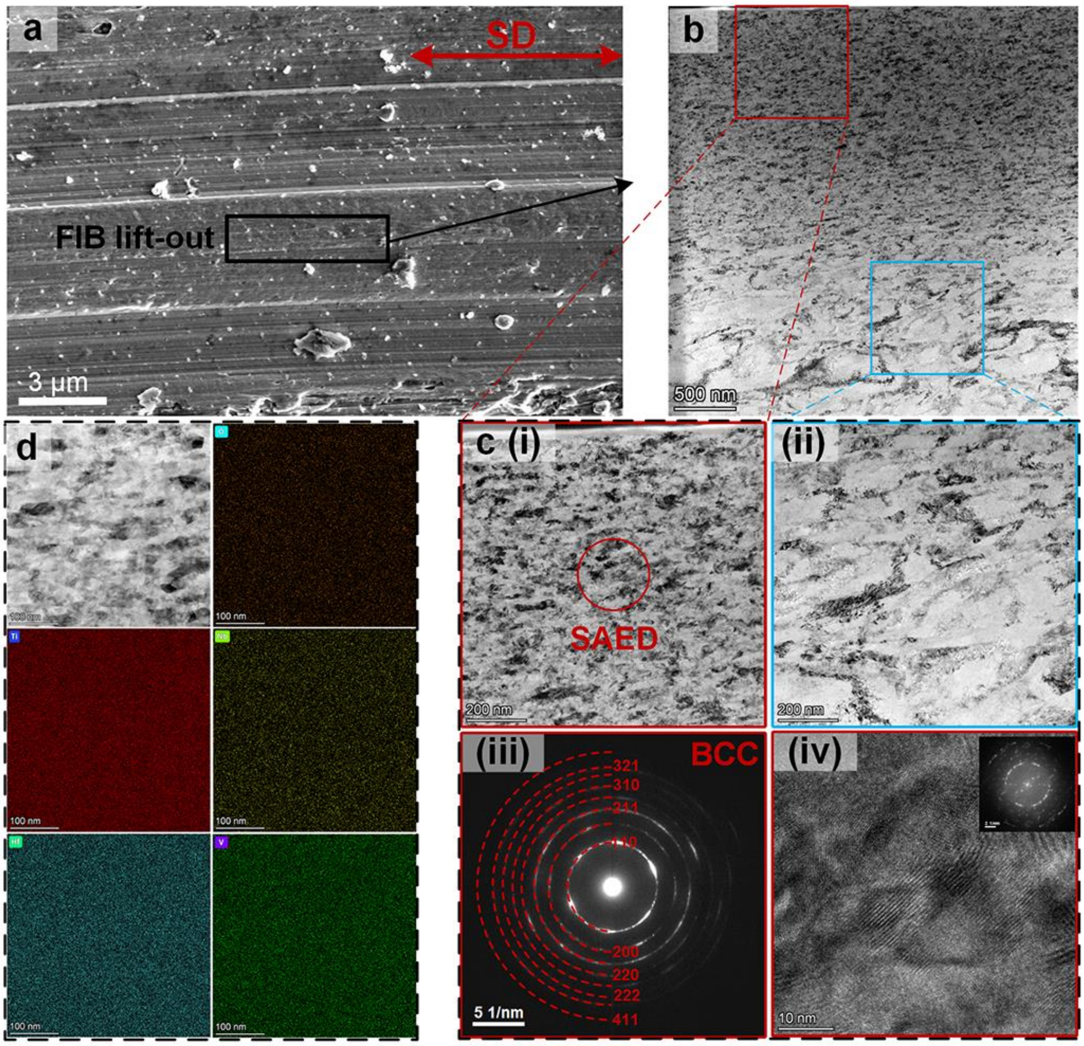

Fig. 6. 8 Cross-sectional microstructure of fabricated RHEA after dry frictional tests at RT. a, Wear surface morphology and FIB lift-out sampling area. **b**, The deformed microstructure of the wear subsurface with enlarged views given in **c**, showing the presence of nano-grains (i) and large density of dislocations (ii), (iii) the corresponding SAED and (iv) the HRTEM image. **d**, partially enlarged view of the deformed structure with corresponding elemental distribution maps.

For the 600°C worn sample with a dramatically low wear rate, **Fig. 6. 9 a** indicates the TEM sampling area, which shows a flattened worn surface with distinct oxide layers. The TEM bright field image reveals a stratified structure formed after the dry sliding test. Under the worn surface, a high density of dislocations is observed (**Fig. 6. 9 b**). The magnified image of the stratified layers in **Fig. 6. 9 c** displays clear boundaries beneath the worn surface. Elemental mapping and the distribution along a marked line (**Fig. 6. 9 c**) show a gradient in oxygen content, with higher levels at the top, diminishing towards the middle, and the lowest area exhibiting relatively low oxygen but increased levels of Hf and Ti. Further analysis of the phase composition of different strata beneath the wear surface is provided by the SAED patterns and HRTEM atomic maps (**Fig. 6. 9 d**). While the upper layer under the wear surface is confirmed to have nano-sized grains, the lattice constant differs from the BCC matrix shown in **Fig. 6. 8**. The bottom layer maintains a single BCC structure, as evidenced by the atomic structure in **Fig. 6. 8 d** collected along the [100] axis, whereas the middle layer appears to have a distorted lattice and is identified as HfO_2. For the upper layer, nanocrystals of a mixture between TiO_2 and HfO_2 were formed in the ultra-thin film based on the SAED pattern, with a thickness of ~ 200 nm.

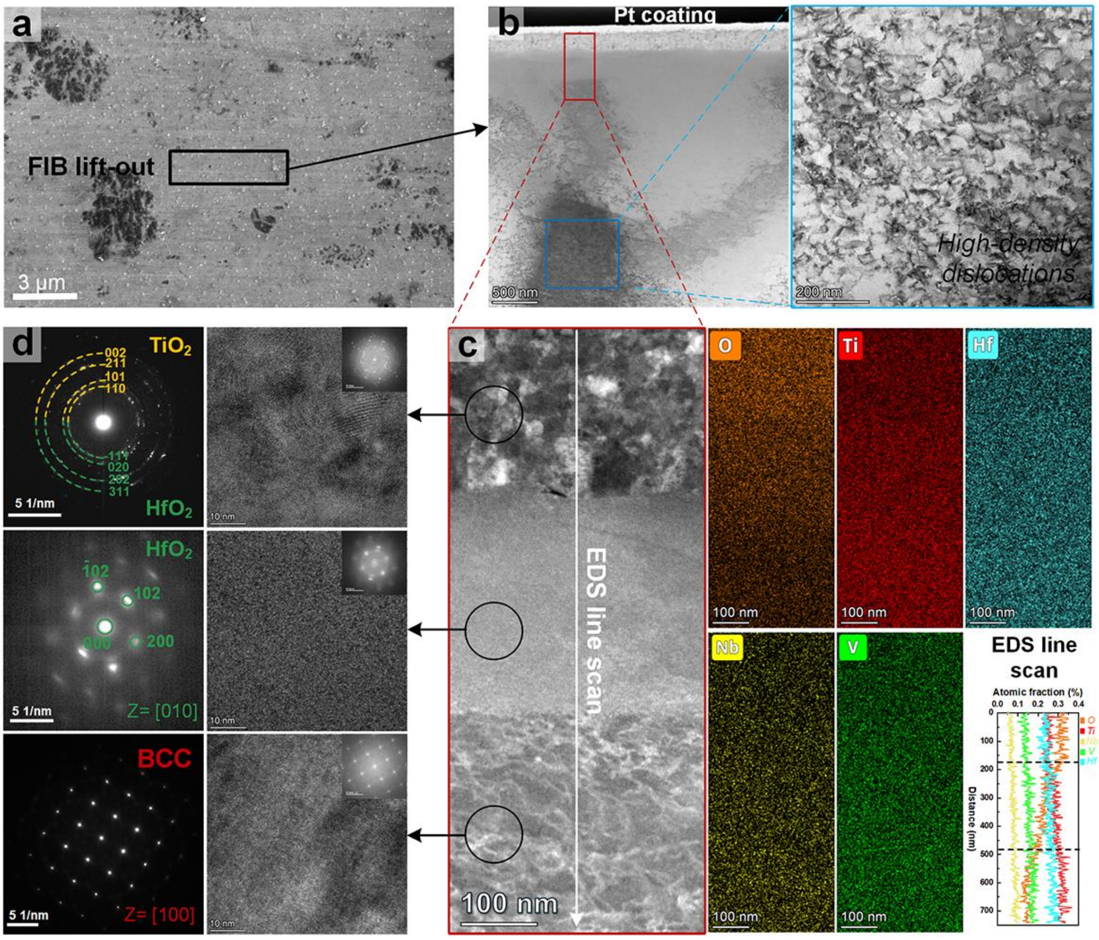

Fig. 6. 9 Microstructure on the cross-section of wear scar after 600 °C friction test. a, SEM image showing the TEM sampling area by FIB lift-out method. **b**, TEM bright field image indicating the presence of layer structure and high density of dislocations. **c**, The corresponding enlargement of marked area in **b** illustrating the obvious laminate structures and the elemental gradient on corresponding elemental distribution images. **d**, The SAED patterns and HRTEM images from different layers beneath the wear scar, giving the presence of various metallic compounds.

6.2.5 High-temperature oxidation behavior

The significant reduction in the wear rate of the sample worn at 600 °C (**Fig. 6. 4 a**), compared to its counterpart worn at 800 °C, suggests a substantial enhancement in wear resistance. This improvement can potentially be attributed to the distinct oxidation behaviors exhibited at these different temperatures. To elucidate this, we explored the oxidation behavior of the fabricated RHEA at 600 °C and 800 °C through static oxidation experiments, with the results presented in **Fig. 6. 10**. **Fig. 6. 10 a** demonstrates the static mass gains of the RHEA as a function of exposure time at varying temperatures, revealing a gradual increase in mass with both rising temperatures and extended dwell times. Notably, the mass gain at 800 °C exhibits a significantly sharper increase, nearly one order of magnitude greater than that observed at 600 °C, suggesting a higher rate of oxide formation at the elevated temperature. XRD analysis of the oxidized RHEA after varying durations at 600 °C (**Fig. 6. 10 b**) identified minor quantities of oxides, such as TiO_2 or HfO_2, alongside a predominantly BCC matrix during the initial stage of oxidation. The left-shifted peak in the XRD pattern indicates lattice expansion might be due to oxygen absorption. In contrast, the XRD patterns of the oxidation products formed after experiments at 800 °C (**Fig. 5. 6 d**) show that a diverse array of oxides emerged at the onset of oxidation, with prolonged exposure not significantly altering the types of oxides formed. Furthermore, the oxidation morphology and corresponding elemental distribution maps at 600 °C and 800 °C , depicted in **Fig. 6. 10 c** and **Fig. 5. 6 b**, respectively, highlight distinct oxidation behaviors at different temperatures during the early stages of oxidation. The increase in temperature from 600 °C to 800 °C resulted in the formation of noticeable oxides of Nb, Ti, Hf, and V, as evidenced by their elemental maps.

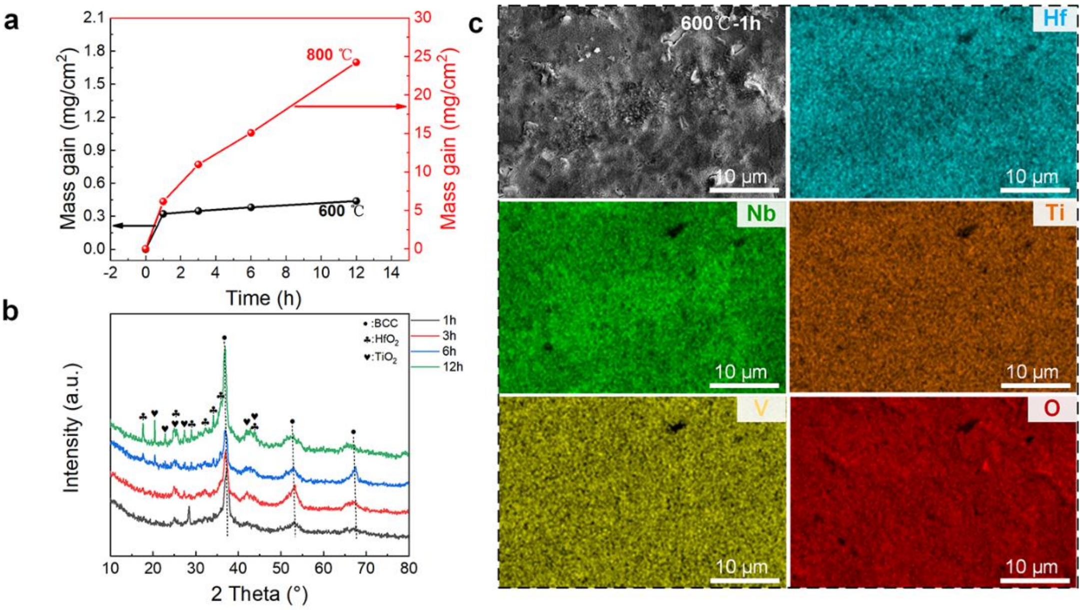

Fig. 6. 10 Oxidation experimental results of the fabricated RHEA at 600 °C. a, The mass gain as a function of processing time. **b,** XRD patterns of the samples oxidized after 600 °C. **c,** Oxidation morphologies with corresponding EDS maps of fabricated RHEA at 600 °Cfor 1 h**.**

6.3 Discussion

6.3.1 Effect of strength on the wear performance

According to the empirical model proposed by Archard [273], which considers adhesive wear as the dominant mechanism, it is assumed that the wear rate of a material has an inverse relationship with its yield strength or hardness. Therefore, high-hardness materials can be expected to have low wear rates and good wear resistance [282–284]. The yield strength of as-fabricated RHEA is ~ 1030 MPa (RT) and ~ 680 MPa (400 °C), respectively, showing the drop in strength with increased temperature (**Fig. 5. 2 a**). However, a better wear resistance at 400 °C than RT was produced, as shown in **Fig. 6. 4**, indicating that adhesive wear is not the main reason for material loss between RT-400 °C. Accordingly, the Archard model does not apply to the counter-grinding system composed of the above alloy and Al_2O_3 in a large temperature range, although the

RHEA has adhesion to the counter-wearing pair and material transfer under dry sliding friction (**Fig. 6. 5**) due to the large shear stress formed at the adhesive node [8]. During the practical wear process, especially at a temperature lower than 600 ℃, the wear surface has an elastic collision effect on the Al_2O_3 ball, and the peeling of Al_2O_3 can participate in the wear process. The peeling off of a large number of Al_2O_3 particles shows that the position of the adhesive layer itself is randomly distributed (**Fig. 6. 5 a** and **b**), and covering the grinding ball has no obvious protective effect, resulting in poor wear resistance at temperatures under 600 ℃.

In the model proposed for abrasive wear [285], the grooves formed by the conical rigid asperities on the material surface are mainly caused by two types of material displacement modes. One is micro-cutting of the material in front of the groove to separate the material directly. The other is that the interplay between the frictional force and the normal load on the contact surface leads to micro-cutting at the leading edge of the contact point, followed by plastic deformation and material accumulation at the base and sides of the wear track [286]. Consequently, strip-shaped grooves form along the sliding direction, as shown in **Fig. 6. 6**. However, the ease with which material separation occurs along both sides of the groove after plastic deformation depends on the overall mechanical properties of the alloy, and wear resistance is not simply attributed to the hardness. As the temperature reaches 400 ℃, due to the excellent thermal softening resistance induced by the large lattice distortion at high temperatures

[48], a decreased wear rate was formed compared to the sample worn at RT, which has also been reported in other HEAs worn at elevated temperatures [276,281,287].

6.3.2 Influence factor of elastic moduli

During the dry friction test, tangential forces arise when there is an attempt at relative motion between contacting solid surfaces. The application of a normal load allows for the calculation of the maximum contact stress (P_{max}) between the sliding ball and the sample using Hertzian contact mechanics [288], which can be used for evaluating the deformation mechanism during the frictional test:

$$P_{max} = \frac{3P}{2\pi a^2} \tag{6. 2}$$

Here, a represents the radius of the contact area, determined by:

$$a = (\frac{3Pr}{4E^*})^{\frac{1}{3}} \tag{6. 3}$$

In this equation, r is the radius of the counter-grinding ball, and $E*$ is the reduced Young's modulus, calculated as:

$$E^* = (\frac{1-\upsilon_1^2}{E_1} + \frac{1-\upsilon_2^2}{E_2})^{-1} \tag{6. 4}$$

Within this formula, v_1, v_2, E_1, and E_2 represent the Poisson's ratios and Young's moduli of the counter-grinding ball and the sample material, respectively.

According to **Eqs 6. 2-4**, the computed P_{max} values are presented in **Table 6. 1**. The temperature-dependent elastic constants of Al_2O_3 were sourced from Ref. [289], while the values for the as-fabricated RHEA were derived using Density Functional Theory (DFT) methods (details are given in **Section 5.2.5**). Across the examined temperature range, the P_{max} under a static load of 10 N is in a range between 910 to 980 MPa, which exceeds the yield strength of the RHEA at elevated temperatures, leading to plastic deformation under high-temperature tribological process. At RT, the value of P_{max} is closed to the yield strength and the wear on the grinding ball transforms its initially near-spherical surface into a flattened plane (**Fig. 6. 3**), changing the load distribution from a planar contact to a micro-scale asperities contact point load. Consequently, the reduced radius of the asperities causes a significant increase in local contact stress, leading to preferential damage. This deformation manifests in the surface layer, along with the formation of a nanocrystalline layer [290], as depicted in **Fig. 6. 8**.

Table 6. 1 The basic physical properties of RHEA and sliding ball to calculate the value of P_{max}.

		Temperature (℃)			
		RT	400	600	800
Sliding ball	E/GPa	398.500	379.771	369.410	359.049
	υ	0.233	0.238	0.240	0.243
Fabricated RHEA	E/GPa	105.993	106.258	106.028	105.553
	υ	0.364	0.359	0.356	0.354
P_{max} (MPa)		929.431	922.201	916.194	909.464

6.3.3 The role of oxidation products

The formation and composition of oxides at elevated temperatures are critical factors in determining the high-temperature tribological behavior of materials, with environmental temperature exerting a significant influence [291]. Under the combined influence of high temperature and mechanical stress, the friction surface and subsurface of RHEAs undergo a series of intricate physical and chemical transformations [8,277]. These include the adhesion of micro-protrusions, the spalling of surface materials, the initiation and growth of subsurface micro-defects, surface oxidation, and the formation and detachment of oxide layers, etc. As temperature increases, a transformation to oxidative wear is formed.

When friction pairs move against each other under high contact pressure, plastic deformation occurs (**Fig. 6. 8**), facilitating the diffusion of oxygen atoms into the metal matrix [292] and the formation of an oxide layer [8]. Typically, this oxide layer is generally harder than the underlying substrate, offering a protective effect against wear [293,294]. Certain metal oxides can act as lubricants in dry friction applications at high temperatures [8,295], which can reduce the direct contact between friction pairs, lowering both the friction coefficient and the wear rate [295]. The high-temperature wear behavior of metallic materials is influenced by both the friction oxide and the matrix [296]. In our study, a proliferation of nanocrystals forms on the subsurface of RHEA worn at 600°C (**Fig. 6. 9 c**), contributing to a reduced wear rate. Under mild oxidative wear conditions, the wear rate depends on the oxide quantity and layer thickness [296]. In general, the formation of an ultra-thin nano-crystal layer during the friction process is considered an efficient approach to improving the wear resistance of alloys [8]. Additionally, the nanocrystalline formed in the oxide-tribo layer due to the crushing of grains by the frictional stress [297] can benefit the bonding strength between the oxidation layer and substrates [8,298], resulting in improved wear resistance.

This is the reason why a superior resistance of the fabricated alloy was produced at 600 ℃ in this study. Additionally, the oxide layer's protective effect requires robust support from the matrix; without it, the oxide cannot effectively mitigate wear [299]. When the temperature further increases to 800 ℃, various oxidation products are produced (**Fig. 5. 6 d**), with different growth and expansion rates, inducing numerous cracks under cyclic loading at this temperature (**Fig. 6. 7 d**). These cracks propagate within the matrix and, upon reaching the surface, allow atmospheric oxygen to react with the RHEA matrix, forming double or multi-layered oxide structures (**Fig. 6. 7 d**). The presence of internal oxides alters the stress field around the crack, hastening its expansion [300]. When the crack reaches a critical size, portions of the matrix detach along with the upper oxide layer, leading to severe wear and the generation of large wear debris, as seen on the grinding ball (**Fig. 6. 3 a**), thus perpetuating the cycle of oxidative wear [301] and leading to the worsened wear resistance compared to the sample worn at 600 ℃.

6.3.4 Designing the formation order of oxidation products

Given that the fabricated RHEA comprises multiple components, its high-temperature oxidation behavior is inherently complex [302]. Generally, the oxidation behavior of alloys is governed by both kinetic and thermodynamic factors [266]. The Gibbs free energy change (ΔG) curves for different oxidation products as a function of temperature (**Fig. 6. 11**) indicate that the ΔG for Hf and Ti elements in the alloy to form their respective oxides is significantly lower than for the other elements, suggesting that these oxides are more likely to form at high temperatures. Initially, Ti and Hf elements are preferentially oxidized, and the sluggish diffusion in HEAs [266] prevents internal elements from replenishing the surface, leading to a compositional gradient (as shown in **Fig. 6. 9 c**) At this stage, a mixed oxide of HfO_2 and TiO_2 forms (**Fig. 6. 9 d**), resulting in a rapid initial weight gain on the oxidation kinetics curve (**Fig. 6. 10 a**). This mixed oxide film impedes the diffusion of O_2 from the air to the alloy surface and the diffusion of alloy elements to the surface, protecting the alloy from severe oxidation [303].

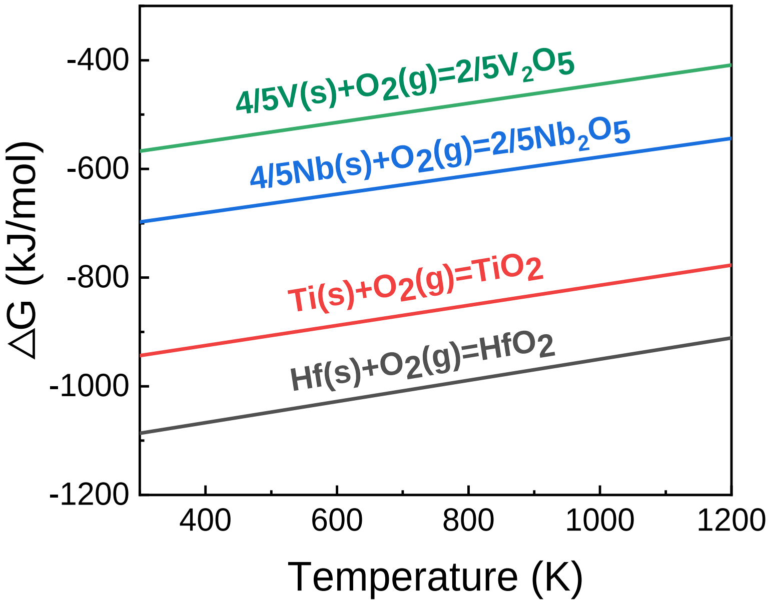

Fig. 6. 11 The Gibbs free energy of oxidation reactions of the alloying constituents in the fabricated alloy.

The growth and expansion rates of different metal oxide products vary, affecting the adhesion of the oxide film to the wear surface [304]. When multiple oxide films coexist, they often experience brittleness [305] under the combined stresses of friction and applied load. The Pilling-Bedworth ratio (R_{P-B}) is a one of the metrics used to assess the degree of oxide expansion during growth [306,307], defined as:

$$R_{P-B} = \frac{V_o}{n \cdot V_m} = \frac{M_o \cdot \rho_m}{n \cdot M_m \cdot \rho_o} \tag{6. 5}$$

This ratio compares the volume of the oxide film (V_o) to the volume of the consumed metal (V_m). In the equation, M_o and M_m represent the relative molecular/atomic mass of the oxide and pure metal, respectively; ρ_m and ρ_o denote the densities of the metal and oxide, respectively; and n is the number of metal atoms in one oxide molecule. The calculated R_{P-B} of different oxidation products is listed in **Table 6. 2**. An R_{P-B} value between 1 and 2 suggests that the oxide adheres well to the material surface, providing protection against further oxidation [308]. In contrast, an R_{P-B} value greater than 2 indicates that the oxide film is prone to expansion, cracking, and is relatively loose, failing to offer adequate protection [309]. When dense and loose oxide films form in the same area, partial delamination between the oxides can occur [310].

Table 6. 2 The values of R_{P-B} of different oxidation products.

	HfO_2	TiO_2	Nb_2O_5	V_2O_5
R_{P-B}	1.592	1.777	2.665	3.240

As the temperature rises to 800°C, needle-like compounds grow internally (see **Fig. 6. 7 d**), and the alloy experiences internal oxidation [311]. At this temperature, the oxide film fractures (**Fig. 6. 7 d**), creating pathways that increase oxygen diffusivity, leading to a sharp rise in the oxidation weight gain curve at 800 °C. During the friction and wear process at this temperature, the oxide film breaks and peels off under the action of friction and normal compressive stress, further promoting internal oxidation. Although the distribution of oxygen elements is relatively uniform at this temperature, there is extensive segregation of alloying elements. This large-scale segregation disrupts the original structure of the composite oxide film, resulting in the precipitation of various oxides (**Fig. 5. 6 b**). Controlling the oxidation order to form the dense oxidation film preferentially, like TiO_2 and HfO_2, which are beneficial to the improvement of the wear resistance [8], accounts for the remarkable wear resistance of the fabricated RHEA at 600 °C.

6.4 Conclusion

In this chapter, a Ti-Hf-Nb-V-based RHEA was synthesized using the LENS technique. The investigation focused on its microstructure, tribological properties, and oxidation behavior across different temperatures. The key findings are summarized as follows:

1) The T42 RHEA, fabricated through the LENS method, exhibited a single-phase bcc structure with homogeneously distributed elements. It demonstrated exceptional yield strength at RT and maintained its strength effectively at elevated temperatures.
2) The wear resistance of the RHEA dramatically improved as the temperature was increased to 600 °C. By strategically controlling the oxidation sequence of the alloying elements in the RHEA, it was possible to pre-form TiO2 and HfO2 layers. These layers formed an ultra-thin nanocrystalline coating, significantly reducing the wear rate to 6.90×10^{-7} $mm^3/(N \cdot m)$.
3) At higher temperatures (800 °C), a variety of oxidation products were generated, which led to the formation of a brittle oxidation film with a loose structure. This film was prone to cracking and detachment from the substrate under frictional stress and normal load, contributing to a lower coefficient of friction (COF) but adversely affecting wear resistance.

Chapter 7 Improved strength-ductility synergy in AM-fabricated Al-doped RHEA at elevated temperatures

7.1 Introduction

The LENS-fabricated T42 alloy offers a solution to the strength-ductility trade-off in additively manufactured RHEA at room temperature [236]. However, the as-fabricated T2 alloy does not maintain remarkable high-temperature tensile properties. Severe oxidation of the designed T42 alloy invalidates its tensile properties at temperatures higher than 873 K. Additionally, the formation of various oxidized products is detrimental to the tribological properties at 1073 K. Designing the oxidation order to form a compact oxidation layer under high temperatures effectively improves its tribological properties, especially at 873 K. To address the issue of unfavorable mechanical properties at relatively higher temperatures, the microalloying approach [78,312,313] has been attempted to improve the mechanical performance of fabricated alloys. Introducing elements that can form compact oxidation films, such as Al [86,224], seems to be an effective solution to improve the mechanical performance of the fabricated alloy under high temperatures. Al has been found to promote the formation of SRO [69] and/or B2 phase [86–88], which significantly regulates the mechanical performance in Al-contained RHEAs. Micro-alloying the T42 alloy with Al might improve its oxidation resistance and expand its working temperature range, requiring further attempts.

In this study, we designed an Al-doped RHEA based on the T42 alloy using an in-situ alloying method achieved during the LENS procedure. Before the fabrication procedure, the phase diagram of the Al-doped alloy was calculated using the CALPHLD approach. We then connected the relationship between the microstructure of the fabricated sample and its high-temperature properties. We compared the differences between the Al-doped RHEA and the original T42 alloy and concluded the reasons for the overall improvement in the high-temperature tensile properties of the Al-doped alloy. As a result, the micro-alloying method can guide the design of well-performing RHEAs, especially in additively manufactured alloys under extreme environments.

7.2 Results

7.2.1 Microstructure and phase compositions of fabricated alloy

To analyze the phase composition of the designed Al-doped alloy, we obtained the phase contents as a function of temperature through CALPHAD, as shown in **Fig. 7. 1** a. It is evident that the addition of Al significantly reduces the liquidus of the alloy and narrows the stable temperature range of the BCC compared to the T42 alloy without Al doping (**Fig. 4. 1**). However, the materials undergo a non-equilibrium solidification process during the LENS procedure. Therefore, the Scheil diagram can be used to predict the phase composition more effectively after the LENS procedure, as shown in **Fig. 7. 1 b**. Similar to the T42 alloy, the in-situ Al-alloyed RHEA prepared by LENS is mainly composed of the BCC phase.

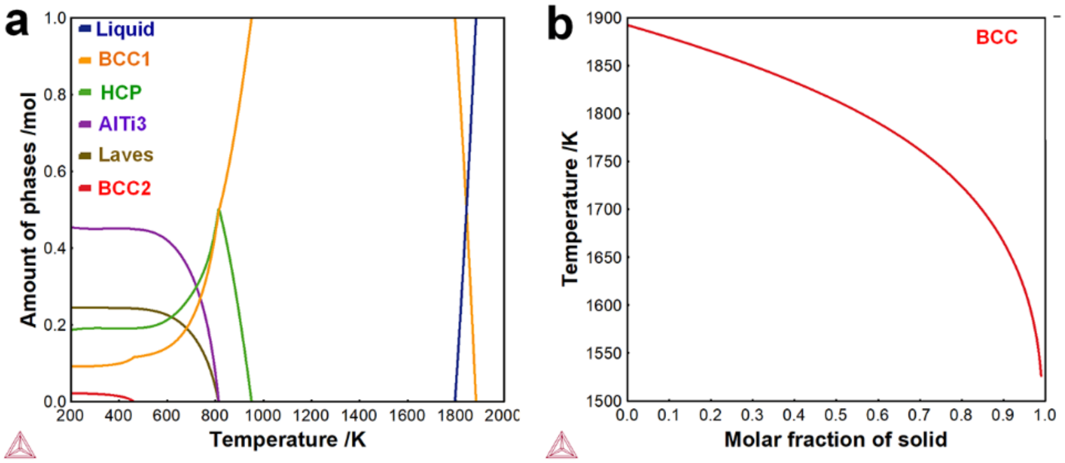

Fig. 7. 1 The calculated phase diagram via the CALPHAD approach. a, The content of formed phases as a function of temperature. **b,** The Scheil diagram showing the single BCC phase formed after the LENS procedure.

We then characterized the structure and composition of the Al-doped RHEA fabricated through LENS and obtained the precise composition of the manufactured RHEA, as shown in **Fig. 7. 2**. The structure was sampled from the upper surface, perpendicular to the BD direction, showing an equiaxed grain formed after the LENS procedure. According to the synchronously collected EDS mappings, there is no obvious element segregation on a macroscopic scale in the RHEA prepared by in-situ Al alloying. Finally, from the EDS results, we determined the actual content of the sample. Although it deviates from the designed composition, it is still within an acceptable error range.

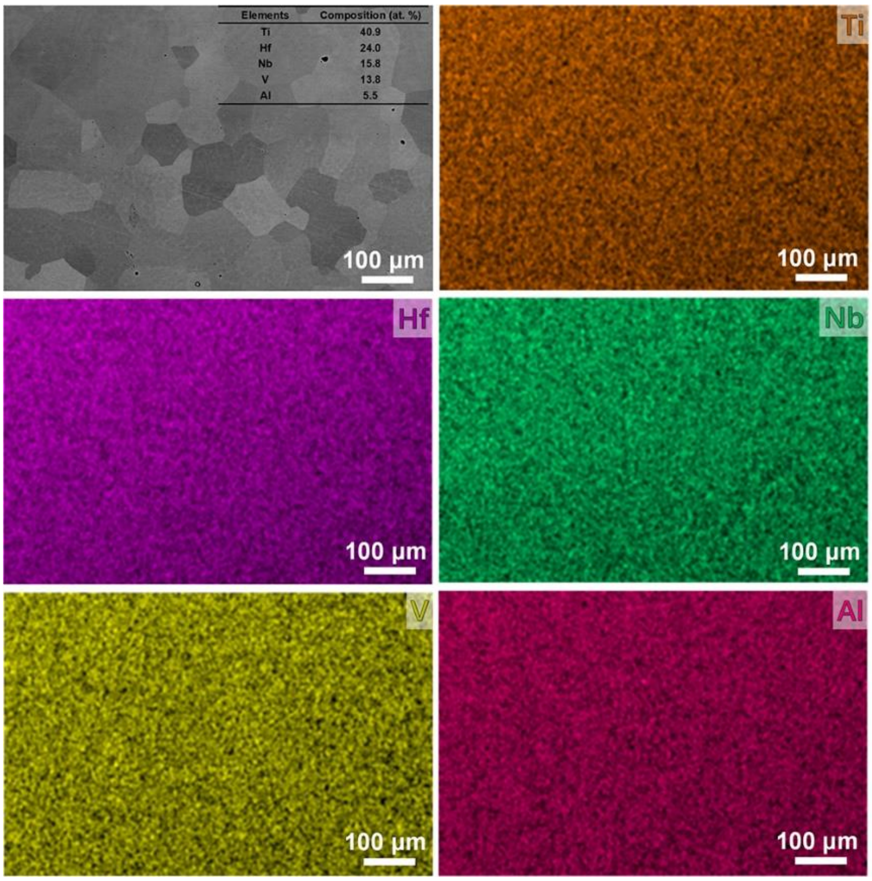

Elements	Composition (at. %)
Ti	40.9
Hf	24.0
Nb	15.8
V	13.8
Al	5.5

Fig. 7. 2 Microstructure of as-fabricated Al-doped alloy showing equiaxed grains and evenly distributed elements on the XY surface.

Based on the results of EBSD and XRD (**Fig. 7. 3**), the upper surface of the Al-doped RHEA prepared by LENS is composed of equiaxed crystals with a grain size of approximately 100 μm (**Fig. 7. 3 a**). Similar to the T42 alloy, there is no dislocation network structure in the Al-doped RHEA, as indicated by the KAM figure in **Fig. 7. 3 b**, which is different from the FCC high-entropy alloy prepared by LBPF [314,315]. The EBSD phase distribution diagram (**Fig. 7. 3 c**) and XRD profile (**Fig. 7. 3 d**) show a single-phase BCC structure in the Al-doped RHEA, with a lattice constant of ~ 3.2856 Å, indicating that adding Al can reduce its lattice constant.

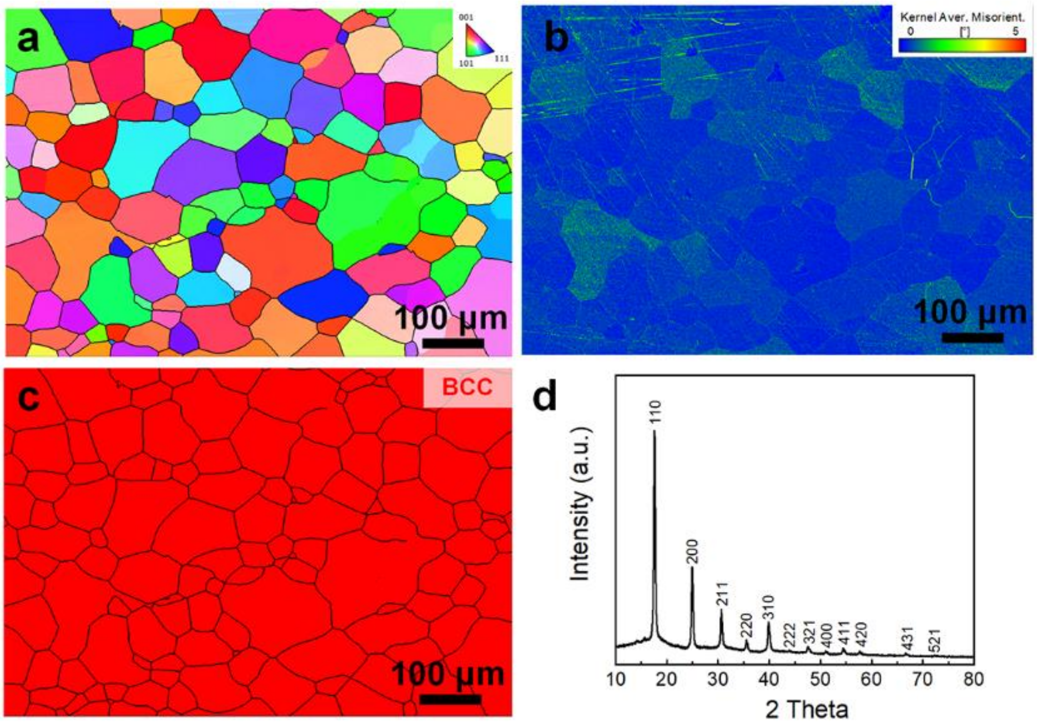

Fig. 7. 3 The microstructure and phase composition of LENS-fabricated Al-doped RHEA. a, The EBSD IPF image. **b,** The KAM figure eliminating the formation of dislocation networks after the LENS procedure. **c,** EBSD phase maps indicating the formation of a single BCC phase and **d,** Corresponding XRD profiles supporting the formation of a single BCC phase after the LENS procedure.

We analyzed the total scattering PDF of the Al-doped RHEA, obtained via Fourier transformation of the total scattering data, as shown in **Fig. 7. 4**. The PDF profile similarity of the Hf in reference [221] indicates the existence of a large local lattice distortion in the Al-doped RHEA, as it also exists in the first and second shell overlap (**Fig. 7. 4 a** (i)). Fitting the overall range of the PDF profile (**Fig. 7. 4 a**) yielded a lattice constant of ~ 3.31665 Å. This indicates a lattice expansion in the T42 alloy compared to the Al-doped RHEA. The calculated local lattice strains based on the fitted results of PDFs are shown in **Fig. 7. 4 b**. The general shift potential reflects the change in LLD, and **Eq. 5. 1** allows for evaluating different intra-regional LDDs. As a result, we obtained an accurate LLD of ~ 3.93% in the Al-doped RHEA, which is higher than that in the T42 alloy.

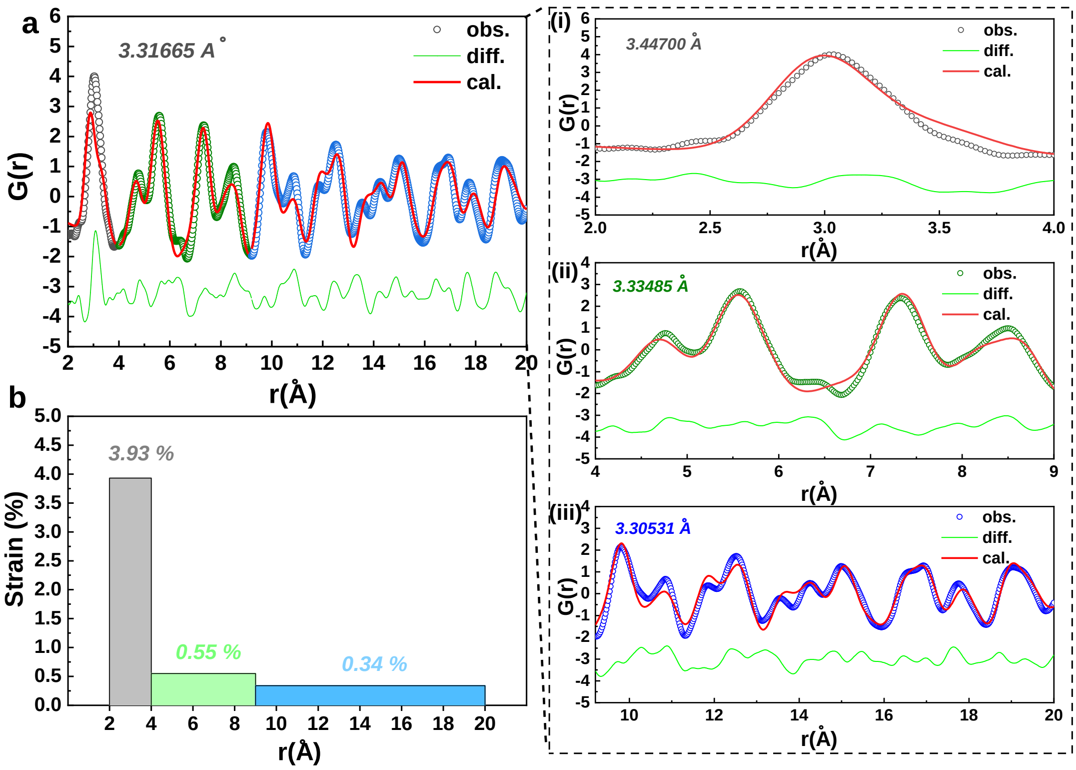

Fig. 7. 4 Precise XRD characterization on the fabricated Al-doped RHEA. a, PDF profile obtained from the total scattering data and fitted curve in the overall range and (i-iii) gives the separated fitted curves under different ranges. **b,** The calculated local lattice strains based on the fitted results of PDFs.

For investigating the nano-scale structure, we characterized it under HRTEM as shown in **Fig. 7. 5**. The HADDF image of the fabricated Al-doped RHEA (**Fig. 7. 5 a**) indicates the tiny possibility of forming phase segregation due to the presence of contrast differences. However, the corresponding SAED collected from the same area shows the presence of a single BCC phase, eliminating the possibility of phase segregation. In the enlarged HADDF image (**Fig. 7. 5 c**), block-like areas were observed, and the corresponding elemental maps indicate tiny segregation of elements, which might be considered as long-range local chemical fluctuations resulting from the addition of Al into the BCC matrix.

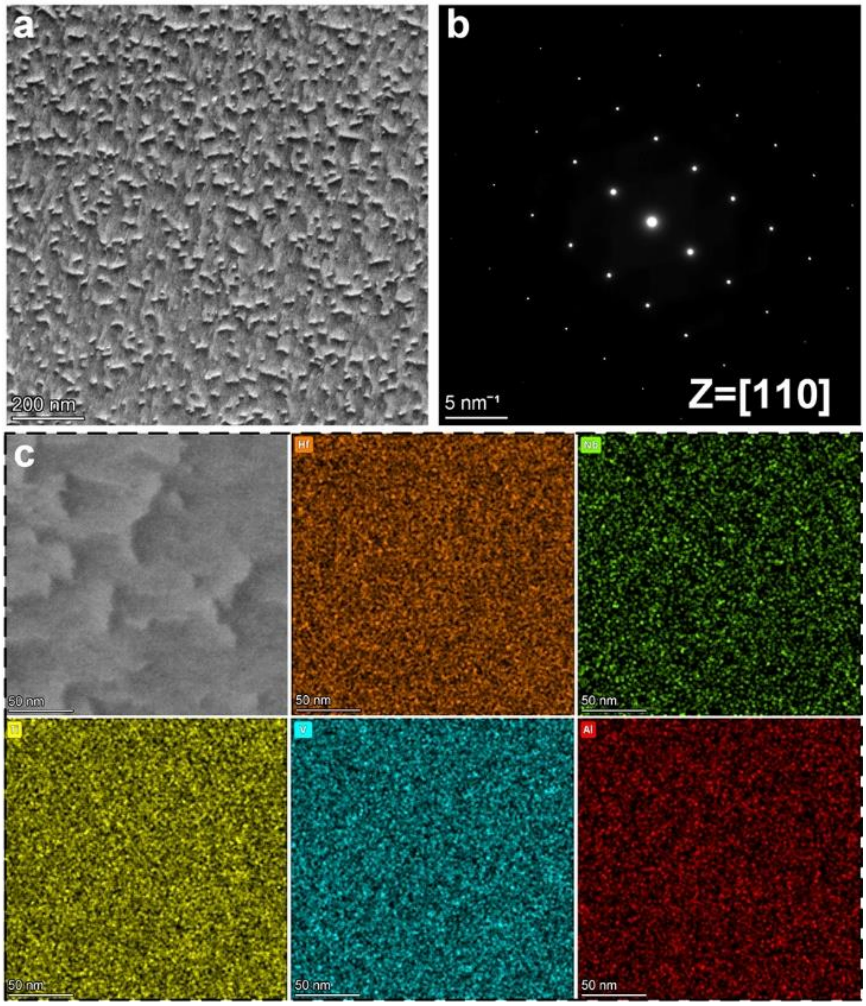

Fig. 7. 5 Nano-scale structure of as-fabricated Al-doped RHEA. a, The HADDF image showing the presence of contrast difference under nano-scale in Al-doped RHEA. **b**, The SAED pattern confirms the formation of a single BCC structure regardless of the formation of contrast differences in **a**. **c**, The enlarged map with corresponding elemental distribution, indicating the formation of local chemical fluctuations when Al was doped into the BCC matrix.

7.2.2 Mechanical properties under elevated temperatures

We conducted high-temperature tensile tests on the fabricated Al-doped RHEA, ranging from 673 K to 1073 K, and obtained typical engineering strain versus stress curves, as shown in **Fig. 7. 6 a**. At 673 K, the LENS-fabricated Al-doped RHEA exhibited a yield strength of 758 MPa and a fracture strain of 26.7%. As the testing temperature increased to 873 K, the yield strength slightly decreased to 707 MPa, and the fracture strain also decreased to 18.5%. Unlike the T42 alloy without Al doping, valid tensile stress and strain curves were obtained when the testing temperature was higher than 873 K. At 973 K, the yield strength sharply decreased to 383.3 MPa, while the fracture strain increased to approximately 35%. Further increasing the temperature to 1073 K resulted in a decrease in yield strength to 123.4 MPa, with the highest fracture strain of 36.5% obtained. At 673 K, the tensile curve shows obvious strain hardening, while obvious dynamic softening occurs in those tensile curves at 873 K and 973 K. The samples tested at 873 K and 973 K display similar trends in their respective tensile curves. Initially, the stress rapidly increases to its peak as strain increases, due to the strain-hardening effect. As the strain continues to increase, the stress sharply declines and then decreases steadily. This behavior is attributed to further deformation providing the driving force for dynamic recovery [316], leading to dislocation annihilation [317] and a marked decrease in stress. At 1073 K, the stress reaches its peak and then gradually decreases with continued stretching, due to the strong softening effect caused by an enhanced dislocation rearrangement rate at the higher temperature [317]. **Fig. 7. 6 b** provides a comparison between the Al-doped alloy and the T42 RHEA fabricated through the LENS procedure, indicating that the addition of Al into the RHEA matrix can improve the high-temperature performance of the T42 alloy.

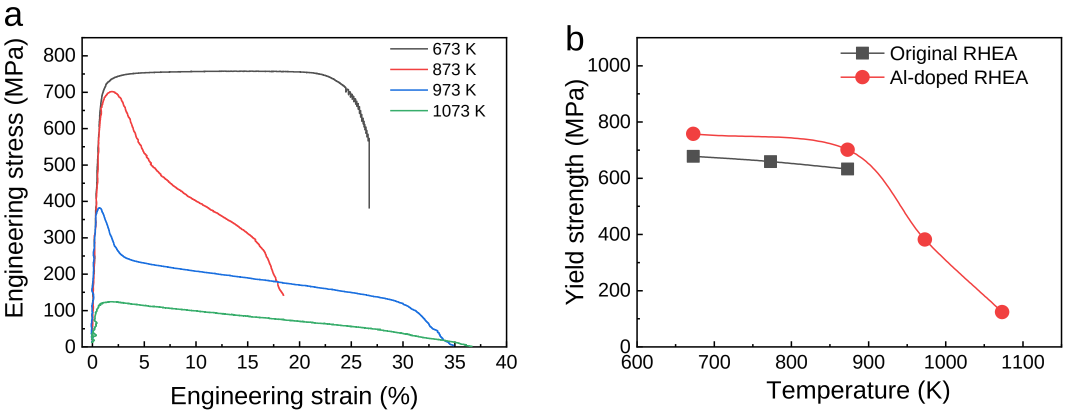

Fig. 7. 6 The hot tensile properties of as-fabricated Al-doped RHEA. a, Typical tensile stress-strain curves of samples tensioned under different temperatures. **b,** Comparison of the yield strength between the Al-doped RHEA and T42 alloy fabricated via the LENS approach.

To further understand the reasons for the improved mechanical properties in the Al-doped sample, we performed XRD experiments to study the microstructure evolution after hot-tensile tests under different temperatures, as shown in **Fig. 7. 7**. The fabricated Al-doped RHEA exhibited a single BCC structure, while the XRD profile of the 673 K tensioned sample only showed the presence of a single BCC structure with a left-shift peak, possibly caused by lattice expansion resulting from the absorption of oxygen. At 873 K, Al_2O_3 was detected alongside the majority of the BCC phase. When the temperature exceeded 873 K, severe oxidation occurred during the hot-tensile tests, resulting in the formation of various oxidation products of the constituents.

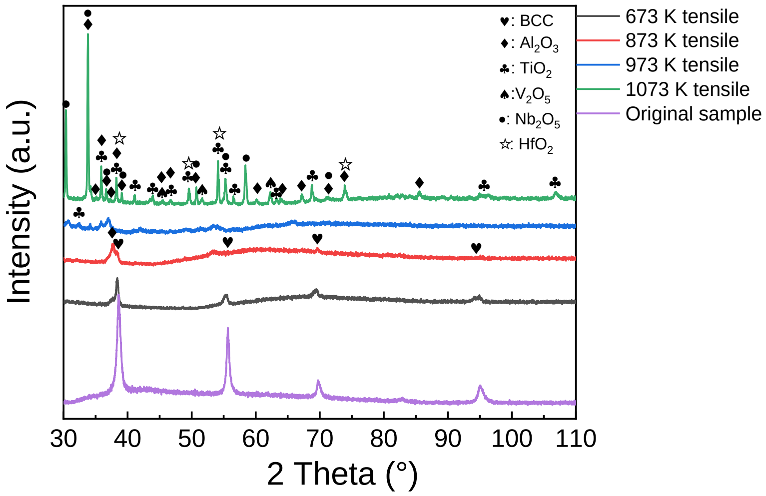

Fig. 7. 7 The XRD results on the sample after hot tensile tests under different temperatures.

The fracture surface morphologies of the fabricated samples after hot tensile tests are presented in **Fig. 7. 8**. At 673 K, a ductile fracture surface with the presence of dimples was produced. As the temperature increased to 873 K, a cleavage fracture surface with typical characteristics of river patterns was formed. Temperatures higher than 873 K resulted in severe oxidized fractures after the hot tensile tests, with the presence of secondary micro-cracks.

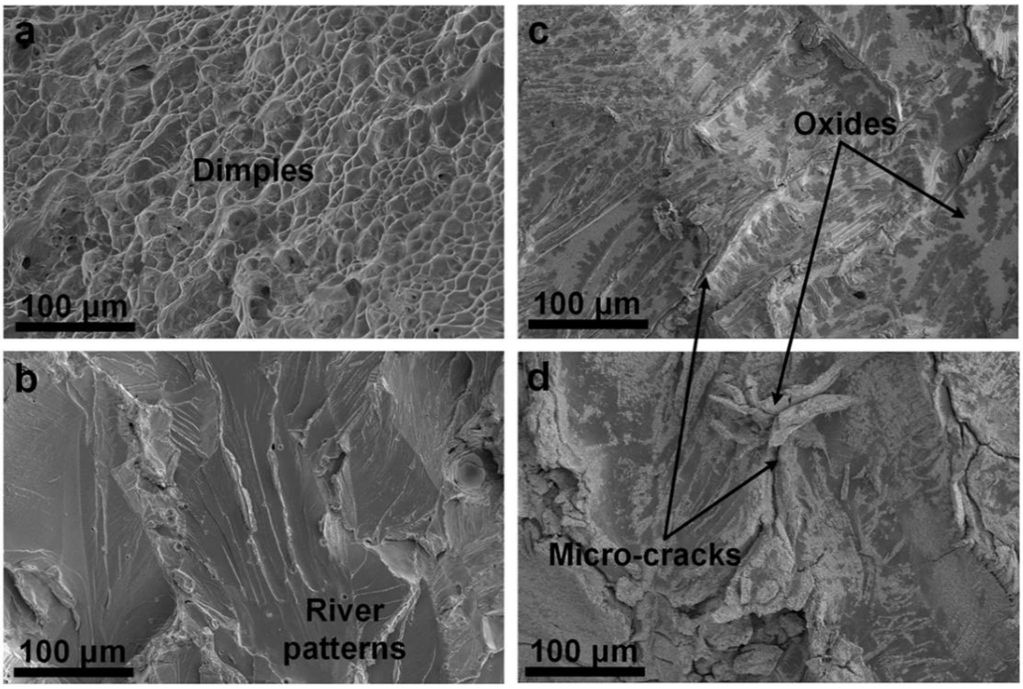

Fig. 7. 8 The fracture surface morphologies of samples after the hot tensile experiments. a, 673 K. **b,** 873 K. **c,** 973 K and **d,** 1073 K.

To understand the deformation behavior of the LENS-fabricated sample, we applied EBSD experiments to study their deformed behaviors near the necking area, as shown in **Fig. 7. 9**. At 673 K, a severely deformed structure with the formation of a high density of shear bands was observed. As the temperature increased to 873 K, microcracks appeared on the fabricated sample surface, promoting the formation of cleavage fractures during the hot tensile tests. At 973 K and 1073 K, microcracks were still present, with the grain size in the 1073 K deformed sample smaller than the original sample, indicating that grain boundary sliding and even dynamic recrystallization might be triggered under the high-temperature deformation process.

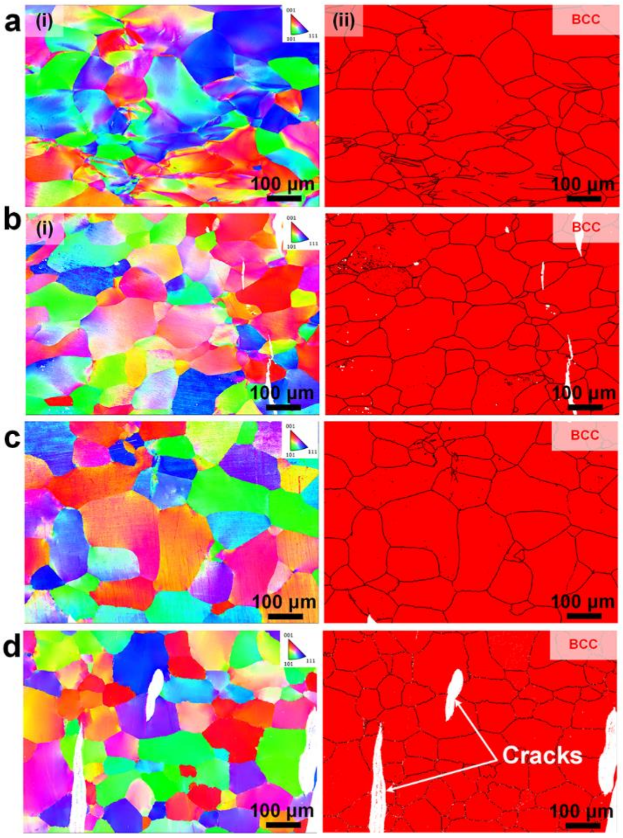

Fig. 7. 9 The microstructure and phase identification of the upper surface after hot tensile experiments. a, 673 K. **b,** 873 K. **c,** 973 K and **d,** 1073 K.

7.2.3 Tribological performance of Al-doped RHEA

We performed a series of reciprocating dry friction tests on the fabricated alloy across a range of temperatures. **Fig. 7. 10 a** presents the COF curves over time under various thermal conditions. The average COFs (**Fig. 7. 10 a**) for the alloy vary between 0.4 and 0.5 at room temperature and 400 °C. However, at 600 and 800 °C, the COF decreases to between 0.2 and 0.3 (**Fig. 7. 10 b**), similar to the behavior observed in the T42 alloy. **Fig. 7. 10 c** illustrates the wear rates as a function of temperature, again showing a pattern akin to the T42 alloy. As depicted in **Fig. 7. 10 c**, the wear rate diminishes as the temperature increases from room temperature to 600 °C. At RT, the wear rate of the RHEA is approximately 6.02 × 10^{-5} $mm^3/(N\cdot m)$, while at 600°C, it drops significantly to about 9.30 × 10^{-7} $mm^3/(N\cdot m)$. When the temperature is further increased to 800 °C, the wear rate rises to 6.02 × 10^{-5} $mm^3/(N\cdot m)$, indicating that the Al-doped RHEA demonstrates optimal wear resistance around 600°C.

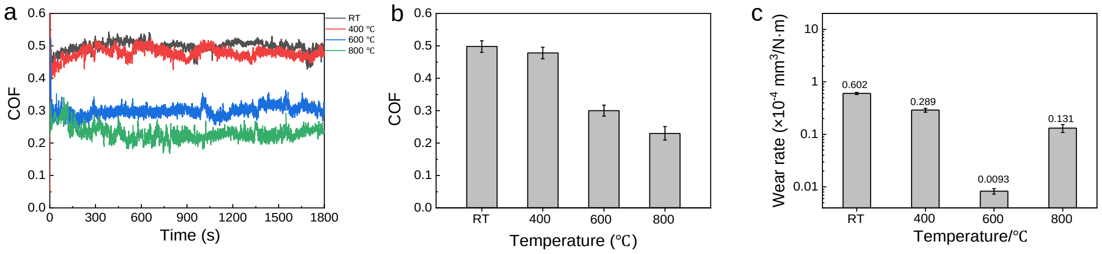

Fig. 7. 10 Tribological performance of Al-doped RHEA. a, Real-time COF. **b**, Average COF. **c**, Wear rates of fabricated alloy under different temperatures.

Fig. 7. 11 displays the three-dimensional morphologies of the worn surfaces of the tested alloy at different temperatures. These 3D profiles illustrate the wear scars on the RHEAs after being ground against Al_2O_3 balls under various thermal conditions. The topographic contours show that the depth and width of the wear tracks change distinctly as the temperature increases. From RT to 400 °C, the wear scar's width and depth decrease, although the maximum depth at 400 °C is slightly greater than that at room temperature. The presence of accumulation ridges around the wear scars indicates that the RHEA tends to extrude laterally during the dry sliding wear tests, highlighting the alloy's excellent plastic deformation capability. At 600 °C, there is a significant reduction in both the width and depth of the wear scar, with the maximum depth being less than 3 μm. However, when the temperature reaches 800 °C, the wear scar becomes wider and deeper compared to the sample tested at 600 °C.

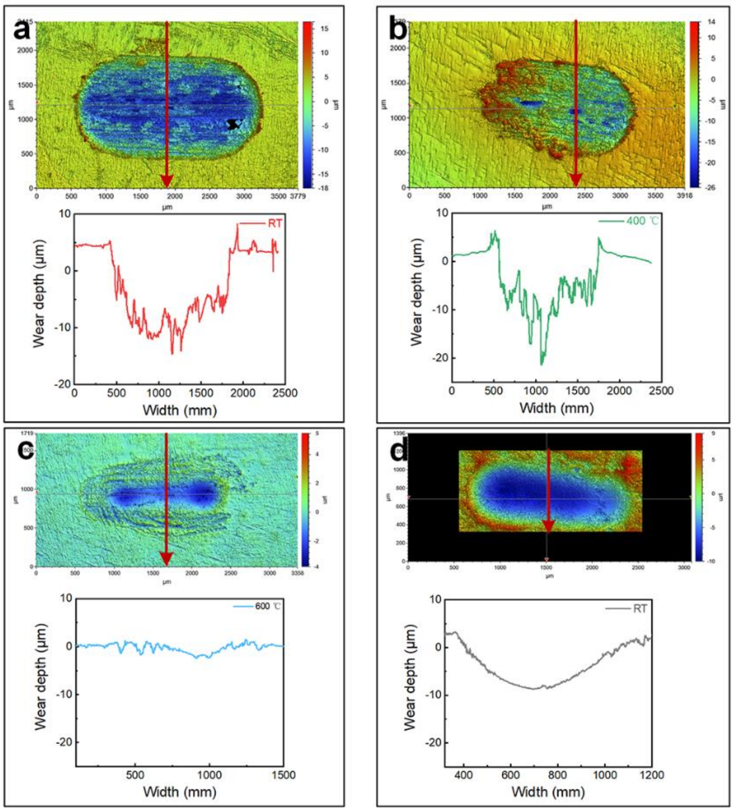

Fig. 7. 11 The worn morphologies and corresponding line profiles of fabricated alloy tested after different temperatures. a, RT. **b,** 400 ℃. **c,** 600 ℃. and **d,** 800 ℃.

7.3 Discussion

Al is considered a stable BCC element in FCC-based HEAs [318], and its addition to the FCC-based HEA matrix can form a BCC structure with high strength [318], or coherent precipitations [319], thereby improving the mechanical properties. In RHEAs, adding Al to the matrix can promote the formation of coherent B2 structures [86–88,320]. However, the B2 phase may not have comparable deformation resistance ability as the L12 phase in FCC-based alloys [319,320]. Consequently, in some cases [320], the addition of Al may not significantly improve the mechanical performance in RHEAs. To enhance the mechanical performance in RHEAs, LCFs [57], and LCOs [69] have been proven to be effective approaches for overcoming the strength-ductility trade-off in RHEAs. To improve the high-temperature performance of RHEAs, severe lattice distortion has been considered an effective method for enhancing high-temperature strength [48]. In Al-doped RHEA, the local lattice distortion is higher than that in the T42 alloy, indicating that the addition of Al into the BCC matrix can enable an even larger lattice distortion. The origins of large lattice distortion are calculated for the theoretical solid strengthening in Al-doped RHEA based on the details provided in **Section 4.3.2.**

Table 7. 1 The basic physical properties of compositional constituents in Al-doped RHEA and their atomic fraction [69,197,321]**.**

Element	Ti	Hf	Nb	V	Al
Melting point (K)	1941	2506	2750	2183	933.5
R (pm)	140	155	145	135	136
G (GPa)	44	30	38	47	26
Yield strength/ MPa	225	230	114	228	40
Atomic fraction	0.409	0.240	0.158	0.138	0.055

The basic physical properties of the alloying constituents are listed in **Table 7. 1**, revealing significant differences in melting points, atomic radius, and shear moduli between Al and the other constituents. Following the rule of mixture [259], the Al-doped RHEA has a shear modulus of approximately 44 GPa in this study. To obtain the lattice distortion (δr_i) and the modulus mismatch (δG_i) value expressed by Labusch's model [202], we calculated the atomic radius difference (δr_{ij}) and shear modulus (δG_{ij}), as listed in **Table 7. 2**. Subsequently, we derived the specific values of lattice distortion (δr_i) and modulus mismatch ((δG_i), as presented in **Table 7. 3**. Finally, based on Eq. 4.13, the calculated solid solution stress is 998 MPa, higher than that in the fabricated T42 alloy. Although the introduction of pure Al, which has the lowest yield strength of 40 MPa [69] among all constituents, results in a relatively lower mixed intrinsic yield strength of pure metals, a higher solid solution strengthening stress would be produced to maintain its higher yield strength under elevated temperatures.

Table 7. 2 The calculation results of atomic radius and shear moduli differences between each constituents in Al-doped RHEA.

Element i/j $\delta r_{ij}/\delta G_{ij}$	Ti	Hf	Nb	V	Al
Ti	0	0.3780	0.1463	-0.0659	0.5143
Hf	0.1017	0	-0.2353	-0.4410	0.1429
Nb	0.0351	-0.0667	0	-0.2118	0.375
V	-0.0364	-0.1379	-0.0714	0	0.5753
Al	-0.0290	-0.0972	-0.0641	0.0074	0

Table 7. 3 The calculated results of lattice distortion and modulus mismatch of each constituent.

Element	Ti	Hf	Nb	V	Al

δr_i	-0.0263	0.0861	0.0132	-0.0671	-0.0498
δG_i	0.1497	-0.2754	-0.0135	0.2226	-0.4312

As previously discussed, lattice distortion plays a crucial role in the high-temperature performance of RHEA [48,256]. The introduction of Al, with a small atomic radius and shear modulus, into the RHEA matrix significantly intensifies the radius and modulus mismatch, resulting in a large local strain of 3.93%, as detected by PDF (**Fig. 7. 4**), which is higher than that in the fabricated T42 alloy (**Fig. 5. 1**). In general, designing a large lattice mismatch, such as introducing Hf or Zr elements with a larger atomic radius, has been proven to be an effective approach to increasing local lattice distortion [183]. This large lattice distortion, which is maintained or even intensified with increased temperatures [48], contributes to superior high-temperature strength under elevated temperatures. Another factor that can affect high-temperature strength is high-temperature elastic constants [48]. However, the elastic moduli of Al show a dramatic decrease trend as temperature increases [322]. The role of the mixture works effectively under elevated temperatures, as proven by first-principles calculations in the T42 alloy (details in **Section 5.2.5**). The elastic moduli of the fabricated Al-doped RHEA would change dramatically under elevated temperatures, especially at temperatures higher than the melting point of Al. Once the severe decrease in the elastic moduli occurs under high temperatures, the initial yield strength would also decrease. Although the lattice strain increases linearly as a function of temperature due to thermal displacements [17], the severe hot softening under high temperatures attributed to the decrease in elastic moduli [257,258] would overcome the strengthening effect of increased local lattice strain, leading to the decrease in yield strength from 707 MPa (873 K) to 383 MPa (973 K). As the temperature further increases to 1073 K, the hot softening would prevail during the hot tensile tests, resulting in a yield strength of 123.4 MPa at this temperature.

The oxidation resistance also affects the deformation of the as-fabricated RHEA. In the T42 alloy, the formation of various oxidized products significantly deteriorates the mechanical properties of the LENS-fabricated RHEA (details seen in **Section 5.3.3**), leading to the absence of valid tensile properties when the temperature is higher than 873 K. When Al is doped into the RHEA matrix, the increased local lattice strain accounts for its strength under high temperatures, while the improved oxidation resistance by introducing Al into the RHEA matrix is responsible for the improved ductility during the high-temperature deformation process. Consequently, we calculated the theoretical Gibbs formation energy ($\triangle G$) of different oxidation products, and the calculation details are provided as follows. The relationship between Gibbs free energy (G), enthalpy (H), temperature (T), and entropy (S) is expressed in the following equation [42]:

$$G = H - TS \tag{7. 1}$$

In general, the change of G (ΔG) is used as the criterion for predicting the spontaneity of a reaction. When the temperature and pressure are kept constant, the standard free energy of formation values (ΔG) is expressed as follows,

$$\Delta G = \Delta H - T\Delta S \quad (7.\ 2)$$

where ΔH is the standard enthalpy change, calculated as:

$$\Delta H = \sum n\Delta G_f(products) - \sum m\Delta G_f(reactants) \quad (7.\ 3)$$

In addition, ΔG and ΔS have a similar relationship as described above. Based on the standard values given in Ref. [323], the most spontaneous reactions are listed in **Table 7. 4**, showing that the oxidation reactions of Al and Hf would be more easily triggered than that of Ti, as Hf and Al have more negative ΔG than Ti. As a result, the presence of Al_2O_3 is detected by XRD, as shown in **Fig. 7. 7**, and various oxidation products form as the temperature is further increased.

Table 7. 4 The oxidation reactions with the corresponding calculated thermodynamic parameters [323]**.**

Reactions	ΔH(kJ/mol)	ΔS(kJ/mol K)	$\Delta G = \Delta H - T\Delta S$ (kJ/mol)
$4/3Al(s)+O_2(g)=2/3Al_2O_3$	-1117.1	-0.209	$\Delta G = -1117.1 + 0.209T$
$Hf(s)+ O_2(g)= HfO_2$	-1144.7	-0.190	$\Delta G = -1144.7 + 0.190T$
$Ti(s)+ O_2(g)= TiO_2$	-944.0	-0.185	$\Delta G = -944.0 + 0.185T$

A compact oxidation film is considered as a functional protection for the matrix, which can help improve the mechanical performance of the sample under elevated temperatures [324]. In the T42 alloy, superior oxidation resistance under 873 K was achieved by controlling the formation sequences of oxidation products, leading to the formation of an ultra-fine and solid oxidation film. When Al was introduced into the

T42 matrix, the Al_2O_3 oxidize film was prone to form initially under elevated temperatures based on the thermal-dynamic criteria, which is a well-recognized compact oxidation film to protect the matrix from over-oxidation [325]. At temperatures higher than 873 K, the permeation of oxygen into the matrix would lead to cleavage fracture [267], forming river patterns on the fracture surface (**Fig. 7. 8**). With further increases in temperature beyond 873 K, the cleavage fracture constantly produces, increasing the contact area with oxygen. As a result, severe oxidized surfaces were observed on those fracture surfaces tensioned at temperatures higher than 873 K.

7.4 Conclusion

In summary, we utilized an in-situ microalloying approach in the LENS process to fabricate the Al-doped RHEA with improved tensile properties under elevated temperatures compared to the T42 pioneer alloy. The relationship between the microstructure of the fabricated Al-doped alloy and high-temperature tensile properties was discussed, and the detailed conclusions are provided below.

1) The in-situ alloying method for fabricating the Al-doped alloy can be directly achieved by the LENS method. The fabricated Al-doped alloy with a single BCC matrix has a smaller grain size compared to the T42 alloy. Although an evenly distributed alloying element was observed, their elemental distribution at the atomic level shows the presence of local chemical fluctuations due to a more negative mixing enthalpy between Al and other alloying elements.

2) The introduction of Al to the BCC matrix can significantly increase the local lattice strain to 3.93%, higher than that in the T42 alloy. The large atomic radius and shear moduli mismatches between Al and other alloying constituents would account for the large local lattice strain in the fabricated Al-doped alloy. As a result, the LENS-fabricated Al-doped alloy exhibits superior strength under 873 K. However, due to the sharply decreased elastic moduli of the fabricated alloy at higher temperatures, the heat softening effect would overcome the strengthening effect caused by large lattice distortion, leading to a decrease in yield strength at higher temperatures.
3) Al is prone to be initially oxidized under high temperatures to form compact oxidation films, which can protect the base metal. The presence of a compact oxidation film can significantly improve the tensile properties of the Al-doped alloy under high temperatures compared to T42 alloys. Ultimately, the fabricated Al-doped RHEA demonstrates an improvement in strength and ductility under elevated temperatures compared to the T42 alloy.

Chapter 8 Overall conclusions

In this project, we additively manufactured a series of RHEAs through the LENS approach, which exhibited satisfactory properties across a large temperature range. The following conclusions were drawn from this project.

1) We fabricated a T42 RHEA with enhanced mechanical properties using a LAM process involving a remelting procedure which was compared to those fabricated by other procedures. The LENS-fabricated T42 RHEA shows a giga-pascal yield strength and a fracture strain of over 22%, which is hard to achieve through the casting approach. The LENS process creates a complex thermal-stress environment and ultra-fast cooling rate, promoting bcc matrix decomposition and coherent interface formation, enhancing the ductility of LENS-fabricated T42 alloy. The increase in the yield strength of those alloys fabricated through LENS compared to other approaches is attributed to interstitial atom strengthening, rather than the formation of commonly found dislocation networks in fcc-based alloys fabricated through the AM process.
2) We investigated the high-temperature properties of the LENS-fabricated RHEA, focusing on its microstructure, high-temperature tensile properties, lattice distortion, and high-temperature elastic constants. The LENS-fabricated T42 alloy exhibited a large local lattice strain of 3.68%, contributing to its excellent yield strength at room temperature. As the temperature increases, the fabricated T42 alloy demonstrates stable yield strength ranging from 680 to

635 MPa in the elevated temperature range, with low sensitivity to temperature, enabling it to overcome heat softening. A combined effect of large lattice distortion and low temperature-sensitivity of the elastic moduli in the designed alloy dominates the strengthening under elevated temperatures. However, increasing the working temperature to 800 °C results in severe oxidation without the formation of a solid oxidation layer, leading to the complete fracture of the fabricated T42 alloy.

3) We examined the microstructure, tribological properties, and oxidation behavior of the LENS-fabricated T42 alloy at various temperatures. The wear resistance of the RHEA significantly improved as the temperature was increased to 600 °C, achieved by strategically controlling the oxidation sequence of the alloying elements to pre-form TiO_2 and HfO_2 layers, resulting in an ultra-thin nanocrystalline coating and a significantly reduced wear rate, which was decreased from 2.69×10^{-4} $mm^3/(N\cdot m)$ at room temperature to 6.90×10^{-7} $mm^3/(N\cdot m)$ at 600 °C. The pre-formation of TiO_2 and HfO_2 would promotes the formation of the compact film, while a variety of oxidation products were generated, at higher temperatures (800 °C), leading to the formation of a brittle oxidation film with a loose structure, adversely affecting wear resistance, despite a lower coefficient of friction.

4) We demonstrated that the in-situ microalloying approach in the LENS process can aid in fabricating an Al-doped RHEA with improved tensile properties at high temperatures compared to the T42 pioneer alloy. The relationship

between the microstructure of the Al-doped alloy and high-temperature tensile properties was also investigated. The in-situ alloying method for creating the Al-doped alloy can be achieved directly by the LENS method, resulting in a smaller grain size and the formation of local chemical fluctuations. The introduction of Al to the BCC matrix significantly increases the local lattice strain, resulting in superior strength at 600 °C, nearly 50 MPa higher than the T42 alloy. Although the heat-softening effect at higher temperatures leads to a decrease in yield strength, the tensile ductility, higher than 30%, was obtained in the Al-doped RHEA at a temperature of 800 °C. Al is prone to be initially oxidized under high temperatures to form compact oxidation films, which significantly improve the tensile properties of the Al-doped alloy under high temperatures compared to T42 alloys, ultimately demonstrating an all-round improvement in strength and ductility under elevated temperatures compared to the T42 alloy.

Chapter 9 Suggested future work

9.1 Tailoring microstructure to enhance mechanical properties in AM-fabricated RHEAs

In this project, although we have achieved excellent results in breaking the long-stand strength-ductility trade-off in metallic materials, more effort should be spent to achieve a better tensile strength-ductility synergy, like introducing heterogeneous structures, including but not limited to the nanoscale and micro-scale interface. For the nano-scale heterogeneous structures, SRO or spinodal structure design can be applied to further improve the mechanical properties of AMed RHEAs. Additionally, introducing micro-scale interfaces, like the coherent B2 phase in the bcc-type RHEA, is promising for excellent strength-ductility synergy in AMed RHEAs.

9.2 Enhancing tensile properties of AM-fabricated RHEAs from room to ultra-high temperatures

Although we successfully improved the mechanical properties of the LENS-fabricated RHEA via the in-situ alloying method, how to maintain the excellent mechanical properties over a large temperature range of the AM-fabricated RHEAs still requires further attempts. More RHEA systems with excellent mechanical properties would be explored, which can be used in the AM field for further high-temperature applications.

References

[1] A. Ostovari Moghaddam, N.A. Shaburova, M.N. Samodurova, A. Abdollahzadeh, E.A. Trofimov, Additive manufacturing of high entropy alloys: A practical review, J. Mater. Sci. Technol. 77 (2021) 131–162. https://doi.org/10.1016/j.jmst.2020.11.029.

[2] J. Yeh, S. Chen, S. Lin, J. Gan, T. Chin, T. Shun, C. Tsau, Nanostructured High-Entropy Alloys with Multiple Principal Elements : Novel Alloy Design Concepts and Outcomes, Adv. Eng. Mater. 6 (2004) 299–303. https://doi.org/10.1002/adem.200300567.

[3] B. Cantor, I.T.H. Chang, P. Knight, A.J.B. Vincent, Microstructural development in equiatomic multicomponent alloys, Mater. Sci. Eng. A. 375–377 (2004) 213–218. https://doi.org/10.1016/j.msea.2003.10.257.

[4] M.H. Tsai, Physical properties of high entropy alloys, Entropy. 15 (2013) 5338–5345. https://doi.org/10.3390/e15125338.

[5] S. Guo, Phase selection rules for cast high entropy alloys: An overview, Mater. Sci. Technol. (United Kingdom). 31 (2015) 1223–1230. https://doi.org/10.1179/1743284715Y.0000000018.

[6] O.N. Senkov, G.B. Wilks, D.B. Miracle, C.P. Chuang, P.K. Liaw, Refractory high-entropy alloys, Intermetallics. 18 (2010) 1758–1765. https://doi.org/10.1016/j.intermet.2010.05.014.

[7] Z. Li, K.G. Pradeep, Y. Deng, D. Raabe, C.C. Tasan, Metastable high-entropy dual-phase alloys overcome the strength-ductility trade-off, Nature. 534 (2016) 227–230. https://doi.org/10.1038/nature17981.

[8] H. Li, X. Li, C. Jin, Q. Li, Q. Ma, K. Hua, H. Wang, W. Liu, Mechanical and tribological performance of AlCr0.5NbTaxTi4–x (x = 0, 0.5, 1) refractory

high-entropy alloys, J. Mater. Sci. Technol. 156 (2023) 241–253. https://doi.org/10.1016/j.jmst.2023.02.016.

[9] B. Gorr, F. Mueller, H.-J. Christ, T. Mueller, H. Chen, A. Kauffmann, M. Heilmaier, High temperature oxidation behavior of an equimolar refractory metal-based alloy 20Nbsingle bond20Mosingle bond20Crsingle bond20Tisingle bond20Al with and without Si addition, J. Alloys Compd. 688 (2016) nationalll.

[10] Y.D. Wu, Y.H. Cai, T. Wang, J.J. Si, J. Zhu, Y.D. Wang, X.D. Hui, A refractory Hf25Nb25Ti25Zr25 high-entropy alloy with excellent structural stability and tensile properties, Mater. Lett. 130 (2014) 277–280. https://doi.org/10.1016/j.matlet.2014.05.134.

[11] Y.F. Ye, Q. Wang, J. Lu, C.T. Liu, Y. Yang, High-entropy alloy: challenges and prospects, Mater. Today. 19 (2016) 349–362. https://doi.org/10.1016/j.mattod.2015.11.026.

[12] N. Eißmann, B. Klöden, T. Weißgärber, B. Kieback, High-entropy alloy CoCrFeMnNi produced by powder metallurgy, Powder Metall. 60 (2017) 184–197. https://doi.org/10.1080/00325899.2017.1318480.

[13] Y. Zhang, T. Bian, X. Shen, Z. Wang, S. Ye, S. Feng, K. Yu, C. Ding, P. Yu, Sintering mechanism and microstructure evolution of a CoCrFeNiMn high entropy alloy fabricated by metal injection molding, J. Alloys Compd. (2021) 158711.

[14] Q. Li, H. Zhang, D. Li, Z. Chen, F. Wang, M. Wu, Comparative study of the microstructures and mechanical properties of laser metal deposited and vacuum arc melted refractory NbMoTa medium-entropy alloy, Int. J. Refract. Met. Hard Mater. 88 (2020) 105195. https://doi.org/10.1016/j.ijrmhm.2020.105195.

[15] T. Yang, S. Mazumder, Y. Jin, B. Squires, M. Sofield, M. V. Pantawane, N.B. Dahotre, A. Neogi, A review of diagnostics methodologies for metal additive manufacturing processes and products, Materials (Basel). 14 (2021) 1–50. https://doi.org/10.3390/ma14174929.

[16] L. Zhang, X. Li, X. Qu, M. Qin, Z. Que, Z. Wei, C. Guo, X. Lu, Y. Dong, Powder Metallurgy Route to Ultrafine-Grained Refractory Metals, Adv. Mater. 35 (2023) 1–25. https://doi.org/10.1002/adma.202205807.

[17] Y. Lu, X. Gao, L. Jiang, Z. Chen, T. Wang, J. Jie, H. Kang, Y. Zhang, S. Guo, H. Ruan, Y. Zhao, Z. Cao, T. Li, Directly cast bulk eutectic and near-eutectic high entropy alloys with balanced strength and ductility in a wide temperature range, Acta Mater. 124 (2017) 143–150. https://doi.org/10.1016/j.actamat.2016.11.016.

[18] B. Berman, 3-D printing: The new industrial revolution, Bus. Horiz. 55 (2012) 155–162. https://doi.org/10.1016/j.bushor.2011.11.003.

[19] S. Hasanov, S. Alkunte, M. Rajeshirke, A. Gupta, O. Huseynov, I. Fidan, F. Alifui-Segbaya, A. Rennie, Review on additive manufacturing of multi-material parts: Progress and challenges, J. Manuf. Mater. Process. 6 (2022). https://doi.org/10.3390/jmmp6010004.

[20] C. Han, Q. Fang, Y. Shi, S.B. Tor, C.K. Chua, K. Zhou, Recent Advances on High-Entropy Alloys for 3D Printing, Adv. Mater. 32 (2020) 1–41. https://doi.org/10.1002/adma.201903855.

[21] H. Dobbelstein, E.L. Gurevich, E.P. George, A. Ostendorf, G. Laplanche, Laser metal deposition of compositionally graded TiZrNbTa refractory high-entropy alloys using elemental powder blends, Addit. Manuf. 25 (2019) 252–262. https://doi.org/10.1016/j.addma.2018.10.042.

[22] M.A. Melia, S.R. Whetten, R. Puckett, M. Jones, M.J. Heiden, N. Argibay, A.B. Kustas, High-throughput additive manufacturing and characterization of refractory high entropy alloys, Appl. Mater. Today. 19 (2020) 100560. https://doi.org/10.1016/j.apmt.2020.100560.

[23] M. Moorehead, K. Bertsch, M. Niezgoda, C. Parkin, M. Elbakhshwan, K. Sridharan, C. Zhang, D. Thoma, A. Couet, High-throughput synthesis of Mo-Nb-Ta-W high-entropy alloys via additive manufacturing, Mater. Des. 187 (2020) 108358. https://doi.org/10.1016/j.matdes.2019.108358.

[24] H. Dobbelstein, E.P. George, E.L. Gurevich, A. Kostka, A. Ostendorf, G. Laplanche, Laser metal deposition of refractory high-entropy alloys for high-throughput synthesis and structure-property characterization, Int. J. Extrem. Manuf. 3 (2020). https://doi.org/10.1088/2631-7990/abcca8.

[25] S. Gou, M. Gao, Y. Shi, S. Li, Y. Fang, X. Chen, H. Chen, W. Yin, J. Liu, Z. Lei, H. Wang, Additive manufacturing of ductile refractory high-entropy alloys via phase engineering, Acta Mater. 248 (2023) 118781. https://doi.org/10.1016/j.actamat.2023.118781.

[26] H. Dobbelstein, M. Thiele, E.L. Gurevich, E.P. George, A. Ostendorf, Direct metal deposition of refractory high entropy alloy MoNbTaW, Phys. Procedia. 83 (2016) 624–633. https://doi.org/10.1016/j.phpro.2016.08.065.

[27] P. Gu, T. Qi, L. Chen, T. Ge, X. Ren, Manufacturing and analysis of VNbMoTaW refractory high-entropy alloy fabricated by selective laser melting, Int. J. Refract. Met. Hard Mater. 105 (2022) 105834. https://doi.org/10.1016/j.ijrmhm.2022.105834.

[28] Y. Zhang, H. Wang, Y. Zhu, S. Zhang, F. Cheng, J. Yang, B. Su, C. Yang, High specific yield strength and superior ductility of a lightweight refractory high-entropy alloy prepared by laser additive manufacturing, Addit. Manuf. 77 (2023) 103813. https://doi.org/10.1016/j.addma.2023.103813.

[29] D. Cui, B. Guo, Z. Yang, X. Liu, Z. Wang, J. Li, J. Wang, F. He, Unraveling microstructure and mechanical response of an additively manufactured refractory TiVHfNbMo high-entropy alloy, Addit. Manuf. 84 (2024) 104126. https://doi.org/10.1016/j.addma.2024.104126.

[30] M.C. Gao, J.-W. Yeh, P.K. Liaw, Y. Zhang, others, High-entropy alloys, Cham Springer Int. Publ. (2016).

[31] B. Gorr, M. Azim, H.J. Christ, T. Mueller, D. Schliephake, M. Heilmaier, Phase equilibria, microstructure, and high temperature oxidation resistance of novel refractory high-entropy alloys, J. Alloys Compd. 624 (2015) 270–278. https://doi.org/10.1016/j.jallcom.2014.11.012.

[32] Z. Lei, X. Liu, Y. Wu, H. Wang, S. Jiang, S. Wang, X. Hui, Y. Wu, B. Gault, P. Kontis, D. Raabe, L. Gu, Q. Zhang, H. Chen, H. Wang, J. Liu, K. An, Q. Zeng, T.G. Nieh, Z. Lu, Enhanced strength and ductility in a high-entropy alloy via ordered oxygen complexes, Nature. 563 (2018) 546–550. https://doi.org/10.1038/s41586-018-0685-y.

[33] K. V. Yusenko, S. Riva, P.A. Carvalho, M. V. Yusenko, S. Arnaboldi, A.S. Sukhikh, M. Hanfland, S.A. Gromilov, First hexagonal close packed high-entropy alloy with outstanding stability under extreme conditions and electrocatalytic activity for methanol oxidation, Scr. Mater. 138 (2017) 22–27. https://doi.org/10.1016/j.scriptamat.2017.05.022.

[34] J. Yi, L. Yang, L. Wang, M. Xu, Novel, equimolar, multiphase CoCuNiTiV high-entropy alloy: phase component, microstructure, and compressive properties, Met. Mater. Int. 27 (2021) 2387–2394.

[35] P. Martin, C.E. Madrid-Cortes, C. Cáceres, N. Araya, C. Aguilar, J.M. Cabrera, HEAPS: A user-friendly tool for the design and exploration of high-entropy alloys based on semi-empirical parameters, Comput. Phys. Commun. 278 (2022) 108398.

[36] U. Mizutani, The Hume-Rothery rules for structurally complex alloy phases, in: Surf. Prop. Eng. Complex Intermet., World Scientific, 2010: pp. 323–399.

[37] X. Yang, Y. Zhang, Prediction of high-entropy stabilized solid-solution in multi-component alloys, Mater. Chem. Phys. 132 (2012) 233–238. https://doi.org/10.1016/j.matchemphys.2011.11.021.

[38] D. Ma, M. Yao, K.G. Pradeep, C.C. Tasan, H. Springer, D. Raabe, Phase stability of non-equiatomic CoCrFeMnNi high entropy alloys, Acta Mater. 98 (2015) 288–296. https://doi.org/10.1016/j.actamat.2015.07.030.

[39] W. Zhang, P.K. Liaw, Y. Zhang, Science and technology in high-entropy alloys, Sci. China Mater. 61 (2018) 2–22.

[40] J.W. Yeh, Recent progress in high-entropy alloys, Ann. Chim. Sci. Des Mater. 31 (2006) 633–648. https://doi.org/10.3166/acsm.31.633-648.

[41] D.B. Miracle, O.N. Senkov, A critical review of high entropy alloys and related concepts, Acta Mater. 122 (2017) 448–511. https://doi.org/10.1016/j.actamat.2016.08.081.

[42] E.P. George, D. Raabe, R.O. Ritchie, High-entropy alloys, Nat. Rev. Mater. 4 (2019) 515–534. https://doi.org/10.1038/s41578-019-0121-4.

[43] Y. Zhang, Y.J. Zhou, J.P. Lin, G.L. Chen, P.K. Liaw, Solid-solution phase formation rules for multi-component alloys, Adv. Eng. Mater. 10 (2008) 534–538. https://doi.org/10.1002/adem.200700240.

[44] H. Wang, Q. He, X. Gao, Y. Shang, W. Zhu, W. Zhao, Z. Chen, H. Gong, Y. Yang, Multifunctional High Entropy Alloys Enabled by Severe Lattice Distortion, Adv. Mater. 2305453 (2023) 1–20. https://doi.org/10.1002/adma.202305453.

[45] S. Ranganathan, Alloyed pleasures : Multimetallic cocktails, Curr. Sci. 85 (2003) 10–12.

[46] D.X. Qiao, H. Jiang, W.N. Jiao, Y.P. Lu, Z.Q. Cao, T.J. Li, A Novel Series of Refractory High-Entropy Alloys Ti2ZrHf0.5VNbx with High Specific Yield Strength and Good Ductility, Acta Metall. Sin. (English Lett. 32 (2019) 925–931. https://doi.org/10.1007/s40195-019-00921-3.

[47] X.-J. Hua, P. Hu, H.-R. Xing, J.-Y. Han, S.-W. Ge, S.-L. Li, C.-J. He, K.-S. Wang, C.-J. Cui, Development and property tuning of refractory high-entropy alloys: a review, Acta Metall. Sin. (English Lett. 35 (2022) 1231–1265.

[48] R. Feng, B. Feng, M.C. Gao, C. Zhang, J.C. Neuefeind, J.D. Poplawsky, Y. Ren, K. An, M. Widom, P.K. Liaw, Superior High-Temperature Strength in a Supersaturated Refractory High-Entropy Alloy, Adv. Mater. 33 (2021). https://doi.org/10.1002/adma.202102401.

[49] S. O.N, W. G.B, S. J.M, M. D.B, Mechanical properties of Nb25Mo25Ta25W25 and V20Nb20Mo20Ta20W20 refractory high entropy alloys, Intermetallics. 19 (2011) 698–706.

[50] Z. Wang, H. Wu, Y. Wu, H. Huang, X. Zhu, Y. Zhang, H. Zhu, X. Yuan, Q. Chen, S. Wang, X. Liu, H. Wang, S. Jiang, M.J. Kim, Z. Lu, Solving oxygen embrittlement of refractory high-entropy alloy via grain boundary engineering, Mater. Today. xxx (2022) 1–7. https://doi.org/10.1016/j.mattod.2022.02.006.

[51] O.N. Senkov, J.M. Scott, S. V. Senkova, D.B. Miracle, C.F. Woodward, Microstructure and room temperature properties of a high-entropy TaNbHfZrTi alloy, J. Alloys Compd. 509 (2011) 6043–6048. https://doi.org/10.1016/j.jallcom.2011.02.171.

[52] H.L. Chen, H. Mao, Q. Chen, Database development and Calphad calculations for high entropy alloys: Challenges, strategies, and tips, Mater. Chem. Phys. 210 (2018) 279–290. https://doi.org/10.1016/j.matchemphys.2017.07.082.

[53] H. Naser-Zoshki, A.R. Kiani-Rashid, J. Vahdati-Khaki, Design of a low density refractory high entropy alloy in non-equiatomic W–Mo–Cr–Ti–Al system, Vacuum. 181 (2020) 109614. https://doi.org/10.1016/j.vacuum.2020.109614.

[54] F.G. Coury, M. Kaufman, A.J. Clarke, Solid-solution strengthening in refractory high entropy alloys, Acta Mater. 175 (2019) 66–81.

[55] Q. Liu, G. Wang, X. Sui, Y. Liu, X. Li, J. Yang, Microstructure and mechanical properties of ultra-fine grained MoNbTaTiV refractory high-entropy alloy fabricated by spark plasma sintering, J. Mater. Sci. Technol. 35 (2019) 2600–2607. https://doi.org/10.1016/j.jmst.2019.07.013.

[56] S. Das, P.S. Robi, A novel refractory WMoVCrTa high-entropy alloy possessing fine combination of compressive stress-strain and high hardness properties, Adv. Powder Technol. 31 (2020) 4619–4631. https://doi.org/10.1016/j.apt.2020.10.008.

[57] Z. An, A. Li, S. Mao, T. Yang, L. Zhu, R. Wang, Z. Wu, B. Zhang, R. Shao, C. Jiang, B. Cao, C. Shi, Y. Ren, C. Liu, H. Long, J. Zhang, W. Li, F. He, L. Sun, J. Zhao, L. Yang, X. Zhou, X. Wei, Y. Chen, Z. Lu, F. Ren, C.T. Liu, Z. Zhang, X. Han, Negative mixing enthalpy solid solutions deliver high strength and ductility, Nature. 625 (2024) 697–702. https://doi.org/10.1038/s41586-023-06894-9.

[58] Q. Liu, G. Wang, Y. Liu, X. Sui, Y. Chen, S. Luo, Hot deformation behaviors of an ultrafine-grained MoNbTaTiV refractory high-entropy alloy fabricated by powder metallurgy, Mater. Sci. Eng. A. 809 (2021) 140922. https://doi.org/10.1016/j.msea.2021.140922.

[59] B. Kang, T. Kong, A. Raza, H.J. Ryu, S.H. Hong, Fabrication, microstructure and mechanical property of a novel Nb-rich refractory high-entropy alloy

strengthened by in-situ formation of dispersoids, Int. J. Refract. Met. Hard Mater. 81 (2019) 15–20. https://doi.org/10.1016/j.ijrmhm.2019.02.009.

[60] C. Yang, K. Aoyagi, H. Bian, A. Chiba, Microstructure evolution and mechanical property of a precipitation-strengthened refractory high-entropy alloy HfNbTaTiZr, Mater. Lett. 254 (2019) 46–49. https://doi.org/10.1016/j.matlet.2019.07.027.

[61] B. Kang, T. Kong, H.J. Ryu, S.H. Hong, Superior mechanical properties and strengthening mechanisms of lightweight AlxCrNbVMo refractory high-entropy alloys (x = 0, 0.5, 1.0) fabricated by the powder metallurgy process, J. Mater. Sci. Technol. 69 (2021) 32–41. https://doi.org/10.1016/j.jmst.2020.07.012.

[62] S.K. Bachani, C.J. Wang, B.S. Lou, L.C. Chang, J.W. Lee, Microstructural characterization, mechanical property and corrosion behavior of VNbMoTaWAl refractory high entropy alloy coatings: Effect of Al content, Surf. Coatings Technol. 403 (2020) 126351. https://doi.org/10.1016/j.surfcoat.2020.126351.

[63] C.C. Juan, M.H. Tsai, C.W. Tsai, C.M. Lin, W.R. Wang, C.C. Yang, S.K. Chen, S.J. Lin, J.W. Yeh, Enhanced mechanical properties of HfMoTaTiZr and HfMoNbTaTiZr refractory high-entropy alloys, Intermetallics. 62 (2015) 76–83. https://doi.org/10.1016/j.intermet.2015.03.013.

[64] X.J. Gao, L. Wang, N.N. Guo, L.S. Luo, G.M. Zhu, C.C. Shi, Y.Q. Su, J.J. Guo, Microstructure characteristics and mechanical properties of Hf0.5Mo0.5NbTiZr refractory high entropy alloy with Cr addition, Int. J. Refract. Met. Hard Mater. 95 (2021) 1–7. https://doi.org/10.1016/j.ijrmhm.2020.105405.

[65] U. Bhandari, C. Zhang, C. Zeng, S. Guo, S. Yang, Computational and experimental investigation of refractory high entropy alloy

mo15nb20re15ta30w20, J. Mater. Res. Technol. 9 (2020) 8929–8936. https://doi.org/10.1016/j.jmrt.2020.06.036.

[66] C. Zhu, Z. Li, C. Hong, P. Dai, J. Chen, Microstructure and mechanical properties of the TiZrNbMoTa refractory high-entropy alloy produced by mechanical alloying and spark plasma sintering, Int. J. Refract. Met. Hard Mater. 93 (2020) 105357. https://doi.org/10.1016/j.ijrmhm.2020.105357.

[67] S. Ge, H. Fu, L. Zhang, H. Mao, H. Li, A. Wang, W. Li, H. Zhang, Effects of Al addition on the microstructures and properties of MoNbTaTiV refractory high entropy alloy, Mater. Sci. Eng. A. 784 (2020) 139275. https://doi.org/10.1016/j.msea.2020.139275.

[68] H. Zhang, Y. Zhao, J. Cai, S. Ji, J. Geng, X. Sun, D. Li, High-strength NbMoTaX refractory high-entropy alloy with low stacking fault energy eutectic phase via laser additive manufacturing, Mater. Des. 201 (2021) 109462. https://doi.org/10.1016/j.matdes.2021.109462.

[69] L. Wang, J. Ding, S. Chen, K. Jin, Q. Zhang, J. Cui, B. Wang, B. Chen, T. Li, Y. Ren, S. Zheng, K. Ming, W. Lu, J. Hou, G. Sha, J. Liang, L. Wang, Y. Xue, E. Ma, Tailoring planar slip to achieve pure metal-like ductility in body-centred-cubic multi-principal element alloys, Nat. Mater. 22 (2023). https://doi.org/10.1038/s41563-023-01517-0.

[70] D. Cui, Y. Zhang, L. Liu, Y. Li, L. Wang, Z. Wang, J. Li, J. Wang, F. He, Oxygen-assisted spinodal structure achieves 1.5 GPa yield strength in a ductile refractory high-entropy alloy, J. Mater. Sci. Technol. 157 (2023) 11–20. https://doi.org/10.1016/j.jmst.2023.01.038.

[71] Z. Lei, Y. Wu, J. He, X. Liu, H. Wang, S. Jiang, L. Gu, Q. Zhang, B. Gault, D. Raabe, Z. Lu, Snoek-type damping performance in strong and ductile high-entropy alloys, Sci. Adv. 6 (2020) 1–9. https://doi.org/10.1126/sciadv.aba7802.

[72] C. Liu, J. Cui, Z. Cheng, B. Zhang, S. Zhang, J. Ding, R. Yu, E. Ma, Direct Observation of Oxygen Atoms Taking Tetrahedral Interstitial Sites in Medium-Entropy Body-Centered-Cubic Solutions, Adv. Mater. 35 (2023) 2209941.

[73] C. Liu, W. Lu, W. Xia, C. Du, Z. Rao, J.P. Best, S. Brinckmann, J. Lu, B. Gault, G. Dehm, G. Wu, Z. Li, D. Raabe, Massive interstitial solid solution alloys achieve near-theoretical strength, Nat. Commun. 13 (2022) 1–9. https://doi.org/10.1038/s41467-022-28706-w.

[74] R. Wang, Y. Tang, Z. Lei, Y. Ai, Z. Tong, S. Li, Y. Ye, S. Bai, Achieving high strength and ductility in nitrogen-doped refractory high-entropy alloys, Mater. Des. 213 (2022) 110356. https://doi.org/10.1016/j.matdes.2021.110356.

[75] X. Gao, L. Wang, N. Guo, L. Luo, G. Zhu, C. Shi, Y. Su, J. Guo, In-situ development of MB2 and their effect on microstructure and mechanical properties of refractory Hf0.5Mo0.5NbTiZr high entropy alloy matrix composites, Int. J. Refract. Met. Hard Mater. 96 (2021) 105473. https://doi.org/10.1016/j.ijrmhm.2021.105473.

[76] J. Pang, H. Zhang, L. Zhang, Z. Zhu, H. Fu, H. Li, A. Wang, Z. Li, H. Zhang, Simultaneous enhancement of strength and ductility of body-centered cubic TiZrNb multi-principal element alloys via boron-doping, J. Mater. Sci. Technol. 78 (2021) 74–80. https://doi.org/10.1016/j.jmst.2020.10.043.

[77] Q. XU, D. zhi CHEN, C. rui WANG, W. chao CAO, Q. WANG, H. zhi CUI, S. yan ZHANG, R. run CHEN, Effects of La on microstructure and mechanical properties of NbMoTiVSi0.2 refractory high entropy alloys, Trans. Nonferrous Met. Soc. China (English Ed. 31 (2021) 512–520. https://doi.org/10.1016/S1003-6326(21)65513-9.

[78] F. Müller, B. Gorr, H.J. Christ, H. Chen, A. Kauffmann, M. Heilmaier, Effect of microalloying with silicon on high temperature oxidation resistance of novel

refractory high-entropy alloy Ta-Mo-Cr-Ti-Al, Mater. High Temp. 35 (2018) 168–176. https://doi.org/10.1080/09603409.2017.1389115.

[79] M. Zhu, L. Yao, Y. Liu, M. Zhang, K. Li, Z. Jian, Microstructure evolution and mechanical properties of a novel CrNbTiZrAlx (0.25 ≤ x ≤ 1.25) eutectic refractory high-entropy alloy, Mater. Lett. 272 (2020) 127869. https://doi.org/10.1016/j.matlet.2020.127869.

[80] J. Han, B. Su, A. Zhang, J. Meng, Y. Wu, Forming and characterization of Al0.2MoNbTaTiW/MC refractory high-entropy alloy composite by spark plasma sintering and hot extrusion, Mater. Lett. 284 (2021) 1–4. https://doi.org/10.1016/j.matlet.2020.128979.

[81] M. Wang, Z.L. Ma, Z.Q. Xu, X.W. Cheng, Designing VxNbMoTa refractory high-entropy alloys with improved properties for high-temperature applications, Scr. Mater. 191 (2021) 131–136. https://doi.org/10.1016/j.scriptamat.2020.09.027.

[82] A. Fu, W. Guo, B. Liu, Y. Cao, L. Xu, Q. Fang, H. Yang, Y. Liu, A particle reinforced NbTaTiV refractory high entropy alloy based composite with attractive mechanical properties, J. Alloys Compd. 815 (2020). https://doi.org/10.1016/j.jallcom.2019.152466.

[83] J. Ren, Y. Zhang, D. Zhao, Y. Chen, S. Guan, Y. Liu, L. Liu, S. Peng, F. Kong, J.D. Poplawsky, others, Strong yet ductile nanolamellar high-entropy alloys by additive manufacturing, Nature. 608 (2022) 62–68.

[84] Y. Long, X. Liang, K. Su, H. Peng, X. Li, A fine-grained NbMoTaWVCr refractory high-entropy alloy with ultra-high strength: Microstructural evolution and mechanical properties, J. Alloys Compd. 780 (2019) 607–617. https://doi.org/10.1016/j.jallcom.2018.11.318.

[85] S. Wei, S.J. Kim, J. Kang, Y. Zhang, Y. Zhang, T. Furuhara, E.S. Park, C.C. Tasan, Natural-mixing guided design of refractory high-entropy alloys with as-cast tensile ductility, Nat. Mater. 19 (2020) 1175–1181. https://doi.org/10.1038/s41563-020-0750-4.

[86] N. Yurchenko, E. Panina, A. Tojibaev, R. Eleti, D. Volosevich, O. Klimova-Korsmik, G. Salishchev, S. Zherebtsov, N. Stepanov, Temperature-dependent plastic deformation of a refractory Al7. 5 (NbTiZr) 92.5 medium-entropy alloy with a bcc+ B2 structure, Materialia. 28 (2023) 101766.

[87] N. Yurchenko, E. Panina, A. Tojibaev, S. Zherebtsov, N. Stepanov, Overcoming the strength-ductility trade-off in refractory medium-entropy alloys via controlled B2 ordering, Mater. Res. Lett. 10 (2022) 813–823.

[88] N. Yurchenko, E. Panina, A. Tojibaev, V. Novikov, G. Salishchev, S. Zherebtsov, N. Stepanov, Tuning the grain and domain sizes to achieve superior room-temperature tensile ductility in a B2-ordered refractory Al15Nb40Ti40V5 medium-entropy alloy, Mater. Sci. Eng. A. 874 (2023) 145073.

[89] O.N. Senkov, J.K. Jensen, A.L. Pilchak, D.B. Miracle, H.L. Fraser, Compositional variation effects on the microstructure and properties of a refractory high-entropy superalloy AlMo0.5NbTa0.5TiZr, Mater. Des. 139 (2018) 498–511. https://doi.org/10.1016/j.matdes.2017.11.033.

[90] S.I. Rao, C. Varvenne, C. Woodward, T.A. Parthasarathy, D. Miracle, O.N. Senkov, W.A. Curtin, Atomistic simulations of dislocations in a model BCC multicomponent concentrated solid solution alloy, Acta Mater. 125 (2017) 311–320. https://doi.org/10.1016/j.actamat.2016.12.011.

[91] N. Yurchenko, E. Panina, M. Tikhonovsky, G. Salishchev, S. Zherebtsov, N. Stepanov, Structure and mechanical properties of an in situ refractory

Al20Cr10Nb15Ti20V25Zr10 high entropy alloy composite, Mater. Lett. 264 (2020) 127372. https://doi.org/10.1016/j.matlet.2020.127372.

[92] Y. Chen, Y. Li, X. Cheng, Z. Xu, C. Wu, B. Cheng, M. Wang, Interstitial strengthening of refractory ZrTiHfNb0.5Ta0.5Ox (x = 0.05, 0.1, 0.2) high-entropy alloys, Mater. Lett. 228 (2018) 145–147. https://doi.org/10.1016/j.matlet.2018.05.123.

[93] T. Grosdidier, A. Hazotte, A. Simon, Precipitation and dissolution processes in $γ$/$γ$′ single crystal nickel-based superalloys, Mater. Sci. Eng. A. 256 (1998) 183–196.

[94] O.N. Senkov, D.B. Miracle, K.J. Chaput, J.P. Couzinie, Development and exploration of refractory high entropy alloys - A review, J. Mater. Res. 33 (2018) 3092–3128. https://doi.org/10.1557/jmr.2018.153.

[95] O.N. Senkov, G.B. Wilks, D.B. Miracle, C.P. Chuang, P.K. Liaw, Refractory high-entropy alloys, Intermetallics. 18 (2010) 1758–1765.

[96] Z.D. Han, H.W. Luan, X. Liu, N. Chen, X.Y. Li, Y. Shao, K.F. Yao, Microstructures and mechanical properties of TixNbMoTaW refractory high-entropy alloys, Mater. Sci. Eng. A. 712 (2018) 380–385. https://doi.org/10.1016/j.msea.2017.12.004.

[97] M. Wang, Z. Ma, Z. Xu, X. Cheng, Microstructures and mechanical properties of HfNbTaTiZrW and HfNbTaTiZrMoW refractory high-entropy alloys, J. Alloys Compd. 803 (2019) 778–785. https://doi.org/10.1016/j.jallcom.2019.06.138.

[98] A. Shafiei, New approach to model the yield strength of body-centered cubic solid solution refractory high-entropy alloys, Tungsten. 2 (2020) 307–320. https://doi.org/10.1007/s42864-020-00052-8.

[99] S. Wang, M. Wu, D. Shu, G. Zhu, D. Wang, B. Sun, Mechanical instability and tensile properties of TiZrHfNbTa high entropy alloy at cryogenic temperatures, Acta Mater. 201 (2020) 517–527. https://doi.org/10.1016/j.actamat.2020.10.044.

[100] H. Huang, Y. Wu, J. He, H. Wang, X. Liu, K. An, W. Wu, Z. Lu, Phase-Transformation Ductilization of Brittle High-Entropy Alloys via Metastability Engineering, Adv. Mater. 29 (2017). https://doi.org/10.1002/adma.201701678.

[101] W. Wang, Z. Zhang, J. Niu, H. Wu, S. Zhai, Y. Wang, Effect of Al addition on structural evolution and mechanical properties of the AlxHfNbTiZr high-entropy alloys, Mater. Today Commun. 16 (2018) 242–249. https://doi.org/10.1016/j.mtcomm.2018.06.004.

[102] Y. Zhu, X. Wu, Perspective on hetero-deformation induced (HDI) hardening and back stress, Mater. Res. Lett. 7 (2019) 393–398. https://doi.org/10.1080/21663831.2019.1616331.

[103] E. Ma, X. Wu, Tailoring heterogeneities in high-entropy alloys to promote strength–ductility synergy, Nat. Commun. 10 (2019) 1–10. https://doi.org/10.1038/s41467-019-13311-1.

[104] Z. An, S. Mao, Y. Liu, L. Wang, H. Zhou, B. Gan, Z. Zhang, X. Han, A novel HfNbTaTiV high-entropy alloy of superior mechanical properties designed on the principle of maximum lattice distortion, J. Mater. Sci. Technol. 79 (2021) 109–117. https://doi.org/10.1016/j.jmst.2020.10.073.

[105] C. Lee, Y. Chou, G. Kim, M.C. Gao, K. An, J. Brechtl, C. Zhang, W. Chen, J.D. Poplawsky, G. Song, Y. Ren, Y.C. Chou, P.K. Liaw, Lattice-Distortion-Enhanced Yield Strength in a Refractory High-Entropy Alloy, Adv. Mater. 32 (2020) 1–9. https://doi.org/10.1002/adma.202004029.

[106] Y. Bu, Y. Wu, Z. Lei, X. Yuan, H. Wu, X. Feng, J. Liu, J. Ding, Y. Lu, H. Wang, others, Local chemical fluctuation mediated ductility in body-centered-cubic high-entropy alloys, Mater. Today. 46 (2021) 28–34.

[107] Q. Ding, Y. Zhang, X. Chen, X. Fu, D. Chen, S. Chen, L. Gu, F. Wei, H. Bei, Y. Gao, M. Wen, J. Li, Z. Zhang, T. Zhu, R.O. Ritchie, Q. Yu, Tuning element distribution, structure and properties by composition in high-entropy alloys, Nature. 574 (2019) 223–227. https://doi.org/10.1038/s41586-019-1617-1.

[108] E. Antillon, C. Woodward, S.I. Rao, B. Akdim, T.A. Parthasarathy, Chemical short range order strengthening in a model FCC high entropy alloy, Acta Mater. 190 (2020) 29–42. https://doi.org/10.1016/j.actamat.2020.02.041.

[109] Q.J. Li, H. Sheng, E. Ma, Strengthening in multi-principal element alloys with local-chemical-order roughened dislocation pathways, Nat. Commun. 10 (2019) 1–11. https://doi.org/10.1038/s41467-019-11464-7.

[110] A. Fantin, G.O. Lepore, A.M. Manzoni, S. Kasatikov, T. Scherb, T. Huthwelker, F. d’Acapito, G. Schumacher, Short-range chemical order and local lattice distortion in a compositionally complex alloy, Acta Mater. 193 (2020) 329–337. https://doi.org/10.1016/j.actamat.2020.04.034.

[111] W.R. Jian, Z. Xie, S. Xu, Y. Su, X. Yao, I.J. Beyerlein, Effects of lattice distortion and chemical short-range order on the mechanisms of deformation in medium entropy alloy CoCrNi, Acta Mater. 199 (2020) 352–369. https://doi.org/10.1016/j.actamat.2020.08.044.

[112] B. Yin, S. Yoshida, N. Tsuji, W.A. Curtin, Yield strength and misfit volumes of NiCoCr and implications for short-range-order, Nat. Commun. 11 (2020) 1–7. https://doi.org/10.1038/s41467-020-16083-1.

[113] R. Zhang, S. Zhao, J. Ding, Y. Chong, T. Jia, C. Ophus, M. Asta, R.O. Ritchie, A.M. Minor, Short-range order and its impact on the CrCoNi medium-entropy alloy, Nature. 581 (2020) 283–287. https://doi.org/10.1038/s41586-020-2275-z.

[114] T. Yang, B.X. Cao, T.L. Zhang, Y.L. Zhao, W.H. Liu, H.J. Kong, J.H. Luan, J.J. Kai, W. Kuo, C.T. Liu, Chemically complex intermetallic alloys: A new frontier for innovative structural materials, Mater. Today. 52 (2022) 161–174. https://doi.org/10.1016/j.mattod.2021.12.004.

[115] Z. An, S. Mao, T. Yang, C.T. Liu, B. Zhang, E. Ma, H. Zhou, Z. Zhang, L. Wang, X. Han, Spinodal-modulated solid solution delivers a strong and ductile refractory high-entropy alloy, Mater. Horizons. 8 (2021) 948–955. https://doi.org/10.1039/d0mh01341b.

[116] X. Wu, Y. Zhu, Heterogeneous materials: a new class of materials with unprecedented mechanical properties, Mater. Res. Lett. 5 (2017) 527–532. https://doi.org/10.1080/21663831.2017.1343208.

[117] E. Ma, T. Zhu, Towards strength–ductility synergy through the design of heterogeneous nanostructures in metals, Mater. Today. 20 (2017) 323–331. https://doi.org/10.1016/j.mattod.2017.02.003.

[118] X. Wu, P. Jiang, L. Chen, F. Yuan, Y.T. Zhu, Extraordinary strain hardening by gradient structure, Proc. Natl. Acad. Sci. U. S. A. 111 (2014) 7197–7201. https://doi.org/10.1073/pnas.1324069111.

[119] Z. Cheng, H. Zhou, Q. Lu, H. Gao, L. Lu, Extra strengthening and work hardening in gradient nanotwinned metals, Science (80-.). 362 (2018). https://doi.org/10.1126/science.aau1925.

[120] C. Zhang, B.E. MacDonald, F. Guo, H. Wang, C. Zhu, X. Liu, Y. Kang, X. Xie, Y. Zhou, K.S. Vecchio, E.J. Lavernia, Cold-workable refractory complex concentrated alloys with tunable microstructure and good room-temperature

tensile behavior, Scr. Mater. 188 (2020) 16–20. https://doi.org/10.1016/j.scriptamat.2020.07.006.

[121] Y. Liu, Y. Zhang, H. Zhang, N. Wang, X. Chen, H. Zhang, Y. Li, Microstructure and mechanical properties of refractory HfMo0.5NbTiV0.5Sixhigh-entropy composites, J. Alloys Compd. 694 (2017) 869–876. https://doi.org/10.1016/j.jallcom.2016.10.014.

[122] V. Soni, O.N. Senkov, B. Gwalani, D.B. Miracle, R. Banerjee, Microstructural Design for Improving Ductility of An Initially Brittle Refractory High Entropy Alloy, Sci. Rep. 8 (2018) 1–10. https://doi.org/10.1038/s41598-018-27144-3.

[123] O.N. Senkov, C. Woodward, D.B. Miracle, Microstructure and Properties of Aluminum-Containing Refractory High-Entropy Alloys, Jom. 66 (2014) 2030–2042. https://doi.org/10.1007/s11837-014-1066-0.

[124] O.N. Senkov, S. V. Senkova, C. Woodward, Effect of aluminum on the microstructure and properties of two refractory high-entropy alloys, Acta Mater. 68 (2014) 214–228. https://doi.org/10.1016/j.actamat.2014.01.029.

[125] T.E. Whitfield, E.J. Pickering, L.R. Owen, O.N. Senkov, D.B. Miracle, H.J. Stone, N.G. Jones, An assessment of the thermal stability of refractory high entropy superalloys, J. Alloys Compd. 857 (2021). https://doi.org/10.1016/j.jallcom.2020.157583.

[126] V. Soni, O.N. Senkov, B. Gwalani, D.B. Miracle, R. Banerjee, Microstructural Design for Improving Ductility of An Initially Brittle Refractory High Entropy Alloy, Sci. Rep. 8 (2018) 1–10. https://doi.org/10.1038/s41598-018-27144-3.

[127] V. Soni, O.N. Senkov, J.P. Couzinie, Y. Zheng, B. Gwalani, R. Banerjee, Phase stability and microstructure evolution in a ductile refractory high entropy alloy Al10Nb15Ta5Ti30Zr40, Materialia. 9 (2020) 100569. https://doi.org/10.1016/j.mtla.2019.100569.

[128] D.B. Miracle, M.H. Tsai, O.N. Senkov, V. Soni, R. Banerjee, Refractory high entropy superalloys (RSAs), Scr. Mater. 187 (2020) 445–452. https://doi.org/10.1016/j.scriptamat.2020.06.048.

[129] P. Ponnusamy, R.A.R. Rashid, S.H. Masood, D. Ruan, S. Palanisamy, Mechanical properties of slm-printed aluminium alloys: A review, Materials (Basel). 13 (2020) 1–51. https://doi.org/10.3390/ma13194301.

[130] L. Wang, Y. Zhang, H.Y. Chia, W. Yan, Mechanism of keyhole pore formation in metal additive manufacturing, Npj Comput. Mater. 8 (2022). https://doi.org/10.1038/s41524-022-00699-6.

[131] Z. Li, S. Sui, X. Ma, H. Tan, C. Zhong, G. Bi, A.T. Clare, A. Gasser, J. Chen, High deposition rate powder- and wire-based laser directed energy deposition of metallic materials: A review, Int. J. Mach. Tools Manuf. 181 (2022). https://doi.org/10.1016/j.ijmachtools.2022.103942.

[132] D. Gu, X. Shi, R. Poprawe, D.L. Bourell, R. Setchi, J. Zhu, Material-structure-performance integrated laser-metal additive manufacturing, Science (80-.). 372 (2021). https://doi.org/10.1126/science.abg1487.

[133] S. Wen, J. Gan, F. Li, Y. Zhou, C. Yan, Y. Shi, Research status and prospect of additive manufactured nickel-titanium shape memory alloys, Materials (Basel). 14 (2021). https://doi.org/10.3390/ma14164496.

[134] H. Khodashenas, H. Mirzadeh, Post-processing of additively manufactured high-entropy alloys - A review, J. Mater. Res. Technol. 21 (2022) 3795–3814. https://doi.org/10.1016/j.jmrt.2022.11.027.

[135] I. Kunce, M. Polanski, J. Bystrzycki, Microstructure and hydrogen storage properties of a TiZrNbMoV high entropy alloy synthesized using Laser Engineered Net Shaping (LENS), Int. J. Hydrogen Energy. 39 (2014) 9904–9910. https://doi.org/10.1016/j.ijhydene.2014.02.067.

[136] H. Zhang, W. Xu, Y. Xu, Z. Lu, D. Li, The thermal-mechanical behavior of WTaMoNb high-entropy alloy via selective laser melting (SLM): experiment and simulation, Int. J. Adv. Manuf. Technol. 96 (2018) 461–474. https://doi.org/10.1007/s00170-017-1331-9.

[137] Y. Zhao, H. Zhang, J. Cai, X. Sun, L. Wang, X. Xu, X. Guo, Z. Tong, D. Li, An efficient pores suppression process design method for high strength BCC high entropy alloys via powder bed fusion, J. Manuf. Process. 101 (2023) 371–385.

[138] F. Huber, D. Bartels, M. Schmidt, In situ alloy formation of a wmotanbv refractory metal high entropy alloy by laser powder bed fusion (Pbf-lb/m), Materials (Basel). 14 (2021) 1–12. https://doi.org/10.3390/ma14113095.

[139] H. Dobbelstein, E.L. Gurevich, E.P. George, A. Ostendorf, G. Laplanche, Laser metal deposition of a refractory TiZrNbHfTa high-entropy alloy, Addit. Manuf. 24 (2018) 386–390. https://doi.org/10.1016/j.addma.2018.10.008.

[140] O.T. Onawale, P.V. Cobbinah, W.R. Matizamhuka, R.A. Nzeukou, Synthesis route, microstructural evolution, and mechanical property relationship of high-entropy alloys (HEAs): a review, (2021).

[141] X. Chang, M. Zeng, K. Liu, L. Fu, Phase Engineering of High-Entropy Alloys, Adv. Mater. 32 (2020) 1–22. https://doi.org/10.1002/adma.201907226.

[142] H. Wang, Q. Liu, Y. Guo, H. Lan, MoFe1.5CrTiWAlNbx refractory high-entropy alloy coating fabricated by laser cladding, Intermetallics. 115 (2019) 1–7. https://doi.org/10.1016/j.intermet.2019.106613.

[143] Y. Zhao, M. Wu, J. Hou, Y. Chen, C. Zhang, J. Cheng, R. Li, Microstructure and high temperature properties of laser cladded WTaNbMo refractory high entropy alloy coating assisted with ultrasound vibration, J. Alloys Compd. 920 (2022) 165888. https://doi.org/10.1016/j.jallcom.2022.165888.

[144] Q. Li, H. Zhang, D. Li, Z. Chen, S. Huang, Z. Lu, H. Yan, WxNbMoTa refractory high-entropy alloys fabricated by laser cladding deposition, Materials (Basel). 12 (2019) 1–14. https://doi.org/10.3390/ma12030533.

[145] H. Zhang, J. Cai, J. Geng, X. Sun, Y. Zhao, X. Guo, D. Li, Study on annealing treatment of NbMoTaTiNi high-entropy alloy with ultra-high strength disordered-ordered transition structure for additive manufacturing, J. Alloys Compd. 941 (2023) 168810. https://doi.org/10.1016/j.jallcom.2023.168810.

[146] H. Zhang, J. Cai, J. Geng, X. Sun, Y. Zhao, X. Guo, D. Li, Development of high strength high plasticity refractory high entropy alloy based on Mo element optimization and advanced forming process, Int. J. Refract. Met. Hard Mater. 112 (2023) 106163. https://doi.org/10.1016/j.ijrmhm.2023.106163.

[147] H.I. Jeong, C.M. Lee, D.H. Kim, Manufacturing of Ti–Nb–Cr–V–Ni high entropy alloy using directed energy deposition and evaluation of materials properties, J. Mater. Res. Technol. 23 (2023) 5606–5617. https://doi.org/10.1016/j.jmrt.2023.02.168.

[148] Y. Guo, X. Li, Q. Liu, A novel biomedical high-entropy alloy and its laser-clad coating designed by a cluster-plus-glue-atom model, Mater. Des. 196 (2020) 109085. https://doi.org/10.1016/j.matdes.2020.109085.

[149] H. Zhang, Y. Zhao, S. Huang, S. Zhu, F. Wang, D. Li, Manufacturing and analysis of high-performance refractory high-entropy alloy via selective laser melting (SLM), Materials (Basel). 12 (2019). https://doi.org/10.3390/ma12050720.

[150] Y. Guo, H. Wang, Q. Liu, Microstructure evolution and strengthening mechanism of laser-cladding MoFexCrTiWAlNby refractory high-entropy alloy coatings, J. Alloys Compd. 834 (2020) 155147. https://doi.org/10.1016/j.jallcom.2020.155147.

[151] J.W. Sears, Development of Laser-Powder Additive Manufacturing for Industry: Historical Perspective, Current and Future Applications, Powder Mater. Curr. Res. Ind. Pract. III. (2010) 211–228.

[152] B.D. Cullity, Elements of X-ray Diffraction, Addison-Wesley Publishing, 1956.

[153] P. Juhás, T. Davis, C.L. Farrow, S.J.L. Billinge, PDFgetX3: a rapid and highly automatable program for processing powder diffraction data into total scattering pair distribution functions, J. Appl. Crystallogr. 46 (2013) 560–566.

[154] C.L. Farrow, P. Juhas, J.W. Liu, D. Bryndin, E.S. Božin, J. Bloch, T. Proffen, S.J.L. Billinge, PDFfit2 and PDFgui: computer programs for studying nanostructure in crystals, J. Phys. Condens. Matter. 19 (2007) 335219.

[155] J.-O. Andersson, T. Helander, L. Höglund, P. Shi, B. Sundman, Thermo-Calc & DICTRA, computational tools for materials science, Calphad. 26 (2002) 273–312.

[156] A.J. Cohen, P. Mori-Sánchez, W. Yang, Challenges for density functional theory, Chem. Rev. 112 (2012) 289–320.

[157] S.J. Clark, M.D. Segall, C.J. Pickard, P.J. Hasnip, M.I.J. Probert, K. Refson, M.C. Payne, First principles methods using CASTEP, Zeitschrift Fur Krist. 220 (2005) 567–570. https://doi.org/10.1524/zkri.220.5.567.65075.

[158] G.I. Taylor, Plastic strain in metals, J. Inst. Met. 62 (1938) 307–324.

[159] J.F.W. Bishop, R. Hill, A theory of the plastic distortion of a polycrystalline aggregate. Phil, (1951).

[160] J.F.W. Bishop, R. Hill, A theoretical derivation of the plastic properties of a polycrystalline face-centred metal, London, Edinburgh, Dublin Philos. Mag. J. Sci. 42 (1951) 1298–1307.

[161] W.A. Curtin, R.E. Miller, Atomistic/continuum coupling in computational materials science, Model. Simul. Mater. Sci. Eng. 11 (2003) R33.

[162] O.C. Zienkiewicz, R.L. Taylor, The finite element method for solid and structural mechanics, Elsevier, 2005.

[163] J.R. Rice, Inelastic constitutive relations for solids: an internal-variable theory and its application to metal plasticity, J. Mech. Phys. Solids. 19 (1971) 433–455.

[164] R.J. Asaro, J.R. Rice, Strain localization in ductile single crystals, J. Mech. Phys. Solids. 25 (1977) 309–338. https://doi.org/10.1016/0022-5096(77)90001-1.

[165] A. Arsenlis, D.M. Parks, Crystallographic aspects of geometrically-necessary and statistically-stored dislocation density, Acta Mater. 47 (1999) 1597–1611.

[166] F. Roters, M. Diehl, P. Shanthraj, P. Eisenlohr, C. Reuber, S.L. Wong, T. Maiti, A. Ebrahimi, T. Hochrainer, H.O. Fabritius, S. Nikolov, M. Friák, N. Fujita, N. Grilli, K.G.F. Janssens, N. Jia, P.J.J. Kok, D. Ma, F. Meier, E. Werner, M. Stricker, D. Weygand, D. Raabe, DAMASK – The Düsseldorf Advanced Material Simulation Kit for modeling multi-physics crystal plasticity, thermal, and damage phenomena from the single crystal up to the component scale, Comput. Mater. Sci. 158 (2019) 420–478. https://doi.org/10.1016/j.commatsci.2018.04.030.

[167] Y.M. Wang, T. Voisin, J.T. McKeown, J. Ye, N.P. Calta, Z. Li, Z. Zeng, Y. Zhang, W. Chen, T.T. Roehling, R.T. Ott, M.K. Santala, P.J. Depond, M.J. Matthews, A. V. Hamza, T. Zhu, Additively manufactured hierarchical stainless steels with high strength and ductility, Nat. Mater. 17 (2018) 63–70. https://doi.org/10.1038/NMAT5021.

[168] L. Liu, Q. Ding, Y. Zhong, J. Zou, J. Wu, Y.L. Chiu, J. Li, Z. Zhang, Q. Yu, Z. Shen, Dislocation network in additive manufactured steel breaks strength–ductility trade-off, Mater. Today. 21 (2018) 354–361. https://doi.org/10.1016/j.mattod.2017.11.004.

[169] I. Kunce, M. Polanski, J. Bystrzycki, Structure and hydrogen storage properties of a high entropy ZrTiVCrFeNi alloy synthesized using Laser Engineered Net Shaping (LENS), Int. J. Hydrogen Energy. 38 (2013) 12180–12189. https://doi.org/10.1016/j.ijhydene.2013.05.071.

[170] M. Polanski, M. Kwiatkowska, I. Kunce, J. Bystrzycki, Combinatorial synthesis of alloy libraries with a progressive composition gradient using laser engineered net shaping (LENS): Hydrogen storage alloys, Int. J. Hydrogen Energy. 38 (2013) 12159–12171. https://doi.org/10.1016/j.ijhydene.2013.05.024.

[171] R. Montanari, G. Costanza, M.E. Tata, C. Testani, Lattice expansion of Ti-6Al-4V by nitrogen and oxygen absorption, Mater. Charact. 59 (2008) 334–337. https://doi.org/10.1016/j.matchar.2006.12.014.

[172] B. Zheng, Y. Zhou, J.E. Smugeresky, J.M. Schoenung, E.J. Lavernia, Thermal behavior and microstructural evolution during laser deposition with laser-engineered net shaping: Part I. Numerical calculations, Metall. Mater. Trans. A Phys. Metall. Mater. Sci. 39 (2008) 2228–2236. https://doi.org/10.1007/s11661-008-9557-7.

[173] K. Choudhary, F. Tavazza, Convergence and machine learning predictions of Monkhorst-Pack k-points and plane-wave cut-off in high-throughput DFT calculations, Comput. Mater. Sci. 161 (2019) 300–308. https://doi.org/10.1016/j.commatsci.2019.02.006.

[174] R. Mayahi, An investigation concerning generalized stacking fault behavior of AlCoxCrFeNi ($0.25 \leq x \leq 2$) high entropy alloys: Insights from first-principles

study, J. Alloys Compd. 818 (2020) 152928. https://doi.org/10.1016/j.jallcom.2019.152928.

[175] J.H. Rose, J.R. Smith, J. Ferrante, Universal features of bonding in metals, Phys. Rev. B. 28 (1983) 1835–1845. https://doi.org/10.1103/PhysRevB.28.1835.

[176] X. Tian, Y. Zhu, C.V.S. Lim, J. Williams, R. Boyer, X. Wu, K. Zhang, A. Huang, Isotropic and improved tensile properties of Ti-6Al-4V achieved by in-situ rolling in direct energy deposition, Addit. Manuf. 46 (2021) 102151. https://doi.org/10.1016/j.addma.2021.102151.

[177] H. Chen, K. Kosiba, C. Suryanarayana, T. Lu, Y. Liu, Y. Wang, K.G. Prashanth, Feedstock preparation, microstructures and mechanical properties for laser-based additive manufacturing of steel matrix composites, Int. Mater. Rev. 68 (2023) 1192–1244. https://doi.org/10.1080/09506608.2023.2258664.

[178] Y. Zhong, F. Yin, T. Sakaguchi, K. Nagai, K. Yang, Dislocation structure evolution and characterization in the compression deformed Mn-Cu alloy, Acta Mater. 55 (2007) 2747–2756. https://doi.org/10.1016/j.actamat.2006.12.012.

[179] I. Serrano-Munoz, R. Fernández, R. Saliwan-Neumann, G. González-Doncel, G. Bruno, Dislocation structures after creep in an Al-3.85 %Mg alloy studied using EBSD-KAM technique, Mater. Lett. 337 (2023) 3–6. https://doi.org/10.1016/j.matlet.2023.133978.

[180] T. Lu, N. Yao, H. Chen, B. Sun, X.Y. Chen, S. Scudino, K. Kosiba, X. Zhang, Exceptional strength-ductility combination of additively manufactured high-entropy alloy matrix composites reinforced with TiC nanoparticles at room and cryogenic temperatures, Addit. Manuf. 56 (2022) 102918. https://doi.org/10.1016/j.addma.2022.102918.

[181] M. Klinger, A. Jäger, Crystallographic Tool Box (CrysTBox): Automated tools for transmission electron microscopists and crystallographers, J. Appl. Crystallogr. 48 (2015) 2012–2018. https://doi.org/10.1107/S1600576715017252.

[182] M.J. Hÿtch, E. Snoeck, R. Kilaas, Quantitative measurement of displacement and strain fields from HREM micrographs, Ultramicroscopy. 74 (1998) 131–146. https://doi.org/10.1016/S0304-3991(98)00035-7.

[183] Y. Tong, S. Zhao, H. Bei, T. Egami, Y. Zhang, F. Zhang, Severe local lattice distortion in Zr- and/or Hf-containing refractory multi-principal element alloys, Acta Mater. 183 (2020) 172–181. https://doi.org/10.1016/j.actamat.2019.11.026.

[184] Z. Liu, B. He, T. Lyu, Y. Zou, A Review on Additive Manufacturing of Titanium Alloys for Aerospace Applications: Directed Energy Deposition and Beyond Ti-6Al-4V, Jom. 73 (2021) 1804–1818. https://doi.org/10.1007/s11837-021-04670-6.

[185] Y. Zhang, T. Wang, S. Jiang, B. Zhang, Y. Wang, J. Feng, Microstructure evolution and embrittlement of electron beam welded TZM alloy joint, Mater. Sci. Eng. A. 700 (2017) 512–518. https://doi.org/10.1016/j.msea.2017.05.076.

[186] Y. Wang, J. Li, A. V Hamza, T.W. Barbee, Ductile crystalline-amorphous nanolaminates., Proc. Natl. Acad. Sci. U. S. A. 104 (2007) 11155–11160.

[187] A.J. Martínez-Donaire, F.J. García-Lomas, C. Vallellano, New approaches to detect the onset of localised necking in sheets under through-thickness strain gradients, Mater. Des. 57 (2014) 135–145. https://doi.org/10.1016/j.matdes.2014.01.012.

[188] S. Sandlöbes, S. Zaefferer, I. Schestakow, S. Yi, R. Gonzalez-Martinez, On the role of non-basal deformation mechanisms for the ductility of Mg and Mg-Y

alloys, Acta Mater. 59 (2011) 429–439. https://doi.org/10.1016/j.actamat.2010.08.031.

[189] D. Yang, Y. An, P. Cizek, P. Hodgson, Development of adiabatic shear band in cold-rolled titanium, Mater. Sci. Eng. A. 528 (2011) 3990–3997. https://doi.org/10.1016/j.msea.2011.01.108.

[190] T.H. Lee, E. Shin, C.S. Oh, H.Y. Ha, S.J. Kim, Correlation between stacking fault energy and deformation microstructure in high-interstitial-alloyed austenitic steels, Acta Mater. 58 (2010) 3173–3186. https://doi.org/10.1016/j.actamat.2010.01.056.

[191] Y.J. Hu, A. Sundar, S. Ogata, L. Qi, Screening of generalized stacking fault energies, surface energies and intrinsic ductile potency of refractory multicomponent alloys, Acta Mater. 210 (2021) 116800. https://doi.org/10.1016/j.actamat.2021.116800.

[192] J.R. Rice, G.E. Beltz, The activation energy for dislocation nucleation at a crack, J. Mech. Phys. Solids. 42 (1994) 333–360. https://doi.org/10.1016/0022-5096(94)90013-2.

[193] A.A. Griffith, Theory of rupture, in: Proc. 1st. Int. Cong. Appl. Mech., Delft, 1924: pp. 55–63.

[194] S.G. Wang, E.K. Tian, C.W. Lung, Surface energy of arbitrary crystal plane of bcc and fcc metals, J. Phys. Chem. Solids. 61 (2000) 1295–1300. https://doi.org/10.1016/S0022-3697(99)00415-1.

[195] J. Mei, Y. Ni, J. Li, The effect of crack orientation on fracture behavior of tantalum by multiscale simulation, Int. J. Solids Struct. 48 (2011) 3054–3062. https://doi.org/10.1016/j.ijsolstr.2011.06.022.

[196] L. Lu, Y. Shen, X. Chen, L. Qian, K. Lu, Ultrahigh Strength and High Electrical Conductivity in Copper, Science (80-.). 304 (2004) 422–426. https://doi.org/10.1126/science.1092905.

[197] A.A. Mohammed, S.M. Haris, W. Al Azzawi, Estimation of the ultimate tensile strength and yield strength for the pure metals and alloys by using the acoustic wave properties, Sci. Rep. 10 (2020) 1–12. https://doi.org/10.1038/s41598-020-69387-z.

[198] N. Hansen, Hall-petch relation and boundary strengthening, Scr. Mater. 51 (2004) 801–806. https://doi.org/10.1016/j.scriptamat.2004.06.002.

[199] Z. Wang, Q. Fang, J. Li, B. Liu, Y. Liu, Effect of lattice distortion on solid solution strengthening of BCC high-entropy alloys, J. Mater. Sci. Technol. 34 (2018) 349–354. https://doi.org/10.1016/j.jmst.2017.07.013.

[200] R. Sriharitha, B.S. Murty, R.S. Kottada, Alloying, thermal stability and strengthening in spark plasma sintered AlxCoCrCuFeNi high entropy alloys, J. Alloys Compd. 583 (2014) 419–426. https://doi.org/10.1016/j.jallcom.2013.08.176.

[201] M. Walbrühl, D. Linder, J. Ågren, A. Borgenstam, Modelling of solid solution strengthening in multicomponent alloys, Mater. Sci. Eng. A. 700 (2017) 301–311. https://doi.org/10.1016/j.msea.2017.06.001.

[202] R. Labusch, A Statistical Theory of Solid Solution Hardening, Phys. Status Solidi. 41 (1970) 659–669. https://doi.org/10.1002/pssb.19700410221.

[203] M.A. Meyers, K.K. Chawla, Mechanical behavior of materials, Cambridge university press, 2008.

[204] D.G. Kalali, S. Antharam, M. Hasan, P.S. Karthik, P.S. Phani, K. Bhanu Sankara Rao, K. V. Rajulapati, On the origins of ultra-high hardness and strain gradient plasticity in multi-phase nanocrystalline MoNbTaTiW based

refractory high-entropy alloy, Mater. Sci. Eng. A. 812 (2021) 141098. https://doi.org/10.1016/j.msea.2021.141098.

[205] T. Ungár, A. Borbély, The effect of dislocation contrast on x-ray line broadening: A new approach to line profile analysis, Appl. Phys. Lett. 69 (1996) 3173–3175. https://doi.org/10.1063/1.117951.

[206] Á. Révész, T. Ungár, A. Borbély, J. Lendvai, Dislocations and grain size in ball-milled iron powder, Nanostructured Mater. 7 (1996) 779–788. https://doi.org/10.1016/S0965-9773(96)00048-7.

[207] A. Borbély, The modified Williamson-Hall plot and dislocation density evaluation from diffraction peaks, Scr. Mater. 217 (2022). https://doi.org/10.1016/j.scriptamat.2022.114768.

[208] T. Ungar, G. Tichy, The effect of dislocation contrast on X-ray line profiles in untextured polycrystals, Phys. Status Solidi. 425 (1999) 425–434.

[209] T. Ungár, I. Dragomir, Á. Révész, A. Borbély, The contrast factors of dislocations in cubic crystals: The dislocation model of strain anisotropy in practice, J. Appl. Crystallogr. 32 (1999) 992–1002. https://doi.org/10.1107/S0021889899009334.

[210] G.K. Williamson, W.H. Hall, X-ray line broadening from filed aluminium and wolfram, Acta Metall. 1 (1953) 22–31. https://doi.org/10.1016/0001-6160(53)90006-6.

[211] Y.J. Yin, J.Q. Sun, J. Guo, X.F. Kan, D.C. Yang, Mechanism of high yield strength and yield ratio of 316 L stainless steel by additive manufacturing, Mater. Sci. Eng. A. 744 (2019) 773–777. https://doi.org/10.1016/j.msea.2018.12.092.

[212] H. Chen, T. Lu, Y. Wang, Y. Liu, T. Shi, K.G. Prashanth, K. Kosiba, Laser additive manufacturing of nano-TiC particles reinforced CoCrFeMnNi high-

entropy alloy matrix composites with high strength and ductility, Mater. Sci. Eng. A. 833 (2022) 142512. https://doi.org/10.1016/j.msea.2021.142512.

[213] L. Lilensten, J.P. Couzinié, L. Perrière, A. Hocini, C. Keller, G. Dirras, I. Guillot, Study of a bcc multi-principal element alloy: Tensile and simple shear properties and underlying deformation mechanisms, Acta Mater. 142 (2018) 131–141. https://doi.org/10.1016/j.actamat.2017.09.062.

[214] R.L. Fleischer, Solution hardening by tetragonal dist ortions: Application to irradiation hardening in F.C.C. crystals, Acta Metall. 10 (1962) 835–842. https://doi.org/10.1016/0001-6160(62)90098-6.

[215] P. Agrawal, S. Karthikeyan, Enhancement in Strain Hardening on Boron Addition in As-Cast Ti–6Al–4V Alloy, Trans. Indian Inst. Met. 68 (2015) 195–205. https://doi.org/10.1007/s12666-015-0560-6.

[216] V. Gerold, H.P. Karnthaler, On the origin of planar slip in f.c.c. alloys, Acta Metall. 37 (1989) 2177–2183. https://doi.org/10.1016/0001-6160(89)90143-0.

[217] J.P. Couzinié, L. Lilensten, Y. Champion, G. Dirras, L. Perrière, I. Guillot, On the room temperature deformation mechanisms of a TiZrHfNbTa refractory high-entropy alloy, Mater. Sci. Eng. A. 645 (2015) 255–263. https://doi.org/10.1016/j.msea.2015.08.024.

[218] J.T. Fong, Fatigue mechanisms, ASTM International, 1979.

[219] S.S. Sohn, A. Kwiatkowski da Silva, Y. Ikeda, F. Körmann, W. Lu, W.S. Choi, B. Gault, D. Ponge, J. Neugebauer, D. Raabe, Ultrastrong Medium-Entropy Single-Phase Alloys Designed via Severe Lattice Distortion, Adv. Mater. 31 (2019) 1–8. https://doi.org/10.1002/adma.201807142.

[220] Y. Tong, K. Jin, H. Bei, J.Y.P. Ko, D.C. Pagan, Y. Zhang, F.X. Zhang, Local lattice distortion in NiCoCr, FeCoNiCr and FeCoNiCrMn concentrated alloys

investigated by synchrotron X-ray diffraction, Mater. Des. 155 (2018) 1–7. https://doi.org/10.1016/j.matdes.2018.05.056.

[221] I.K. Jeong, R.H. Heffner, M.J. Graf, S.J.L. Billinge, Lattice dynamics and correlated atomic motion from the atomic pair distribution function, Phys. Rev. B - Condens. Matter Mater. Phys. 67 (2003) 9. https://doi.org/10.1103/PhysRevB.67.104301.

[222] F.X. Zhang, H.Q. Song, Effect of atomic size mismatch and chemical complexity on the local lattice distortion of BCC solid solution alloys, Mater. Today Commun. 33 (2022) 104367. https://doi.org/10.1016/j.mtcomm.2022.104367.

[223] Y. Tong, G. Velisa, S. Zhao, W. Guo, T. Yang, K. Jin, C. Lu, H. Bei, J.Y.P. Ko, D.C. Pagan, Y. Zhang, L. Wang, F.X. Zhang, Evolution of local lattice distortion under irradiation in medium- and high-entropy alloys, Materialia. 2 (2018) 73–81. https://doi.org/10.1016/j.mtla.2018.06.008.

[224] R. Huang, W. Wang, T. Li, L. Zhang, A. Amar, X. Chen, Z. Ren, Y. Lu, A novel AlMoNbHfTi refractory high-entropy alloy with superior ductility, J. Alloys Compd. 940 (2023) 168821.

[225] Y. Jia, S. Wu, Y. Mu, L. Xu, C. Ren, K. Sun, J. Yi, Y. Jia, W. Yan, G. Wang, Efficient Coarse-Grained Superplasticity of a Gigapascal Lightweight Refractory Medium Entropy Alloy, Adv. Sci. 10 (2023) 2207535.

[226] S.Y. Chen, L. Wang, W.D. Li, Y. Tong, K.K. Tseng, C.W. Tsai, J.W. Yeh, Y. Ren, W. Guo, J.D. Poplawsky, others, Peierls barrier characteristic and anomalous strain hardening provoked by dynamic-strain-aging strengthening in a body-centered-cubic high-entropy alloy, Mater. Res. Lett. 7 (2019) 475–481.

[227] S. Chen, W. Li, F. Meng, Y. Tong, H. Zhang, K.-K. Tseng, J.-W. Yeh, Y. Ren, F. Xu, Z. Wu, others, On temperature and strain-rate dependence of flow serration in HfNbTaTiZr high-entropy alloy, Scr. Mater. 200 (2021) 113919.

[228] A. Shaji Karapuzha, D. Fraser, D. Schliephake, S. Dietrich, Y. Zhu, X. Wu, A. Huang, Room and elevated temperature tensile and fatigue behaviour of additively manufactured Hastelloy X, Mater. Sci. Eng. A. 882 (2023) 145479. https://doi.org/10.1016/j.msea.2023.145479.

[229] A. Poudel, P.R. Gradl, S. Shao, N. Shamsaei, Tensile deformation behavior of laser powder direct energy deposited Inconel 625: Cryogenic to elevated temperatures, Mater. Sci. Eng. A. 889 (2024) 145826. https://doi.org/10.1016/j.msea.2023.145826.

[230] T. Zhang, H. Li, H. Gong, Y. Wu, A.S. Ahmad, X. Chen, Effect of rolling force on tensile properties of additively manufactured Inconel 718 at ambient and elevated temperatures, J. Alloys Compd. 884 (2021) 161050. https://doi.org/10.1016/j.jallcom.2021.161050.

[231] S. Wang, J. Yang, J. Sun, W. Shu, H. Yang, A.H.W. Ngan, Y. Huang, Tensile properties of Ti6.5Al2Zr1Mo1V titanium alloy fabricated via electron beam selective melting at high temperature, Mater. Sci. Eng. A. 888 (2023) 145806. https://doi.org/10.1016/j.msea.2023.145806.

[232] D. Lin, L. Xu, H. Jing, Y. Han, L. Zhao, F. Minami, Effects of annealing on the structure and mechanical properties of FeCoCrNi high-entropy alloy fabricated via selective laser melting, Addit. Manuf. 32 (2020) 101058. https://doi.org/10.1016/j.addma.2020.101058.

[233] G. Laplanche, P. Gadaud, L. Perrière, I. Guillot, J.P. Couzinié, Temperature dependence of elastic moduli in a refractory HfNbTaTiZr high-entropy alloy, J. Alloys Compd. 799 (2019) 538–545. https://doi.org/10.1016/j.jallcom.2019.05.322.

[234] S.Y. Chen, Y. Tong, K.K. Tseng, J.W. Yeh, J.D. Poplawsky, J.G. Wen, M.C. Gao, G. Kim, W. Chen, Y. Ren, R. Feng, W.D. Li, P.K. Liaw, Phase transformations of HfNbTaTiZr high-entropy alloy at intermediate temperatures, Scr. Mater. 158 (2019) 50–56. https://doi.org/10.1016/j.scriptamat.2018.08.032.

[235] H.Y. Yasuda, Y. Yamada, K. Cho, T. Nagase, Deformation behavior of HfNbTaTiZr high entropy alloy singe crystals and polycrystals, Mater. Sci. Eng. A. 809 (2021) 140983. https://doi.org/10.1016/j.msea.2021.140983.

[236] Y. Zhang, B. Qin, D. Ouyang, L. Liu, C. Feng, Y. Yan, S. Ye, H. Ke, K.C. Chan, W. Wang, Strong yet ductile refractory high entropy alloy fabricated via additive manufacturing, Addit. Manuf. 81 (2024) 104009. https://doi.org/10.1016/j.addma.2024.104009.

[237] L. Chen, X. Hao, Y. Wang, X. Zhang, H. Liu, First-principles calculation of the effect of Ti content on the structure and properties of TiVNbMo refractory high-entropy alloy, Mater. Res. Express. 7 (2020). https://doi.org/10.1088/2053-1591/abbf11.

[238] A. Otero-De-La-Roza, D. Abbasi-Pérez, V. Luaña, Gibbs2: A new version of the quasiharmonic model code. II. Models for solid-state thermodynamics, features and implementation, Comput. Phys. Commun. 182 (2011) 2232–2248. https://doi.org/10.1016/j.cpc.2011.05.009.

[239] F. Birch, Finite elastic strain of cubic crystals, Phys. Rev. 71 (1947) 809.

[240] X.W. Sun, L.C. Cai, Q.F. Chen, X.R. Chen, F.Q. Jing, Structural, thermodynamic, electronic, and optical properties of NaH from first-principles calculations, Mater. Chem. Phys. 133 (2012) 346–355. https://doi.org/10.1016/j.matchemphys.2012.01.036.

[241] H. Stout, A five-parameter temperature-corrected Murnaghan equation for P-V-T surfaces, J. Geophys. Res. 94 (1989) 9477–9483.

[242] F. Mouhat, F.X. Coudert, Necessary and sufficient elastic stability conditions in various crystal systems, Phys. Rev. B - Condens. Matter Mater. Phys. 90 (2014) 4–7. https://doi.org/10.1103/PhysRevB.90.224104.

[243] F. Roters, P. Eisenlohr, L. Hantcherli, D.D. Tjahjanto, T.R. Bieler, D. Raabe, Overview of constitutive laws, kinematics, homogenization and multiscale methods in crystal plasticity finite-element modeling: Theory, experiments, applications, Acta Mater. 58 (2010) 1152–1211. https://doi.org/10.1016/j.actamat.2009.10.058.

[244] E. Orowan, Zur kristallplastizität. III: Über den mechanismus des gleitvorganges, Zeitschrift Für Phys. 89 (1934) 634–659.

[245] A. V. Amirkhizi, S. Nemat-Nasser, A framework for numerical integration of crystal elasto-plastic constitutive equations compatible with explicit finite element codes, Int. J. Plast. 23 (2007) 1918–1937. https://doi.org/10.1016/j.ijplas.2007.05.003.

[246] U.F. Kocks, A. As, A. Mf, Thermodynamics and kinetics of slip, (1975).

[247] W. Blum, P. Eisenlohr, Dislocation mechanics of creep, Mater. Sci. Eng. A. 510–511 (2009) 7–13. https://doi.org/10.1016/j.msea.2008.04.110.

[248] M.A. Groeber, M.A. Jackson, DREAM.3D: A Digital Representation Environment for the Analysis of Microstructure in 3D, Integr. Mater. Manuf. Innov. 3 (2014) 56–72. https://doi.org/10.1186/2193-9772-3-5.

[249] S. Gao, Y. Sun, Q. Li, Z. Hao, B. Zhang, D. Gu, G. Wang, Research on the hot tensile deformation mechanism of Ti-6Al-4 V alloy sheet based on the α + β dual phase crystal plasticity modeling, J. Alloys Compd. 932 (2023) 167701. https://doi.org/10.1016/j.jallcom.2022.167701.

[250] K. Sedighiani, K. Traka, F. Roters, J. Sietsma, D. Raabe, M. Diehl, Crystal plasticity simulation of in-grain microstructural evolution during large deformation of IF-steel, Acta Mater. 237 (2022) 118167. https://doi.org/10.1016/j.actamat.2022.118167.

[251] J.W. Yeh, S.Y. Chang, Y. Der Hong, S.K. Chen, S.J. Lin, Anomalous decrease in X-ray diffraction intensities of Cu-Ni-Al-Co-Cr-Fe-Si alloy systems with multi-principal elements, Mater. Chem. Phys. 103 (2007) 41–46. https://doi.org/10.1016/j.matchemphys.2007.01.003.

[252] M.H. Tsai, J.W. Yeh, High-entropy alloys: A critical review, Mater. Res. Lett. 2 (2014) 107–123. https://doi.org/10.1080/21663831.2014.912690.

[253] L.R. Owen, N.G. Jones, Lattice distortions in high-entropy alloys, J. Mater. Res. 33 (2018) 2954–2969. https://doi.org/10.1557/jmr.2018.322.

[254] X. Chen, Q. Wang, Z. Cheng, M. Zhu, H. Zhou, P. Jiang, L. Zhou, Q. Xue, F. Yuan, J. Zhu, X. Wu, E. Ma, Direct observation of chemical short-range order in a medium-entropy alloy, Nature. 592 (2021) 712–716. https://doi.org/10.1038/s41586-021-03428-z.

[255] O.N. Senkov, J.M. Scott, S. V. Senkova, F. Meisenkothen, D.B. Miracle, C.F. Woodward, Microstructure and elevated temperature properties of a refractory TaNbHfZrTi alloy, J. Mater. Sci. 47 (2012) 4062–4074. https://doi.org/10.1007/s10853-012-6260-2.

[256] Q.F. He, J.G. Wang, H.A. Chen, Z.Y. Ding, Z.Q. Zhou, L.H. Xiong, J.H. Luan, J.M. Pelletier, J.C. Qiao, Q. Wang, L.L. Fan, Y. Ren, Q.S. Zeng, C.T. Liu, C.W. Pao, D.J. Srolovitz, Y. Yang, A highly distorted ultraelastic chemically complex Elinvar alloy, Nature. 602 (2022) 251–257. https://doi.org/10.1038/s41586-021-04309-1.

[257] F. Maresca, W.A. Curtin, Mechanistic origin of high strength in refractory BCC high entropy alloys up to 1900K, Acta Mater. 182 (2020) 235–249. https://doi.org/10.1016/j.actamat.2019.10.015.

[258] C. Lee, F. Maresca, R. Feng, Y. Chou, T. Ungar, M. Widom, K. An, J.D. Poplawsky, Y.C. Chou, P.K. Liaw, W.A. Curtin, Strength can be controlled by edge dislocations in refractory high-entropy alloys, Nat. Commun. 12 (2021) 6–13. https://doi.org/10.1038/s41467-021-25807-w.

[259] A. Roy, T. Babuska, B. Krick, G. Balasubramanian, Machine learned feature identification for predicting phase and Young's modulus of low-, medium- and high-entropy alloys, Scr. Mater. 185 (2020) 152–158. https://doi.org/10.1016/j.scriptamat.2020.04.016.

[260] C. Lee, G. Song, M.C. Gao, R. Feng, P. Chen, J. Brechtl, Y. Chen, K. An, W. Guo, J.D. Poplawsky, S. Li, A.T. Samaei, W. Chen, A. Hu, H. Choo, P.K. Liaw, Lattice distortion in a strong and ductile refractory high-entropy alloy, Acta Mater. 160 (2018) 158–172. https://doi.org/10.1016/j.actamat.2018.08.053.

[261] Y.T. Shao, R. Yuan, H.W. Hsiao, Q. Yang, Y. Hu, J.M. Zuo, Cepstral scanning transmission electron microscopy imaging of severe lattice distortions, Ultramicroscopy. 231 (2021) 113252. https://doi.org/10.1016/j.ultramic.2021.113252.

[262] J. Li, Y. Chen, Q. He, X. Xu, H. Wang, C. Jiang, B. Liu, Q. Fang, Y. Liu, Y. Yang, P.K. Liaw, C.T. Liu, Heterogeneous lattice strain strengthening in severely distorted crystalline solids, Proc. Natl. Acad. Sci. U. S. A. 119 (2022) 1–7. https://doi.org/10.1073/pnas.2200607119.

[263] C. Lu, L. Niu, N. Chen, K. Jin, T. Yang, P. Xiu, Y. Zhang, F. Gao, H. Bei, S. Shi, M.R. He, I.M. Robertson, W.J. Weber, L. Wang, Enhancing radiation tolerance by controlling defect mobility and migration pathways in

multicomponent single-phase alloys, Nat. Commun. 7 (2016) 1–8. https://doi.org/10.1038/ncomms13564.

[264] C. Lee, G. Kim, Y. Chou, B.L. Musicó, M.C. Gao, K. An, G. Song, Y.C. Chou, V. Keppens, W. Chen, P.K. Liaw, Temperature dependence of elastic and plastic deformation behavior of a refractory high-entropy alloy, Sci. Adv. 6 (2020) 1–12. https://doi.org/10.1126/sciadv.aaz4748.

[265] M. Reihanian, M. Naseri, An analytical approach for necking and fracture of hard layer during accumulative roll bonding (ARB) of metallic multilayer, Mater. Des. 89 (2016) 1213–1222. https://doi.org/10.1016/j.matdes.2015.10.088.

[266] D. Ouyang, Z. jie Chen, H. bin Yu, K.C. Chan, L. Liu, Oxidation behavior of the Ti38V15Nb23Hf24 refractory high-entropy alloy at elevated temperatures, Corros. Sci. 198 (2022) 110153. https://doi.org/10.1016/j.corsci.2022.110153.

[267] H.E. Evans, Stress effects in high temperature oxidation of metals, Int. Mater. Rev. 40 (1995) 1–40. https://doi.org/10.1179/imr.1995.40.1.1.

[268] P.M. Scott, An overview of internal oxidation as a possible explanation of intergranular stress corrosion cracking of alloy 600 in PWRs, 9th Int. Conf. Environ. Degedation Mater. Nucl. Power Syst. - Water React. - Miner. Met. Mater. Soc. (1999).

[269] C.R. Gagg, P.R. Lewis, Wear as a product failure mechanism - Overview and case studies, Eng. Fail. Anal. 14 (2007) 1618–1640. https://doi.org/10.1016/j.engfailanal.2006.11.064.

[270] J. Wang, H. Yang, Z. Liu, L. Fan, W. Yan, D. Qiu, M.W. Fu, Compositional regulation in additive manufacturing of precipitation-hardening (CoCrNi)94Ti3Al3 medium-entropy superalloy: Cellular structure stabilization

and strength enhancement, Compos. Part B Eng. 281 (2024). https://doi.org/10.1016/j.compositesb.2024.111570.

[271] S. Sonal, J. Lee, Recent advances in additive manufacturing of high entropy alloys and their nuclear and Wear-resistant applications, Metals (Basel). 11 (2021) 1–47. https://doi.org/10.3390/met11121980.

[272] K. Lu, J. Zhu, D. Guo, M. Yang, H. Sun, Z. Wang, X. Hui, Y. Wu, Microstructures, Corrosion Resistance and Wear Resistance of High-Entropy Alloys Coatings with Various Compositions Prepared by Laser Cladding: A Review, Coatings. 12 (2022). https://doi.org/10.3390/coatings12071023.

[273] J.F. Archard, Contact and rubbing of flat surfaces, J. Appl. Phys. 24 (1953) 981–988. https://doi.org/10.1063/1.1721448.

[274] W. Xiong, A.X.Y. Guo, S. Zhan, C.T. Liu, S.C. Cao, Refractory high-entropy alloys: A focused review of preparation methods and properties, J. Mater. Sci. Technol. 142 (2023) 196–215. https://doi.org/10.1016/j.jmst.2022.08.046.

[275] C. Jin, X. Li, H. Li, Q. Li, H. Wang, Tribological performance of a TiZrNbMo0.6 refractory high entropy alloy at elevated temperatures, J. Alloys Compd. 920 (2022) 165915. https://doi.org/10.1016/j.jallcom.2022.165915.

[276] X. Pei, Y. Du, X. Hao, H. Wang, Q. Zhou, H. Wu, H. Wang, Microstructure and tribological properties of TiZrV0.5Nb0.5Alx refractory high entropy alloys at elevated temperature, Wear. 488–489 (2022) 204166. https://doi.org/10.1016/j.wear.2021.204166.

[277] X. You, J. Song, P. Lin, X. Zhang, Y. Su, H. Wang, Y. Zhang, L. Hu, Tribological properties and wear mechanisms of TixVNbTaWy RHEAs sliding against Si3N4 ceramic balls: The effects of Ti and W contents, Tribol. Int. 175 (2022) 107801. https://doi.org/10.1016/j.triboint.2022.107801.

[278] M. Pole, M. Sadeghilaridjani, J. Shittu, A. Ayyagari, S. Mukherjee, High temperature wear behavior of refractory high entropy alloys based on 4-5-6 elemental palette, J. Alloys Compd. 843 (2020) 156004. https://doi.org/10.1016/j.jallcom.2020.156004.

[279] L. Mengis, C. Grimme, M.C. Galetz, Tribological properties of the uncoated and aluminized Ti–48Al–2Cr–2Nb TiAl alloy at high temperatures, Wear. 477 (2021) 203818. https://doi.org/10.1016/j.wear.2021.203818.

[280] S. Alvi, F. Akhtar, High temperature tribology of CuMoTaWV high entropy alloy, Wear. 426–427 (2019) 412–419. https://doi.org/10.1016/j.wear.2018.12.085.

[281] C. Nguyen, A.K. Tieu, G. Deng, D. Wexler, B. Tran, T.D. Vo, Study of wear and friction properties of a Co-free CrFeNiAl0.4Ti0.2 high entropy alloy from 600 to 950 °C, Tribol. Int. 169 (2022) 107453. https://doi.org/10.1016/j.triboint.2022.107453.

[282] J.M. Wu, S.J. Lin, J.W. Yeh, S.K. Chen, Y.S. Huang, H.C. Chen, Adhesive wear behavior of AlxCoCrCuFeNi high-entropy alloys as a function of aluminum content, Wear. 261 (2006) 513–519. https://doi.org/10.1016/j.wear.2005.12.008.

[283] J. Joseph, N. Haghdadi, K. Shamlaye, P. Hodgson, M. Barnett, D. Fabijanic, The sliding wear behaviour of CoCrFeMnNi and AlxCoCrFeNi high entropy alloys at elevated temperatures, Wear. 428–429 (2019) 32–44. https://doi.org/10.1016/j.wear.2019.03.002.

[284] C.Y. Hsu, T.S. Sheu, J.W. Yeh, S.K. Chen, Effect of iron content on wear behavior of AlCoCrFexMo0.5Ni high-entropy alloys, Wear. 268 (2010) 653–659. https://doi.org/10.1016/j.wear.2009.10.013.

[285] E. Rabinowicz, A. Mutis, Effect of abrasive particle size on wear, Wear. 8 (1965) 381–390.

[286] A.I. Vakis, V.A. Yastrebov, J. Scheibert, L. Nicola, C. Minfray, A. Almqvist, M. Paggi, S. Lee, J.F. Molinari, G. Anciaux, S.E. Restrepo, A. Papangelo, P. Nicolini, R. Aghababei, C. Putignano, S. Stupkiewicz, J. Lengiewicz, G. Costagliola, F. Bosia, R. Guarino, N.M. Pugno, D. Dini, M.H. Müser, M. Ciavarella, Models and Methods for Tribology Across Scales : an Overview, Tribint_D_17_01694. (n.d.) 1–66.

[287] J. Zhang, Y. Peng, H. min Liu, Y. fei Liu, Influence of Normal Load, Sliding Speed and Ambient Temperature on Wear Resistance of ZG42CrMo, J. Iron Steel Res. Int. 19 (2012) 69–74. https://doi.org/10.1016/S1006-706X(12)60090-9.

[288] I.M. Hutchings, Tribology: Friction and Wear of Engineering Materials, in: 1992. https://api.semanticscholar.org/CorpusID:136809159.

[289] N. SOGA, O.L. ANDERSON, High-Temperature Elastic Properties of Polycrystalline MgO and Al2O3, J. Am. Ceram. Soc. 49 (1966) 355–359. https://doi.org/10.1111/j.1151-2916.1966.tb13283.x.

[290] R. Pourzal, R. Theissmann, M. Morlock, A. Fischer, Micro-structural alterations within different areas of articulating surfaces of a metal-on-metal hip resurfacing system, Wear. 267 (2009) 689–694. https://doi.org/10.1016/j.wear.2009.01.012.

[291] S.Q. Wang, L. Wang, Y.T. Zhao, Y. Sun, Z.R. Yang, Mild-to-severe wear transition and transition region of oxidative wear in steels, Wear. 306 (2012) 311–320. https://doi.org/10.1016/j.wear.2012.08.017.

[292] X. Wang, D. Mao, X. Wei, J. Li, H. Meng, W. Wang, Sliding friction induced atom diffusion in the deformation layer of 0.45% C steel rubbed against Tin

alloy, Tribol. Int. 64 (2013) 128–134. https://doi.org/10.1016/j.triboint.2013.03.008.

[293] X.L. An, Z.D. Liu, L.T. Zhang, Y. Zou, X.J. Xu, C.L. Chu, W. Wei, W.W. Sun, A new strong pearlitic multi-principal element alloy to withstand wear at elevated temperatures, Acta Mater. 227 (2022). https://doi.org/10.1016/j.actamat.2022.117700.

[294] K. Feng, T. Shao, The evolution mechanism of tribo-oxide layer during high temperature dry sliding wear for nickel-based superalloy, Wear. 476 (2021) 203747. https://doi.org/10.1016/j.wear.2021.203747.

[295] S.M. Hsu, M.C. Shen, A.W. Ruff, Wear prediction for metals, Tribol. Int. 30 (1997) 377–383.

[296] S.C. Lim, The relevance of wear-mechanism maps to mild-oxidational wear, Tribol. Int. 35 (2002) 717–723. https://doi.org/10.1016/S0301-679X(02)00033-6.

[297] J.E. Mogonye, T.W. Scharf, Tribological properties and mechanisms of self-mated ultrafine-grained titanium, Wear. 376–377 (2017) 931–939. https://doi.org/10.1016/j.wear.2016.10.016.

[298] P. Pérez, J.A. Jiménez, G. Frommeyer, P. Adeva, The Influence of the Alloy Microstructure on the Oxidation Behavior of Ti-46Al-1Cr-0.2Si Alloy, Oxid. Met. 53 (2000) 99–124. https://doi.org/10.1023/a:1004534830767.

[299] H. Kato, Severe-mild wear transition by supply of oxide particles on sliding surface, Wear. 255 (2003) 426–429. https://doi.org/10.1016/S0043-1648(03)00077-2.

[300] P. Hancock, R.C. Hurst, The Mechanical Properties and Breakdown of Surface Oxide Films at Elevated Temperatures, in: M.G. Fontana, R.W. Staehle (Eds.),

Adv. Corros. Sci. Technol. Vol. 4, Springer US, Boston, MA, 1974: pp. 1–84. https://doi.org/10.1007/978-1-4615-9059-0_1.

[301] H. So, The mechanism of oxidational wear, Wear. 184 (1995) 161–167. https://doi.org/https://doi.org/10.1016/0043-1648(94)06569-1.

[302] J. Jayaraj, P. Thirathipviwat, J. Han, A. Gebert, Microstructure, mechanical and thermal oxidation behavior of AlNbTiZr high entropy alloy, Intermetallics. 100 (2018) 9–19. https://doi.org/10.1016/j.intermet.2018.05.015.

[303] P. Kumar, T.N. Lam, P.K. Tripathi, S.S. Singh, P.K. Liaw, E.W. Huang, Recent progress in oxidation behavior of high-entropy alloys: A review, APL Mater. 10 (2022) 1–16. https://doi.org/10.1063/5.0116605.

[304] E.A.A. Jarvis, E.A. Carter, Exploiting covalency to enhance metal–oxide and oxide–oxide adhesion at heterogeneous interfaces, J. Am. Ceram. Soc. 86 (2003) 373–386.

[305] K. Holmberg, H. Ronkainen, A. Laukkanen, K. Wallin, Friction and wear of coated surfaces - scales, modelling and simulation of tribomechanisms, Surf. Coatings Technol. 202 (2007) 1034–1049. https://doi.org/10.1016/j.surfcoat.2007.07.105.

[306] N. Pilling, R. Bedworth, The oxidation of metals at high temperatures, (1923).

[307] C. Xu, W. Gao, Pilling-Bedworth ratio for oxidation of alloys, Mater. Res. Innov. 3 (2000) 231–235.

[308] Q. Jiang, D. Lu, C. Liu, N. Liu, B. Hou, The Pilling-Bedworth Ratio of Oxides Formed From the Precipitated Phases in Magnesium Alloys, Front. Mater. 8 (2021) 1–12. https://doi.org/10.3389/fmats.2021.761052.

[309] Q. Tan, A. Atrens, N. Mo, M.X. Zhang, Oxidation of magnesium alloys at elevated temperatures in air: A review, Corros. Sci. 112 (2016) 734–759. https://doi.org/10.1016/j.corsci.2016.06.018.

[310] Z.X. Zhu, X.B. Liu, Y.F. Liu, S.Y. Zhang, Y. Meng, H. Bin Zhou, S.H. Zhang, Effects of Cu/Si on the microstructure and tribological properties of FeCoCrNi high entropy alloy coating by laser cladding, Wear. 512–513 (2023) 204533. https://doi.org/10.1016/j.wear.2022.204533.

[311] ROBERT A. RAPP, Kinetics, Microstructures and Mechanism of Internal Oxidation - Its Effect and Prevention in High Temperature Alloy Oxidation, Corrosion. 21 (1965) 383–401.

[312] Y. Jia, Z. Wang, Q. Wu, Y. Wei, X. Bai, L. Liu, J. Wang, X. Liu, L. Wang, F. He, J. Li, J. Wang, Boron microalloying for high-temperature eutectic high-entropy alloys, Acta Mater. 262 (2024) 119427. https://doi.org/10.1016/j.actamat.2023.119427.

[313] X. Pei, Y. Du, H. Wang, M. Hu, H. Wang, W. Liu, Investigation of high temperature tribological performance of TiZrV0.5Nb0.5 refractory high-entropy alloy optimized by Si microalloying, Tribol. Int. 176 (2022) 107885. https://doi.org/10.1016/j.triboint.2022.107885.

[314] Y. Zhang, S. Ye, H. Ke, K.C. Chan, W. Wang, In situ synthesis of N-containing CoCrFeNi high entropy alloys with enhanced properties fabricated by selective laser melting, Mater. Des. 229 (2023) 111891. https://doi.org/10.1016/j.matdes.2023.111891.

[315] Y. Zhang, C. Yang, H. Ke, K.C. Chan, W. Wang, A study on the microstructure and mechanical behavior of CoCrFeNi high entropy alloy fabricated via laser powder bed fusion: Experiment and crystal plasticity finite element modelling, Mater. Sci. Eng. A. 893 (2024) 146111. https://doi.org/10.1016/j.msea.2024.146111.

[316] G. Gottstein, U.F. Kocks, Dynamic recrystallization and dynamic recovery in< 111> single crystals of nickel and copper, Acta Metall. 31 (1983) 175–188.

[317] H.J. McQueen, J.J. Jonas, Recovery and recrystallization during high temperature deformation, in: Treatise Mater. Sci. \& Technol., Elsevier, 1975: pp. 393–493.

[318] T. Yang, S. Xia, S. Liu, C. Wang, S. Liu, Y. Zhang, J. Xue, S. Yan, Y. Wang, Effects of AL addition on microstructure and mechanical properties of AlxCoCrFeNi High-entropy alloy, Mater. Sci. Eng. A. 648 (2015) 15–22. https://doi.org/10.1016/j.msea.2015.09.034.

[319] T. Yang, Y.L. Zhao, Y. Tong, Z.B. Jiao, J. Wei, J.X. Cai, X.D. Han, D. Chen, A. Hu, J.J. Kai, K. Lu, Y. Liu, C.T. Liu, Multicomponent intermetallic nanoparticles and superb mechanical behaviors of complex alloys, Science (80-.). 362 (2018) 933–937. https://doi.org/10.1126/science.aas8815.

[320] K. Gao, Y. Chu, W. Zhou, Y. Tian, Y. Zhang, Y. Li, Phase inversion in a lightweight high Al content refractory high-entropy alloy, J. Mater. Sci. \& Technol. 150 (2023) 124–137.

[321] B.B. Wang, G.M. Xie, L.H. Wu, P. Xue, D.R. Ni, B.L. Xiao, Y.D. Liu, Z.Y. Ma, Grain size effect on tensile deformation behaviors of pure aluminum, Mater. Sci. Eng. A. 820 (2021). https://doi.org/10.1016/j.msea.2021.141504.

[322] D. Gerlich, E.S. Fisher, The high temperature elastic moduli of aluminum, J. Phys. Chem. Solids. 30 (1969) 1197–1205. https://doi.org/10.1016/0022-3697(69)90377-1.

[323] D.R. Lide, CRC handbook of chemistry and physics, CRC press, 2004.

[324] J. Dai, J. Zhu, C. Chen, F. Weng, High temperature oxidation behavior and research status of modifications on improving high temperature oxidation resistance of titanium alloys and titanium aluminides: A review, J. Alloys Compd. 685 (2016) 784–798. https://doi.org/10.1016/j.jallcom.2016.06.212.

[325] L.P.H. Jeurgens, W.G. Sloof, F.D. Tichelaar, E.J. Mittemeijer, Composition and chemical state of the ions of aluminium-oxide films formed by thermal oxidation of aluminium, Surf. Sci. 506 (2002) 313–332. https://doi.org/10.1016/S0039-6028(02)01432-2.